# UC Irvine
## UC Irvine Electronic Theses and Dissertations

### Title
Characterization and Use of Vibrational Tags in Coherent Raman Microscopy

### Permalink
https://escholarship.org/uc/item/1ds6860n

### Author
Prince, Richard Cody

### Publication Date
2021

### Copyright Information
This work is made available under the terms of a Creative Commons Attribution-NoDerivatives License, available at https://creativecommons.org/licenses/by-nd/4.0/

Peer reviewed|Thesis/dissertation

eScholarship.org Powered by the California Digital Library
University of California

UNIVERSITY OF CALIFORNIA,
IRVINE

# Characterization and Use of Vibrational Tags in Coherent Raman Microscopy

DISSERTATION

submitted in partial satisfaction of the requirements
for the degree of

DOCTOR OF PHILOSOPHY

in Biomedical Engineering

by

Richard C. Prince

Dissertation Committee:
Professor Eric O. Potma, Chair
Associate Professor Michelle A. Digman
Professor Rachel W. Martin

2021

Chapter 1 © 2021 © The Authors. Published by SPIE under a Creative Commons Attribution 4.0 Unported License
Chapter 2 © 2016 American Chemical Society
Portions of Chapter 3© 2016 American Chemical Society
Figure 6.1 © 2020 Elsevier
Portions of Chapter 6 © 2020 Elsevier
Figure 6.8 © 2019 Springer Nature
Figure 7.2a © 2018 Springer Nature
All other materials © 2021 Richard C. Prince

# DEDICATION

This work is dedicated to the memory of two great men in my life, my uncle, Conrad Spain, and my undergraduate advisor, Dr. Jon Levin. Without the support and encouragement of them both, I might have never pursued this degree, left Tennessee, or learned to put myself out there and step up to organizational leadership.

# TABLE OF CONTENTS

Page

**LIST OF FIGURES** **vi**

**LIST OF TABLES** **viii**

**ACKNOWLEDGMENTS** **ix**

**VITA** **x**

**ABSTRACT OF THE Dissertation** **xiv**

**1 Introduction: A Technique Searching for Applicability** **1**
1.1 Perspective on Coherent Raman Scattering . . . . . 2
1.2 Growing Pains . . . . . 3
1.3 Specificity . . . . . 4
1.4 Sensitivity . . . . . 7
1.5 Speed . . . . . 8
1.6 Taking Stock and Looking Ahead . . . . . 11

**2 Decreasing volume, Increasing Impact: A History of Stimulated Raman Scattering** **13**
2.1 The Birth & Evolution of Stimulated Raman Scattering . . . . . 14
2.1.1 The Birth of SRS: Light Conversion & Early Spectroscopy . . . . . 17
2.1.2 First Wave: Picosecond Time-resolved Spectroscopy . . . . . 18
2.1.3 Second Wave: Ultrafast and Impulsive Regimes . . . . . 18
2.1.4 Third Wave: Diffraction-Limited Microscopy . . . . . 21
2.1.5 Fourth Wave: Nanoscale and single molecule spectroscopy . . . . . 23
2.1.6 Towards SRS Nanoscopy . . . . . 24
2.2 Probing molecules with SRS Spectroscopy . . . . . 26
2.2.1 SRS Spectroscopy in the Time Domain . . . . . 27
2.2.2 Features of time-domain SRS . . . . . 31
2.2.3 Femtosecond stimulated Raman scattering (FSRS) . . . . . 34
2.3 Probing Smaller Samples: The Transition to Microscopy . . . . . 37
2.3.1 Shrinking the probing volume . . . . . 37
2.3.2 Phase matching in coherent Raman microscopy . . . . . 39
2.3.3 Instrumentation for SRS Microscopy . . . . . 41

2.3.4 Applications of SRS Microscopy . . . 44
2.4 From Ensembles to Single Molecules . . . 47
2.4.1 Enhancing SRS with electronic resonances . . . 47
2.4.2 Enhancing SRS with plasmonic resonances . . . 50
2.4.3 Advanced techniques: Non-Optical Detection . . . 53

**3 Coherent Raman Scattering: a Nonlinear Optical Process 55**
3.1 A Brief History of Nonlinear Microscopy . . . 56
3.2 Understanding Nonlinear Optical Processes . . . 57
3.2.1 The Lorentz Model and the Harmonic Oscillator . . . 58
3.2.2 Good Vibrations: A Model of Linear Raman Scattering . . . 61
3.3 An Overview of Stimulated Raman Scattering . . . 69
3.3.1 Field picture . . . 70
3.3.2 Classical vibrational motions . . . 73
3.3.3 Quantum mechanical description: density matrix . . . 77
3.3.4 Magnitude of the Raman response . . . 83
3.3.5 SRS versus CARS . . . 85
3.4 Information from an SRS Experiment . . . 87

**4 Instrumentation & Methodology 90**
4.1 Common Modalities . . . 91
4.2 Spontaneous Raman Micro-Spectrocopy . . . 94
4.3 The Narrowband CRS Microscope . . . 95
4.4 Hyperspectral Imaging . . . 98

**5 Deuterated Raman Probes: Elucidating Lipogenesis in Cartilage 100**
5.1 A Background on Cartilage . . . 101
5.2 Germ Layer Origins of Lipochondrocytes . . . 103
5.3 Lipid and Gene Profiling . . . 106
5.4 Lipochondrocytes Activate Lipogenesis . . . 107
5.5 Lipochondrocytes require *de novo* Lipogenesis . . . 111
5.6 Human Facial Cartilage Cells Accumulate Lipids . . . 114
5.7 Discussion of Results . . . 117
5.8 Study Specific Methodology . . . 118
5.8.1 Glucose-d7 *Ex Vivo* Ear Culture . . . 118
5.8.2 SRS Microscopy . . . 118
5.8.3 Mouse models . . . 119
5.8.4 OilRedO . . . 119
5.8.5 Histochemistry, immunostaining, and imaging . . . 120
5.8.6 Measurements . . . 121
5.8.7 Modified Diet Experiments . . . 121
5.8.8 Topical Drug Treatment . . . 121

**6 Exploring the Origins of Meibum Lipids with SRS Microscopy 122**
6.1 Meibomian Gland Dysfunction . . . 123
6.2 PPAR$\gamma$ Signaling in Meibocytes . . . 125
6.2.1 Introduction . . . 125
6.2.2 EPA induced lipid accumulation via PPAR$\gamma$ signaling in meibocytes . 127
6.2.3 EPA induced upregulation of lipogenic genes by activating PPAR$\gamma$ signaling . . . 131
6.2.4 EPA and rosiglitazone induced cell cycle exit of meibocytes . . . 131
6.2.5 Discussion . . . 132
6.2.6 Study specific materials and methods . . . 136
6.2.7 Conclusions . . . 138
6.3 *De Novo* Lipogenesis and Lipid Uptake in Meibogenesis . . . 139
6.3.1 Introduction . . . 139
6.3.2 Assessment of Uptake of Deuterated Precursors . . . 140
6.3.3 Acetate or Lipid . . . 148
6.3.4 Discussion . . . 152
6.3.5 Study specific methodologies . . . 152
6.3.6 Conclusion . . . 153

**7 The Search for Raman Probes: Isocyanides and Elusive Natural Products 155**
7.1 Introduction . . . 156
7.2 Predicting & Characterizing Isocyanides . . . 158
7.2.1 A Brief Review of DFT . . . 159
7.2.2 Predicting Peak Position . . . 161
7.2.3 EdU: A Molecular Standard for SRS . . . 165
7.3 Discussion . . . 166
7.4 Specific Methods . . . 167

**8 Conclusion & Future Directions 168**
8.1 Introduction . . . 169
8.2 Isotope Labeling in Lipochondrocytes . . . 170
8.3 Imaging Lipid Distribution & Lipid Origins . . . 170
8.4 Towards More Specific Probes . . . 171
8.5 Final Thoughts . . . 172

**Bibliography 173**

# LIST OF FIGURES


Page

1.1 The first coherent Raman microscope . . . . . 12

2.1 Bibliometrics of stimulated Raman scattering . . . . . 14
2.2 Author's Interpretation of the first SRS System . . . . . 16
2.3 Timeline of major developments in SRS technology . . . . . 19
2.4 SRS microspectroscopy with a high numerical aperture objective. . . . . 21
2.5 The First Demonstration of SRS Microscopy in Biology . . . . . 23
2.6 SRS Imaging in the Visible Regime . . . . . 26
2.7 Diagrammatic representation of the SRS process . . . . . 30
2.8 Frequency and Time dependence of the third-order polarization . . . . . 32
2.9 An Example of Femptosecond Stimulated Raman Scattering . . . . . 36
2.10 A typical SRS setup with two synchronized beams. . . . . 41
2.11 Examples of SRS imaging of various samples in the high frequency range ($2000\ \mathrm{cm}^{-1} - 3300\ \mathrm{cm}^{-1}$) . . . . . 45
2.12 Different forms of electronic enhancement of the SRS signal. . . . . 48
2.13 The First Demonstration of Surface-Enhanced SRS . . . . . 52

3.1 Simple Harmonic Oscillators . . . . . 59
3.2 . . . . . 61
3.3 Diagrammatic Representation of Classical Molecular Scattering . . . . . 65
3.4 Diagrammatic Representation of recorded scattering peaks . . . . . 66
3.5 Jablonski Diagrams for Elastic and Inelastic Scattering . . . . . 67
3.6 Double-Sided Feynman Diagram for the Spontaneous Raman Process . . . . 68
3.7 Schematic of the SRS light-matter interaction. . . . . 70
3.8 Frequency (a,c,e,g) and time (b,d,f,h) dependence of the third-order polarization as probed under different experimental conditions. . . . . 82
3.9 Raman Spectra of DMSO and deuterated DMSO. . . . . 87
3.10 SRS imaging at 2120 $cm^{-}1$ corresponding to CD2 stretches and 2841 $cm^{-}1$ corresponding to CH2 symmetric stretches. . . . . 89

4.1 Illustration of the Focal Volume of a High Numerical Aperture Objective . . 91
4.2 Jablonski Diagrams for NLO Imaging . . . . . 92
4.3 Second Harmonic Generation of Biological Materials . . . . . 93
4.4 Spontaneous Raman Spectra of L-DOPA and L-DOPA-d3 . . . . . 94
4.5 Illustrated Layout of a Raman System . . . . . 96

4.6 Vertex Component Analysis of Cultured Meibocytes . . . . . 99

5.1 Comparison between adipocytes and lipochondrocytes . . . . . 101
5.2 Multiple cartilages show presence of Lipochondrocytes . . . . . 104
5.3 SRS images of mouse ear cartiledge showing fenestrae without (a) and with (b) lipid bearing cells. . . . . 105
5.4 Phases of ear pinna growth in mice. . . . . 108
5.5 Expression patterns of SOX9 and PCNA in the developing ear cartilage. . . 110
5.6 Lipogenesis dominates lipochondrocyte differentiation. . . . . 111
5.7 SRS Finds Direct Evidence of De Novo Lipogenesis . . . . . 112
5.8 Inhibition of Key Enzymes Alters Morphology . . . . . 113
5.9 Genetic Inhibition Disrupts LC Differentiation . . . . . 114
5.10 Human Facial Cartilages Accumulate Lipids . . . . . 115
5.11 Staining and Nonlinear Microscopy Reveals Lipid Accumulation . . . . . 116
5.12 Structure of the Diazo Dye Oil Red O . . . . . 119

6.1 Layers of the Tear Film . . . . . 123
6.2 Rosiglitazone Application Leads to Lipid Accumulation . . . . . 125
6.3 Molecular Structure of Rosiglitazone (a) Eicosapentanoic acid (b) . . . . . 127
6.4 Effect of EPA on lipid synthesis in hMGEC . . . . . 128
6.5 SRS Analysis of Lipid Droplet Composition in HMGEC . . . . . 129
6.6 Effect of PPAR$\gamma$ Signaling on mRNA expression. . . . . 132
6.7 Effect of EPA on Ki-67 labeling in cultured hMGEC. . . . . 133
6.8 Deuterium Transfer Along Major Biosynthetic Pathways . . . . . 140
6.9 Structure Diagrams of Deuterated Molecules . . . . . 141
6.10 Spontaneous Raman Scattering Spectra of Deuterated Compounds . . . . . 142
6.11 Deuterium Incorporated from Deuterated Glucose . . . . . 143
6.12 SRS Imaging of Deuterium Incorporated from Deuterated Acetate . . . . . 145
6.13 SRS Imaging of Deuterium Incorporated from Deuterated EPA . . . . . 146
6.14 SRS Imaging of Deuterium Incorporated from Palmitic Acid . . . . . 148
6.15 CRS Images of Meibocytes with Acetate and Palmitic Acid . . . . . 150

7.1 Normalized Raman Spectra in the Cell-Silent Region . . . . . 156
7.2 Deuterium Oxide Labeling and SRS Imaging . . . . . 158
7.3 Spontaneous and Stimulated Raman Scattering Spectra of DICA . . . . . 159
7.4 Mean Error Between Predicted and Measured Spectra . . . . . 164
7.5 Mean Error between cRIE and measured RIE . . . . . 165

# LIST OF TABLES

Page

3.1 Absolute Raman differential scattering cross sections in $cm^2$ per molecule per steradian for various compounds. . . . . 85

6.1 Culture Additions for RB-14 Meibocytes . . . . . 149
6.2 Summarized Results of Acetate and Lipid Experiments . . . . . 151

7.1 List of Molecules for DFT Calculations . . . . . 160
7.2 Functionals and Basis Sets Used in Calculations . . . . . 161
7.3 PBE/tzvp results of DFT Calculations . . . . . 162
7.4 B3LYP/tzvp results of DFT Calculations . . . . . 162
7.5 Comparison of Predicted Values vs. Measured Values . . . . . 163
7.6 Percent Error Between Predicted Values and Measured Values . . . . . 164
7.7 Measured and Computed RIE . . . . . 166

# ACKNOWLEDGMENTS

I owe a debt of gratitude to my advisor Eric, for being more patient with me than I ever should have asked. To my mother and grandparents, for their unyielding support, and to Amy for being there every step of the way. I would be remiss not to thank my lab mates especially Adam Hanninen, Dave Knez, Yong Li, Alex Fast, and Brian Albee, for always being willing to answer questions or let me vent. Thank you everyone for your help along the way.

The text of this dissertation is a reprint of several papers as they appear in the Journal of Biomedical Optics, Chemical Reviews, and The Optical Surface. The co-author, Dr. Eric O. Potma, listed in this publication directed and supervised research which forms the basis for the thesis/dissertation.

I would like to acknowledge the co-authors that made much of this work possible: Professor James Jester, Dr. Raul Ramos, Dr. Adam Hanninen. Dr. Sun Woong Kim and Professor Maksim Plikus. Their ideasm contributions, and guidance was fundamental to the completion of this work.

Funding for my research provided by the National Science Foundation and the National Institutes of Health. Grants NIH R01-GM132506, NSF CBET-2013814, and NSF DGE-1144901 were instrumental in completion of this work and my training as a scientist.

# VITA

## Richard C. Prince

### EDUCATION

**Doctor of Philosophy in Biomedical Engineering** **2021**
University of California, Irvine *Irvine, California*

**Master of Science in Biomedical Engineering** **2018**
University of California, Irvine *Irvine, California*

**Bachelor of Arts in College Scholars & Physics** **2015**
University of Tennessee, Knoxville *Knoxville, Tennessee*

### RESEARCH EXPERIENCE

**Graduate Student Researcher** **2016-2021**
Potma Labs - Advancing Vibrational Imaging
University of California, Irvine *Irvine, California*

**Undergraduate Researcher** **2014-2015**
Bredesen Center for Interdisciplinary Research
University of Tennessee, Knoxville *Knoxville, Tennessee*

**Undergraduate Researcher** **2013-2014**
Calhoun Laser Spectroscopy Group
University of Tennessee, Knoxville *Knoxville, Tennessee*

**Undergraduate Researcher** **2012-2013**
Soft Matter Biophysics Research Group
University of Tennessee, Knoxville *Knoxville, Tennessee*

## TEACHING EXPERIENCE

**Teaching Assistant** **S2021**
BME170 - Measurement and Analysis of Biological Systems
University of California, Irvine *Irvine, California*

**Teaching Assistant** **S2020-F2020**
BME60A - Introduction to Data Acquisition
University of California, Irvine *Irvine, California*

**Student Instructor** **Summer 2015**
Governor's School for the Sciences and Engineering
University of Tennessee, Knoville *Knoxville, Tennessee*

**Teaching Assistant** **2013-2015**
PHYS250 - Modern Physics, PHYS211-212 - Elements of Physics
University of Tennessee, Knoville *Knoxville, Tennessee*

## PUBLICATIONS

**Coherent Raman scattering microscopy: capable solution in search of a larger audience** **2021**
Journal of Biomedical Optics

doi:10.1117/1.JBO.26.6.060601

**Infrared chemical imaging through non-degenerate two-photon absorption in silicon-based cameras** **2020**
Light: Science & Applications

doi:10.1038/s41377-020-00369-6

**Eicosapentaenoic acid (epa) activates ppar-$\gamma$ signaling leading to cell cycle exit, lipid accumulation, and autophagy in human meibomian gland epithelial cells (hmegec)** **2020**
The Ocular Surface

doi:10.1016/j.jtos.2020.04.012

**Visualizing tpp structures with coherent raman scattering microscopy** **2020**
Micro and Nano Technologies

doi:10.1016/B978-0-12-817827-0.00055-2

**Going Visible: high-resolution coherent raman imaging of cells and tissues** **2019**
Light: Science & Applications

doi:10.1038/s41377-018-0119-5

**High-resolution infrared imaging of biological samples with third-order sum-frequency generation microscopy** **2018**
Biomed. Opt. Express

doi:10.1364/BOE.9.004807

**Triple modal coherent nonlinear imaging with vibrational contrast** **2018**
IEEE Journal of Selected Topics in Quantum Electronics

doi:10.1109/JSTQE.2018.2846030

**Crossing the arterial wall with cars** **2017**
Proceedings of the National Academy of Sciences

doi:10.1073/pnas.1704101114

**Stimulated Raman scattering: from bulk to nano** **2016**
Chemical Reviews

doi:10.1021/acs.chemrev.6b00545

**Food for thought . . . and travel** **2013**
SPS Observer

**Oral Presentations**

**Cellular Metabolism and Chemical Dynamics through the Lens of Vibrational Microscopy** **March 2021**
Invited Speaker - CSULB BUILD Colloquium

**Analysis of Lipid Expression in Meibomian Glands by Stimulated Raman Scattering** **February 2019**
SPIE Photonics West

**Letting Evidence Lead the Way: How Scientific Principles Can Improve Government** **January 2018**
Brews & Brains

# ABSTRACT OF THE DISSERTATION

Characterization and Use of Vibrational Tags in Coherent Raman Microscopy

By

Richard C. Prince

Doctor of Philosophy in Biomedical Engineering

University of California, Irvine, 2021

Professor Eric O. Potma, Chair

In this work, we outline the current state of coherent Raman scattering microscopy with a special emphasis on the sub-field of stimulated Raman scattering. This field has seen tremendous growth in development and applicability over the last twenty years. Much of the work has focused on demonstrating the utility of both CARS and SRS to the field of lipid metabolism, and there it has seen great success. However, it has not managed to get into the hands of as many users as might be desired. CRS is often criticized for a lack of specificity. Here we have demonstrated the successful use of isotopic Raman probes to the study of metabolism in multiple cell types including an understudied form of cartilage and in the origins of meibum lipid as it related to dry eye disease. We will also discuss the application of computational chemistry techniques to the study and design of molecular probes for Raman imaging.

# Chapter 1

# Introduction: A Technique Searching for Applicability

Parts of this chapter were published in 2021 in the Journal of Biomedical Optics as *Coherent Raman scattering microscopy: capable solution in search of a larger audience* by R.C. Prince and E. O. Potma.

## 1.1 Perspective on Coherent Raman Scattering

Almost 40 years since the coherent Raman scattering (CRS) microscope produced its first image; the CRS technology has brought together an active community of developers poised to deliver unique imaging capabilities to a broad group of users.[1;2] The technical performance of the CRS microscope has improved dramatically over the years. Still, these developments have not yet translated into a substantial user base beyond a strong core of enthusiasts. To understand the current state of the field, we reflect on the birth, rapid rise, and inescapable growing pains of the technique. We look back on nearly four decades of development to examine where the CRS imaging approach might be headed in the next decade.

The benefits and applications of new optical imaging approaches are not always evident at the inception of the technique. The first CRS microscope, built in 1982 and shown in Figure 1.1, was an unmistakable technological advance. The system produced images of onion cells in heavy water[1] as well as deuterated multilamellar vesicles.[3] At the same time, the immediate impact of the device remained largely unclear. Although it was recognized that the CRS signal levels could "exceed those produced in spontaneous Raman processes"[4] and that spurious fluorescence contributions could be largely avoided, an application space in which the attributes of CRS microscopy made a clear difference stayed out of sight.

Even after substantial improvements to the CRS microscope were reported in 1999[5], experts in the field of optical microscopy continued to be skeptical about the prospects of the still-nascent CRS technology.[6] Such skepticism was not surprising since images required up to

30 minutes to record. Yet, less than a decade later, further developments had improved the imaging rate to such an extent that speed became CRS microscopy's most celebrated asset.[7–10]

The Raman effect senses molecules through their characteristic vibrational modes. Using this capability in a microscope makes it possible to generate chemically selective images without the use of labels. The much higher image acquisition rate offered through the nonlinear CRS mechanism implies that the Raman effect can now be used for label-free mapping of live cells and tissues - applications for which fast imaging capabilities are of essence. After the advances of the early 2000s, it was now possible to create molecular time-lapses of dynamic processes and image 3D tissue volumes with rates comparable to fluorescence.

The speed of CRS imaging allowed the study of water dynamics in cells and tissues.[11–14] And the exceptional contrast generated by lipids led to visualization of lipids in cultured cells, tissue slices, and live animals. The high CRS signals obtained from pooled lipid in otherwise aqueous environments enabled a wide range of studies that uncovered various aspects of lipid biology[15], with applications in the areas of intracellular lipid metabolism[16–18], atherosclerosis[19–21], neurodegenerative diseases[22–26], the role of lipids in cancer biology[27–29], and many more. Thanks to the technique's successes in lipid imaging, its reputation as a biological and biomedical imaging technique grew. On the other hand, these successes also cemented the notion that CRS microscopy is synonymous with lipid mapping and not much else.

## 1.2 Growing Pains

The adoption of coherent Raman scattering (CRS) microscopy has been a slow and seemingly protracted process. Primarily driven by a core group of devoted developers, CRS techniques

have begun making inroads into university imaging facilities, neuroscience laboratories, and clinic bedsides. However, widespread adoption is still lacking, with many instruments existing only in large optical development labs. The high cost, complexity, and limited supplier base of turn-key devices have undoubtedly contributed to CRS's undersized adoption, but so too has a focus in the literature on development. The first CRS images were produced nearly forty years ago, and the technique has become virtually synonymous with lipid imaging. However, recent progress on Raman probes to address fundamental questions of cellular metabolism and translation into bedside devices may pave the way for CRS to become a practitioner's tool.

Many of the growing pains associated with the adoption of CRS imaging techniques boil down to a need for dedicated probes. A reckoning with the limitations of CRS imaging was inevitable to push the technique into widespread use. Hyperspectral imaging speed, sensitivity, and molecular specificity have all played a central role in driving the development of CRS systems in the past decade as underperformance in each limited CRS's applicability for widespread use. It is crucial that we take stock of the improvements in each of these performance areas and demonstrate the potential to answer fundamental biomedical questions.

## 1.3 Specificity

In the past decade, the development and use of Raman tags have grown significantly to identify specific metabolites. The general strategy of Raman tagging is that particular targets are equipped with chemical groups that have their characteristic vibrations in a frequency range free of overlapping band structures. Perhaps the gentlest form of Raman tagging is the substitution of a given element with one of its isotopes, which alters the effective mass of the mode and this shifts its vibrational energy. A prime example is the replacement of

carbon-bonded hydrogen atoms with deuterons, which moves the mode vibration into the cell silent region of the spectrum. This concept was already employed to improve specificity of the world's first CRS microscope[3], and has proven early on a reliable strategy for identifying specific fatty acids in membranes.[30;31]

The need for Raman tags arose from limited molecular information available from endogenous sources. Lipid imaging is so successful, in part, due to the isolated frequency range of the carbon-hydrogen (C-H) bond vibrations. In the absence of overlapping bands from other chemical group vibrations, the C-H stretching vibrations are confidently assigned. Their signal is used as a reliable source of contrast in CRS images. In direct contrast is the fingerprint region, known for its richness in information, but correspondingly, an intensely congested spectral range where individual bands' assignment is immensely challenging due to their overlapped nature.

The molecular specificity of vibrational bands is limited, even when vibrational lines can be resolved and pinpointed. For instance, the Amide I vibrational mode can often be discriminated from nearby vibrational lines, but targeting this mode provides information on all protein structures in the probed volume rather than a specific enzyme's whereabouts. Similarly, the strong stretching mode of the carbon-carbon double bond (C=C) reports on the presence of numerous molecular species that contain a C=C moiety, complicating the identification of a specific target based on this band alone. Given these challenges, it is no surprise that the idea of Raman labeling has proved powerful in dramatically improving the molecular specificity of Raman-based imaging techniques.

The use of deuterated probes gained new momentum during the past decade through the realization that isotopic analogs of endogenous molecules can be metabolically converted in live cells and tissues, thus providing a "hook" to track metabolic processes. For instance, uptake and subsequent esterification of deuterated fatty acids or cholesterol offer a direct view of the cellular machinery a work.[32–34] This principle can be extended to deuterated

amino acids to follow protein synthesis de novo[35;36], deuterated glucose analogs to monitor lipogenesis[37;38], glycogen[39] and biomass production[40], as well as D2O to study protein and lipid metabolism in live animals.[41] The ability to directly examine metabolic pathways in live biological systems offers a unique view of fundamental processes such as cellular homeostasis, tissue growth, aging and oncogenesis. Hence, although the use of deuterated probes may appear a small technical feat, it is transformative in the way it has expanded the biomedical impacts of CRS microscopy.

Whereas the carbon-deuterium (C-D) bond offers a labeling strategy of minimal chemical interference, the Raman response from individual bonds is relatively weak, necessitating probes that incorporate numerous deuterons to achieve nominal CRS signals. Alternatively, molecular targets can be equipped with small chemical motifs that exhibit much higher Raman cross sections. The approach was popularized for CRS through the use of bio-orthogonal alkyne tags, small chemical groups with an exceptionally strong Raman response and a vibrational resonance in the cell silent region of the spectrum.[42–44] Alkyne tags are unreactive under typical physiological conditions and small enough to avoid compromised metabolism of its molecular carrier. These tags have been incorporated into a wide range of small molecules, enabling the visualization of specific nucleic acids[43;44], amino acids[43;44], glucose[45], fatty acids[42;46], sterols[47], choline[43], and many more, in live cells and tissues. This idea has been expanded to include other tags, including nitriles and isonitriles. Nitriles have the added benefit of a resonance frequency that is sensitive to the local electrostatics of its immediate chemical environment, allowing, for instance, local probing of water content.[48]

The use of Raman tags is not unique to CRS microscopy per se. In fact, the concept was introduced to improve the molecular specificity in conventional Raman microscopy, and many of the tag-bearing small molecules now used in CRS imaging were first developed for linear Raman applications.[49;50] Nonetheless, the isolated nature of the spectral bands associated with these tags allows direct identification with narrowband CRS microscopy. Here, the fast

imaging capabilities of CRS imaging offer tangible benefits, as metabolic processes in live cells and organisms can be tracked in real time, a capability that is simply out of reach for spontaneous Raman microscopy.

## 1.4 Sensitivity

The sensitivity of CRS imaging is generally in the range of 1-10 $mM$ for endogenous compounds. The use of Raman tags, which typically have higher Raman cross sections, can push the sensitivity into the 100 $\mu$M range. Although impressive, this detection limit is often higher than the concentration of small endogenous molecules and metabolites in the cell. The application space of CRS microscopy would thus widen significantly if ways can be found to improve the sensitivity.

Since the illumination power is limited by sample damage, the only conceivable way to improve the CRS sensitivity is to increase the effective Raman cross section of the molecular responders. For endogenous compounds, the Raman cross-section is an inherent property of the molecule, which is essentially immutable to change when excitation wavelengths are far from electronic resonances. For extrinsic probes, however, Raman cross-sections can be boosted significantly when electronic resonances are present near the frequency of the excitation beam. The principle of resonance Raman scattering can be ported to CRS excitation and correspondingly improve the molecular concentration detection limits.[51–53] This strategy requires chromophores that exhibit vibrational modes with good couplings to the electronic resonance. Select fluorophores developed for the purpose of fluorescence labeling display excellent enhancement of the vibrational response of up to 106 times when the excitation frequencies are tuned near the electronic transition, as demonstrated for stimulated Raman scattering (SRS).[52;53] The result is that such fluorescent probes can be detected through the CRS process at sub-$\mu$M concentrations. This is significant, because it opens up the possi-

bility to map distinct probes in a multi-label sample, with the number of different probes ultimately limited by the bandwidth of the Raman line rather than by the bandwidth of fluorescence. Whereas it is challenging to label the sample with more than four probes in fluorescence microscopy because of cross talk between the detection channels, in resonance enhanced SRS imaging multiplex labeling can be extended to tens of different probes.[53;54] In terms of multiplex imaging, this capability is a big win as many cell biological studies require the visualization of multiple molecular actors to uncover intracellular processes and pathways.

The multiplex capability offered through resonance enhanced SRS can be pushed even further to lower probe concentrations. By letting the probe selectivity be determined by the SRS excitation process alone, the bandwidth on the detection side can, in principle, be relaxed. This implies that after a Raman transition, the molecule can be excited in a second step to an emitting electronic state, allowing efficient detection of the chromophore via fluorescence emission. If the electronic transition is conditional on a successful Raman transition, then the chromophore can be selected based on its narrow Raman band while the probing sensitivity is boosted by the highly efficient fluorescence detection strategy. This process, called stimulated Raman excited fluorescence (SREF), makes it possible to detect molecules at concentrations down to the single molecule limit.[55] The SREF method combines the advantages of multiplex imaging offered by SRS with the high sensitivity of fluorescence microscopy, enabling imaging studies that were hitherto impossible with either of these techniques alone.

## 1.5 Speed

The advances discussed in the previous two Sections focused on CRS improvements through exploiting and optimizing the target molecule's response. The intelligent use of molecular probes expands CRS's application landscape without technical advancements of the micro-

scope instrument itself. Next, we will focus on increasing the image acquisition speed of the microscope, an advance that often involves modifications of the system's hardware. In particular, we are interested in ways that fast hyperspectral CRS imaging can be accomplished. The term "hyperspectral" is used here to denote the acquisition of data cubes where there are two spatial dimensions (typically the lateral coordinates x and y) and one spectral dimension, resulting in a 2D spatial image where each spatial pixel is expanded along the third coordinate to represent the vibrational spectrum.

Over the last decade, there has been a proliferation of approaches for recording CRS hyperspectral data cubes. The variety of approaches is vast, which implies that there are also numerous ways to categorize them.[2;56;57] For the discussion here it will be helpful to categorize hyperspectral CRS techniques in terms of the detection strategy, namely either the use of a single pixel detector or the involvement of a detector array. For the case of a detector array, a spectral dispersion element is used, and numerous spectral values are recorded simultaneously. Where a single pixel detector is used, a data stream of values needs to be recorded in time from which spectral information can then derived.

By the early 2000s, it was recognized that spectral information in microscopic CARS measurements could be obtained efficiently by using a standard spectrometer as the detector.[58–60] The speed of the resulting images is then limited primarily by the strength of the signal and the data processing time of the arrayed detector. Various optimization strategies have led to the acquisition of broadband CARS spectra, spanning the $600cm^{-}1$ to $3100cm^{-}1$ range, with pixel dwell times as short as 3.5 ms for biological samples.[61] For comparison, the fastest spontaneous Raman microscope requires at least 100 ms to obtain similar quality spectra.

The use of conventional arrayed detectors is more challenging in SRS microscopy because of the necessity of high frequency modulation. One approach is the use of multiple lock-in detectors, each capturing the information from a spectral bin[62], a strategy that has been expanded to no less than 128 lock-in amplifiers.[63] Other arrayed detectors used for SRS have

included fast CMOS detectors[64;65] and arrayed photodiodes where each element is equipped with a resonant LC filter.[66] Using the latter recipe, SRS spectra consisting of 32 bins have been recorded within only 5 $\mu$s, corresponding to 200,000 spectra/s.[67]

Arrayed detectors offer limited flexibility in balancing the number of spectral data points with acquisition speed. For this reason, many CRS methods have focused on variations in the use of fast single element detectors. The most straightforward method is the rapid spectral scanning of one of the input beams in narrowband CRS while recording images sequentially for each spectral setting.[68–70] If starting from a broadband beam, a rapid tunable filter, such as a galvanometric mirror and a grating[71] or acousto-optic tunable filter (AOTF)[72], offers a viable way to collect CRS hyperspectral data cubes swiftly. Another popular approach is the spectral focusing method, used both for CARS[73–75] and SRS[76–78], where the spectral dimension is obtained through a temporal scan of the delay between the chirped broadband pump and Stokes pulses. Rapid scanning of the delay is possible through various means, for instance with the aid of acousto-optic filters, producing spectral scans in as little as 12.5 $\mu$s per pixel.[79] Other approaches use spectral modulation techniques, whereby the spectrum is amplitude modulated by a spatial light modulator[80], digital micromirror device[81] or AOTF[82], and the spectrum is retrieved computationally from a sequence of CRS measurements obtained for different realizations of the spectral content of the input beams. A similar concept can also be applied when a single broadband beam is employed to drive the CRS process, using amplitude and phase shaping to achieve the desired resolution. Many spectral shaping techniques exist, most of them comprehensively summarized in reference.[56]

A final development of note is found in the area of Fourier transform CRS, which rapidly collects temporal interferograms that can subsequently be transformed to the spectral domain to retrieve Raman-based spectra.[83]Several optical designs for enabling fast sweeps in the temporal domain have made it possible to acquire spectra at very high rates. In point-scanning CARS microscopy, the Fourier transform approach has produced spectral ac-

quisition times of 42 $\mu$s per spatial pixel.[84] A related strategy has also been implemented in a wide-field CARS microscope.[85] Outside of the microscope, even higher spectral acquisition rates have been reached[86], up to 100,000 spectra/s in the form of dual-comb coherent Raman spectroscopy.[87;88]

## 1.6 Taking Stock and Looking Ahead

The last decade's technological developments are exciting as they push CRS microscopy to its ultimate speed and sensitivity limits. Nonetheless, many implementations thus far remain rather complex, which has kept these solutions out of the hands of routine microscopy users. The success of an imaging technique like CRS is ultimately measured by the quality of the science and discoveries it enables, and this requires the user base to expand beyond the community of microscope developers. Despite its impressive capabilities, the CRS microscope, in many ways, is still grappling with similar questions that bubbled up when the first CRS imaging system saw the light of day: how can this technology be tailored to benefit a much wider research community? Buttressed by a strong portfolio of biological applications in the scientific literature, CRS developers have put their hopes on commercial releases of the SRS microscope as a way to bring fast vibrational imaging properties to a larger group of users. An affordable and user-friendly SRS microscope would no doubt expand access to the technique and multiply the number of studies in which CRS's label free imaging capability is a decisive factor of success.

Dominated so long by the emphasis on instrument development alone, this impasse might finally yield. By expanding the uses of fast Raman-based imaging to include mapping of metabolic processes, multiplex probe microscopy and optimized Raman label strategies for visualizing key molecular actors, the technique is likely to reach new audiences in the decade ahead. In the work that follows, a small step in that direction is taken.

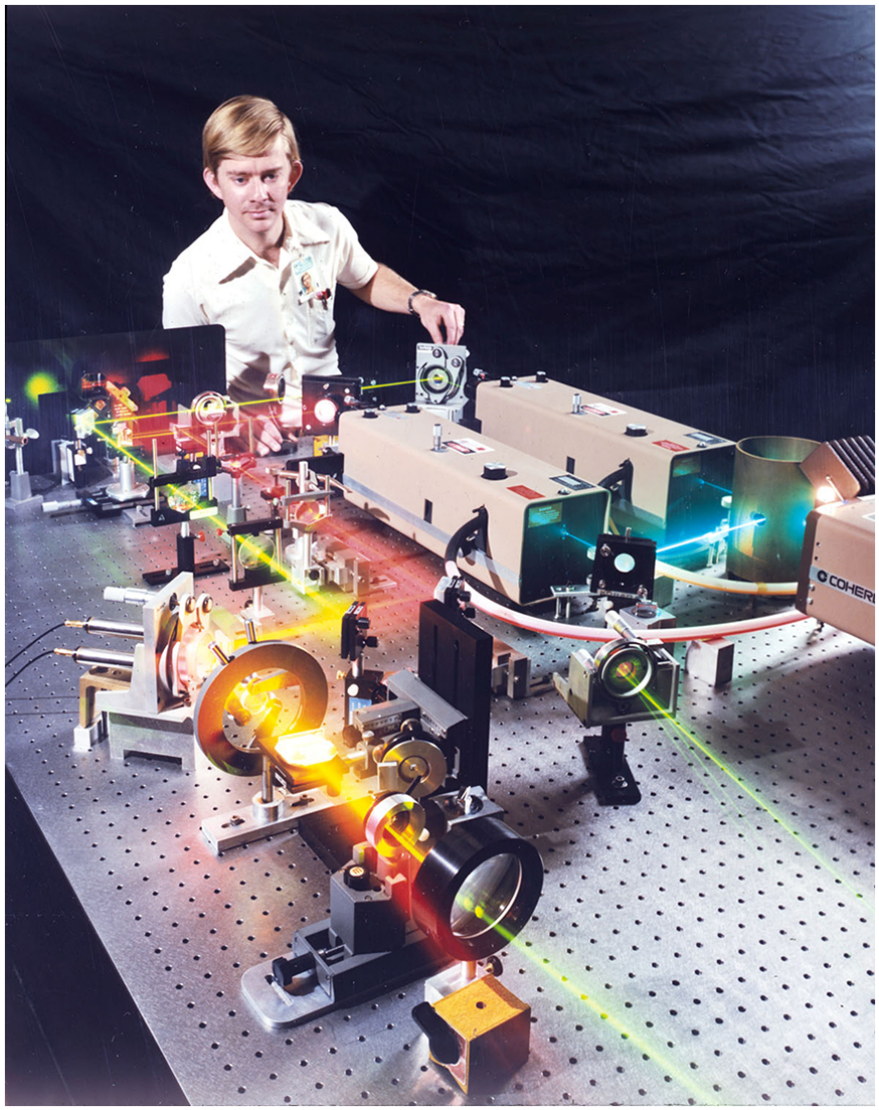


Figure 1.1: The first coherent Raman microscope
Dr. Michael Duncan adjusts the world's first coherent Raman microscope built at Naval Research Laboratory in 1981. Courtesy of Michael Duncan.

# Chapter 2

# Decreasing volume, Increasing Impact: A History of Stimulated Raman Scattering

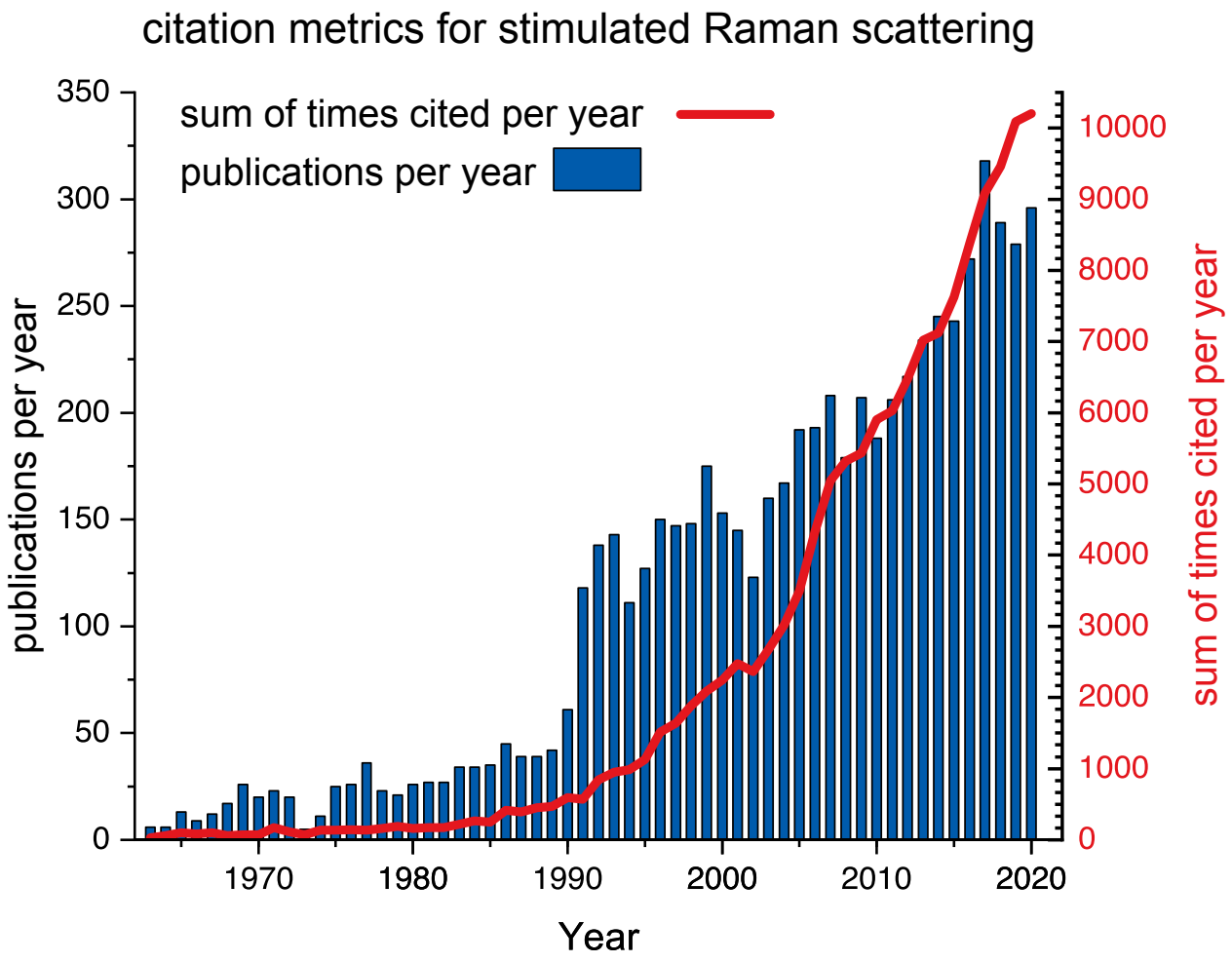



Figure 2.1: Bibliometrics of stimulated Raman scattering
The number of publications per year in the topic of stimulated Raman scattering and the sum of the total citations to articles mentioning stimulated Raman scattering per year. The academic product of stimulated Raman scattering has grown extensively since the discovery of the technique.

## 2.1 The Birth & Evolution of Stimulated Raman Scattering

Over the last few decades, the use of SRS as an analytical technique has grown rapidly, and will continue to grow as more commercial turn-key systems enter the market. According to *Clarivate Analytics* Web of Science, there are more than 6,000 publications in the field of

*stimulated Raman scattering* and more than 70,000 articles citing work in that collection.[89] This is shown graphically in Figure 2.1. In this Section, we will discuss the origin of the SRS approach, its coming of age as a sensitive molecular spectroscopy technique and its growth into a popular label-free imaging technique.

Discovered shortly after the first demonstration of a working laser, the phenomenon of stimulated Raman scattering (SRS) has closely tracked that of the laser itself.[90] The pulsed action of some lasers, including Maiman's first ruby laser, create extremely intense bursts of light, and it was quickly realized that these intense fields would enable the generation of various nonlinear phenomena.[91] The first prediction of a nonlinear optical effect had been worked out by Maria Göppert-Mayer in 1930.[92] Remarkably, the demonstration of nonlinear optics occurred a year after the birth of the laser with Franken et. al. demonstrating second harmonic generation (SHG) and Kaiser demonstrating two-photon excitation.[93;94] A year after these, in 1962, third-harmonic generation (THG) requiring even higher electric fields was demonstrated by Terhune.[95] In each of these cases, observation of a color different than that of the input light revealed the nonlinear process. The discovery of SRS would be no different.

The discovery of SRS was serendipitous. To achieve pulsed laser action, known then as a "giant ruby-laser pulse", and thus the high peak intensity necessary to generate nonlinear effects, many labs turned to the use of Kerr-cell shutters to modulate the output of their lasers.[96–101] The common material for Kerr shutters of the time was nitrobenzene, a material with several Raman active modes.[102;103] In 1962, Woodbury and colleagues at the Hughes Research Laboratories reported in a brief correspondence anomalous laser lines from their ruby laser and identified that the lines depended on the operation of their nitrobenzene Kerr shutter.[104] An interpretation of the first Raman laser is shown in Figure 2.2. An interesting historical note about this discovery was that it was made while conducting research on lasers for the United States Air Force, and was reported in a now unclassified report.[105]

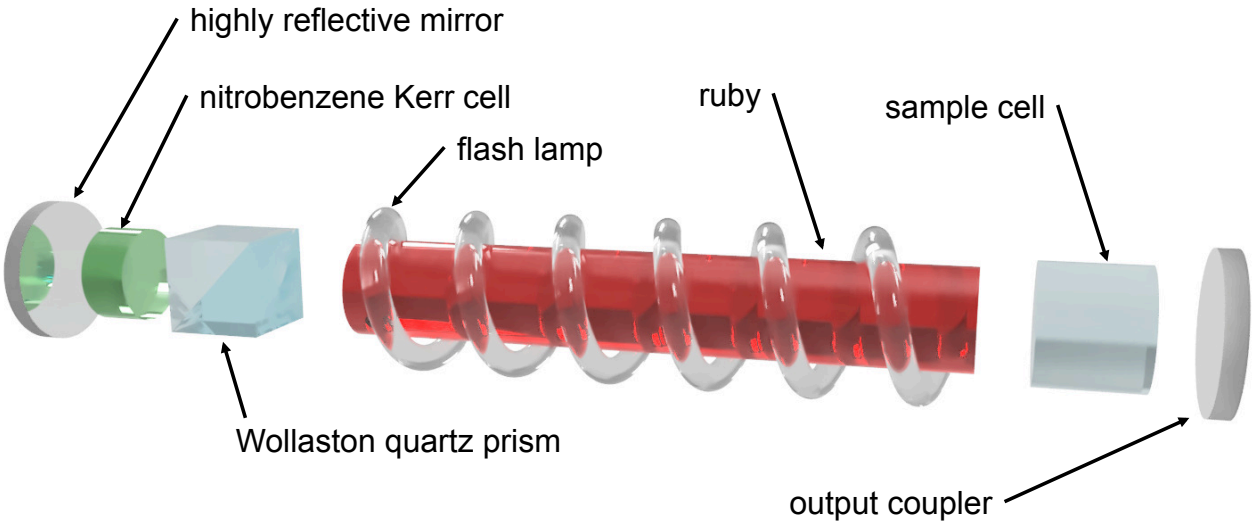



Figure 2.2: Author's Interpretation of the first SRS System
Modern diagram of the original Ruby laser Raman oscillator arrangement as used by Woodbury and Ng. Reproduced from a diagram in Bloembergen 1967.[106] Intense Stokes radiation is produced from the fluid in the sample cell and from the Raman active mode of the nitrobenzene in the Kerr shutter.

These anomalous "satellite" lines of their pulsed reflector laser were correctly identified as a version of Raman scattering in research published later in 1962.[107] By comparison to literature values, it was determined that the R-line of the ruby laser was shifted by an amount corresponding to the energy of the symmetric stretching mode of the $NO_2$ group of nitrobenzene, and subsequent measurements were made with different organic liquids to confirm Raman scattering as the origin of the effect. The authors made the realization that the amplification of the Raman lines was due to a similar process to that of the stimulated fluorescence emission that produces laser action. Thus, the name of *stimulated Raman scattering* was stuck to this process.

By 1962, a theory of four-wave mixing to explain nonlinear light-matter interactions was already in place,[108] and by the end of the decade, a semiclassical theory of SRS in terms of four-wave mixing was readily described.[109;110] Explanations in the classical wave[110;111] and quantized field regimes[112] were delineated, and it became possible to fully describe the SRS process in the laser cavity.[106]

### 2.1.1 The Birth of SRS: Light Conversion & Early Spectroscopy

The first demonstrations of stimulated Raman scattering were inherently spectroscopic in nature. The presence of a sufficient quantity of a Raman-active material produces additional laser lines at the Stokes and anti-Stokes frequency. In brief, the fundamental (pump) laser line, $\omega_1$ produces lower energy Stokes-shifted radiation through spontaneous Raman scattering, which involves Raman mode $\omega_\nu$, producing radiation at $\omega_2 = \omega_1 - \omega_\nu$. The highly reflective cavity mirrors allow Stokes photons to travel the cavity and return to the Raman active medium where they, in turn, stimulate the emission of more stokes photons. Just as in stimulated fluorescence, this generates a coherent and highly directional beam at frequency $\omega_2$. It is important to note that unlike stimulated emission no energy is stored in electronically excited states. Instead the difference in energy between the pump and Stokes photons is transferred to the Raman active material in the form of excited vibrational modes at frequency $\omega_\nu$. This follows the usual Raman relation: $\hbar\omega_\nu = \hbar(\omega_1 - \omega_2)$. Analogous to linear Raman scattering, stimulated anti-Stokes scattering is also observed wherein a beam blue shifted from the fundamental is produced, giving rise to radiation at $\omega_3 = \omega_1 + \omega_\nu$.[113–116]

Early on the use of SRS diverged into two distinct paths. The first path of research focused on the generation of coherent radiation, most widely in the form of Raman shifters. It was realized that SRS could be achieved by placing the Raman active material outside of the laser cavity, and in this way, external Raman based shifters were achieved.[117] These first shifters used transparent crystals such as diamond and calcite, but use of other materials quickly became commonplace.[118–120] Of particular importance, is the use of SRS to red-shift light in silica fibers by excitation of the Si-O modes around 13 THz (440 $cm^{-1}$).[121;122] SRS in fibers forms the basis of fiber Raman lasers and broadband Raman amplifiers.[123;124] Both of these technologies have found major use in the fiber based telecommunications industry.[125;126] Research into Raman shifters and Raman lasers continues several decades since their invention as a popular source of frequency conversion. The second path of research

aimed to use SRS for studying the spectroscopic properties of materials, which is discussed next.

### 2.1.2 First Wave: Picosecond Time-resolved Spectroscopy

Early on, many experts were skeptical about the utility of SRS as a spectroscopic tool. Bloembergen stated in a review from 1967 that "The spectroscopic information that may be obtained from the stimulated process is very restricted compared to the results from spontaneous scattering." [106] Others realized the implication that coherent radiation implies coherent molecular motion. Early work focused on studying the dephasing dynamics of the Raman active modes of various materials. [127–129] These lines of research were enabled by continually progressing research into lasers themselves as pulses into the picosecond became available. [130;131] The short temporal pulse widths of these lasers were shorter than the dephasing times of Raman lines. As such, molecular vibrations could be coherently prepared in a material and the free induction decay of the excitation could me measured. Throughout the 1970s, SRS research followed the advances in picosecond laser technology. Many coherent Raman studies focused on the ground-state vibrations of materials in all three major physical states. The increasingly shorter pulse widths promised to allow SRS to disentangle the broadening mechanisms behind Raman line widths. [132]

### 2.1.3 Second Wave: Ultrafast and Impulsive Regimes

During the late 1970s and 1980s, SRS had a limited effect on the field of nonlinear optics and ultrafast spectroscopy. In many cases it was experimentally easier to use the anti-Stokes signal at $2\omega_1 - \omega_2$ or the coherent Stokes signal at $2\omega_2 - \omega_1$. Coherent anti-Stokes Raman scattering (CARS) and coherent Stokes Raman scattering (CSRS), both third-order nonlinear techniques like SRS, overshadowed SRS during this time period.

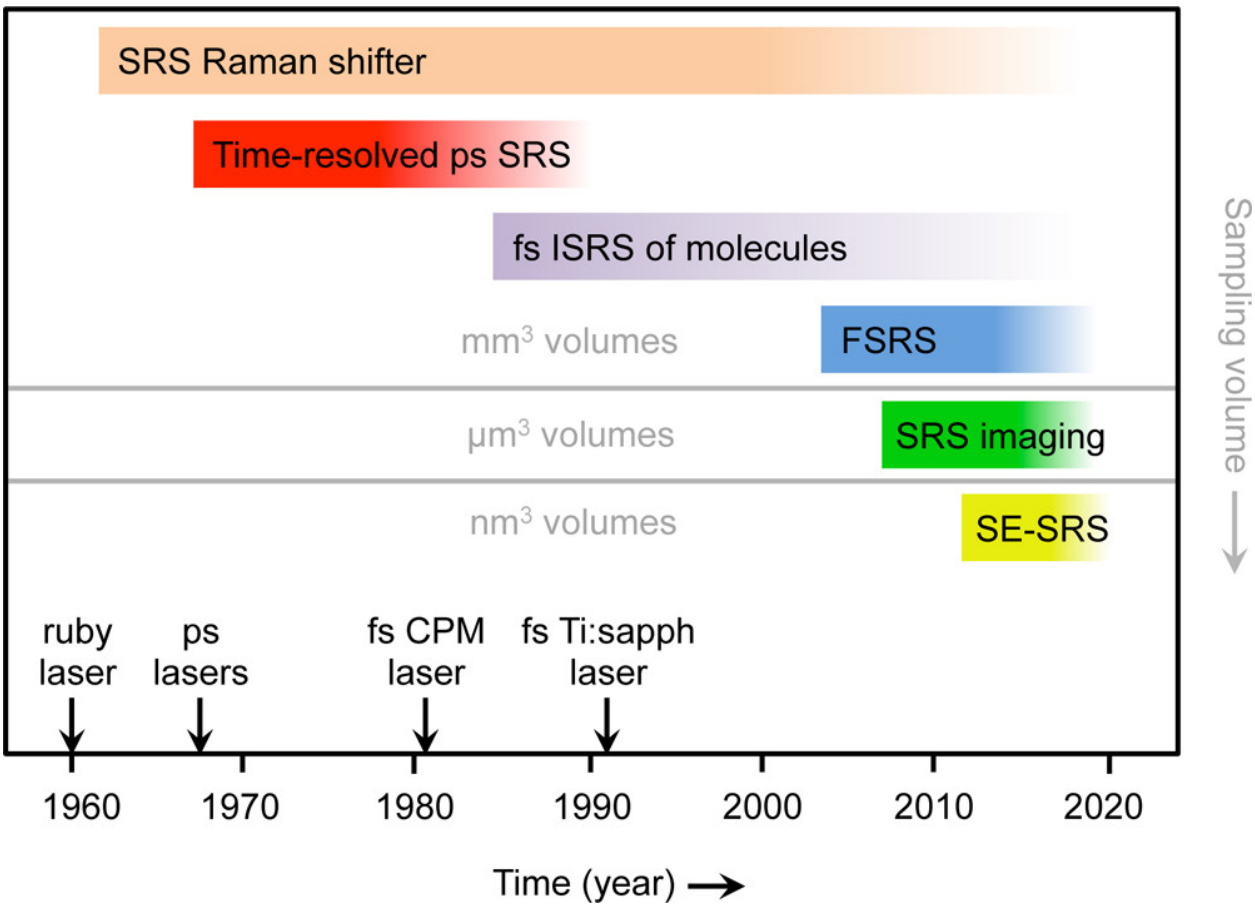



Figure 2.3: Timeline of major developments in SRS technology

The resurgence of SRS as a technique coincided with the invention of femtosecond laser sources, operating through various kinds of mode-locking mechanisms, including Kerr-lens mode-locking.[133–135] This timeline of use is shown graphically in Figure 2.3. Similar to stimulated Brillouin scattering, femtosecond pulses could be used to *impulsively* excite phonons in crystals.[136;137] Due to the broad spectral profile of these pulses, both the $\omega_1$ and $\omega_2$ frequencies could be achieved in a single pulse and drive the phonon at the Raman frequency, $\omega_\nu = \omega_1 - \omega_2$.[138]

This new technique was given the name of impulsive stimulated Raman scattering (ISRS) as the temporal width of the pulses is shorter than the period of the vibrational modes under study. The study of crystalline solids was quickly expanded to include low energy modes in liquids as well.[139] Low energy modes, $< 200$ cm$^{-1}$, are typically hard to probe with CARS

or CSRS because of the difficulty of spectrally filtering small Raman shifted contributions so close to the laser lines. Thus SRS was able to fill a gap in the spectroscopist's repertoire allowing access to intra- and inter-molecular vibrations and orientational modes of liquids as well as lattice dynamics in solids. Using ISRS it was possible to resolve the evolution and dephasing of vibrational motion as a function of time.[140]

The advent of ISRS led to a resurgence in the use of SRS for spectroscopy. While early experiments were conducted in optically transparent solids, ISRS was shown quite capable at studying electronically resonant molecules. With ISRS, the vibrational modes of excited states can be directly probed, thus offering a coherent view of electronic and vibrational coherences. As discussed elsewhere in this work, electronic resonances enhance the Raman response and boost signal. This allows for measurements at very low concentration of the chromophores, down to the $\mu$M range. This technique has been used extensively to study the vibrational dynamics of chromophores in solution.[141–143]

Throughout the nineties and into the early 2000s, the increasing versatility and availability of ultrashort Ti:sapphire lasers allowed for further advances in SRS techniques. In 2003, McCamant demonstrated what they called femtosecond stimulated Raman spectroscopy (FSRS) named for the time-resolution of the measurement.[144] The FSRS was famously used to elucidate structural dynamics of biologically important molecules such as $\beta$-carotene and retinal.[145] Besides ISRS and FSRS, the family of vibrational spectroscopy methods that rely on a stimulated Raman transition also contains techniques such as the time-resolved optical Kerr effect (OKE)[146], used for studying low energy Raman-active modes, and the Raman induced Kerr effect (RIKES)[147], used for interrogating high energy vibrational modes. Some of the principles of time-resolved SRS spectroscopy will be discussed in Section 2.2.

### 2.1.4 Third Wave: Diffraction-Limited Microscopy

Maturation of the laser technologies of the late twentieth century have led to great increases in the sensitivity of SRS measurements. By combining these with various modulation techniques and lock-in based detection, SRS measurements have been pushed to the point where the signal is limited only by laser shot-noise. This directly translates into measurements of small volumes and lower concentrations.

Gains in sensitivity enabled the use of higher numerical aperture lenses and, eventually, microscopic imaging.[148;149] Previous SRS techniques were performed in samples with an interaction distance on the order of several millimeters by focusing with a long focal length lens. With a high-NA lens the focal length becomes on the order of a micrometer and the focal volume that of a femtoliter (fL). CARS was the first demonstration of a coherent Raman scattering process in a fL volume, performed in 1999 by Zumbusch.[5] CARS turned out to be the proving ground for coherent Raman microscopies, and is itself a widely used technique, as underlined by the release of commercial CARS microscopes.[150–153]

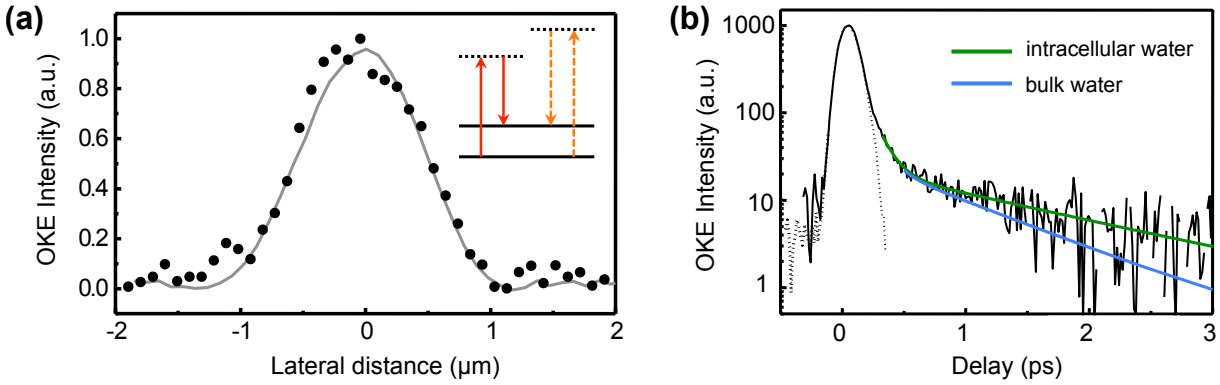



Figure 2.4: SRS microspectroscopy with a high numerical aperture objective. (a) Optical Kerr effect signal of a 1 $\mu$m diameter glass bead as it is scanned through focus. Inset shows a Jablonski diagram with the femtosecond pump (red) and probe (orange) field interactions indicated. (b) Impulsive optical Kerr effect microspectroscopy of water inside a live cell (black curve). A fit reveals a structural relaxation time of 1.35 ps for cell water (green) and a relaxation time of 0.79 ps for water of the growth medium. Adapted with permission form Ref[154].

Converting SRS for the purpose of microscopy proved to be a more difficult task than that

of CARS. Unlike a spectroscopy experiment where the larger volumes would permit spatial separation of the input beams, high-NA conditions utilize a collinear excitation. An early implementation of the SRS principle with collinear excitation in an optical microscope came in 2001 in the form of optical Kerr effect spectroscopy. In this implementation of ISRS, low energy librational Raman modes of water in cells were excited and probed in a time resolved fashion,[154] as shown in Figure 2.4. The first demonstration of SRS as a contrast mechanism for *imaging* followed several years later, in the form of broadband SRL and SRG using a white light probe pulse and a modulated, spectrally narrow pump pulse.[148] In the configuration as used by Freudiger et al., two input beams at frequencies $\omega_p$ and $\omega_s$ and picosecond pulsewidth are tuned to match a vibrational mode of interest in the sample.[149] The first application of picosecond SRS microscopy to biological systems is reproduced in Figure 2.5. However, in all these cases the SRS signal cannot be spectral isolated from the input beams. This necessitates the use of modulation techniques wherein a modulation applied to one beam is transferred onto the SRS signal imprinted onto the other beam. One enabling factor for SRS microscopy was selecting a modulation frequency that is high enough such that the 1/f noise from the laser is minimized, resulting in modulation frequencies of $> 1$ MHz.[155] Using variations on these techniques, concentrations as low as 100 $\mu$M have been demonstrated.[47;53]

While these advances in sensitivity are already commendable, the resulting molecular concentration limit is still higher than the intracellular concentration of many small metabolites, with concentrations in the $\mu$M range being typical. Additionally, Raman scattering cross-sections of the vibrational modes of biomolecular molecules are inherently low (in the $10-28\text{-}10^{-32}$ cm$^2$/sr range). Several groups have turned to developing other ways of boosting the SRS signal. Of particular note, is the use of electronic resonance conditions similar to that of ISRS.[156] It well known that the SRS signal can be greatly enhanced by tuning the frequency of the incident radiation to be near or at an electronic transition. By exploiting the electronic resonance, imaging of molecules at sub-$\mu$M concentrations has been

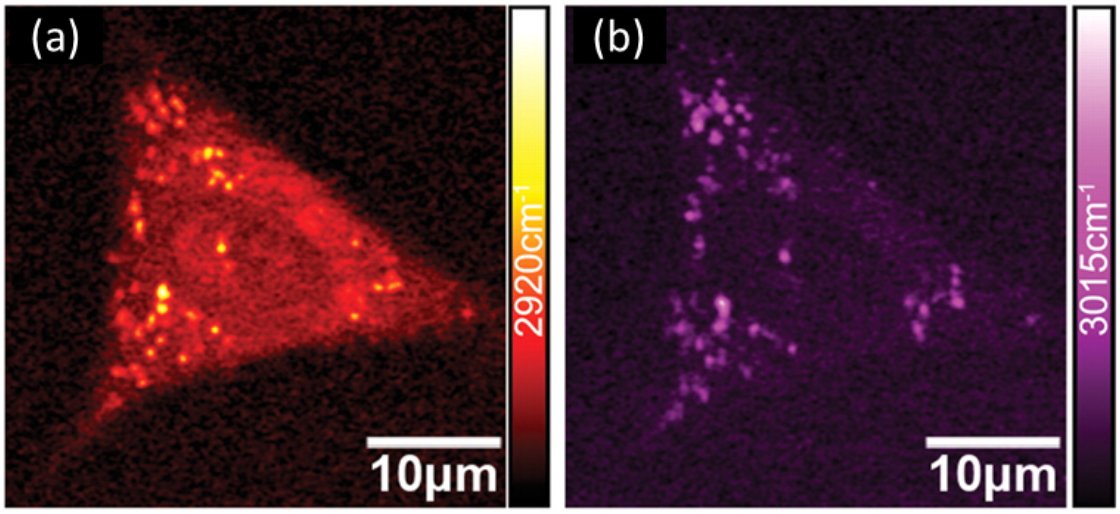



Figure 2.5: The First Demonstration of SRS Microscopy in Biology
SRS is shown to be a powerful tool to image lipid distribution for cell cultures and tissues in the first biological SRS microscopy report. Here, Omega-3 fatty acid uptake is monitored in A549 human lung-cancer cells. (**A**) SRL image taken at 2920 $cm^{-1}$. (**B**) SRL image of the same cell taken at 3015 $cm^{-1}$ which is indicative of unsaturated fatty acids. Reproduced with permission from Ref[149]. Copyright 2008 American Association for the Advancement of Science.

reported.[51;52;157]

Some of the underlying principles in SRS microscopy and its applications will be further discussed in Section 2.3.

### 2.1.5 Fourth Wave: Nanoscale and single molecule spectroscopy

Inspired by the successes of nanoscale spectroscopy and single molecule spectroscopy techniques, the last decade has seen a growing effort by the SRS community to push the sensitivity of the technique to the nanoscale. At the nanometer level, the number of molecules is necessarily smaller, and this, in turn, affects the detectability of the signal. The Raman effect alone is too weak to allow for measurements at this level, and the effect of stimulating the Raman transition, which effectively increases the detected signal by $10^5 - 10^6$ times, remains insufficient to enable the observation of molecules at this scale. Additional mechanisms are

needed to boost the signal, and some of these mechanisms are discussed in Section 2.4 of this Chapter.

Among the developments that pushed the SRS technology to the nanoscale, and, by extension, to the single molecule limit, is the technique of using surface plasmons to enhance the Raman response. The fields of surface and cavity enhanced Raman spectroscopy are well established in their own right.[158–160] Following much the same evolution from Raman to SRS, surface enhanced Raman scattering (SERS) has been translated into the surface-enhanced stimulated Raman scattering (SE-SRS) family of techniques. While much of the advances in SE-SRS occurred in the twenty-first century, it was first proposed and demonstrated in 1979 at Bell Labs.[161;162] These techniques have been used to probe a variety of scientific problems, including the promise of creating "molecular movies" of targets in plasmonic cavities at the ultrashort time scales.[163] This technique also shows promise in studying plasmonic catalysis, for detection of small drug compounds, and of plasmonic processes in nano-aggragates. The process can also be utilized in a variation of tip-enhanced Raman spectroscopy.[164] These advances did not come without challenges however. The high peak intensities inherent in surface enhanced picosecond and femtosecond spectroscopies have been shown to be on the order of 1 V/nm; a regime where chemical changes in the molecules of interest may be induced by the applied fields themselves.

### 2.1.6 Towards SRS Nanoscopy

As can be imagined, the Raman imaging community, spurred on by super-resolution techniques in other imaging fields,[165] is pushing the limits of what SRS can do with the ultimate goal of developing a nanoscopy with single-molecule detection capabilities. This is an emerging field, and as such, much of its history is yet to be written. We will provide a brief overview of major trends here.

Early work towards this goal appears in theory by 2014 with a method similar to that of stimulated emission depletion microscopy(STED)[166]. Under this proposed scheme, an additional third pulse would be utilized in the form of a doughnut-shaped Stokes beam to saturate the SRS signal at and around the perimeter of the pump beam.[167;168] In 2015, work by Silva and colleagues demonstrated that using a STED like approach can yield sub-diffraction level resolution.[169] In this technique, the added toroidal pulse depletes vibrational coherences in the molecules of interest by driving population away from the ground state into the vibrationally excited state, thus reducing the normal SRS signal through ground state depletion. This effectively eliminates SRS signal generation in the overlap of the SRS coherence and the depletion beam through the process of Raman saturation. However, the low repetition rate of their laser makes this approach impractical for biological imaging. The same strategy was expanded on by Graefe et al, who demonstrated sub-diffraction limited SRS imaging with a MHz laser, which brings this technique closer to applicability in biological imaging.[170] Though it should be noted that a demonstration on a biological sample was not provided in that work. Another way to achieve the higher resolution afforded by Raman saturation is to use a special modulation/demodulation scheme that is sensitive to the nonlinear dependence of the saturation process.[171] In this fashion, no extra doughnut-shaped beam is needed, thereby significantly simplifying the experiment. This method has been used to visualize biological cells with sub-diffraction limited resolution. Among other recent efforts to improve the resolution in SRS comes a surprisingly simple solution: use shorter wavelength pump and Stokes beams and a very high NA objective lens. Following this recipe, images of cultured cells were obtained with a lateral resolution of 113 nm,[172] as highlighted in Figure 2.6. A possible downside of this method is the increased probability of photo-bleaching and possible photo-damaging due to the use of pulsed visible light beams.

These advances demonstrate the rapid progress being made towards a true label-free vibrational nanoscopy. However, many challenges remain to demonstrate a technique fully capable of generating such visually stunning images like those currently available with fluorescence

based super-resolution techniques.

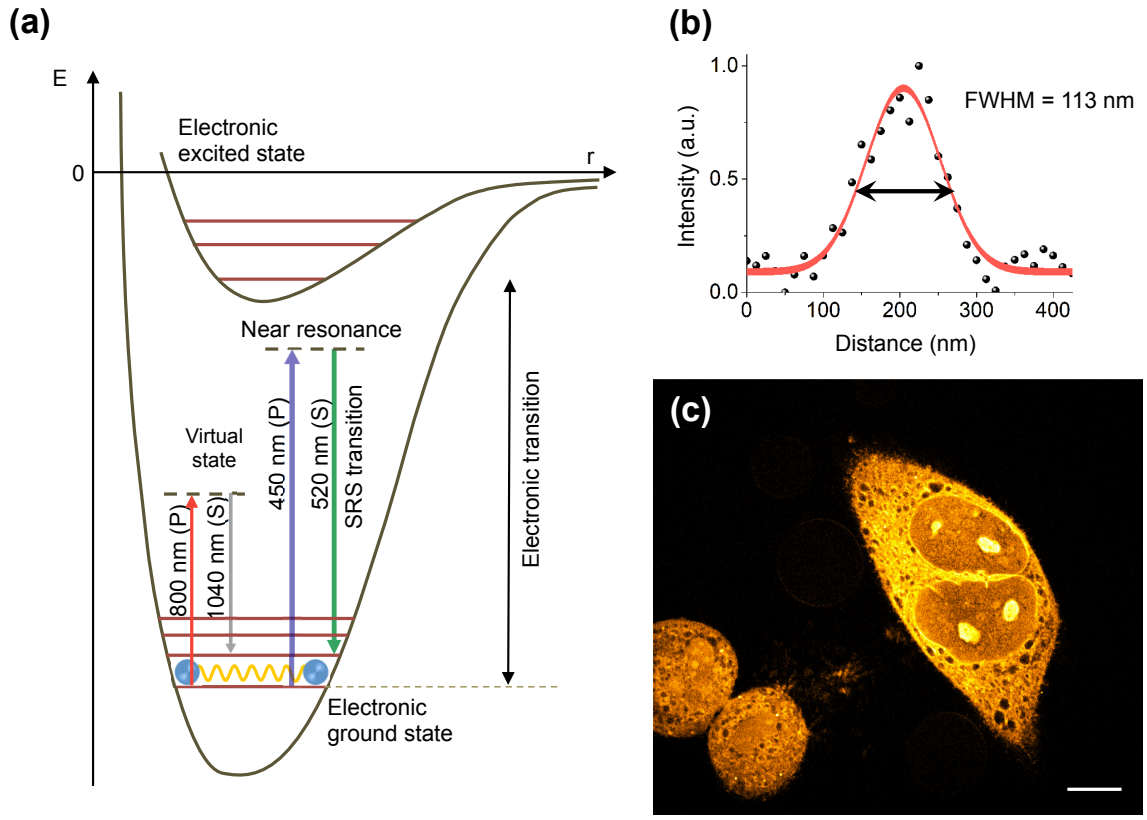



Figure 2.6: SRS Imaging in the Visible Regime
High resolution SRS imaging using visible pump and Stokes beams. (a) Energy level diagram of SRS with near-infrared excitation beams, shown on the left, and visible excitation beams on the right. The near-resonant condition provides an additional boost to the signal. (b) Cross section of the SRS signal from a 60 nm polystyrene bead, showing a full width half maximum (FWHM) of 113 nm. (c) High resolution SRS image of a cell taken with visible excitation beams. Images were obtained with a NA = 1.49 oil immersion objective lens. Adapted with permission from Ref[172].

## 2.2 Probing molecules with SRS Spectroscopy

Readers with a primary interest in imaging and microscopy may be unfamiliar with the principles of SRS *spectroscopy*, the technology on which the imaging version of the SRS technique is based. In SRS spectroscopy, the emphasis is on the spectroscopic properties and physical interactions of molecules. Sample volumes in SRS spectroscopy are often in

the 10 $\mu$L - 1 mL range, much larger than the $\sim$fL volumes typical for SRS microscopy. As highlighted in earlier Sections, the spectroscopy version of SRS dates back to the 1960s, the decade in which the laser was developed. With the subsequent availability of shorter laser pulses, the SRS techniques was used predominantly to offer a time domain version of the spectra collected with spontaneous Raman scattering. The development of the ISRS technique, in particular, made it possible to follow the evolution of vibrational coherences of solids and liquids on the femto and picosecond timescales, prompting numerous research activities. In the following, we will discuss some of the properties of SRS spectroscopy, with an emphasis on the time domain version of the technique.

### 2.2.1 SRS Spectroscopy in the Time Domain

The spectra acquired in spontaneous Raman spectroscopy contain a lot of information. Besides the spectral positions and relative intensities of the Raman lines, the spectra also hold information about the dynamics of the induced Raman polarization. The longer the polarization is able to retain its induced oscillatory motion, the narrower the Raman spectral profile. Vice versa, shorter lived Raman polarizations give rise to broader linewidths. The frequency and time domain are related to one another by a Fourier transformation. However, while the frequency domain reports on the overall timescales on which the Raman polarization unfolds, it does not provide a time consecutive picture of the evolution of the vibrational motion. In the time domain, on the other hand, the vibrational dynamics are resolved directly as function of time, revealing the actual chronology of the vibrational movements involved. The ability to 'see' the motion of chemical bond vibrations is rather compelling, and it has led to the development of a broad arsenal of time-resolved SRS techniques.

To describe the SRS experiments in the time domain, it is helpful to invoke the quantum mechanical picture of the material states while the light fields are treated classically.[173] In

general, we may write the eigenstates of the molecular system as $|n\rangle$. A useful tool in describing evolution of the system as it interacts with the incident fields is found in the so-called density matrix operator. It is defined as:

$$\hat{\rho}(t) \equiv \sum_{nm} \rho_{nm}(t) \, |n\rangle \, \langle m| \tag{2.1}$$

The diagonal elements of the density matrix operator, $\rho_{nn}$, give the probability that the molecule is in state $|n\rangle$, whereas the off-diagonal elements describe the system as it is in a coherent superposition of states $|n\rangle$ and $|m\rangle$. The operator $|n\rangle \langle m|$ is called a *coherence* when $n \neq m$, and $\rho_{nm}(t)$ gives the time-dependent amplitude of this coherence. When $n = m$, the operator $|n\rangle \langle n|$ is referred to as the system's *population* of state $|n\rangle$. In this case, the system is not in a superposition of states, but resides in a well defined eigenstate. It is the evolution of $\hat{\rho}(t)$ that we are interested in, as it conveniently describes the light-induced couplings between the material's states and the subsequent dynamics that follows.

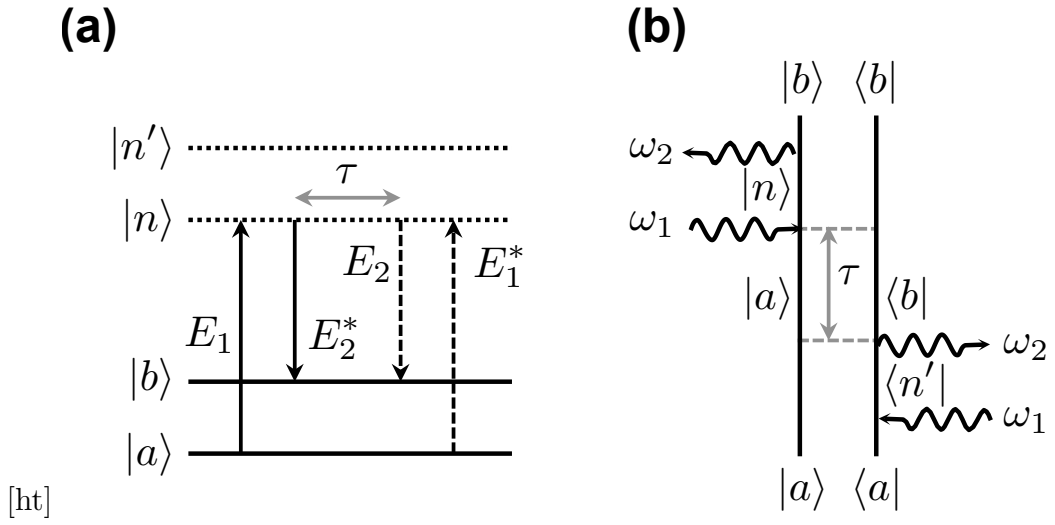
To follow the evolution of the system, it is convenient to consider the four-level system sketched in Figure 2.7a. Here the ground state is indicated as $|a\rangle$, the first vibrationally excited state as $|b\rangle$, and two virtual states as $|n\rangle$ and $|n'\rangle$. Note that the virtual states are not eigenstates of the material and thus the system cannot evolve in such states any longer than dictated by the time uncertainty in the experiment. In the semi-classical description of SRS, the material is subjected to three interactions with incoming fields. Before any field interactions, the system is in the ground state population, expressed by the operator $|a\rangle \langle a|$. Each field interaction can change the bra or the ket of the density matrix operator.

In the time domain SRS experiment, the first two field interactions are with a pump and probe field, indicated by $E_1$ and $E_2$, respectively, in Figure 2.7a. These two field interactions can manipulate $\hat{\rho}$ in many ways, but here we will focus on a particular manipulation, or pathway, that forms a dominant contribution to the SRS signal. This pathway is represented

in terms of a double-sided Feynman diagram in Figure 2.7b, which is read from bottom to top. Starting in population $|a\rangle\langle a|$, both the pump ($\omega_1$) and the Stokes ($-\omega_2$) interact on the bra side, producing the coherence $|a\rangle\langle b|$. After the preparation step, the system will evolve in this superposition of two vibrational states (Raman coherence) during time $\tau$ as the molecule interacts with its surroundings. Two important effects can alter the amplitude of the coherence. First, the vibrational lifetime of $|b\rangle$ limits the time the superposition of states can be maintained, resulting in a decaying coherence with a rate of $\gamma_{bb}$. Second, because each molecule is affected by its immediate surroundings differently, the phase evolution of the superposition of states in one molecule will differ from that of another molecule. This implies that the amplitude of the total Raman coherence in the sample will decrease as individual components run out of phase. This effect is known as pure dephasing of the coherence of the molecular ensemble, and characterized by the dephasing rate $\hat{\gamma}_{ab}$. The joint effect of vibrational lifetime and inter-molecular dephasing gives rise to an overall decay rate $\gamma_{ab} = \gamma_{bb}/2 + \hat{\gamma}_{ab}$ for the Raman coherence. Here the $\gamma_{bb}$ is divided by 2 because the populated decay rate is defined through the modulus square of the density matrix amplitude as $|e^{-\gamma_{bb}t/2}|^2 = e^{-\gamma_{bb}t}$.

After an evolution period $\tau$, the system is probed by a third field interaction, here with the pump field $\omega_1$ that interacts from the left with the ket, as shown in Figure 2.7b. During this interaction time, the system radiates a photon at $\omega_2$, upon which the material is left in the population $|b\rangle\langle b|$. The end result is that the system is in a higher energy state because of the Raman interaction. The radiation probability of the $\omega_2$ photon in the probing step is related to the amplitude of the density matrix operator after three incident field interactions. Computationally, the density matrix can be determined using third-order perturbation theory, yielding $\hat{\rho}^{(3)}(t)$, which in turn can be used to calculate the third-order polarization in the material:

$$P^{(3)}(t) = N\mathrm{tr}\left[\hat{\mu}\hat{\rho}^{(3)}(\mathrm{t})\right] \tag{2.2}$$




[ht]

Figure 2.7: Diagrammatic representation of the SRS process
(a) Energy level diagram with four material states, and four *field* interactions. (b) Double-sided Feynman diagram of one of the contributions to the SRS signal. Time $\tau$ indicates the time delay between the preparation and probing step in the time-resolved SRS process.

where $N$ is the number density of molecules, $\hat{\mu}$ is the dipole operator, and the tr symbol indicates the trace over the matrix elements of the operator product between the brackets. This procedure thus gives access to the temporal evolution of $P^{(3)}(t)$, which is the key quantity measured in time-resolved SRS experiments. In general, the detected SRS signal $S$ in the detection channel ($\omega$) can be written as:[174]

$$S(\omega_i, t) = \frac{n(\omega_i)c}{4\pi} \mathrm{Re}\left\{\mathrm{E_s(t)} \cdot \mathrm{E_i^*(t)}\right\} \tag{2.3}$$

where $i = 1, 2$ for the pump and Stokes detection channels, respectively, and the signal field is written as $E_s$. Assuming far-field detection of a plane wave, the signal field is proportional to the nonlinear polarization, i.e. $E_s \propto iP^{(3)}$, and the detected signal can be written as:

$$S(\omega_i, t) \propto -\mathrm{Im}\left\{\mathrm{P^{(3)}(t)} \cdot \mathrm{E_i^*(t)}\right\} \tag{2.4}$$

In case the dynamics of $P^{(3)}(t)$ are followed as a function of the time delay between the preparation step and the probing step, then the amplitude of the polarization can be moni-

tored as a function of $\tau$. The measured quantity, $P^{(3)}(\tau)$, contains all the information about the frequencies of the driven vibrational modes as well as the dephasing parameters of all excited Raman lines. Note that the far-field SRS signal is sensitive to the *imaginary* part of the material polarization. Physically, the imaginary part of the material response is related to the exchange of energy between the material and the light fields. From this notion, it can be understood that the SRS signal is directly proportional to the energy gained by the material or, vice versa, the energy lost by the (combined) light fields.

### 2.2.2 Features of time-domain SRS

The characteristics of the time profile of the measured third-order polarization dependent on the way the experiment is conducted. In particular, different features can be observed as the bandwidth of the pump and Stokes pulses is changed. Typical features of the time-resolved SRS signal are shown in Figure 2.8. In the column on the left hand side, the real and imaginary parts of the Raman polarization are shown in the frequency domain. The gray shaded area indicates the convolved width of the femtosecond pump ($\omega_1$) and Stokes ($\omega_2$) pulse pair. In panel (a), a high frequency Raman mode at $\omega_\nu = 1000$ cm$^{-1}$ is driven by the frequency difference ($\omega_1 - \omega_2$) of the pump and Stokes pulse pair. The spectral width of the effective driving frequency $\omega_1 - \omega_2$ is sufficient to cover the width of the Raman line, but insufficient to cover multiple lines. When another pump/Stokes pulse pair of similar duration is used to probe the induced polarization as a function of $\tau$, the profile in panel (b) is observed. The frequency domain and the time domain are related by a Fourier transformation, and thus the exponential decay of the polarization directly corresponds to the linewidth of the excited mode.

In panel (c), the width of the $\omega_1 - \omega_2$ driving frequency is broad enough to coherently excite two nearby Raman lines. Now the induced polarization oscillates at two frequencies, which

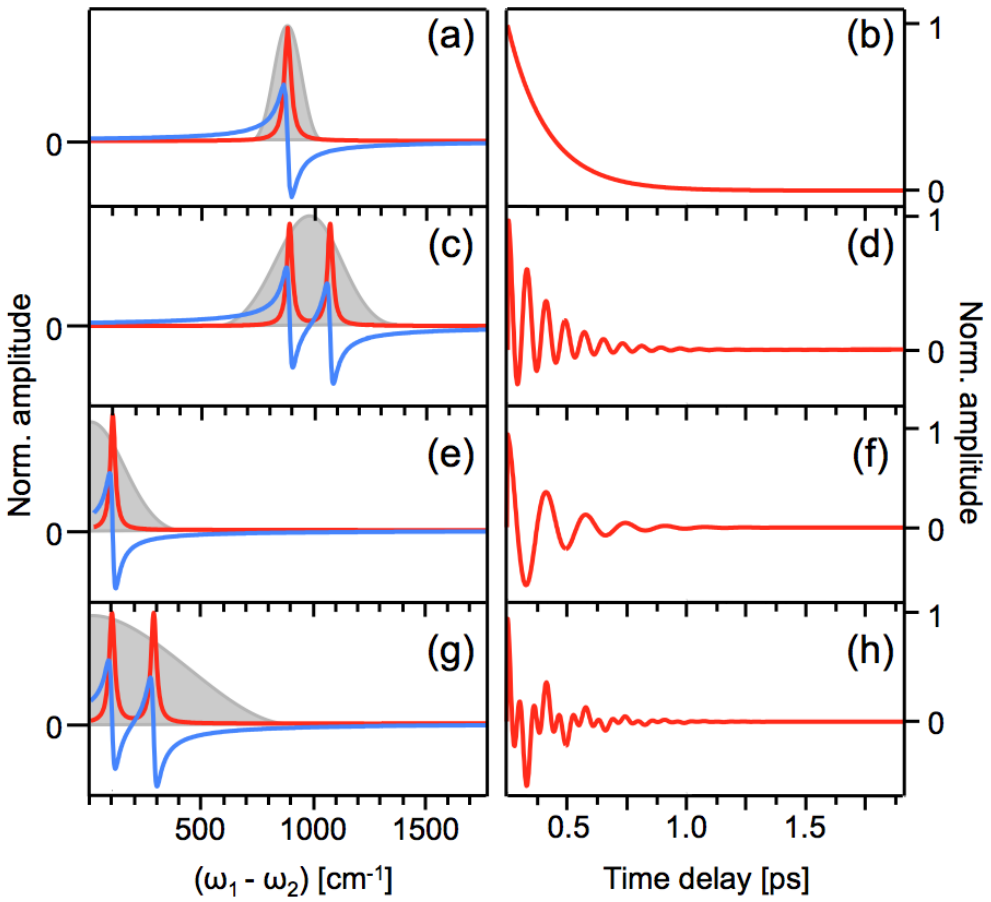



Figure 2.8: Frequency and Time dependence of the third-order polarization Simulated frequency (a,c,e,f) and time (b,d,f,h) dependence of the third-order polarization $P^{(3)}$ as probed under different experimental conditions. (a) Amplitude of the real (blue) and imaginary (red) part of the nonlinear polarization due to the presence of a single high-frequency Raman resonance. The Raman coherence is driven by the pump ($\omega_1$) and Stokes ($\omega_2$) fields at ($\omega_1 - \omega_2$). Gray region indicates the spectral profile of the effective driving field ($\omega_1 - \omega_2$). (b) Amplitude of $P^{(3)}$ as a function of time delay $\tau$, corresponding to the situation in (a). (c) Driving two high-frequency Raman resonances with two broadband laser fields in the spectral domain and in the (d) time domain. (e) Driving one low-frequency Raman resonance with one broadband laser field in the spectral domain and in the (f) time domain. (g) Driving two low-frequency Raman resonances with one broadband laser field in the spectral domain and in the (h) time domain. Reprinted with permission from Ref.[175] Copyright 2017 American Chemical Society.

coherently beat against one another. These quantum beats are directly visible in the time-resolved SRS trace. The periodicity of the quantum beat is inversely related to the spectral difference between the two lines, whereas the linewidth of the individual bands is reflected in the overall decay of the time-dependent profile.

In Figure 2.8e, the system is not driven by two spectrally separated pump and Stokes pulses, but rather by a single broad bandwidth femtosecond pulse. This single pulse is broad enough to provide both the pump and Stokes frequencies for driving a low frequency mode, shown here at $\omega_1 - \omega_2 \sim 100$ cm$^{-1}$. In the spectral domain the pulse covers all frequencies from zero to well beyond the mode of 100 cm$^{-1}$, which in the time domain corresponds to a pulse duration much shorter than the periodicity of the molecular vibration. The mode is now excited *impulsively*. Panel (f) depicts the time profile as the polarizaton is probed with the probe pulse of similar duration, revealing oscillations that now directly track the motion of the molecular vibration. Finally, in panel (g), the single preparation pulse coherently excites two low frequency Raman modes, resulting in the time profile of panel (h). In the latter case, the time trace exhibits oscillations of the individual modes as well as quantum beats between the modes.

If the driven vibrational modes are those of the ground state potential, then the information in the time-resolved SRS signal is directly related to that of the Raman spectrum. In this case, the time profiles can be obtained by a simple Fourier transformation of the spontaneous Raman spectrum and no new insights are to be gleaned from the time-resolved SRS measurements. This is an important realization, as there is, in principle, no reason to perform a much more complicated ground state SRS experiment in the time domain when a simple spectral Raman measurement suffices. In many ways, earlier picosecond and femtosecond time-resolved SRS studies of ground state vibrations, while technically important advances, have added very few new fundamental insights into the dynamics of molecules. Nonetheless, time-resolved impulsive SRS remains an important approach for detecting low frequency

modes that are difficult to detect in the frequency domain because of their proximity to the Rayleigh line. This higher sensitivity to low frequency modes has recently been exploited in microscopy as well, in the form of impulsive SRS microscopy.

The information content offered through either time- or frequency-resolved Raman experiments is no longer strictly identical, however, when the molecule is excited first to an electronically excited state, and then allowed to evolve on the excited state potential while the SRS process is used to probe vibrational motions. This scenario is relevant to a wide variety of photochemical processes. A frequency domain measurement is unable to resolve the time consecutive steps of the wavepacket dynamics, and a time-resolved measurement is the only way to fully appreciate the dynamics on the excited state potential. An important form of SRS spectroscopy in the latter category of experiments is called femtosecond stimulated Raman scattering (FSRS), to which we will turn next.

### 2.2.3 Femtosecond stimulated Raman scattering (FSRS)

The FSRS approach follows a specific scheme that proved to be very favorable for studying molecular conformational dynamics after a photo-induced excitation. This situation is relevant to chromophores with electronic resonances in the visible range of the spectrum that undergo dynamical changes upon photo-excitation. Examples include photo-isomerization reactions, internal conversion dynamics, and excited state electron and proton transfer processes.

The FSRS technique involves the excitation of the target molecule by a short actinic pump pulse, which prepares a wavepacket on the excited state potential, shown in Figure 2.9a. The actinic pulse is typically a short femtosecond pulse, which plays an important part in defining the temporal resolution of the experiment. The vibrational modes in the excited state are then probed through a SRS process as the wavepacket evolves on the excited state

potential. The SRS process is achieved through a combination of a spectrally narrow Raman pump pulse and a spectrally broad probe pulse. This is a common scheme for acquiring SRS spectra, as the spectral resolution $\Delta\nu$ is determined by the narrow Raman pump pulse, which imprints narrow SRL and SRG features onto the broadband probe, as well as the resolution of the spectrometer that is used to collect the spectra. In the time domain, the Raman pump pulse duration is in the picosecond range while the probe pulse is in the sub-100 fs range. Time delaying the probe pulse relative to the actinic pulse will allow the collection of SRS spectra at different time points as determined by the time delay $\tau$ of the actinic pulse and the probe pulse, both of which are in the femtosecond range. The cross correlation between these short pulses sets the time resolution $\Delta t$ along the $\tau$-axis. The long picosecond pulse envelope of the Raman pump is virtually flat over the examined time delay and is thought not to limit the time resolution of the experiment. In this fashion, vibrational spectra with a spectral resolution of $\Delta\nu \sim 10$ cm$^{-1}$ have been recorded with a temporal resolution of $\Delta t \sim 100$ fs as the photo-physical process on the excited state potential unfolds.

The principle of FSRS was first developed in 1994.[177] Subsequent improvements showed the utility of the approach for following the photoisomerization of a dye molecule, the conformational dynamics of $\beta$-carotene, and the isomerization of retinal chromophores.[144;178] Ever since the early 2000s, the FSRS has been applied to numerous other molecular systems.[145;179] An example of the power of FSRS is shown in Figure 2.9b for the case of 11-cis retinal in rhopdopsin, a study that uncovered the primary structural changes of the chromophore responsible for vision.

As can be seen in Figure 2.9b, the vibrational features of the FSRS Raman gain spectra display changes on the $< 100$ fs timescale, suggesting that simultaneous high $\Delta t$ and $\Delta\nu$ can be achieved. This is remarkable, as the time-bandwidth product $\Delta t \Delta\nu$ in a typical optical experiment is constrained by the Fourier relationship between the conjugated variables of time and frequency. For instance, for optical experiments conducted with Gaussian pulses,

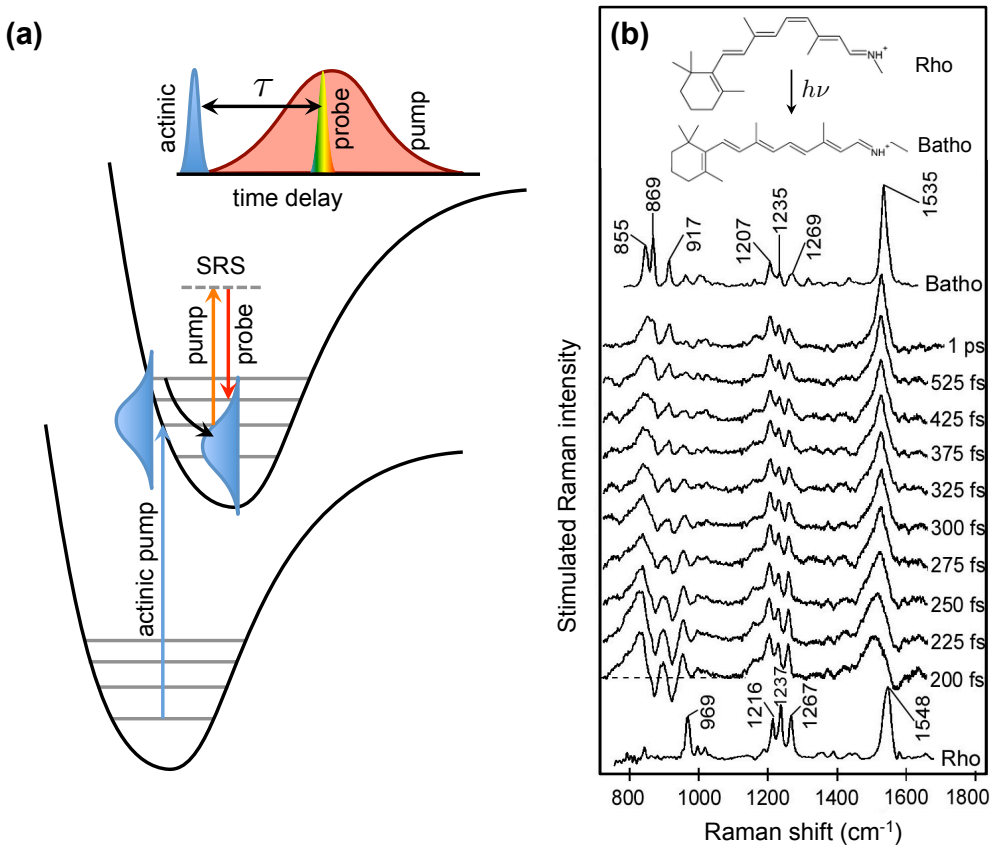



Figure 2.9: An Example of Femptosecond Stimulated Raman Scattering (a) The FSRS excitation scheme where a fs actinic pulse prepares a wavepacket on the excited state, which is subsequently examined by SRS spectroscopy as it evolves on the potential surface. Inset shows the time domain picture. (b) Application of FSRS to the photoisomerization of 11-cis retinal in rhodopsin to the all-trans bathorhodopsin photoproduct. Time-resolved FSRS spectra are shown for different delay times $\tau$ between the actinic pulse and the SRS pump pulse. Resonance Raman spectra of ground-state rhodopsin (Rho) and the trapped bathorhodopsin (Batho) product are included for comparison. Adapted with permission from Ref[176].

the time-bandwidth product is found as $\Delta t \Delta \nu \approx 15$ ps cm$^{-1}$. In FSRS, time-bandwidth products of 1 ps cm$^{-1}$ or lower have been reported[180], raising questions about violation of the fundamental uncertainty between time and frequency. The argument that the delay time $\tau$ and the spectral resolution on the spectrometer are independently controllable parameters, and thus not Fourier conjugates, seeks to dispel such concerns.

However, others have pointed out that it is not the system's evolution along the $\tau$ dimension that is of direct relevance to the time-bandwidth product of the vibrational lines, but rather

the time evolution of the system during the generation of the stimulated Raman gain photons.[181] For these photons to acquire a narrow spectral width of 10 $cm^{-1}$, the light-matter interaction must have a duration of $\sim$ 1.5 ps for this spectral content to develop. During this interaction time with the Raman pump and probe pulses, the wavepacket would sample different parts of the excited state potential. In this scenario, dynamics can still be observed on shorter timescales, but the vibrational part of the time-dependent polarization needs a longer time to develop its signatures and, thus, cannot be resolved with the same $\Delta t$ as the electronic contributions to the polarization. Despite these concerns, theoretical methods have been developed that promise to retrieve the dynamic peak frequencies of the relevant Raman modes from the FSRS spectra on a timescale much faster than the time needed to develop a narrow line.[182]

## 2.3 Probing Smaller Samples: The Transition to Microscopy

As alluded to in Section 2.1, the use of SRS as a contrast mechanism for microscopy has been a fruitful area of scientific research and engineering over the last two decades. Getting to that point, however, required significant work in the realm of spectroscopy, and several important realizations and considerations about the spatial nature of light propagating in smaller and smaller interaction volumes.

### 2.3.1 Shrinking the probing volume

As discussed in Section 2.2, the experimental configuration for SRS changes quite dramatically when moving from a typical SRS spectroscopy experiment to an SRS measurement in an optical microscope. One of the most striking and important differences that occurs

between these configurations is the size and form of the probing volume. In a typical ISRS experiment the pump and probe beams are incident on the sample at different angles, forming an overlap region that constitutes the interaction volume. Typically, the interaction length is on the order of 0.1 - 10 mm. The interaction volume is orders of magnitude larger than the optical wavelength, and the nonlinear polarization radiates a signal in a well-defined, phase-matched direction. The issue of phase matching is important in both SRS spectroscopy of bulk samples as well as in SRS microscopy, albeit in different ways.

Spatial phase matching is an important consideration for all coherent nonlinear optical experiments. In SRS, phase matching describes the process of matching the spatial phase of the induced polarization $P^{(3)}$ to that of the propagating signal beam. Each field $\omega_i$ involved in the SRS interaction is described with a spatial phase $\phi_j = \mathbf{k_j} \cdot \mathbf{L}$, where $k_j$ is the associated wavevector and $\mathbf{L}$ is the vector describing the propagation distance inside the interaction volume. The three incident fields that drive $P^{(3)}$ assign a spatial phase to the induced polarization. In SRL, the nonlinear polarization is driven by the effective driving field $E_1(\mathbf{r})E_2^*(\mathbf{r})E_2(\mathbf{r})$, whereas in SRG the effective driving field is $E_2(\mathbf{r})E_1^*(\mathbf{r})E_1(\mathbf{r})$, resulting in the following spatial phases:

$$\phi_{SRL} = (\mathbf{k}_1 - \mathbf{k}_2 + \mathbf{k}_2) \cdot \mathbf{L} \tag{2.5}$$

$$\phi_{SRG} = (\mathbf{k}_2 - \mathbf{k}_1 + \mathbf{k}_1) \cdot \mathbf{L} \tag{2.6}$$

The spatial phase of the nonlinear polarization needs to match that of a propagating beam at the signal frequency, with in the case of SRS corresponds to the phase of the (forward propagating) probe beams. For SRL, the phase required to generate a propagating beam at $\omega_1$ is $\phi_{\omega_1} = \mathbf{k_1} \cdot \mathbf{L}$, and for SRG the required phase is $\phi_{\omega_2} = \mathbf{k_2} \cdot \mathbf{L}$. The phase difference $\Delta\Phi$ between the induced polarization and the probe field is then given as:

$$\Delta\Phi_{SRL} = \phi_{SRL} - \phi_{\omega_1} = (\mathbf{k}_1 - \mathbf{k}_2 + \mathbf{k}_2 - \mathbf{k}_1) \cdot \mathbf{L} = \Delta\mathbf{k} \cdot \mathbf{L} \quad (2.7)$$

$$\Delta\Phi_{SRG} = \phi_{SRG} - \phi_{\omega_2} = (\mathbf{k}_2 - \mathbf{k}_1 + \mathbf{k}_1 - \mathbf{k}_2) \cdot \mathbf{L} = \Delta\mathbf{k} \cdot \mathbf{L} \quad (2.8)$$

In equations 2.7 and 2.8, we now define the wavevector mismatch, $\Delta\mathbf{k}$. In general, if $\Delta\Phi > \pi$, the radiation originating from the induced polarization cannot propagate into the far field. It is serendipitous that for both SRG and SRL experiments $\Delta\mathbf{k} = 0$ and consequently $\Delta\Phi = 0$. In other words, there is no phase mismatch between the induced polarization and a propagating signal field. The signal is said to be phase matched in the forward propagation direction of $\mathbf{k_i}$. For homogeneous bulk samples, $\mathbf{L}$ is very long compared to an optical wavelength, so $\Delta\mathbf{k} \approx 0$ is a crucial condition. Importantly, in the backward direction, the wavevector of the propagating signal field is $-\mathbf{k}_i$, and it can be seen that $\Delta\mathbf{k} \neq 0$ for both SRG and SRL. Consequently, even for small $\mathbf{L}$ the total phase difference $\Delta\Phi$ easily surpasses $\pi$, resulting in a complete phase mismatch and thus no signal in the backward direction.

### 2.3.2 Phase matching in coherent Raman microscopy

While the above section focuses on the wavevector mismatch, $\Delta\mathbf{k}$, the full equation for the phase difference, $\Delta\Phi = \Delta\mathbf{k} \cdot \mathbf{L} < \pi$, leaves open the possibility of experimental conditions where the above criterion can be satisfied even if the wavevector mismatch is nonzero. This becomes highly relevant in the case of microscopic probing volumes. In a typical SRS microscopy setup, the pump and Stokes beams propagate collinearly and are not spatially separated. As stated above, in the forward direction $\Delta\mathbf{k} = 0$, yet in the backward direction $\Delta\mathbf{k} >> 0$ and we might expect an absence of detectable signal on an epi-direction detector.

However, the beams are focused by an objective lens to a very small focal volume. For a high numerical aperture objective, $\mathbf{L} \sim 1$ $\mu$m, on the order of an optical wavelength. If the focal volume contains very small objects, then the interaction distance $\mathbf{L}$ can be very small such that the condition $\Delta\mathbf{k}\cdot\mathbf{L} < \pi$ is met for backward radiated fields.[183;184] Hence, unlike in SRS spectroscopy of bulk samples, in SRS microscopy situations exists where phase-matched signal can be detected in the epi-direction as well.

Another difference between regular SRS spectroscopy and SRS microscopy is how the signal is modeled. In SRS spectroscopy the propagating fields are assumed to be plane waves and the signal is commonly described by the one-dimensional nonlinear wave equation. This approximation is no longer valid when describing the signal in SRS microscopy. The wavefront passing through the objective lens spans a wide distribution of propagation angles, which are needed to form a tightly focused interaction volume. This negates the use of the one-dimensional wave equation as a tool for modeling signal generation. Additionally, a collimated beam with a linear transverse polarization will be transformed by the focusing lens to produce a focal field with non-negligible polarization components along both the transverse and longitudinal dimensions.[185] To further complicate the matter, the Gouy phase shift becomes manifest over a distance similar to an optical wavelength under microscopic focusing. These distinctions from macroscopic SRS has led to the development of a different class of models to describe the generation and propagation of the SRS signal from microscopic volumes. A more intuitive approach is to model the sample as an ensemble of dipole emitters driven nonlinearly by the excitation fields. The radiation generated by the dipoles can be collected in the far-field, and the magnitude and direction of the signal computed as a function of particle size, shape, position and other material properties.[174;184]

### 2.3.3 Instrumentation for SRS Microscopy

Despite the difficulty in modeling, SRS experiments at the microscopic level have proven to be feasible and practical. The field of SRS microscopy is flourishing especially in its use to image and study biological samples. The traditional appeal of the technique is its ability to generate label-free, chemically specific samples. Experiments are often conducted with near infrared beams, such that sample heating and photodamage is generally not a concern. As a multifaceted tool, it is capable of imaging tissues, cell cultures in both monolayer and three-dimensional form, and molecular distribution inside single cells. In this section, we examine the common instrumentation builds utilized in SRS microscopy.

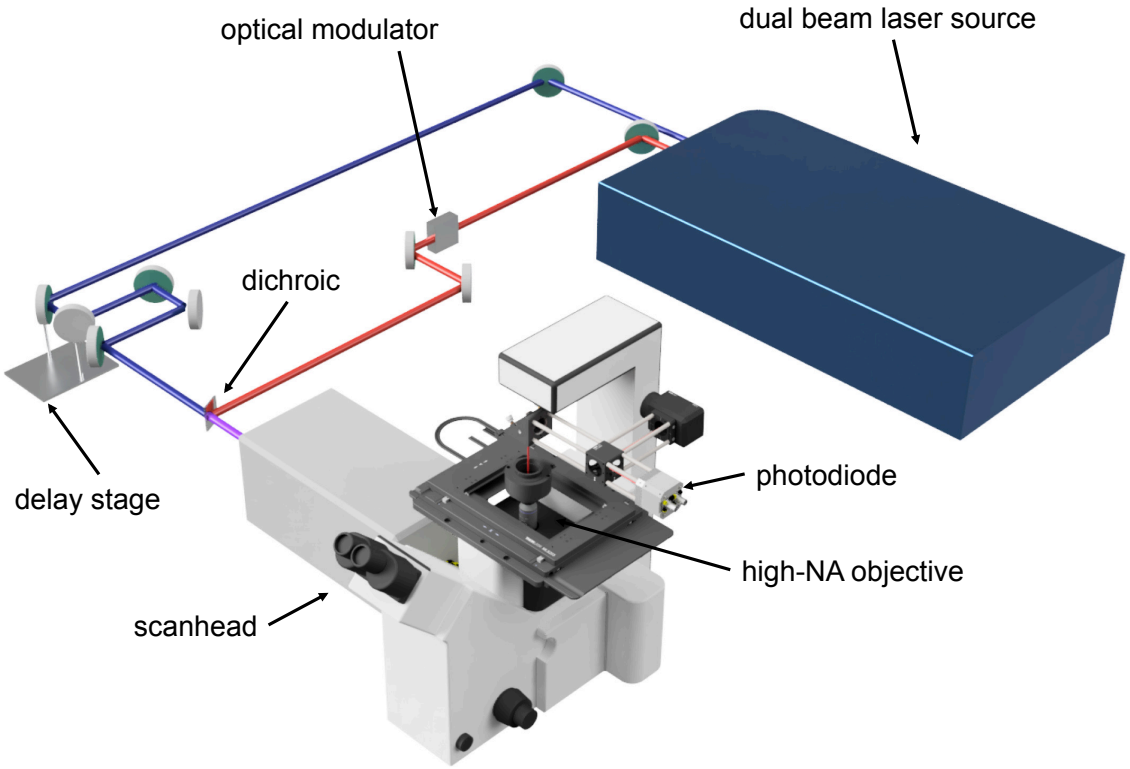



Figure 2.10: A typical SRS setup with two synchronized beams.
During the SRS process the modulation applied to one beam is transferred to the other.
The signal can then be demodulated with a lock-in detector.

SRS systems and experiments can be divided into two broad categories based on the laser being used: 1) broadband techniques, using a femtosecond laser, or 2) narrowband tech-

niques, which typically make use of a picosecond laser. In an SRS experiment, the two light fields, pump $\omega_1$ and Stokes $\omega_2$, must be supplied in a synchronized manner. This can take the form of two synchronized lasers, a laser and an optical parametric oscillator (OPO), or a single laser whose output is split and modified in some way.

The major difference between broadband SRS and narrowband SRS is in how the condition $\omega_\nu = \omega_1 - \omega_2$ is fulfilled. In SRS microscopy, the Raman-active mode, $\omega_\nu$ is the source of contrast. In narrowband, or frequency-tuned, SRS experiments, a picosecond light source with a repetition rate near 80 MHz is commonly used. The light source is coupled with an OPO which allows one of the two beams to be tuned such that $\omega_\nu$ can be selected. The other beam may be provided by a second laser output, through residual OPO-pump light, or from the idler beam of the OPO depending on the specifics of the setup. After one of the beams is modulated — pump for SRG, Stokes for SRL — the beams are spatially and temporally overlapped. The overlapped beams are raster-scanned through a high-NA objective incident onto the sample. From there, the output beams are spectrally filtered to remove the originally modulated beam, and the one carrying the SRS signal is detected. In this setup, the choice of the variable wavelength beam is the determining factor in what Raman mode is probed. The narrow spectral bandwidth of picosecond pulses gives rise to the ability to be highly selective of which mode is probed. For hyperspectral imaging, multiple images — each at a different wavelength — are acquired and analyzed. The down side of this method is that spectrally tuning is generally a slow procedure, so obtaining a relatively wide spectrum of images is time-consuming. Additionally, the relatively lower power of picosecond pulses compared to femtosecond pulses reduces the overall signal.

For broadband SRS microscopy, the technique further can be separated into two distinct methodologies: shaping techniques and the multiplex techniques.[2;56] Two different but similar approaches are used to shape pulses for SRS microscopy, namely pulse shaping and spectral focusing. In both techniques the output of a femtosecond laser is shaped to im-

prove the spectral resolution of the experiment. In the pulse shaping technique a 4-f pulse shaper, consisting of a grating and a motorized slit or spatial light modulator, is employed to spectrally shape either the Stokes or pump beams, or both. In one implementation, a pulse shaper picks a color out of a broadband femtosecond pulse. By holding one line at a constant wavelength, the other can be quickly scanned to allow for rapid spectral imaging. Nonetheless, this method presents some difficulties however, as it adds complexity to the setup and requires high-output power from the laser source as only a small percentage of the total light in each pulse makes it to the sample. In the spectral focusing technique, adequate spectral resolution is created by positively chirping both the pump and Stokes beam. This creates a quasi-linear distribution of frequencies as a function of time. By scanning the time delay of one beam relative to the other, the difference frequency for driving a specific Raman mode is selected. This method is easier to implement than pulse shaping, however, the spectral resolution is relatively low, $\sim 20$ cm$^{-1}$ in practical applications.

In multiplex SRS microscopy, a combination of broadband and narrowband pulses is used. The combination of the two pulses excites multiple Raman modes simultaneously. This idea is similar to what is used in SRS spectroscopy. However, whereas in spectroscopy applications a spectrometer is used for resolving the spectral components, such an approach is too slow for signal collection in microscopy. For this purpose, alternative detection strategies have been developed. In one such scheme, the pump beam is spectrally dispersed and the various wavelengths are amplitude modulated at distinct frequencies. The beam is recombined and overlapped with a narrowband Stokes beam. After interaction with the sample, the SRS signal is encoded onto the Stokes with distinct frequency components. The signal is recorded by a single photodiode in the time domain. A Fourier transform of each pixel will then give rise to the SRS spectrum.[186–188] Many other strategies exist for capturing the SRS spectrum. One implementation involves spectrally dispersing the detected beam onto a photodiode array with either tuned or resonant amplifiers or multi-channel lock-in detectors for demodulation of each spectral component[62–64;66;189].

### 2.3.4 Applications of SRS Microscopy

The broad array of instrumentation types as well as abilities conferred by the nature of nonlinear microscopy allow SRS to be deployed to a wide array of use cases. While we attempt to highlight these cases here, the reader is also referred to a number of review articles on the subject of SRS microscopy.[2;190–193] With an axial resolution of approximately 1$\mu$m, SRS offers excellent optical slicing capabilities for three dimensional imaging. For certain cases, the signal generation efficiency is high enough to enable video-rate imaging in biological samples.[194] This corresponds to a frame rate of 30 frames per second and a pixel dwell time around 100 ns. Like other microscopy techniques, multiple SRS images can be combined and overlapped to produce mosaics of tissue samples several centimeters in diameter.[10;195] Some examples of the myriad uses of SRS microscopy are shown in Figure 2.11.

Perhaps the area where SRS microscopy has really stood out is in metabolic imaging through the use of hyperspectral and multiplex acquisition and analysis. By producing images targeting different Raman modes, chemically informative maps can be produced and quantitative measurements made. Lipid mapping and lipid-to-protein ratios are a mainstay of SRS microscopy.[32;39;196–202] The 3015 $cm^{-1}$ band associated with C=C-H stretching modes in unsaturated fatty acids and the $CH_2$ stretching mode of lipids at 2845 $cm^{-1}$ provide excellent sources of contrast. Of particular note, these bands were used to follow in vivo myelination of tadpoles.[203] They have been used to image various fatty acids in multiple types of cancer cells. Protein and nucleic acid distributions can also be distinguished inside cells and within the extracellular matrix.[204;205]

One of the earliest demonstrations of SRS was performed on human lung cancer cells. This work provided prelude to the extensive use of the technique for studies of various kinds of cancers including breast cancer[29;206], skin cancers[207], brain tumors[208;209], and gastro-intestinal

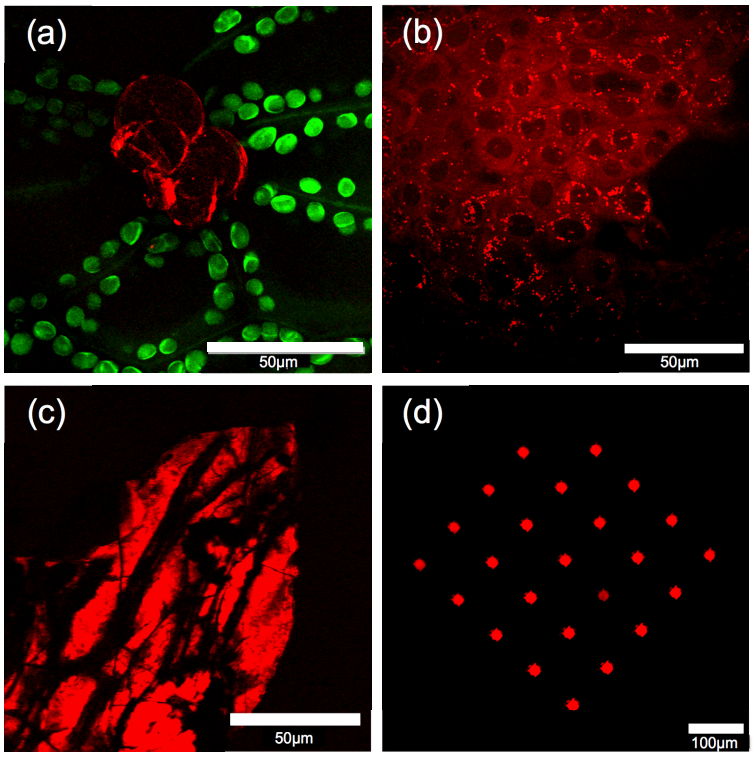



Figure 2.11: Examples of SRS imaging of various samples in the high frequency range (2000 $cm^{-1}$ – 3300 $cm^{-1}$)
(a) Lipid secreting gland of *Drosera capensis* at 2845 $cm^{-1}$ (red) and pump-probe signal from the surrounding choloroplasts (green). Sample courtesy of Jessica Kelz (UC Irvine). (b) Lipid droplet distribution in cultured rabbit meibocytes at 2845 $cm^{-1}$. Sample courtesy of Dr. James Jester (UC Irvine). (c) Crystallized d38-cholesterol crystal imaged at 2140 $cm^{-1}$. (d) Polymer cubes printed with two-photon polymerization visualized at 2900 $cm^{-1}$.

tumors[210]. The reader is directed to Austin et. al. for a more through review of SRS applications in cancer diagnostics.[211] SRS has also proven useful in other areas of biomedicine. It can be used to characterize vascular structure and atherosclerotic plaques[21;212;213], as well as monitor a host of other pathologies.[214–222]

In addition to using the intrinsic contrast of native biomolecules, much work has recently gone into using small molecule Raman tags such as carbon-deuterium bonds (C-D), alkyne tags (C≡C), the carbon fluoride bond (-C-F), azides ($-N_3$), nitriles (-C≡N) and isonitriles (-N≡C).[14;41;43;215;223–225;225–228] These various tags occur in what is commonly called the cell-silent region of the Raman spectrum between $\sim$ 2000 $cm^{-1}$–2700 $cm^{-1}$. The use of deuterium

labeling has been developed to allow tracing of lipogenesis from glucose, protein metabolism and other small precursor molecules.[34;35;37;229;230] It has been shown to have little to no biological effects even to a high percentage of use.[41;203;231] In addition to the use of small functional group tags, other reporter molecules with unique Raman signatures have been developed for both the Raman microspectroscopy community and for SRS imaging.[50;232–235] The development of bioorthogonal tags and their use is SRS microscopy is an extremely promising technique.

While all the above applications focus on biology or disease, SRS has also found a niche in research on materials, biofuels, plant research, and pharmaceutical analysis. In the realm of materials-science SRS has been used alongside other methodologies to study microstructures in two-photon polymerization additive manufacturing,[236;237], as well as crystal orientation and more basic research.[238–240] Research into plant materials has been demonstrated several times with algae, lignin, and cellulose for biofuels and other purposes.[9;187;241–244] Additionally, SRS microscopy has been used to study and suggest improvements for drug delivery and manufacture, to examine drug breakdown over time in pellets, and drug release in drug delivery systems.[245–251]

While the field of SRS microscopy is barely a decade old, it has resulted in a large number of publications and meaningful impacts across a variety of fields. Researchers are actively developing new techniques, new tags, and examining new systems. As these technologies mature, SRS is sure to serve as an impactful and fruitful tool for new discoveries in the microscopist's workbench.

## 2.4 From Ensembles to Single Molecules

The success of SRS microscopy, where sample volumes are orders of magnitude smaller than in regular SRS spectroscopy, suggests that further reduction of the sample volume might be possible. This notion has raised the prospect of pushing SRS microspectroscopy all the way to the single molecule limit. In this Section, we will discuss work that explores the possibility of single molecules SRS and its tentative applications.

The transition from small microscopic volumes to single molecules is quite a leap. For instance, a tightly focused laser beam with a high numerical aperture objective reaches effective excitation volumes of $\sim 0.1$ fL. When this light is focused in aqueous media, the focus roughly encompasses $3.3 \times 10^9$ water molecules. The signal from a single water molecule can thus be expected to be several billion times less than the SRS signal measured in a microscope when the sample is bulk water - signals that are many order of magnitude below practical detection levels. Clearly, to reach single molecule detection levels, regular SRS microscopy techniques come up short. Some form of enhancement is needed to lift the SRS signal from single molecules to detectable levels. Currently, two mechanisms for signal enhancement are actively explored: 1) the enhancement of the Raman cross section through electronic resonances in the molecule, and 2) enhancement through confining the electromagnetic modes to nano-scopic volumes, reaching the molecular size.

### 2.4.1 Enhancing SRS with electronic resonances

As discussed in Section 2.2, the use of an electronic resonance in the molecule to enhance the response is a well known strategy to improve the sensitivity and selectivity of the SRS signal. Similar to the resonance Raman effect, stronger SRS signals can be expected when the frequency of the pump beam is tuned close to an electronic resonance. This mechanism

is sketched in Figure 2.12a. In addition, the vibrational mode needs to be coupled to the electronic transition in order to maximally benefit from the electronic enhancement. Usually, this condition is met for vibrational modes closely associated with the $\pi$-conjugated network of the molecule, such as the C=C vibrations of bonds that are directly implicated in the electronic transition. The effective Raman cross section of such vibrational modes can be up to six orders of magnitude higher than for similar modes that lack the benefit of electronic enhancement. Resonance-enhanced SRS has been extensively used to study the vibrational dynamics of chromophores in solution, and has recently also been used in SRS microscopy. By choosing or designing optimal chromophores and tuning the excitation wavelength of the incident beams on or near the electronic resonance, effective enhancements of the SRS signal by $10^6$ have been reached[51;52;252]. In combination with microscopic focusing, resonance-enhanced SRS signals of as little as $\sim$ 500 molecules have been detected[157].

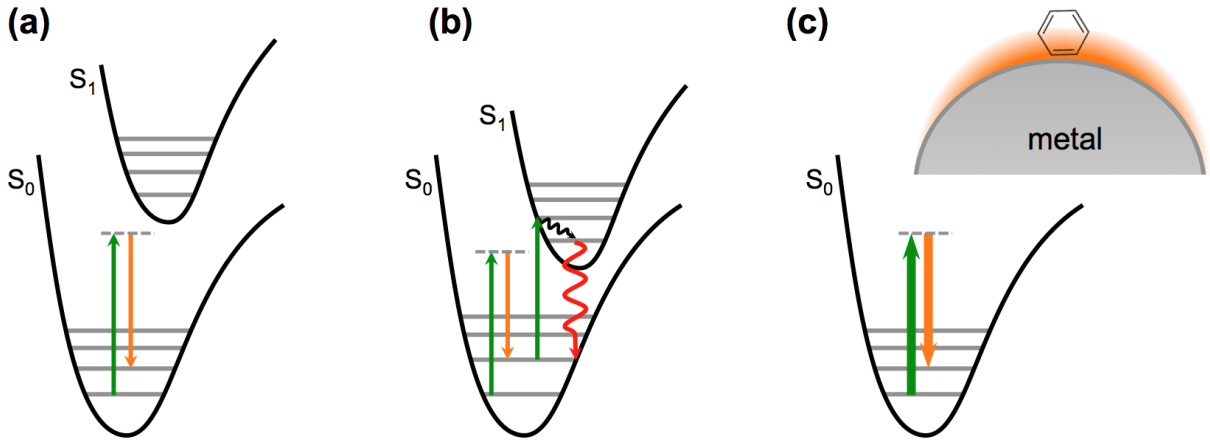



Figure 2.12: Different forms of electronic enhancement of the SRS signal. (a) (Pre-)resonant SRS. The molecular Raman polarizability is enhanced by an electronic resonance of the molecule. (b) Stimulated Raman excited fluorescence (SREF). An SRS process in the ground state is followed by an excitation to the excited state of a fluorophore, followed by fluorescence emission. (c) Surface-enhanced SRS. The transition rate in the molecule is accelerated by the presence of enhanced local excitation fields, provided by a plasmonic antenna.

Whereas the well-known strategy of resonance-enhanced SRS has reached impressive sensitivities, comfortably reaching the single molecule limit with this approach remains a challenge,

and it remains to be seen how practical the method is for SRS measurements of individual molecules. This notion has prompted the development of alternative methods that leverage the strong response of electronic transition in molecules. Inspired by fluorescence-encoded infrared absorption spectroscopy, recent efforts have focused on using the mechanism of SRS-assisted fluorescence as an effective means to perform vibrational measurements on molecules that exhibit strong fluorescent emission. In this approach, a vibrational state is first populated in the ground state potential through the SRS mechanism and subsequently probed by exciting the molecule to an electronically excited state with an additional light-matter interaction. The fluorescence that follows is then a measure of the successful population of the vibrational state[55]. This process is illustrated in Figure 2.12b. The beauty of this approach is that it takes maximally advantage of the efficiency of the fluorescence process. Using molecules that exhibit high fluorescence quantum yields, the fluorescence probing step can reach efficiencies close to 1, thus completely eliminating the tentative challenges of detecting the loss of a single pump photon in a regular stimulated Raman loss experiment on a single molecule. Hence, whereas stimulated Raman excited fluorescence (SREF) involves an additional molecular excitation in addition to the ground state SRS transition, the fluorescence detection strategy is orders of magnitude more sensitive than the common SRS detection scheme. This optimization of detection scheme has led to new SRS sensitivities that were hitherto deemed impossible, enabling reproducible measurements of single molecules with good signal to noise ratios[55;253]. This method is thus suitable for mapping fluorescent probes with a spectral resolution defined by the vibrational linewidth of the chosen marker band. On the other hand, the requirement of specific fluorophores with favorable properties for SREF renders the method unsuitable as a general approach to increase the SRS detection sensitivity for any given molecule. In this regard, methods that do not rely on the presence of electronic resonances in the target molecule remain of great interest. The most successful approach in this category is the use of nanoscale antenna systems that support plasmonic resonances, which we wil discuss next.

### 2.4.2 Enhancing SRS with plasmonic resonances

In 1974, Fleischmann et al made a very curious observation. They found that the spontaneous Raman signal of pyridine was much stronger if the target molecule was adhered to a roughened silver electrode[254]. Several years later, members of the Van Duyne group figured out why: the surface plasmon resonances supported by the nano-structured silver provided local fields are strong enough to enhance the Raman response from the molecules in close vicinity to the surface[255]. Subsequent work underlined the favorable properties of localized surface plasmon resonances for surface spectroscopy[256], and Raman spectroscopy in particular[158]. Structures that support such resonances, typically made of noble metals that display resonances in the visible range of the spectrum, act like efficient antennas in that they couple propagating radiation to strongly localized evanescent fields[257]. The spatial confinement of such surface bound electromagnetic fields can be so effective that 'hotspots' of less than a nanometer can be reached. At these scales, far below the diffraction limit of propagating light, the fields are confined to dimensions that approach the molecular size, allowing efficient coupling of the field to the charges in the molecule. Vice versa, the radiative properties of the induced polarization are enhanced by the presence of the plasmonic antenna, allowing the near-field molecular polarization to couple efficiently to the far-field.

In this picture of electromagnetic enhancement of the signal, the surface enhanced Raman scattering (SERS) response can be understood as:

$$S(\omega_s) \propto N\beta^2(\omega_p) I_p \beta^2(\omega_s)\sigma_s \tag{2.9}$$

where $\omega_s$ is the Stokes frequency, $\omega_p$ is the pump frequency, $\mathrm{I}_p$ is the pump intensity $N$ is the number of molecules in the illuminated volume and $\sigma_s$ is the Raman cross section. The field enhancement factor is denoted as $\beta$. Both the excitation (at $\omega_p$) and radiation (at $\omega_s$) processes are enhanced by a $\beta^2$ factor by the antenna, giving rise to an effective enhancement

of the Raman signal by $\beta^4$. Well designed nano-antenna systems offer $\beta$ factors of well over 100 times, producing overall enhancement factors in the range $\beta^4 \sim 10^8 - 10^{12}$. Such enhancements have been shown to be sufficient to generate spontaneous Raman signals from single molecules[258–260]. Given the infamous weakness of the Raman effect, the ability to perform Raman experiments at the single molecule level is truly a remarkable achievement, and it underscores the tremendous efficiency of plasmonic antennas to improve the optical interaction between propagating radiation and the molecule.

The success of SERS suggests that even stronger signals can be expected when surface enhancement is combined with SRS, shown schematically in Figure 2.12c. The Raman signal of the simple picture presented in equation (2.9) would then be further amplified by a factor proportional to $I_s$, the intensity of the stimulating Stokes beam. Whereas the surface enhancement factor of the surface enhanced SRS signal would still be $\beta^4$, the effect of the stimulating beam can be expected to increase the transition rate in the molecule by another factor of $10^5 - 10^6$. The motivation for developing surface enhanced version of SRS is thus to collect Raman signals from low concentration samples, down to single molecules, at much higher signal acquisition rates than what can behttps://www.overleaf.com/project/608bafee05e5010838e54e05 achieved with SERS.

As stated earlier, the first indications that the SRS process can be enhanced by surface plasmons were provided in 1979, only a few years after the SERS mechanism was established[161;162]. In the same year, it was unambiguously shown that the surface plasmon polaritons (SPPs) provided by flat silver films were responsible for the enhancement of coherent anti-Stokes Raman scattering (CARS) from benzene molecules in close proximity to the film[261]. Despite these encouraging early indications, surface-enhanced SRS was not further pursued until much later. In 2011, interest in surface enhanced SRS was rekindled by a femtosecond SRS study on molecules adhered to gold dimer antennas[262]. The resulting spectrum is shown in Figure 2.13. Besides the encouraging observation that clear vibrational signa-

tures of the molecules were visible on the spectrally resolved signal, this study also revealed a somewhat unexpected feature, namely the dispersive nature of the vibrational lines and the presence of a relatively strong pump-probe background. Subsequent studies confirmed that this observation was no fluke but rather an intrinsic property of surface enhanced SRS.

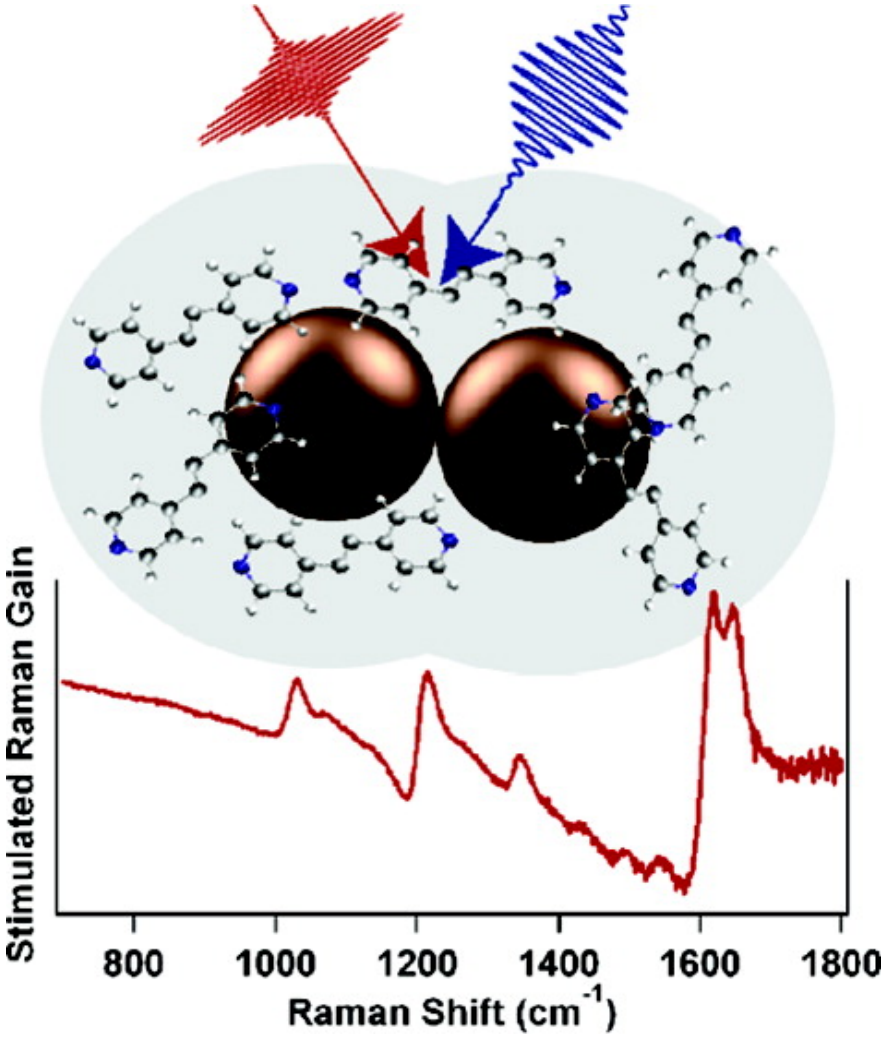



Figure 2.13: The First Demonstration of Surface-Enhanced SRS
Surface-enhanced SRS was first demonstrated on nanoantennas containing trans-1,2-bis(4-pyridyl)-ethylene molecular reporters. Adapted with permission from Ref[262]. Copyright 2011 American Chemical Society.

The virtually background-free signals and the Lorentzian lineshapes that make SRS spectroscopy in many cases preferable over CARS microscopy seem no longer applicable when the SRS process is mediated by surface plasmons. Several theoretical works have attempted

to explain the observed dispersive lineshapes. What is clear from the analysis is that the Raman polarization is no longer driven by the propagating field, but by the local surface plasmon field instead. The phase of the local field can differ markedly from the phase of the incident field. The local field enhancement factors are thus complex quantities that can alter the phase relation between the driving fields and the radiated polarization in the far-field. This principle largely explains the trends observed in the surface enhanced SRS signals collected in a microscope[263].

Is the surface enhancement effect sufficient to bring SRS sensitivity into the realm of single molecules? This indeed appears to be the case. Experiments in the Cheng group have focused on individual hotspots in nano-sphere aggregates and have found convincing evidence that vibrational signatures from single adenine molecules can be detected.[264] Using a bianalyte method and a special denoising algorithm to improve the SRS images, reproducible spectra that can be assigned to individual molecules were obtained. Similar to previous measurements, the spectra display dispersive lineshapes on a rather strong background. It was identified that the photothermal effect was a major contributor to the background, offering hopes that improvements in experimental design can increase the SRS sensitivity for single molecules even more.

### 2.4.3 Advanced techniques: Non-Optical Detection

In SRS, the coherent Raman polarization in the sample is probed through the radiation that reaches the far-field detector. Whereas in surface enhanced SRS the near-field interactions are amplified by the action of surface plasmon fields, the detection principle remains the same: the near-field Raman polarization is detected by the successful radiation of photons into the far-field. However, optical detection is not the only mechanism by which the Raman polarization can be examined. Several forms of non-optical detection of SRS have emerged

and they turn out to be specifically relevant for measurements at the nanoscale.

One form of probing the induced Raman polarization is by detecting the force between the oscillating charges in the molecule and the dipole in an atomically sharp tip that is placed in the immediate vicinity of the molecule. This electromagnetic dipole-dipole force is weak, typically less than a pN[265], but it is sufficient to be picked up by a modern scanning probe microscope. This principle was used to detect the stimulated Raman signal from chromophore molecules on a glass surface.[266] Using cw pump and Stokes beams, this force detection method, named photo-induced force microscopy, was able to resolve small clusters of molecules with a spatial resolution well under 10 nm.

Another form of scan probe microscopy uses the electron tunneling current between the sample and the sharp tip as the contrast parameter. In a very elegant piece of work, the Ho group recorded the changing tunneling current of a molecule bound to the surface as it flip flops under the influence of a femtosecond pulse pair.[267] The flopping rate, recorded through the current, is a function of the successful transfer of energy from the light to the molecule, i.e. energy that is needed to complete the flip flop. This energy transfer is only successful if a Raman mode is excited. By time-delaying the pulse pair, the Raman coherence induced by the first pulse is converted to a vibrational population only periodically by the second pulse. This results in periodic modulation of the flopping rate as a function of the time delay between the pulses. In essence, this is a time-resolved ISRS experiment detected through the tunneling current, performed on a single molecule!

The examples above illustrate that other sensitive techniques can be employed to study molecules on the nano-scale through the principle of the stimulated Raman effect. It is likely that non-optical techniques, which do not suffer from the challenge of detecting a small signal relative to the intensity of the probe beam, will gain importance as efforts increasingly focus on the coherent Raman response of single molecules.

# Chapter 3

# Coherent Raman Scattering: a Nonlinear Optical Process

## 3.1 A Brief History of Nonlinear Microscopy

Since the invention of the microscope, the role of optics in understanding biology and medicine has been difficult to overstate. During the middle and late twentieth century, many new techniques such as phase-contrast, differential interference contrast, and dark-field contrast were developed that expanded the role of microscopy and opened many new aspects of the microscopic world to investigation. The first theoretical prediction of multiphoton phenomena occurred in 1931, and the first demonstration was not until after the invention of the laser enabled access to high energy density, coherent sources of light.[94;268] Afterwards, nonlinear microscopy techniques, e.g. second harmonic generation (SHG), two-photon excited fluorescence (TPEF), third-harmonic generation (THG), were developed at the turn of the twenty-first century, evolving from experimental work done in spectroscopy and laser development over the preceding decades.[112;269–271]

During this same period, the development of Raman spectroscopy and its use as a microscopic tool accompanied the invention of the various refractive contrast methods, harmonic generation spectroscopies, and many fluorescence techniques.[272;273] Raman spectroscopy provides a means of studying the chemical constituents of a sample. The information available in a Raman experiment includes chemical subgroups, their relative concentration to one another, bond strength and dynamics, and molecular symmetry. Raman spectroscopy is often said to give a *fingerprint* from which to identify molecules.[274] Raman has proven to be a powerful tool in many areas including gas phase, condensed matter, and more recently biology. However, it it not without its weaknesses. Raman measurements are notoriously slow, and it is often difficult to extract the weak Raman scattering signal from a large fluorescent background.

The origin of the Raman effect is inherently found within quantum mechanics, and it is within that framework that several alternatives to it can be found. Much as Göppert-Mayer

predicted multiphoton absorption and emission to act as counterpart to linear absorption and fluorescence, so to were a set of phenomena analogous to Raman scattering discovered and characterized.[107;112;275] Of particular note, are Coherent Anti-Stokes Raman Scattering (CARS) and Stimulated Raman Scattering (SRS). Collectively, they fall into the classification of Coherent Raman Scattering (CRS) techniques. Both phenomena provide information based on the linear Raman spectra, but they rely on different experimental parameters.

As discussed in Chapter 1, the application of CRS as a microscopic tool significantly lagged behind the development of theory and spectroscopy applications. The first demonstration of a CARS microscope was in 1982[1], nearly twenty years after the first demonstration of the CARS effect.[115]. The first demonstration of an SRS in a microscope occurred even later in 2007, and was it quickly followed the next year with an application to biological systems.[148;149] Given the multitude of uses of CARS and SRS, it behooves us to spend some time discussing the fundamentals of nonlinear optical interactions in more detail than in Chapter 1

## 3.2 Understanding Nonlinear Optical Processes

> My gratitude to Dr. Dimitry Fishman for the opportunity to work as an instructor, and to the undergraduates who have had to work with me while I parsed this out for myself.

*How does a material respond to the presence of light* serves as the fundamental inquiry associated with much of optical science and spectroscopy. All matter is composed of particles possessing charge, and to varying degrees, charged particles will rearrange themselves perturbed an electric field. The rearrangement of charges on the macroscopic level is described

by the time-varying *polarization*, $\vec{P}(t)$, defined as in 3.1

$$\vec{P}(t) = \epsilon_0 \chi_e \vec{E}(t) \tag{3.1}$$

where $\chi_e$ is the *electric susceptibility* and $\vec{E}(t)$ is an applied electric field. This quantity is of immense interest as it can be shown that an oscillating polarization will itself satisfy the electromagnetic wave equation, thus acts as a source of radiation.

### 3.2.1 The Lorentz Model and the Harmonic Oscillator

A clear understanding of the origin of the time varying polarization in matter begins with an analysis based on one of the most ubiquitous models in physics, the harmonic oscillator.[276;277] It is a model that describes many natural phenomena, and its utility seemingly knows no bounds. It finds uses in phenomena as far-ranging as the vibrations of a guitar string[278] to electronic circuits[279] to finally spectroscopy.[280] The commonality between these systems lies in the mathematics of oscillatory systems, and within the classical regime the vibrations of molecules is no difference. In this section the basics of harmonic systems is reviewed and a classical description of the Raman effect is introduced. These descriptions and the simplest forms of the equations involved have served as a useful didactic tool for introducing spectroscopy, and the spectroscopy for introducing basic physics.

The use of the harmonic oscillator to describe optical systems traces itself to the Lorentz model for simple atoms, and is further developed in many texts for diatomic and polyatomic molecules.[151;281–284] The simplest case concerns a mass attached to a spring as shown in Figure 3.1 (a). This system is subject to two laws governing its motion: Newton's 2nd Law, $\vec{F(t)} = m\frac{d^2x}{dt^2}$ and Hooke's Law, $\vec{F(x)} = -kx$.

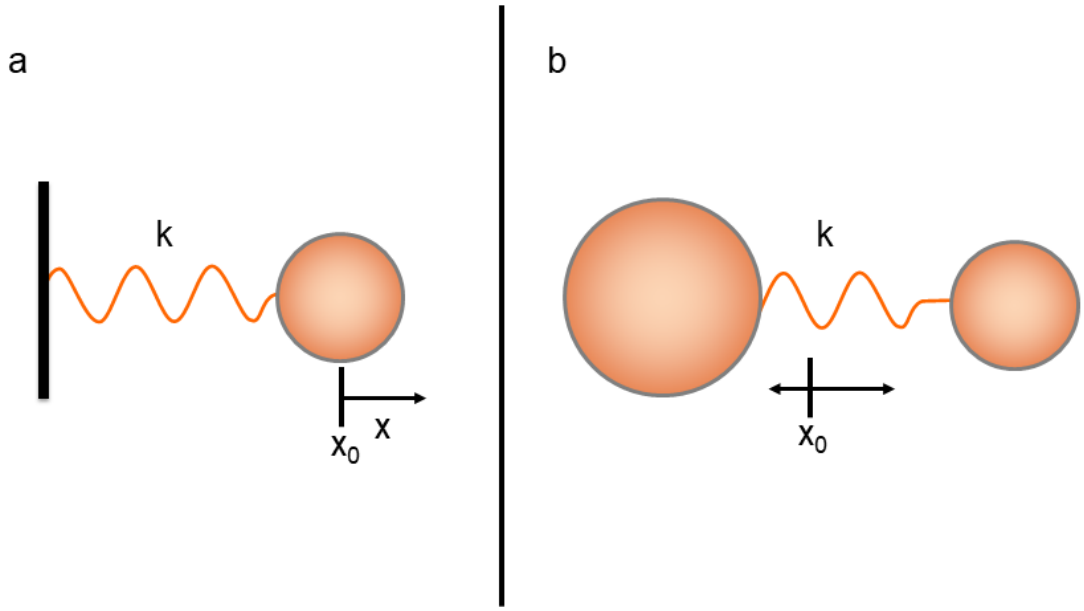



Figure 3.1: Simple Harmonic Oscillators
(a) A simple case of a mass on a spring. $x_0$ is the equilibrium position of the mass. (b) A simplified representation of a diatomic molecule. The In this case the bonds between atoms serve as the spring. $x_0$ is the center of mass of the two atom system.

Equating both equations and setting to zero gives equation 3.2.

$$\frac{d^2x}{dt^2} + \frac{k}{m}x = 0 \tag{3.2}$$

This is the simplest form of the harmonic oscillator without either damping or driving. It has a solution of $x(\vec{t}) = Acos(\omega_0 t + \psi)$ The spring constant and the mass together define the resonant frequency of the system, $\omega_0$, where $\omega_0^2 = \frac{k}{m}$. Adding in a damping term, $\vec{F} = -2\gamma m\frac{dx}{dt}$ and a driving term $\vec{F_{driving}}(t)$ yields the driven, damped harmonic oscillator, equation 3.3 from which our analysis will be based.

$$\frac{d^2x}{dt^2} + 2\gamma\frac{dx}{dt} + \frac{k}{m}x = \vec{F}_{driving}(t) \tag{3.3}$$

In terms of optics, it can be genrally assumed that the the driving force will take the form of a rapidly oscillating wave with angular frequency $\omega$. Thus,

$$\vec{F}_{driving}(t) = \vec{F}_0 e^{-i\omega t} \tag{3.4}$$

By making a reasonable ansatz, we can look for a solution to the equation of motion with the form $\vec{x}(t) = \vec{x}(\omega)e^{-i\omega t}$. By taking the derivatives of the ansatz, we can substitute into equation 3.3 as below:

$$\frac{dx}{dt} = -i\omega x(\omega)e^{-i\omega t} \tag{3.5}$$

$$\frac{d^2x}{dt^2} = -\omega^2 x(\omega)e^{-i\omega t} \tag{3.6}$$

$$-\omega^2 x(\omega)e^{-i\omega t} - i2\gamma\omega x(\omega)e^{-i\omega t} + \omega_0^2 x = \frac{\vec{F}_0 e^{-i\omega t}}{m} \tag{3.7}$$

after gathering like terms and rearranging we find the solution to the general equation of the damped driven harmonic oscillator with a harmonic driving force:

$$x(\omega) = \frac{\frac{\vec{F}_0}{m}}{\omega_0^2 - \omega^2 - 2iw\gamma} \tag{3.8}$$

Equation 3.8 is a form of the complex lorentzian function which is commonly used in describing lineshapes in various spectroscopies.[284;285] Analysis of it's real and imaginary components will be expounded on later in the description of CARS and SRS.

### 3.2.2 Good Vibrations: A Model of Linear Raman Scattering

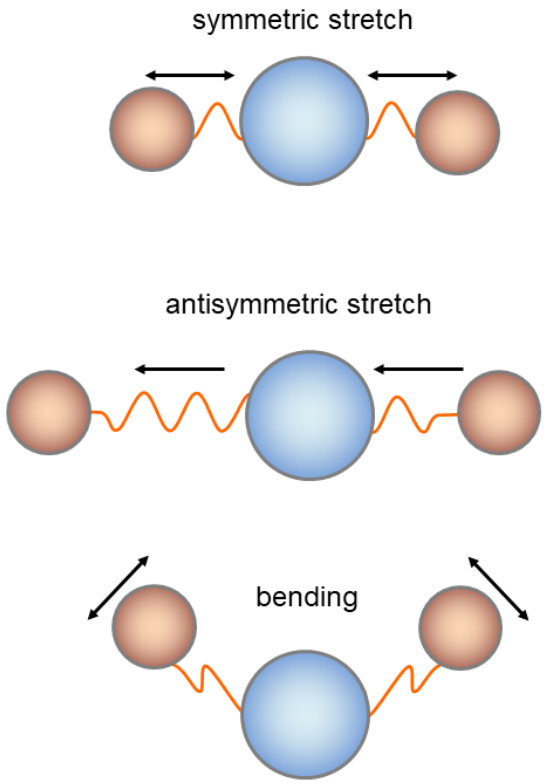



Figure 3.2

Our analysis of linear Raman scattering begins with the a fairly simple idea: molecules vibrate. A fact that Richard Feynman considered so important that it is laid out in Chapter 1 of the Feynman Lectures.[286] The nuclei of various atoms move towards and away from each other, they may rotate around bonds, and molecular orientation can change. Each motion of a molecule has an associated energy and, in general, vibrations and rotations may be described by characteristic normal modes. The specific normal mode is may be associated with a stiffness correlated with its energy. The strength of bonds, the mass of the nuclei, electronegativities, and bath interactions can all play a role in determining this stiffness, but in general the energies involved for a molecular vibrations are on the order of $10^2 - 10^4 cm^{-2}$, $10^{-20} J$.[282] The geometry of molecules defines the number of possible vibrational modes and defines the selection rules that are applicable to Raman spectroscopy. A linear molecule will

have $3n-5$ normal modes and a nonlinear molecule will have $3n-6$ where n is the number of atoms. These modes have been given names characteristic of the classical interpretation of their motion such as symmetric and anti-symmetric stretching modes, twisting modes, bending modes, and wagging modes among others.[280] A schematic of some of these modes is presented in figure 3.2

Given that molecules vibrate and have normal modes with characteristic energy, how does this explain the Raman effect? To that we want to return to the key quantity $\vec{P}(t)$, the polarization. We defined the polarization above in equation 3.1 with respect to the macroscopic susceptibility. We shall return to that definition, but for now we want to consider a single molecule. We know that as before the molecules of a material are made of charged particles that will respond to electromagnetic waves. The electron clouds forming the bonds of the molecules in particular are low enough in mass to respond adiabatically to the quickly oscillating light waves. The electrons will attempt to follow the electric field according to $\vec{F}(t) = -q\vec{E}(t)$ This shift in the electron clouds from equilibrium define an electric dipole moment given in equation 3.9

$$\vec{\mu}(t) = \alpha\vec{E}(t) \tag{3.9}$$

On this nanoscopic level we define the molecular polarizability $\alpha$ as the property of the material that describes the ability of the material to polarize in response to an electric field. In general, this can vary according to direction in space and is thus a tensor quantity. For simplicity's sake we only treat the isotropic case here. It can safely be assumed that in the general case the incident light field can be described as a sinusoidally varying function such that $\vec{E}(t) = \vec{E}_0 cos(\omega t)$, where we know that the cos function is the real portion of the complex exponential used above.

Of course, the electrons are not the only charged particles in the molecules. The nucleus of each atom has charge and will respond as well. However, the much greater mass of the of the nuclei means that they are unable to follow the rapidly varying electric field. The motion of the nuclei is defined by the relative motion of the between one another according to $\vec{q}(t) = q_0 cos(\Omega_R t)$ where $q_0$ is the amplitude of the vibration and $\Omega_R$ is the nuclear resonance. Changing the relative position of the nucleus will further modify the response of the electron cloud and in that sense the molecular polarizability $\alpha$. It is therefore a time-dependent quantity, and the induced dipole moment of the molecule can be written in the form below:

$$\vec{\mu}(t) = \alpha(t)\vec{E}(t) = \alpha(t)\vec{E}_0 cos(\omega t) \tag{3.10}$$

To a good approximation, it can be assumed that the nuclear displacement, $\vec{q}(t)$, is relatively small. This allows us to expand $\alpha(t)$ in a Taylor expansion around the nuclear displacement such that:

$$\alpha(t) = \alpha_0 + \left(\frac{\partial \alpha}{\partial q}\right)_0 q(t) + ... = \alpha_0 + \left(\frac{\partial \alpha}{\partial q}\right)_0 q_0 cos(\Omega_R t) + ... \tag{3.11}$$

Introducing the expanded molecular polarizability into formula 3.10 and ignoring higher order terms it follows that:

$$\begin{aligned}\vec{\mu}(t) = \alpha(t)\vec{E}(t) &= \left[\alpha_0 + \left(\frac{\partial \alpha}{\partial q}\right)_0 q_0 cos(\Omega_R t)\right]\vec{E}_0 cos(\omega t) \\ &= \alpha_0 \vec{E}_0 cos(\omega t) + \left(\frac{\partial \alpha}{\partial q}\right) q_0 cos(\Omega_R t) cos(\omega t)\end{aligned}$$

Applying the product identity to the second term above yields:

$$\vec{\mu}(t) = \alpha_0 \vec{E}_0 cos(\omega t) + \frac{\vec{E}_0 q_0}{2} \left(\frac{\partial \alpha}{\partial q}\right) [cos((\omega + \Omega_R)t) + cos((\omega - \Omega_R)t)] \tag{3.12}$$

Equation 3.12 defines the classical origins of the Raman effect. In fact, it contains three separate scattering phenomena. The first term on the right is interpreted as Rayleigh scattering. The fundamental incident field creates an oscillation in the molecule at the same frequency as itself. This is a form of elastic scattering. No energy is loss from the light field to the molecule The second and third term represent Raman scattering; an inelastic process. Specifically, the second term with frequency $\omega + \Omega_R$ corresponds to the so-called anti-Stokes scattering. In this process, molecular vibrations characterized by $\Omega_R$ lose energy to the incident light generating a blue shifted radiation field. The last term, $\omega - \Omega_R$, is the term corresponding to Stokes scattering. In this case, the incident light induces vibrations in the material at frequency $\Omega_R$ and loses a corresponding amount of energy causing a red-shift. All three processes are shown diagrammatically in figure 3.3. The equataion also defines the major selection rule in Raman spectroscopy. That is that to be Raman active a vibrational mode must affect the polarizability of the molecule. This is given by the derivative, $\left(\frac{\partial \alpha}{\partial q}\right)_0 \neq 0$ Thus, symmetric vibrations are generally very strong in Raman spectroscopy.

Mathematically, it is evident that the two inelastic processes produce shifted light symmetrically around the central incident frequency by $\Omega_R$. Stokes and anti-Stokes scattering thus give complementary information about the chemicals in a sample. From this level of theory, it would seem that Stokes and anti-Stokes scattering would scatter at the same rate as shown in figure 3.4 (a). However, this is not the case experimentally. In experiment, the intensity of the anti-Stokes radiation is significantly less than the Stokes scattering. The explanation for this phenomenon is in both quantum mechanics and thermodynamics.

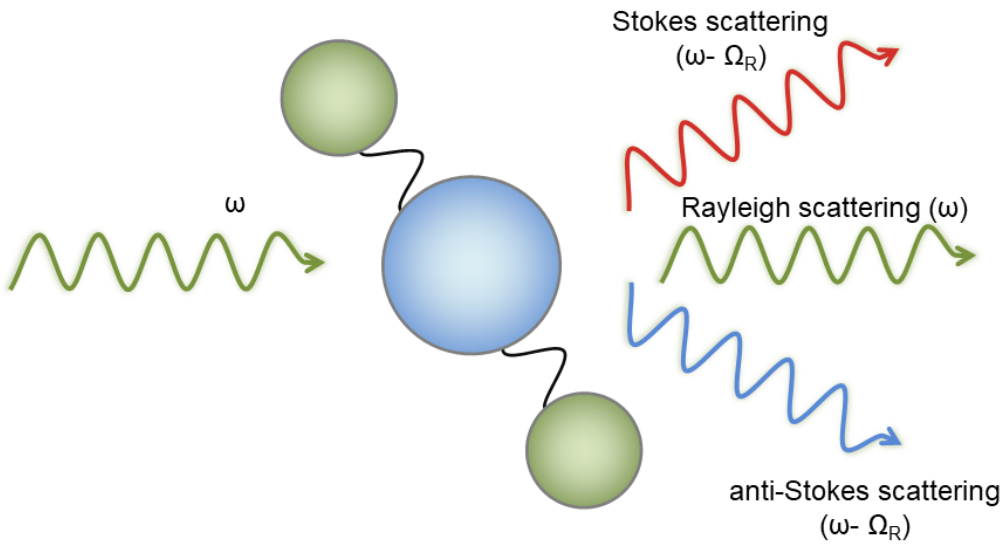



Figure 3.3: Diagrammatic Representation of Classical Molecular Scattering
Incident light at frequency $\omega$ is incident on a Raman active molecule (left arrow). On the right hand side three forms of scattering are shown: Rayleigh at the fundamental frequency, Stokes scattering $(\omega - \Omega_r)$, and anti-Stokes scattering $(\omega + \Omega_r)$.

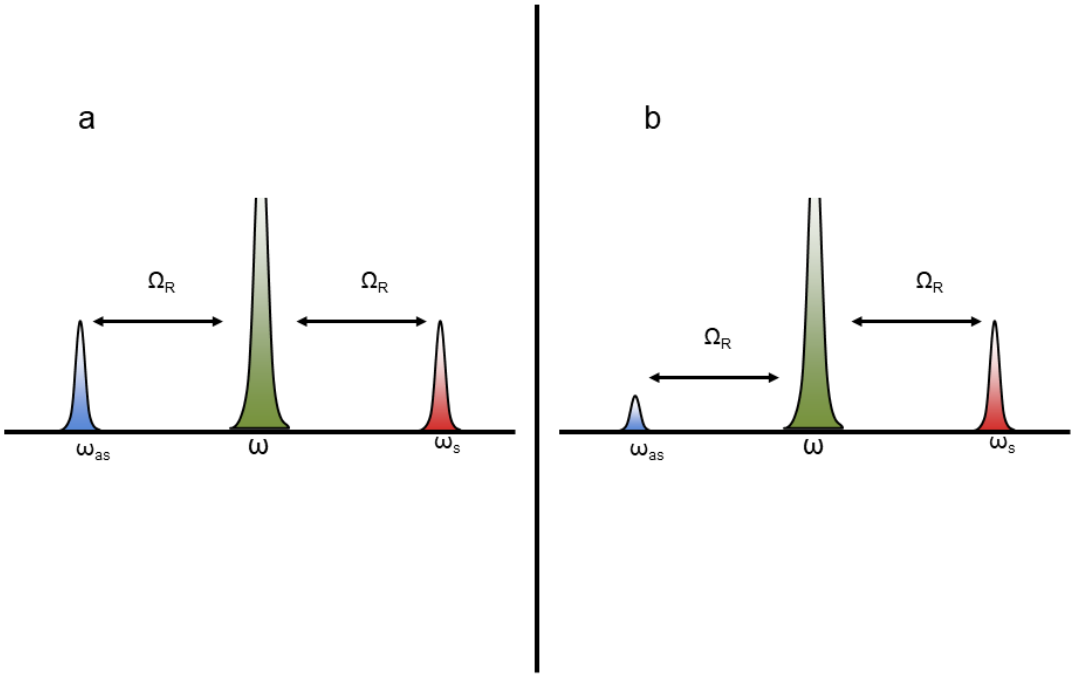



Figure 3.4: Diagrammatic Representation of recorded scattering peaks

To understand the intensities of the scattered light, it is necessary to consider the states of the molecules being probed by the incident field as well as the occupation number of photons in the three fields. Under normal circumstances at room temperature molecules exist in the the ground state both electronically and vibrationally. This is known due to the Maxwell-Boltzmann distribution shown in the equation below. The population of molecules in the first excited vibrational state, $P_{\nu=1}$ is much much less than the number in the ground state $P_{\nu=0}$.

$$\frac{P_{\nu=1}}{P_{\nu=0}} = e^{-\Delta E/kT} \tag{3.13}$$

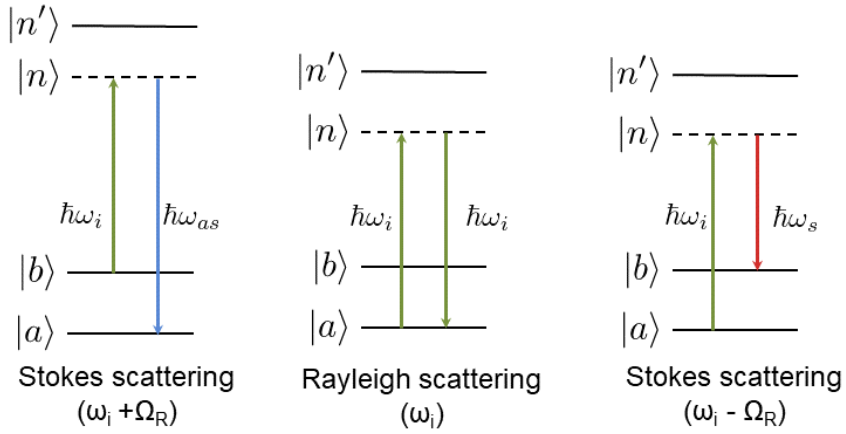



Figure 3.5: Jablonski Diagrams for Elastic and Inelastic Scattering

Unlike IR spectroscopy, Raman scattering probes molecules with optical laser light. The energy of light in the optical range is much greater than the energy of a molecule's vibrational levels indicating that Raman is an indirect process. The Jablonski diagrams illustrating this are shown in figure 3.5. Raman probes nuclear motion through the coupling of electrons to nuclear motion. Quantum mechanically this is an odd situation. A molecule is forbidden from absorbing light unless the energy of that light $\hbar\omega$ matches the energy of the transition.

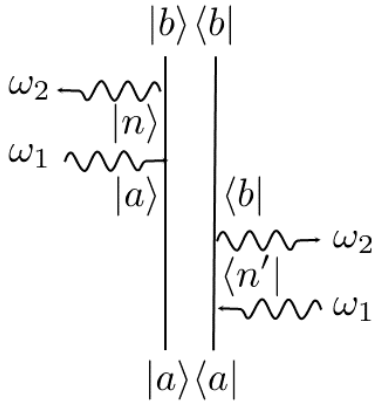



Figure 3.6: Double-Sided Feynman Diagram for the Spontaneous Raman Process

To explain this, we can consider a quantized approach wherein interaction with the incident light field initially interacts with a system in the ground state $|a\rangle\langle a|$. This process is shown in the time ordered double-sided Feynman in figure 3.6. The incident frequency here is represented as $\omega_1$ and the anti-stokes scattered frequency is $\omega_2$. This first interaction changes the bra $\langle a|$ to $\langle n'|$. The states $n$ and $n'$ are referred to as virtual states as they do exist as eigenstates of the system. The second interaction on the bra side occurs with $\omega_2$. This field

is initially unpopulated and thus is supplied by the vacuum field. The lack of any photons initially in the $\omega_2$ state accounts for the extreme weakness of Raman scattering compared to other linear light matter interactions. This interaction generates the coherence $|a\rangle\, b$. This coherence couples the ground and vibrationally excited states, and it is during this time that the density matrix of the system is said to evolve. On the ket side the system again interacts with $\omega_1$ changing to a virtual state. The final interaction occurs with the emission of a stokes photon, $\omega_2$ and the system converting to the vibrationally excited state $|b\rangle\, b$. Effectively, the Raman interaction has moved the population from the ground state to the first vibrationally excited state.

## 3.3 An Overview of Stimulated Raman Scattering

> Work in this section is included in R. C. Prince, R. R. Frontiera, and E. O. Potma, *Stimulated Raman Scattering: From Bulk to Nano*, *Chemical Reviews* **117**(7), 2017, 5070–5094

In this Section, the nature of the SRS light-matter interaction is briefly reviewed. We will first consider the process from the perspective of the light fields, which undergo amplitude changes due to the SRS interaction. We will next connect the observed changes in the light fields to vibrational motions in the material. For this purpose, we will qualitatively discuss the material response in both the classical picture as well as the quantum mechanical picture. In particular, we will highlight the use of the density matrix formalism that is commonly used to interpret time-resolved SRS experiments.

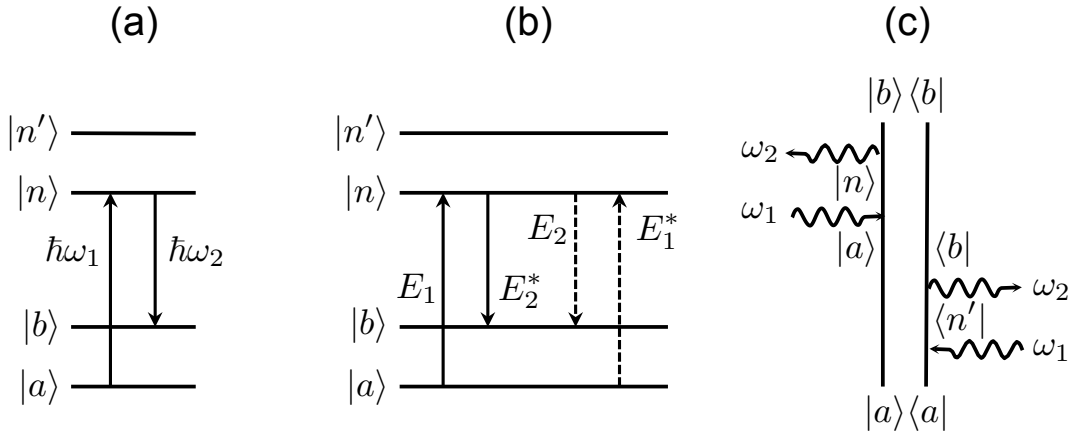



Figure 3.7: Schematic of the SRS light-matter interaction.
(a) Energy level diagram in the intensity representation showing the absorption of an $\omega_1$ photon and the emission of a $\omega_2$ photon. (b) Energy level diagram in the field representation showing the interaction of the fields $E_1$ and $E_2$ with the quantum mechanical states of the material. Note that the arrows are not time-ordered. (c) Double sided Feynman diagram of one of the SRS pathways, showing how the field interactions affect the density matrix of the material. This diagram also represents the spontaneous Raman scattering process, with $\omega_2$ a photon mode provided by the vacuum field.

### 3.3.1 Field picture

In the following, we will assume two incident light fields $E_i$ with frequency $\omega_i$, where $i = 1, 2$ and $\omega_1 > \omega_2$. We will call $E_1$ the pump field and $E_2$ the Stokes field. These fields are typically delivered by a laser source. The intensity of each beam is directly proportional to $|E_i|^2$, or can quantum mechanically be expressed as $n_i\hbar\omega_i$, where $n_i$ is the number of photons in the mode $\omega_i$. In a typical SRS experiment, both beams are incident on the sample, where they interact with the material. After passing through the sample, the intensity of either the pump or the Stokes beam is measured with a photodetector. The measurement thus reveals changes in the intensity of the pump and Stokes beams. Any changes in the material have to be inferred from the intensity changes of the light beams, as we only measure the molecular response indirectly through the fields. Although it does not explain the nature of the photo-induced response in the material, the field perspective of the SRS process is intuitive and very helpful in recognizing the flow of energy between the light fields and the

material.

Figure 3.7a shows the well known Jablonski diagram of the SRS process. This diagram shows the SRS interaction in terms of the beam intensities. Quantum mechanically, the interpretation is straightforward: upon interacting with the material, a $\omega_1$ photon is absorbed (annihilated) and a $\omega_2$ photon is emitted (created). The difference in photon energies, $\hbar(\omega_1 - \omega_2)$, is absorbed by the material. The SRS interaction can thus be measured by probing the loss of photons in the pump beam or by detecting the gain of photons in the Stokes channel. The first detection method is called stimulated Raman loss (SRL) and the latter is called stimulated Raman gain (SRG). Note that both detection methods result from the same light-matter interaction, i.e. the Raman information detected in SRL and SRG is identical.

The Jablonski diagram for the spontaneous Raman process is the same as shown in Figure 3.7a, as the diagram does not explicitly show the occupation numbers of the photon modes. In spontaneous Raman scattering, the $\omega_1$ mode is occupied with a high number of photons, $n_1 >> 1$, whereas the $\omega_2$ mode is initially empty, i.e. $n_2 = 0$. The Raman interaction changes the occupation numbers to $n_1 - 1$ for the $\omega_1$ mode and to $n_2 + 1$ for the $\omega_2$ mode, where the new $\omega_2$ photon is created from the vacuum field. The same is true for SRS, with the important difference that the initial occupation number of $\omega_2$ is high ($n_2 >> 1$). In SRS, the rate of photon generation in the $\omega_2$ channel, $W_{stim}$, is proportional to both the $n_1$ and $n_2$ occupation numbers, i.e. $n_1(n_2 + 1)$[112]. On the other hand, for spontaneous Raman scattering the rate of emission, $W_{spon}$, is proportional to $n_1$, because $n_2 = 0$. The effect of the stimulating field is thus to increase the rate of $\omega_2$ emission[287;288]:

$$\frac{W_{stim}}{W_{spon}} \propto n_2 + 1 \tag{3.14}$$

Because the number of photons in the stimulating beam is high, the increase of the emission

rate in $\omega_2$ is significant. This implies that information about the Raman transition can be retrieved much faster in SRS than in spontaneous Raman scattering by many orders of magnitude. This increase in signal acquisition speed is the key advantage of SRS microscopy over spontaneous Raman scattering microscopy[10]. In practice, the useful information is not determined solely by the number of $\omega_2$ photons, but rather by the signal to noise (S/N) ratio. Both spontaneous Raman and SRS are ultimately limited by the shot noise limit, which states that the signal needs to exceed the photon shot noise of $\sqrt{n_i}$, where $n_i$ is the total number of photons in the detection mode $\omega_i$. Because the SRS signal is detected against a background of $n_2$ of incident photons, nominally the signal needs to be higher than the shot noise limit set by the background, i.e. $\sqrt{n_2}$. This implies that the gain in SRS must be sufficient in order to reach the shot noise limit and to fundamentally outperform spontaneous Raman scattering. Empirically, for a given Raman line, the increase in the signal acquisition rate from a microscopic probing volume typically exceeds $10^5$. In this limit, SRS offers clear benefits. For instance, if a spontaneous Raman measurement of a particular vibrational mode takes 100 ms, SRS can provide the same information with comparable S/N in only 1 $\mu$s.

The intensity diagram in 3.7a also reveals that annihilation of a $\omega_1$ and the creation of a $\omega_2$ is accompanied by a Raman transition in the material. The molecule has absorbed the residual energy from the light fields and is left in a vibrationally excited state. However, this representation does not provide detailed information about the vibrational motions in the molecule or the Raman coherence in the material. In Figure 3.7b, the SRS interaction is depicted in terms of fields rather than intensities. As is clear from the diagram, the SRS interaction involves four fields, which classifies SRS as a four-wave mixing technique. As discussed in Section 3.3.3, keeping track of the field interactions with the material is a much more useful way for analyzing the material response in terms of vibrational coherences. For this purpose, it is convenient to describe the material response in terms of the density matrix. Before discussing the SRS signal in the context of the density matrix, which involves a

quantum mechanical treatment of the molecule, we will briefly describe the material response in a classical fashion.

### 3.3.2 Classical vibrational motions

The classical description of the stimulated Raman process provides a very intuitive picture of molecular motions driven by two external fields $\omega_1$ and $\omega_2$ [289–291]. Unlike the field picture discussed above, the classical SRS model explicitly takes the vibrational motions of the material into account. The model aims to determine the magnitude of the polarization in the material, due to the presence of vibrational oscillators that are actively driven by the incident fields. The frequency of the incident radiation is typically in the visible to near-infrared range ($\sim 10^3$ THz), whereas the frequencies of the nuclear vibrational motions in molecules are of much lower frequencies (1–100 THz). Therefore, the nuclei cannot follow the incident fields adiabatically. Instead, the molecules couple to the fields through their electrons, which can follow the rapid oscillations of the driving fields. In case there is coupling between the electron motions and the nuclear modes, the resultant electron oscillation contains information about the nuclear vibrations as well. Raman processes thus probe nuclear motions in the molecule indirectly through the motion of electrons.

The response of the electrons to an optical field, $E(t) = Ae^{-i\omega t} + c.c.$, is classically modeled by the electronic polarizability $\alpha$. This quantity is a tensor, but to simplify the discussion we will consider it here as a scalar. The time-dependent molecular polarization $\mu$(t) induced by the optical field is then written as $\mu(t) = \alpha(t)E(t)$. In the absence of nuclear modes or any nonlinearities, $\alpha$ can be considered a constant ($\alpha_0$) and the molecular polarization depends linearly on the field. In the presence of a nuclear mode, written as $Q(t)$, which describes the displacement of the nuclei along the generalized nuclear coordinate $Q$, the electron motion can be distorted in case $\alpha$ is dependent on the nuclear positions. In this scenario, there is a

change in $\alpha$ if there is a change in $Q$, or in other words $(\partial\alpha/\partial Q)_0 \neq 0$[292]. Vice versa, this coupling between electronic and nuclear motions implies that the nuclear displacements may be affected when the electrons are set in motion. In the presence of the driving fields $E_1(t)$ and $E_2(t)$, the nuclear mode can experience a driving force $F(t)$ at the difference frequency $\Omega = \omega_1 - \omega_2$:

$$F(t) = \left(\frac{\partial\alpha}{\partial Q}\right)_0 \left[A_1 A_2^* e^{-i\Omega t} + c.c.\right] \tag{3.15}$$

Note that the magnitude of the force depends explicitly on the coupling term $(\partial\alpha/\partial Q)_0$, which acts as a nonlinearity because it drives a material motion in response to two incoming fields. The time-varying nuclear displacement $Q(t)$ in the presence of the force in Eq. 3.15 can be modeled with an equation of motion for a damped harmonic oscillator[275]. The solution of the equation is $Q(t) = Q(\Omega)e^{-i\Omega t} + c.c.$, which describes a harmonic motion of the nuclear mode with the amplitude[289;291]:

$$Q(\Omega) = \frac{1}{m}\left(\frac{\partial\alpha}{\partial Q}\right)_0 \frac{A_1 A_2^*}{\omega_\nu^2 - \Omega^2 - 2i\Omega\gamma} \tag{3.16}$$

where $m$ is the reduced mass of the nuclear oscillator, $\gamma$ is the damping constant and $\omega_\nu$ is the resonance frequency of the harmonic nuclear mode. Eq. 3.16 shows that the nuclear motion is significant when the electronic-nuclear coupling is high, underlining that the $(\partial\alpha/\partial Q)_0$ term plays a central role in (stimulated) Raman scattering. The amplitude also scales linearly in both driving fields $E_1$ and $E_2$. In addition, the amplitude grows when the frequency difference $\Omega$ coincides with the resonance frequency of the nuclear mode, i.e. when $\Omega = \omega_\nu$.

In general, the induced polarization of the sample is given by $P(t) = N\alpha(t)E(t)$, where $N$ is the number of molecules in the interaction volume and $E(t)$ is the total applied field. In the presence of Raman active modes, the electronic polarizability is no longer a constant, as the electron oscillation is affected by the mobility of the nuclei. The electronic polarizability

can be expanded in a Taylor series to include the effect of the nuclear modes to lowest order as[292]:

$$\alpha = \alpha_0 + \left(\frac{\partial \alpha}{\partial Q}\right)_0 Q(t) + ... \tag{3.17}$$

Given that the total electric field in the material is $E(t) = E_1(t) + E_2(t)$, the induced polarization in the interaction volume can be written as:

$$P(t) = N\left[\alpha_0 + \left(\frac{\partial \alpha}{\partial Q}\right)_0 Q(t)\right]\{E_1(t) + E_2(t)\} \tag{3.18}$$

The terms in the polarization that depend on $(\partial\alpha/\partial Q)_0$ include the contribution of three field interactions: two interactions to drive $Q(t)$ and one final interaction with either $E_1$ or $E_2$. These three interactions of two frequencies $(\omega_1, \omega_2)$ produce polarization components at four distinct frequency combinations in the material: $\omega_{cs} = 2\omega_2 - \omega_1$ (coherent Stokes frequency), $\omega_{SRG} = \omega_2 - \omega_1 + \omega_1$ (Stokes frequency), $\omega_{SRL} = \omega_1 - \omega_2 + \omega_2$ (pump frequency), and $\omega_{as} = 2\omega_1 - \omega_2$ (anti-Stokes frequency). The amplitude of the SRS polarization components are found at $\omega_{SRG}$ and $\omega_{SRL}$, and are given as:

$$P(\omega_{SRG}) = 6\epsilon_0 \chi^*_{NL}(\Omega)\left|A_1\right|^2 A_2 \tag{3.19}$$

$$P(\omega_{SRL}) = 6\epsilon_0 \chi_{NL}(\Omega)\left|A_2\right|^2 A_1 \tag{3.20}$$

where $\epsilon_0$ is the vacuum permittivity and $\chi_{NL}$ is the Raman-dependent nonlinear susceptibility of the material, which is written as:

$$\chi_{NL}(\Omega) = \frac{N}{6m\epsilon_0}\left(\frac{\partial \alpha}{\partial Q}\right)_0^2 \frac{1}{\omega_\nu^2 - \Omega^2 - 2i\Omega\gamma} \tag{3.21}$$

The nonlinear susceptibility is a material quantity, it describes the frequency dependent

response of the material to the incoming fields. Eq. 3.21 shows that the Raman-related material response scales with the square of the $(\partial\alpha/\partial Q)_0$ coupling term. The material also becomes more responsive when the frequency difference $\Omega$ coincides with the resonance frequency of the nuclear mode.

Using this classical model, we see that the SRS process induces oscillating polarization components at the pump and Stokes frequencies in the material, as indicated by Eqs. 3.19 and 3.20. Using this formalism, we can also relate the material response to the measured optical signal by the photodetector. Both the $P(\omega_{SRG})$ and $P(\omega_{SRL})$ components depend on the same Raman nonlinear susceptibility. They exhibit similar amplitudes but oscillate with different phases. Consequently, as the nonlinear polarization radiates, it produces the field components $E_{SRG}(\omega_2)$ and $E_{SRL}(\omega_1)$, which arrive in the far-field detector with distinct phases. If the signal is detected in a phase-matched direction that is different from the direction of the probing fields, the signal is proportional to $|P|^2$. On the other hand, if the signal is detected in the phase-matched direction that coincides with the probe field, the induced field components interfere with the incident fields components $E_1$ and $E_2$, respectively. For instance, at the Stokes frequency, the measured intensity is $I(\omega_2) = \epsilon_0 c/2\,|E_{SRG} + E_2|^2$. The interference term between the signal fields and the incident fields constitutes the SRS signal in the $\omega_1$ and $\omega_2$ channels:

$$S_{SRG}(\omega_2) \propto |A_1|^2 |A_2|^2 \Im\{\chi_{NL}(\Omega)\} \tag{3.22}$$

$$S_{SRL}(\omega_1) \propto -|A_1|^2 |A_2|^2 \Im\{\chi_{NL}(\Omega)\} \tag{3.23}$$

The SRG and SRL signals both scale linearly with the intensity of the pump and Stokes laser beams, and both signals probe the imaginary part of the nonlinear susceptibility, which describes the dissipative part of the material response. Similar to the quantized field picture,

the classical description of SRS predicts a gain in the $\omega_2$ channel and a loss in the $\omega_1$ channel. Both models thus arrive at the same conclusion regarding the energy transfer between the field modes, albeit in different ways. Although intuitive, the descriptions thus far do not provide a lot of insight in the material coherences nor take fully account of the various quantum mechanical states of the material that partake in the SRS process. The density matrix approach provides a deeper understanding of the material response in terms of quantum coherences, which is discussed in the next Section.

### 3.3.3 Quantum mechanical description: density matrix

The semi-classical model of nonlinear optical spectroscopy describes the electromagnetic fields as classical waves but treats the material quantum mechanically. In the quantum mechanical picture, the state of the material is described by molecular wavefunctions, which are written as a superposition of the molecular eigenstates $\psi_n$:

$$\Psi(r,t) = \sum_n c_n \psi_n(r,t) \tag{3.24}$$

where $c_n$ are the amplitude coefficients of the wavefunction for each of the eigenstates. In the bra and ket notation, the eigenstates of the material $\psi_n$ are indicated by their ket notation as $|n\rangle$. The operator $\hat{H}_0$ is the unperturbed Hamiltonian, which, upon acting on the wavefunction, produces an eigenvalue that corresponds to the energy of the system. In the presence of light, the state of the material can be altered due to light-matter interactions. In the dipole limit, light-matter interactions are described by the interaction Hamiltonian $\hat{V}(t) = \hat{\mu} \cdot E(t)$, where $\hat{\mu}$ is the dipole operator which tracks the motion of charged particles (electrons and nuclei) in response to the optical field $E(t)$. The interaction Hamiltonian perturbs the system and changes the state of the material by enabling transitions between material eigenstates. The probability that the system is in a certain eigenstate $|n\rangle$ and the

mutual coherence between the eigenstates after the interaction is conveniently captured by the density matrix operator:

$$\hat{\rho}(t) \equiv |\Psi(t)\rangle \langle \Psi(t)| = \sum_{nm} \rho_{nm}(t) |n\rangle \langle m| \tag{3.25}$$

Here $\rho_{nm}$ are the matrix elements $\langle n| \hat{\rho} |m\rangle$ in bra-ket notation. The diagonal elements ($n = m$) of the density matrix correspond to the probability that the system is in eigenstate $|n\rangle$. In this case, the operator in Eq. 3.25 takes on the form $|n\rangle \langle n|$, which represents the *population* of the molecular eigenstate $\psi_n$. The off-diagonal elements, $\rho_{nm}$ with $n \neq m$, are associated with the operator $|n\rangle \langle m|$, which is called the *coherence* between eigenstates $\psi_m$ and $\psi_n$. Following the time-dependent density matrix after a light-matter interaction thus reveals information about the population and coherence dynamics in the material.

In Section 3.3.2 it was clear that in the SRS process, a nonlinear polarization is induced in the material through three interactions between the matter and the incident fields. The induced polarization then radiates to produce a fourth field. This process can be described in the density matrix formalism by monitoring the time-dependent evolution of $\hat{\rho}(t)$ following three interactions with the light fields. Generally, $\hat{\rho}(t)$ evolves in the Schrödinger picture as:

$$\frac{d\hat{\rho}}{dt} = -\frac{i}{\hbar} \left[ \hat{H}, \hat{\rho} \right] \tag{3.26}$$

where the total Hamiltonian includes both $\hat{H}_0$ and $\hat{V}$. The evolution of $\hat{\rho}$ in the SRS process is commonly modeled through third-order perturbation theory, where the density operator is calculated to the third order in the electric field[108;173]. In evaluating the density matrix contribution that is third order in the field, $\hat{\rho}^{(3)}(t)$, many pathways for the material evolution are found. Double-sided Feynman diagrams are a convenient tool for analyzing such pathways. An example is shown in Figure 3.7c, which shows one pathways that contributes

to the overall SRS response. The diagram can be interpreted as follows. The system starts out in the ground state, indicated by the $|a\rangle\langle a|$ population at the bottom of the diagram. The first light-matter interaction is with the field of frequency $\omega_1$, which changes the bra from $\langle a|$ to $\langle n'|$. The states indicated by $n$ and $n'$ can be either real or virtual states. For ground state SRS, these electronic states are virtual states and the $n, n'$ labels are dummy indices. The second field interaction on the bra side generates the coherence $|a\rangle\langle b|$. This is the Raman coherence in the material which, in the absence of fields, evolves according to the unperturbed Hamiltonian $\hat{H}_0$. The density matrix $\rho_{ab}$ is said to propagate during this period, tracking the time-dependent material response to the light-induced superposition of the ground state and the vibrationally excited states. The density matrix is then interacting with fields $\omega_1$ and $\omega_2$ on the ket side, generating the population $|b\rangle\langle b|$. Effectively, in this diagram, the SRS interaction has moved population from the ground state to the first vibrationally excited state.

It should be noted that the diagram shown in Figure 3.7c also denotes the quantum pathway of the spontaneous Raman process, with the important difference that the $\omega_2$ field is provided by the vacuum field. This does not mean, however, that all possible pathways probed in SRS are necessarily accessible through the spontaneous Raman process. This is related to the fact that the photon occupation numbers $n_1$ and $n_2$ in SRS and spontaneous Raman scattering are different. The field interactions with $\omega_2$ in the spontaneous Raman process are restricted as they must change the occupation number from zero to one, which limits the freedom of arranging the field interactions in the Feynman diagrams. This restriction is not present for SRS, in which case both $n_1$ and $n_2$ are high, allowing more permutations of the field interactions, and thus producing more permissible quantum pathways[173]. Another important difference between SRS and spontaneous Raman is that SRS offers the possibility to time-resolve the evolution of the Raman coherence $|a\rangle\langle b|$, by preparing the coherence with a pump and Stokes pulse pair and probing its propagation by a time-delayed probe pulse.

The third-order polarization in the sample can be obtained from the expectation value of the dipole operator, which can be obtained within the density matrix formalism as:

$$P^{(3)}(t) = N\mathrm{tr}\left[\hat{\mu}\hat{\rho}^{(3)}(t)\right] \tag{3.27}$$

where tr indicates the trace over the matrix elements of the operator product between the brackets. Once the nonlinear polarization of the material is known, the signal can be calculated in the same manner as in the classical model. The exact time-dependence of the polarization depends on the evolution of the density matrix, which depends, in turn, on the details of the material Hamiltonian. Predictions of the SRS signal thus rely on proper knowledge of Hamiltonian-dictated dynamics in the system. The simplest model assumes a general dephasing rate $\gamma_{nm}$ for the $|n\rangle\langle m|$ coherence, and the population relaxation rate $\gamma_{nn}$ for describing the energy relaxation between material states[108].

In this scenario and assuming that the Raman line is only homogeneously broadened, a typical time-resolved SRS experiment with ultrashort laser pulses can then be understood as follows. The molecule is subjected to pulsed fields at frequencies $\omega_1$ and $\omega_2$, which induce a vibrational coherence $|a\rangle\langle b|$ in the sample. In Figure 3.7c, this corresponds to the first two field interactions. The duration of the laser pulses is generally much shorter than the dephasing rate $\gamma_{ab}$. After preparation, the Raman coherence will decay with a rate $\gamma_{ab} = \gamma_{bb}/2 + \hat{\gamma}_{ab}$, where $\hat{\gamma}_{ab}$ is usually referred to as the pure dephasing rate. After a time delay $\tau$, a second pulse with the frequencies $\omega_1$ and $\omega_2$ is incident on the sample to probe the Raman coherence. The probe pulse transfers information about the $\tau$-dependence of the Raman coherence to the $\omega_1$ and $\omega_2$ frequency channels, which are detected by a photo-detector. The time-dependence of the resulting third-order polarization, which is encoded in the detection fields, depends on the details of the experiment.

Figure 3.8 depicts the material response in terms of the frequency and time dependent third-

order polarization under several different experimental conditions. The frequency dependent responses, on the left panels, display the real (red) and imaginary (blue) components of the nonlinear polarization. The gray shaded areas represent the driving field ($\omega_1$ - $\omega_2$), which in all examples overlaps with the material resonance(s). The panels on the right depict the time dependent response of the third-order polarization. In panels (a) and (b), a single mode is driven by two narrowband laser fields, and the polarization decays with a dephasing time of several hundred femtoseconds, corresponding to the frequency domain linewidth. No oscillatory pattern is observed in the time domain as the experimental setup does not have sufficient time resolution to resolve the carrier frequency. In panel (c), the system has two Raman active modes which are driven by two broadband laser fields. The beat pattern between the two modes is visible in the time-dependent response in panel (d). Panels (e) and (f) depict a system with one low frequency Raman active mode which is driven by a single broadband pulse. The temporal response shows a single oscillatory feature corresponding to the vibrational period. In panels (g) and (g), a single broadband pulse drives two low frequency Raman active vibrations. The time-dependent response shows oscillatory features from each of the modes as well as their beat frequency.

Similar to the classical model, once the nonlinear polarization is known, the frequency-dependent nonlinear susceptibility of the material can be determined. Within the simple dephasing model discussed above, the contribution $\chi^{(3)}(-\omega_2;\omega_1,\omega_2,-\omega_1)$ to $\chi^{(3)}$ from the pathway shown in Figure 3.7c is[173]:

$$\frac{N}{6\hbar^3\epsilon_0}\sum_{ab,nn'}\rho_{aa}^{(0)}\frac{\mu_{bn}\mu_{na}\mu_{an'}\mu_{n'b}}{\left[\omega_{bn}+\omega_2+i\gamma_{nb}\right]\left[\omega_{ba}-(\omega_1-\omega_2)+i\gamma_{ab}\right]\left[\omega_{n'a}-\omega_1+i\gamma_{an'}\right]} \tag{3.28}$$

where $\omega_{nm}$ denotes the difference frequency $\omega_n-\omega_m$, and $\mu_{mn}$ indicates the transition dipole moment for $|n\rangle \rightarrow |m\rangle$. The second denominator in Eq. 3.28 contains the information of the density matrix propagator of the Raman coherence $|a\rangle\langle b|$. Similar to the classical form of the nonlinear susceptibility (Eq. 3.21), the contribution to $\chi^{(3)}$ shown above grows large

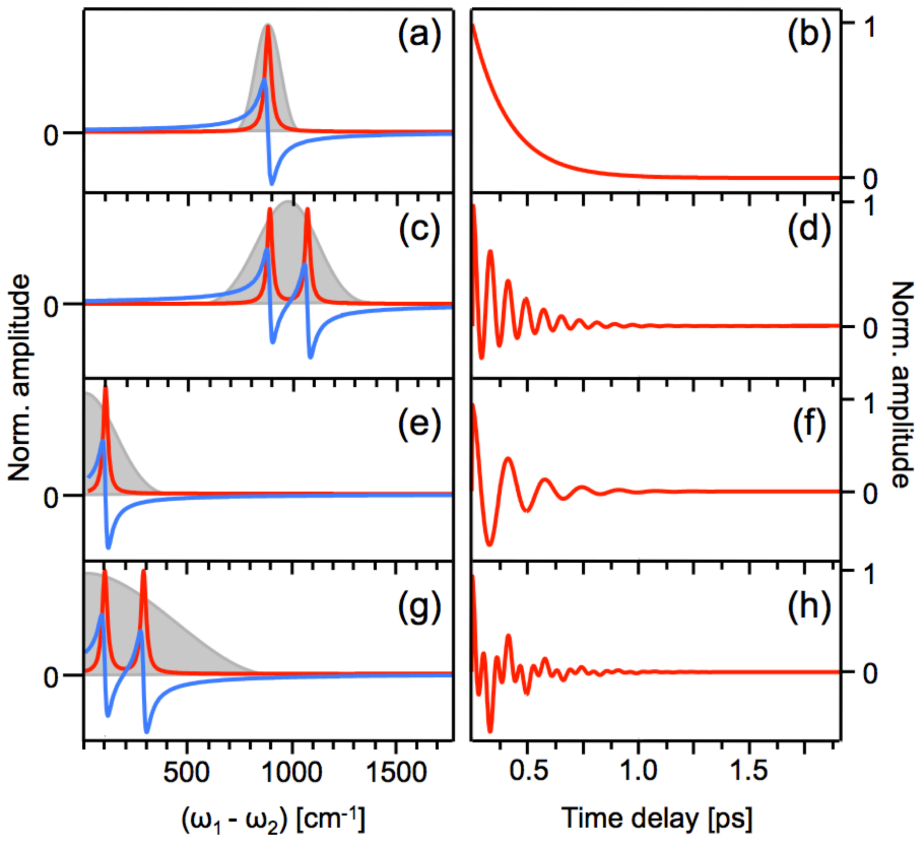



Figure 3.8: Frequency (a,c,e,g) and time (b,d,f,h) dependence of the third-order polarization as probed under different experimental conditions.
(a) Amplitude of the real (red) and imaginary (blue) part of the nonlinear polarization due to the presence of a single high-frequency Raman resonance. The Raman coherence is driven at $(\omega_1 - \omega_2)$, where $E_1$ and $E_2$ are narrowband fields of ps duration. Gray shaded region indicates the spectral profile of the effective driving field $(\omega_1 - \omega_2)$. (b) Amplitude of the third-order polarization as a function of time delay $\tau$, corresponding to the situation in (a). (c) Driving two high-frequency Raman resonances with two broadband laser fields, such that the spectrum of the effective driving field $(\omega_1 - \omega_2)$ overlaps with both resonances. (d) Temporal response corresponding to the situation in (c). (e) Driving one low-frequency Raman resonance with one broadband laser field. (f) Temporal response corresponding to the situation in (e). (g)

when the frequency difference $\omega_1 - \omega_2$ approaches a Raman resonance at $\omega_{ba}$. The spectral dependence of the Raman resonant $\chi^{(3)}$ contributions follows a Lorentzian lineshape with a width directly proportional to $\gamma_{ab}$. Note that the $\chi^{(3)}(-\omega_2;\omega_1,\omega_2,-\omega_1)$ contribution contains more resonances, such as the resonance at $\omega_1 = \omega_{n'a}$, which occurs when $\omega_1$ is resonant with an electronic transition in the material. Since the diagram in Figure 3.7c is also a good representation of the spontaneous Raman scattering process[173], we may relate the measured Raman spectrum to this $\chi^{(3)}$ contribution as follows:

$$S_{Raman} \approx \Im\left\{\chi^{(3)}(-\omega_2;\omega_1,\omega_2,-\omega_1)\right\} \tag{3.29}$$

The approximate sign is present because in spontaneous Raman scattering the field interactions with $\omega_1$ and $\omega_2$, including their independent polarization orientations, cannot be arbitrarily chosen, as discussed above. For ground state SRS with linear and parallel polarized fields, far from electronic resonances, the diagram in Figure 3.7c is a dominant contributor to the overall SRS response and the expression in Eq. 3.29 is generally true. This implies that for ground state vibrational Raman excitations, the dephasing parameters $\gamma_{ab}$ extracted from a time-resolved SRS experiment are identical to the dephasing parameters derived from the Raman linewidth. This is no longer true when electronic excitations are involved, in which case specific time-consecutive processes in the excited state can be resolved in time domain SRS that cannot always be reconstructed in a time-ordered fashion from the spectral Raman response.

### 3.3.4 Magnitude of the Raman response

From Eq. 3.14 it is clear that the rate of SRS emission is much higher than the rate of spontaneous Raman emission. When a Raman active material is illuminated with the $\omega_1$ mode, the number of photons scattered into the $\omega_2$ mode is very small, emphasizing

that spontaneous Raman scattering is a very weak effect. The rate of photon emission in spontaneous Raman scattering, measured in all directions, for a transparent sample of length $z$ with an incident light intensity of $I(\omega_1)$ (in $W/cm^2$), can be written as:

$$W_{spon}(\omega_2) = N_d A z \sigma(\omega_2) I(\omega_1). \tag{3.30}$$

where $N_d$ is the molecular number density, $A$ is the illuminated area and $\sigma(\omega_2)$ is the Raman cross section (in $\text{cm}^2$). The most important material characteristic is $\sigma$, which is a measure for the responsiveness of a given material. It is useful to define the rate of photon emission in a particular direction defined by the solid angle element $d\Omega$. In this case, the material response is defined through the Raman differential cross section $d\sigma/d\Omega$. The differential cross section can be related to the material properties in the previous sections, i.e. $d\sigma/d\Omega \propto (\partial\alpha/\partial Q)_0^2 \propto \Im\left\{\chi^{(3)}\right\}$. The differential cross sections of various materials are listed in Table 3.1. For example, the differential cross section for the O-H stretching mode is $8 \times 10^{-30}$ $\text{cm}^2$/molecule·sr when excited at 488 nm. This roughly translates into about three Raman scattered photons out of $10^7$ incident photons when propagating through 1 mL of liquid. Given that 1 mL of liquid contains $3.3 \times 10^{22}$ of water molecules, the Raman scattering efficiency per molecule is indeed very small. Other modes, such as the ring breathing mode at 992 $\text{cm}^{-1}$ in benzene exhibit higher polarizabilities, resulting in slightly stronger Raman signals. Even so, for smaller volumes, the number of Raman scattered photons remains low. For microscopic volumes of 1 fL, roughly 2 out of $10^{11}$ incident photons are Raman scattered off of the 992 $\text{cm}^{-1}$ mode of benzene.

Clearly, enhancing the photon emission rate as provided through the SRS process offers an attractive strategy to overcome the small Raman signals from fewer molecules and smaller volumes. We have also seen that the Raman reponse of the material can be directly enhanced when the pump beam is tuned close to an electronic resonance (Eq. 3.28). The compounds $\beta$-carotene and rhodamine 6G listed in Table 3.1 have electronic resonances in the visible

Table 3.1: Absolute Raman differential scattering cross sections in $cm^2$ per molecule per steradian for various compounds.

| compound | mode ($cm^{-1}$) | $\lambda_{ex}$ (nm) | cross Section $\left(\frac{cm^2}{\text{molecule}\cdot\text{sr}}\right)$ | reference |
|---|---|---|---|---|
| water | 3400 | 488 | $8 \times 10^{-30}$ | 293;294 |
| cyclohexane | 802 | 514 | $8.29 \times 10^{-30}$ | 295 |
| ethanol | 2880 | 488 | $1.7 \times 10^{-29}$ | 296 |
| benzene | 992 | 488 | $3.65 \times 10^{-29}$ | 297 |
| $\beta$-carotene | 1520 | 514 | $2.04 \times 10^{-24}$ | 298 |
| rhodamine 6G | 604 | 532 | $4.1 \times 10^{-23}$ | 51 |

range, resulting in differential Raman cross sections that are several orders of magnitude higher than for materials that are transparent in this range.

### 3.3.5 SRS versus CARS

The CARS technique has its own history and application niches, which are not the focus of the current work. Nonetheless, since the comparison between these two coherent Raman techniques is a topic that is frequently discussed in the literature, we will briefly touch on it here as well. It is important to underline that both techniques rely on the same Raman coherences in the sample, driven at $\omega_1 - \omega_2$, for generating a detectable signal. The main difference between SRS and CARS is the way in which the amplitude and phase of the excited Raman coherence are translated into a measurable change in the light fields. In terms of the dual color excitation configuration discussed in Section 3.3.2, in the CARS experiment the information about the Raman coherence is probed in the $\omega_{as} = 2\omega_1 - \omega_2$ signal channel, whereas in SRL it is detected in the $\omega_2$ channel. The difference is strictly in the detection mode: from the material's point of view it does not matter whether the $\omega_1 - \omega_2$ vibrational motion is probed in either the $\omega_{as}$ channel or the $\omega_2$ channel. However, the choice of detection channel does have experimental implications, and the preference for either SRS or CARS is largely driven by practical factors that determine how easy the information about the Raman vibration can be extracted from the experimentally measured signal.

One important difference between the two techniques is the fact that SRS, detected in the phase-matched direction of the probe, is dictated by the interference term between the signal field and the incident probe field, and CARS is not. This intrinsic interference of the SRS signal, which is sometimes called the self-heterodyning of the signal, gives rise to signals proportional to the nonlinear polarization $P$. The resulting signal is thus linearly dependent on the nonlinear susceptibility, and is in-phase with its imaginary component, see Eqs. 3.22 and 3.23. Since $\Im\chi^{(3)}$ is proportional to the Raman cross section, the SRS signal exhibits the same spectral lineshapes as probed in spontaneous Raman scattering. For the same reason, the SRS signal scales linearly with the number of Raman scatterers in the probing volume. The CARS signal, on the other hand, is commonly detected in a homodyne manner. This implies that it is not (self-)heterodyned, and that the signal is instead proportional to the square of the induced nonlinear polarization, $|P|^2$.[291] As a result, the CARS signal scales as $\left|\chi^{(3)}\right|^2$, giving rise to a spectral response that is not directly proportional to the spectral lineshapes measured in spontaneous Raman scattering. Furthermore, the CARS signal displays a nonlinear dependence on the concentration of Raman scatterers. Additionally, the CARS signal carries purely electronic contributions to the nonlinear susceptibility, which gives rise to a background that is not easily separated from the vibrationally resonant contributions. These attributes make SRS a better choice for certain frequency-domain experiments, especially when the concentration of the target Raman scatterers in heterogeneous samples is relatively low compared to other sample constituents, in which case the electronic background contributions in CARS can be overwhelming. This limit is relevant for coherent Raman microscopy, and explains why SRS is sometimes advertised as being superior to CARS microscopy.

For time-domain coherent Raman experiments, the specific advantages of SRS mentioned above are less relevant. In fact, for molecular vibrations of higher energy ($> 200$ cm$^{-1}$), the CARS experiment is often less complicated because of the ease of detecting the signal in a new frequency channel ($\omega_{as}$). Experimentally, the frequency shift between the incident

light and the signal is sufficient for isolating the CARS photons with modern spectral filters. In SRS, spectral filtering cannot be applied and instead some type of modulation is needed to separate the coherent Raman signal from the incident beam, which can complicate the experiment. The spectral filtering advantage of CARS, however, disappears for low frequency vibrations ($< 200$ cm$^{-1}$), which produce Raman signals that are too close in frequency to the incident frequencies to spectrally separate them. Here, time-domain SRS is preferred. The ISRS technique provides access to such low energy vibrations and offers a mechanism to fully time-solve their coherent motions.

## 3.4 Information from an SRS Experiment

As was alluded to in the sections above, it is possible to gain a wealth of information from the SRS experiment on microscopic samples. A brief description is provided here, and specific examples will be shown and discussed in the sections on current work and the research plan.

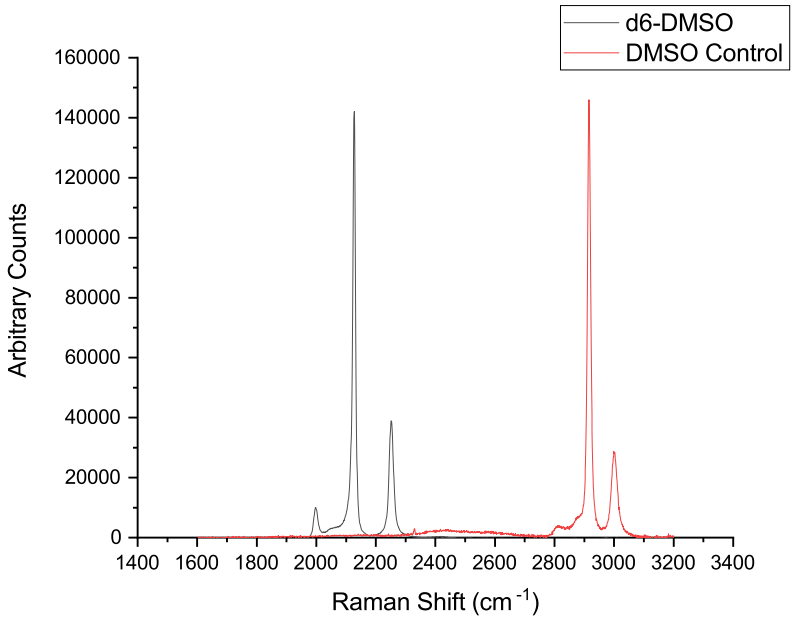



Figure 3.9: Raman Spectra of DMSO and deuterated DMSO.

As Raman scattering spectroscopy probes the various vibrations of molecular bonds it is possible to retrieve a large amount of information from the Raman spectrum. An example of the spectra of DMSO and it's deuterated version are provided in Figure 3.9. In these spectra, functional group vibrational modes are recognizable in the form of the CH modes centered around $2900cm^{-}1$. The comparison of these two spectra show how a slight adjustment in the reduced mass of the oscillator, in this case substituting deuterium for hydrogen, makes a large difference in the position of the Raman peaks.

Detailed analysis of hyperspectral images in SRS, such as that provided with principle component analysis, can utilize this information to produce chemical contrast for images by varying the wavelength of the pump beam over a series of images. In fact, as shown in[152], a range much smaller than that shown in 3.9 can provide enough information to sort out differences in compounds such as protein and lipid. Additionally, rapid imaging at one band is available on the order of one frame per second. This creates the ability of SRS to generate images mapping the location of select functional groups in cells and tissues.

As the primary focus of this work, the addition of small molecule or isotopic tags allows for high chemical contrast not otherwise present in the cell. This is ongoing work by many different research groups. Chapter 4 will disucss the background of using tags for various Raman spectroscopies, and some of the methods used with them. Chapters 5-7 display original work based on the application and analysis of various Raman tags towards answering biological questions.

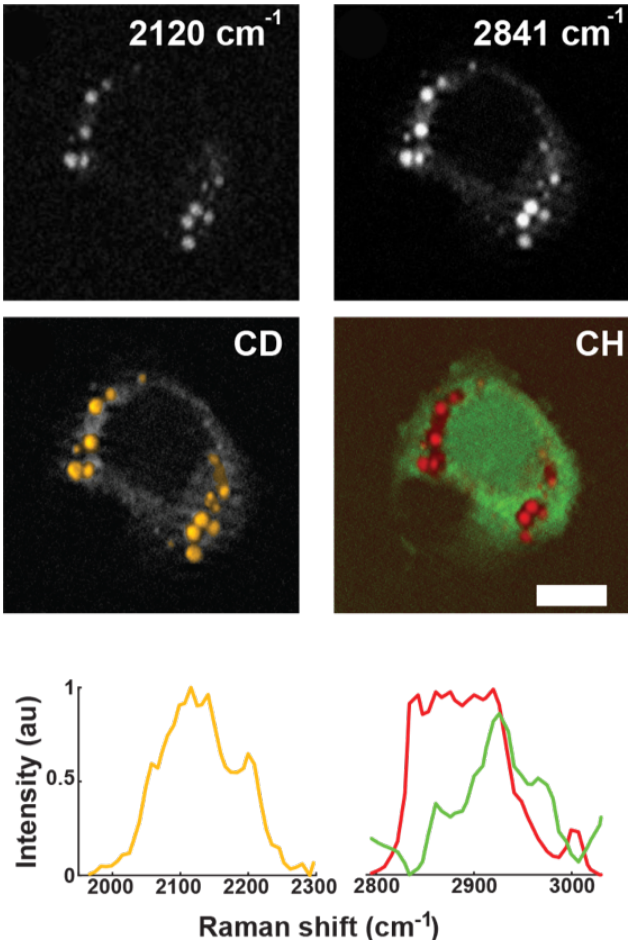



Figure 3.10: SRS imaging at 2120 $cm^{-}1$ corresponding to CD2 stretches and 2841 $cm^{-}1$ corresponding to CH2 symmetric stretches.
The result of hyperspectral SRS imaging and multivariate analysis is depicted in yellow for D38-cholesterol in the CD region , overlaid on the maximum intensity projection of the CH spectral scan in gray scale, and in red for lipid and green for protein in the CH region.

# Chapter 4

# Instrumentation & Methodology

## 4.1 Common Modalities

During the course of my dissertation work, a number of instruments and experimental techniques have been used repeatedly. As discussed in Chapter 2 stimulated Raman scattering microscopy is one of a number of increasingly popular techniques within the larger field of nonlinear optical(NLO) microscopies. NLO microscopies provide a method of imaging that is relatively noninvasive and can provide excellent spatial resolution and three-dimensional sectioning.

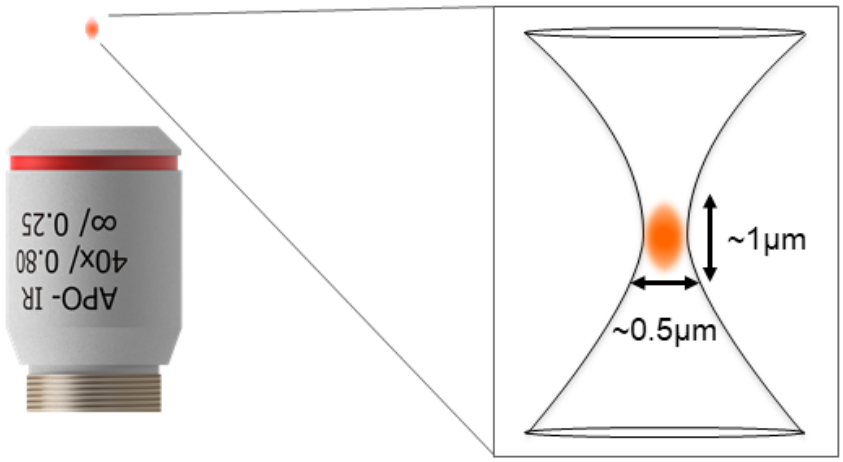



Figure 4.1: Illustration of the Focal Volume of a High Numerical Aperture Objective
The tight focusing conditions of a high-NA objective create the E-field intensities required to excite nonlinear optical processes. Techniques such as SHG and CARS posses an intrinsic sectioning ability in the axial dimension that eliminates the need for a confocal pinhole.

While each technique is a field of research all of its own, a number of similarities unite the techniques. Chief among these is the use of high numerical aperture objectives. While high-NA objectives provider tighter resolution even for linear imaging, the effect is enhanced in NLO processes. NLO signal generation requires very high electric fields. Under typical powers used in microscopy, these fields are only realized within the region known as the focal volume of the objective.[289;299;300] An illustration of this effect is shown in Figure 4.1. Outside of the focal volume, field intensities are low enough that their is little to no signal generated

in the surrounding sample. This eliminates the need for a confocal pinhole common to linear microscopy. Photobleaching outside the focal volume is also greatly reduced increasing the imaging life of samples.

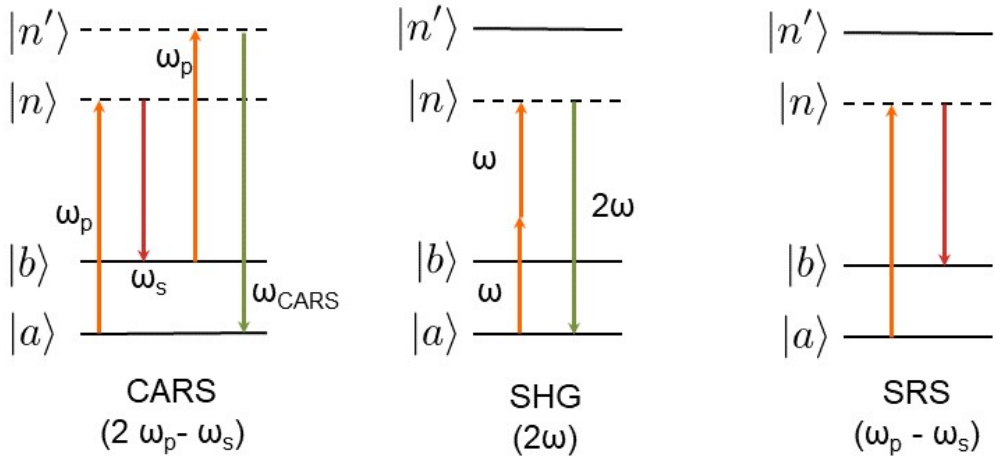



Figure 4.2: Jablonski Diagrams for NLO Imaging
The diagrams for CARS, SHG, and SRS are presented here. The energy of their signal photon is in parenthesis below each process.

There are a large number of commonly used NLO imaging techniques, I have commonly used three across my work. Those three are coherent anti-Stokes Raman scattering (CARS), second harmonic generation (SHG), and stimulated Raman scattering (SRS). The Jablonski diagrams for these three processes are shown in Figure 4.2. The theoretical backgrounds for CARS and SRS are covered extensively in Chapter 3. Briefly, both are four-wave mixing processes that interrogate the chemical properties of molecules by probing the vibrational resonances of molecules in the focal volume of the objective. CARS is a parametric process, *i.e.* the state of the probed molecules remains unchanged after the process. SRS, however, results in an excited vibrational state of the probed molecules making it a non-parametric process. Imaging contrast in both modalities results from an enhancement of signal when the condition $\Omega = \omega_p - \omega_s$ matches a vibrational mode of the molecule. CARS is easier to detect because the signal photons are produced at wavelength blue-shifted from the input, whereas SRS signal is produced as a modulation of the two inputs. It should be noted that

in CARS a nonresonant background is generally present. The phase of the resonant and non-resonant component are shifted from one another.[291] This causes a mismatch between the CARS spectrum and the spontaneous Raman spectrum. This is not the case for SRS. SRS thus is relatively background free under ideal conditions, and it can directly reproduced the spontaneous Raman spectrum.

While second Harmonic generation is not the focus of my dissertation, it is a useful imaging modality for examining certain structural components of tissues. SHG is a special case of sum-frequency generation, and both arise from the second order susceptibility, $\chi^{(2)}$; making them a three-wave process. As a second-order process, SHG is sensitive to materials that non-centrosymmetric.[289] Under the microscope, SHG is particularly useful for detecting and imaging materials such as collagen and cholesterol crystals among others.[19–21;301] Figure 4.3 shows SHG of collagen fibers (a) and protein crystals (b).

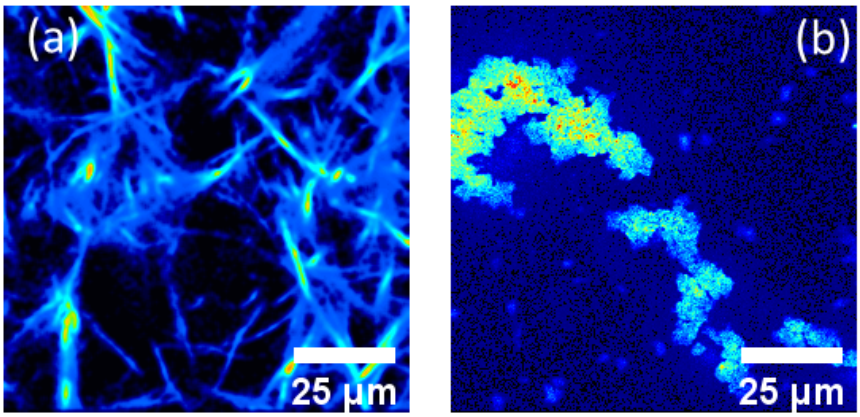



Figure 4.3: Second Harmonic Generation of Biological Materials
SHG images of (a) type-II collage and (b) protein crystals. SHG signal is only produced in materials with non-centrosymmetric symmetry.

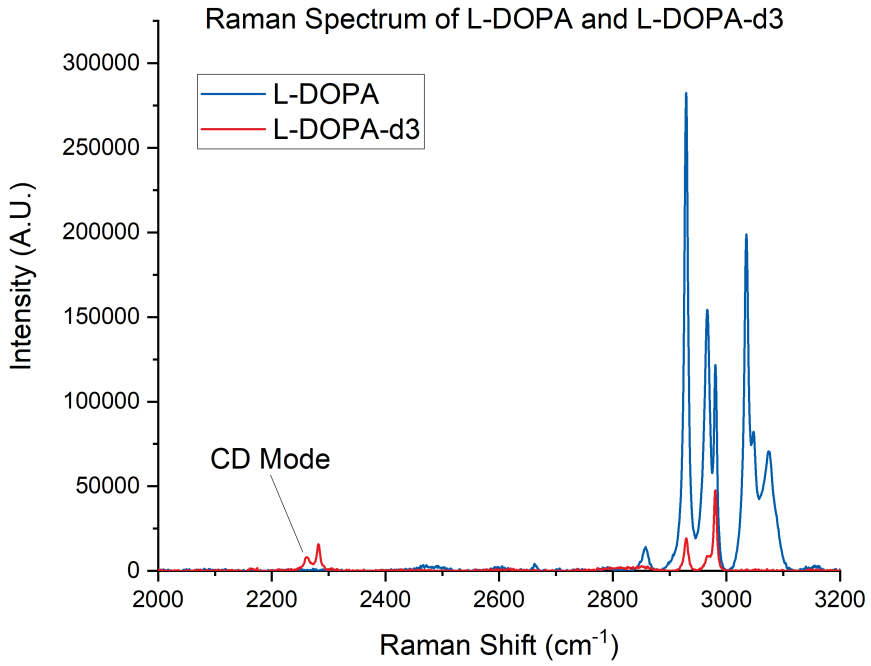



Figure 4.4: Spontaneous Raman Spectra of L-DOPA and L-DOPA-d3

## 4.2 Spontaneous Raman Micro-Spectrocopy

One of the essential questions in any CRS experiment is: "what are the vibrational resonances of the target sample?" As discussed in Chapter 3, spontaneous Raman scattering provides a wealth of information about the vibrational characteristics of molecules. It can be used to identify unknown samples, elucidate structural properties of molecules, a monitor reactions. For CRS however, it is often used to identify specific classes of molecules in order to zero-in on a particular resonance for contrast. An example of this is shown in figure 4.4. In this figure, the spectra of L-DOPA (blue) and a thrice deuterated version of L-DOPA (red) are presented. Spontaneous Raman is useful for finding the peaks of the different modes of the two compounds. It also easily shows the difference in modes due to deuteration. Of particular note, two CD peaks are evident at $2260cm^{-1}$ and $2280cm^{-1}$, whereas they are completly absent in the native compound. Conversely the peaks associated with methyl

stretches at $2940cm^{-1}$ and the modes of the benzene ring between $3000 - 3100cm^{-1}$ are greatly reduced.

For the studies presented here, all spontaneous Raman spectra were taken on a single instrument. The Laser Spectrocopy Lab at UCI is a user facility with several instruments for linear and nonlinear spectroscopy. For obtaining high-quality Raman spectra, the facility posses a system developed by Renishaw Inc. (United Kingdom). The system is based on their InVia micro-spectroscopy system. It posses the capability for three different laser excitation wavelengths: 405nm, 532nm, 785nm. The system uses custom holograph notch filters that allow measurements starting at $100cm^{-1}$. For both 405nm and 532nm, the system is capable of better than $1cm^{-1}$ spectral resolution. The microscope embedded in this system is a Leica confocal model that supports multiple objectives. Unless otherwise specified, spectra were taken using a 40x 0.85NA objective. All spectra are collected in a backscatter geometry.

Figure 4.5 shows an illustration of a typical Raman micro-spectroscopy setup. Lasers transverse the same path and are reflected from a dichroic mirror into an objective. In epi-detection, or backscatter, geometry the objective serves to both illuminate the sample and collect scattered light. The objective focuses the laser beam incident to the sample. Both Rayleigh and Raman scattered light are collected by the objective, but only the Raman scattered light passes through the dichroic and into the spectrometer. A motorized grating disperses the Raman light onto a CCD array where the intensity is read into a computer system.

## 4.3 The Narrowband CRS Microscope

In Potma Labs, narrowband CRS, where the temporal width of excitation pulses is on the order of $7ps$, is the preferred method for nonlinear imaging. Narrowband SRS offers several

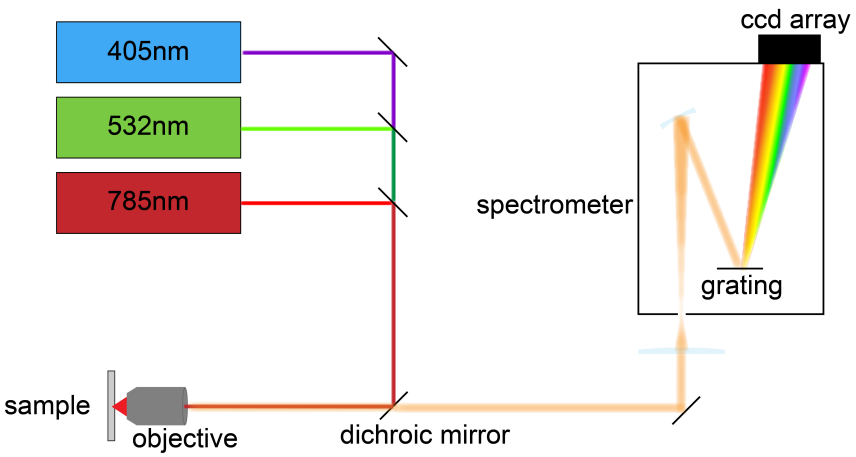



Figure 4.5: Illustrated Layout of a Raman System with non-centrosymmetric symmetry.

distinct advantages for biological imaging. With a temporally long pulse length, comes a correspondingly narrow spectral full-width at half max for each pulse.[302] Effectively, this means that the spectral resolution for our system is less than $0.5nm$. Under ideal circustances the time-bandwidth product for the fundamental laser line is given by Equations 4.2 and 4.3 assuming a $sech^2$ pulse envelope. Narrow spectral resolution correspondingly means that we are able to create hyperspectral data sets that can map out the Raman spectra for each pixel of an image. This will be discussed in more detail in Section 4.4.

$$TBP = \Delta\nu\Delta\tau \tag{4.1}$$

$$TBP_{sech^2} = \left(\frac{2log(1+\sqrt{2})}{\pi}\right)^2 \approx 0.315 \tag{4.2}$$

$$\tag{4.3}$$

For nearly all CRS measurements in this work, the following equipment specifications were used. Stimulated Raman loss (SRL) was measured using a combination of a fixed stokes beam at $1064nm$ generated by a $76MHZ$ mode-locked Nd:Vanadate laser (Picotrain, High-

Q) delivering seven picosecond pulses ($ps$) and a variable pump beam generated through an optical parametric oscillator (OPO, Levante Emerald, APE) pumped by the second harmonic of the laser at $532nm$. For imaging of the $CH_2$ stretching mode commonly associated with lipids at $2840cm^{-1}$, the OPO was tuned to $817nm$ and for carbon-deuterium imaging it was tuned between $866nm$ and $868nm$ to match the resonance that occurs between $2120cm^{-1}$ and $2140cm^{-1}$ depending on the specific compound under study. For stimulated Raman loss the stokes beam was modulated at $10MHz$ using an acousto-optic modulator (AOM, Crystal Technology). After modulation, the two beams were combined with a dichroic mirror and directed into a laser scanning inverted microscope (Fluoview 300 & IX71, Olympus) where both laser beams are raster scanned across the sample. Two objectives were used extensively in my research: a 20x, 0.75NA air objective (UPlanSApo, Olympus) and a 40x, 1.14 NA water-immersion objective (Olympus). Acquisition times varied between samples and are specified in individual studies. Generally, the pixel dwell time is between $7\mu s$ and $20\mu s$, though in the case of extremely low concentration samples this has been increased as high as $100\mu s$ per pixel. The signal is collected in the forward direction by a high-NA condensing optic, NA=1.4 (Olympus). This high NA is chosen to be larger than that of any objective used to avoid apparent erroneous signal caused by cross-phase modulation effects. The signal is further filtered before being incident on a wide-area photodiode (S6967, Hamamatsu). The electrical signal is filterd by a $10MHz$ bandpass filter and amplified by transimpedance amplifier. Finally the electrical signal is demodulated by a lock-in amplifier (HF2LI, Zurich Instruments). The SRS signal was collected on an output channel of the lock-in by the synced Fluoview system to form the intensity image.

## 4.4 Hyperspectral Imaging

One of the most powerful features of narrowband SRS is its ability to create hyperspectral datasets. To explain, the wavelength of the pump can be scanned over some range. At each set point in that range, and image can be taken. A three-dimensional data stack is created wherein the pixels all correspond to the same spatial dimensions, (X,Y), but the third dimension is in $\lambda$. In practice, this yields a Raman spectra for each pixel. This enables in-depth analysis of the spatial distribution of different chemicals.[34;152;303] From this data, further analysis techniques can be used. An example of this is shown in Figure 4.6 wherein the distribution and contribution of lipids and protein in cultured meibocytes are analyzed through vertex component analysis.

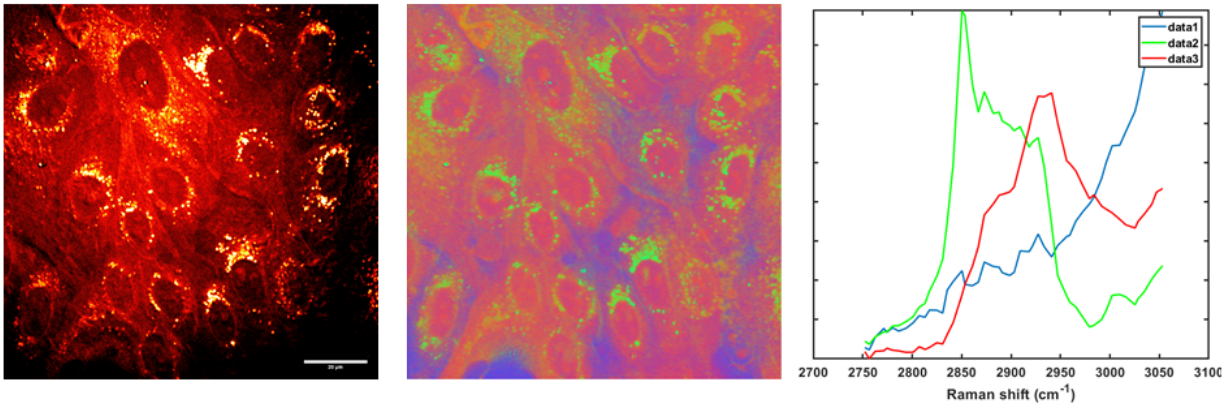



Figure 4.6: Vertex Component Analysis of Cultured Meibocytes
(a) mean intensity image of cultured meibocyte cells. (b) false color image where color corresponds to a component spectra. (c) Vertex component analysis identifies three major components to the CH spectra of the image. A lipid-like contribution (green), protein-like contribution (red), and background contribution (blue).

# Chapter 5

# Deuterated Raman Probes: Elucidating Lipogenesis in Cartilage

Material in this section is being prepared for publication under the title *Lipogenesis is an evolutionarily conserved strategy for cartilage morphogenesis* by Raul Ramos et. al.

As discussed already in Chapter 4, recent work has shown that the use of deuterium labeled molecules as Raman tags is a fruitful avenue for metabolic analysis of cells and tissues. This was recently applied to the study of cartilaginous tissues in small mammals. In this work, spontaneous Raman scattering, stimulated Raman scattering microscopy, and second harmonic microscopy were applied to an under-described cell type, the lipochondrocyte.

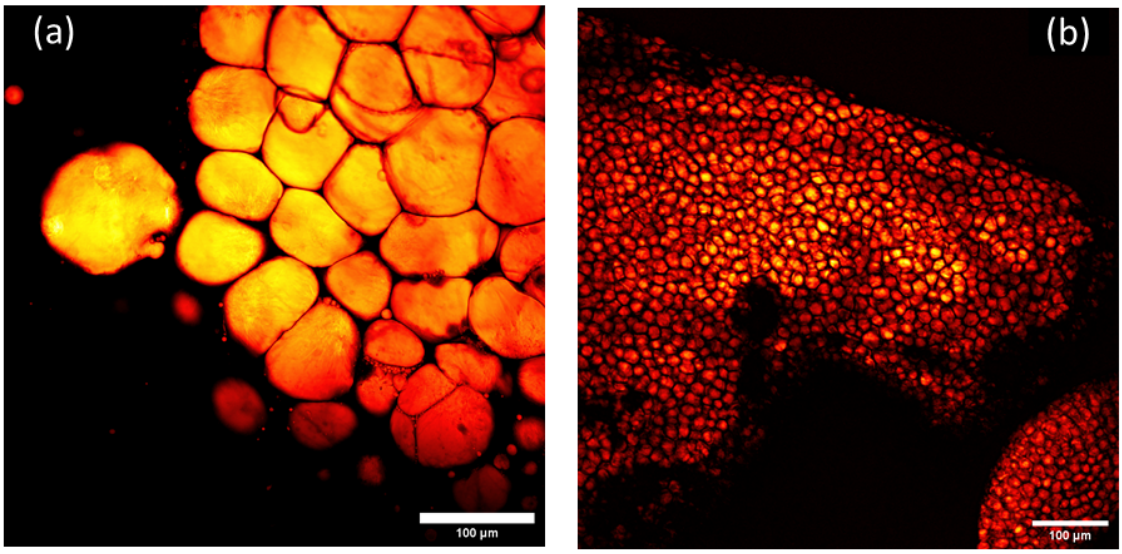



Figure 5.1: Comparison between adipocytes and lipochondrocytes
Stimulated Raman scattering images of (a) adipocytes and (b) lipochondrocytes shows significant size and other morphological differences between cell types. Both tissues imaged at $2840cm^{-1}$ where the maximum signal is derived from lipids.

## 5.1 A Background on Cartilage

Cartilage cells are generally thought to be characterized and identified through a process of extracellular matrix deposition. However, evidence presented in this work indicates that

this is not a universal process. In the neck and head cartilages of mice, a differentiated cell known as a lipochondrocyte are found. These cells resemble white adipocytes morphologically in that the central feature is large lipid-laded vacuoles. However, lipochondrocytes do not mobilize lipids and lack expression of key lipid uptake components. They do not change upon obesity or caloric restriction. Figure 5.1 shows a comparison between adipocytes and lipochondrocytes imaged with SRS microscopy. Synthesis of the lipid vacuole in ear pinna lipochondrocytes relies on *de novo* lipogenesis, and inhibition of lipogenesis through either pharmacological or genetic means disrupts the formation of cartilage. In mice, this leads to shrunken and misshapen ears. Research suggests that lipochondrocytes are present across multiple mammalian clades. This includes bats, primates, and marsupials. The research herein indicates that lipid vacuolation is an evolutionarily conserved strategy for cartilage differentiation. It is established through this work that *de novo* lipogenesis is a novel regulator for morphogenesis of craniofacial features, and future work is needed to establish whether other tissues utilize similar mechanisms for formation of stable lipid vacuoles.

Within vertebrate skeletal systems, cartilaginous tissues form an essential components that plays both mechanical and morphogenetic roles.[304] Annelid worms, cephalopod mollusks, horseshoe crabs, and other invertebrates posses similar cartilage-like tissues.[305;306]. The mechanical properties of which are ascribed to the large amount of extracellular matrix (ECM) secreted by the cartilage cells. It has been shown that cartilage tissues arise from both mesoderm and the neural crest during morphogenesis, and that developmentally distinct cartilages can merge within the cranium.[307–309]

During previous work on mouse ear skin, it was noticed that samples possessed "lipid ghost" artefacts after histological processing.[310] It is common to see lipid ghosts after processing of adipose tissue, but generally uncommon for other healthy tissue types as most cells do not possess large lipid vacuoles. Literature review revealed allowed for the rediscovery that mice have multiple lipid-laden cartilage tissues consisting of vacuolated adipocyte-like cells called

lipochondrocytes (LCs). These cells were first recognized by the famed anatomist Franz von Leydig during investigations in the 1850s.[311] They were again described in only a handful of hisological studies more than a century later.[312–319] They remain an obscure cell and little is known about their lineage, biochemistry, gene regulatory program or function. This is despite their prevalence in many head and neck structures in many mammals.

## 5.2 Germ Layer Origins of Lipochondrocytes

Given the unique and understudied nature of this tissue, a number of investigations were conducted to elucidate their genomic, lipodomic, and metabolmic profiles. Additionally, tissue from multiple species was examined in order to better understand where LCs fit evolutionarily. In order to better understand the morphology and origins of these cells, extensive fluorescence staining and genetic tagging studies were carried out. This is shown in Figure 5.2. Using the Wnt1-Cre2;mT/mG mouse model tissues derived from the neural crest express green fluorescent (GFP). As shown in 5.2(b), nasal cartilage is positive for GFP (n=5) and contain lipid-laden vacuolated cells which stain positive under treatement with OilRedO (n=3). This is shown in 5.2(c,d). Fig. 5.2(e,f) show tissue taken from the larynx consisting of a composite of neural-crest and non-NC derived cells in the thyroid cartilages, while epiglottic tissue is derived from the neural crest. Cricoid and arytenoid tissues are negative for neural crest-derived tissues.[320] Staining indicates that tissues from the epiglottis and thyroid cartilage both have many lipid rich cells (n=3) Fig. 5.2(g,h). However, the non-neural crest portion of the thyroid cartilage is devoid lipid positive vacuoles 5.2(f,g).

Demonstrated in Figure 5.2(i-k), ear cartilage demonstrates high levels of OilRedO staining (n=8). The lipid filled cells in this tissue organize into a thin plate, and show many fenestrae that are often occupied by clusters of large lipid-filled cells Fig. 5.2(k) and 5.3. Using Wnt1-Cre;R26R mice (n=4) Fig. 5.2(m) and cartilage-specific $Col2a1-CreER^T;R26R$ (n=3)

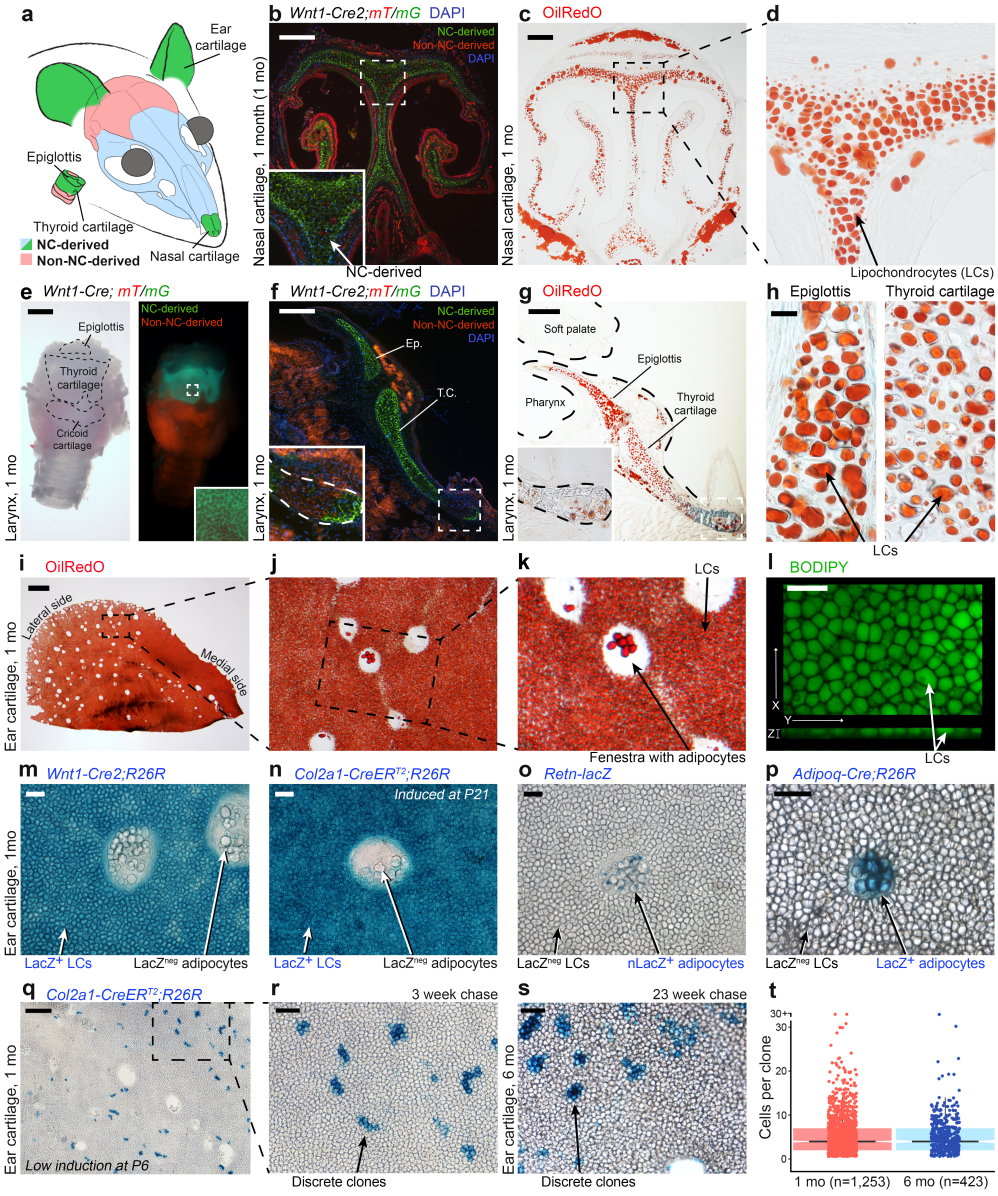



Figure 5.2: Multiple cartilages show presence of Lipochondrocytes
(a) Schematic drawing of mouse cartilages color-coded by embryonic origin. LC-containing neural crest (NC)-derived cartilages are in green. (b-h), OilRedO staining and lineage tracing in Wnt1-Cre2;mT/mG mice shows lipid-laden LCs in NC-derived nasal (b-d), epiglottic and thyroid cartilages (e-h), except for the posterior end (inlets on f, g). Ear cartilage consists of OilRedO+ and BODIPY+ LCs and contains fenestrae occupied by adipocytes. (m-p), On lineage analysis ear LCs are lacZ-positive in Wnt1-Cre2;R26R and Col2a1-CreERT;R26R mice, but negative in adipocyte-specific Retn-lacZ and Adipoq-Cre;R26R mice. (q-t), On clonogenic analysis in Col2a1-CreERT;R26R mice, lacZ-labeled LC form discrete clones that are stable in size for 6 months. Scale bars, h – 25 $\mu$m; l – 50 $\mu$m; m-p, r, s – 100 $\mu$m; b, c, f – 200 $\mu$m; g – 250 $\mu$m; q – 500 $\mu$m; e, i – 1 mm.

Fig. 5.2(n) mice, surrounding plate cells and not fenestra cells are positive for lacZ, and the staining pattern for lacZ is reversed in the adipocyte-specific Retn-lacZ (n=4) Fig 5.2(o) and Adipoq-Cre;R26R (n=6) Fig.5.2(p) models. Taken together these results identify ear cartilage plate cells as neural crest-derived lipid-filled lipochondrocytes, while the cells inside of the fenestra are identified as non-neural crest-derived white adipocytes.

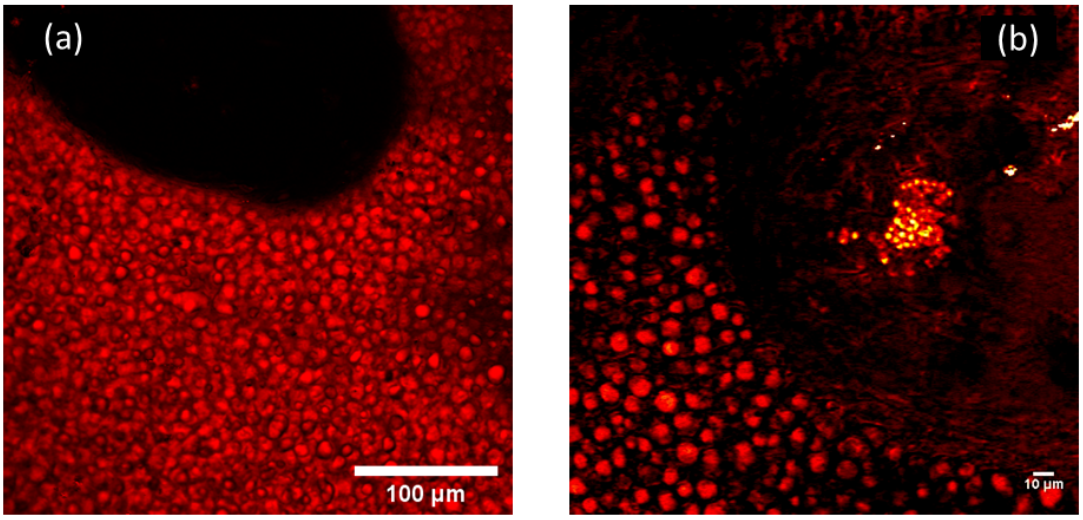



Figure 5.3: SRS images of mouse ear cartiledge showing fenestrae without (a) and with (b) lipid bearing cells.

With nearly two-dimensional morphology, ease of isolation, and abundance of cells, ear cartilage tissues became the focus of latter studies. $Col2al - CreER^T; R26R$ mice were treated with low doses of tamoxifen at P6. This causes recombination of individual cartilage progenitors, leading to discretely labeled LC clones in adult ears as shown in Figure 5.2 (q). The size of clones at 3 weeks (n=1,253 clones)(5.2(r)) and 23 weeks (n=423 clones)(5.2(s)) after labeling were not statistically different, Figure 5.2(t). These results suggest that LCs experience a long lifespan with limited turnover.

## 5.3 Lipid and Gene Profiling

As examined above, lipochondrocytes appear to be a unique form of cartilage and are distinct from other lipid-laden cells. Presented as such, these curiosities necessitated further investigations into the nature of LCs. An obvious line of research was to examine the lipodomic profile of ear cartilage compared to adipocytes. A full description of the lipid profiles is beyond the scope of this dissertation, but the full results can be found in the peer-reviewed work. Here I highlight the most significant points leading to further imaging studies.

Electrospray ionization-MS was performed on a TripleTOF 5600+ (SCIEX) system and quantification was done using an in-house library. See section 5.8 for full specification of lipidomics methodologies. Lipodomic profiles were compared between ear cartilage (n=5) and inguinal white adipose tissue (WAT; n=5) of wild type mice at age one month. The two tissue types display markedly different lipid profiles in lipid abundance and diversity. Critically, ear cartilage contains nearly half the quantity of of triglycerides (86.5% vs. 43.3%) and substantially more fatty acid hydroxyl-fatty acids (9.4% vs. 31.1%). Substantially more saturated fatty acid chains (3.8% vs. 19.7%). This is particularly notable as saturated fatty acid chains are the main product of *de novo* lipogenesis.

Transcriptomes of ear LCs (n=3) and inguinal WAT adipocytes (n=3) were compared to those of hyaline rib cartilage chondrocytes available in literature.[321] Full data for transcriptomics is available in the published work. The transcriptome of the LCs is distinct from the other two cell types. 8,455 genes are expressed differently in LCs than in adipocytes and chondrocytes. LCs are simultaneously enriched for both cartilage terms and metabolic terms, highlighting these as a distinct cell type. Intersetingly, LCs and chondrocytes express similar ECM genes, while these are otherwise minimal in adipocytes.

It should be noted that while LCs are morphologically similar to adipocytes, LCs do not express adipokines *Adipoq, adipsin, Lep, Retn, Retnla* and several pro-adipogenic transcrip-

tional regulators. These differences extend to key genes of the lipid synthesis, catabolism, and vacuole formation and maintenance systems. Importantly, LCs do not express *Cd36* and show only low levels of *Slc27al*. Both of these are major transporters of free fatty acids in adipocytes. Notably, key glucose transporters and key *de novo* lipogenesis enzymes are expressed along with many enzymes required at all steps of triglyceride synthesis. *Pnpla2, Lipe, and Mgll* are prominently downregulated in LCs. These enzymes are important for mobilization and breakdown of triglycerides. Key enzymes *Plin1* and *Abhd5* are not expressed and downregulated respectively; both are critical for hormone-stimulated lipolysis. This all shows that LCs express a unique transcriptome that shares features of both hyaline chondrocytes, such as ECM and signaling gene expression, and adipocytes, including essential lipogenesis and lipid storage genes.

## 5.4 Lipochondrocytes Activate Lipogenesis

In developing a description of lipochondrocytes, it was important to determine when during lineage formation LCs activate lipogenesis. To this end, a time course for the development of ear cartilage was established. In mice, external ear structure develops after birth.[310;316;322] Ear surface measurements in wild type mice (n-5) allowed identification of two distinct and consecutive growth phases. The first phase occurs slowly between postnatal days P1-P15. During this phase, ears unfold and grow approximately nine times in size. During the second phase between P15 and one month, ears rapidly expand before plateauing. They increase in size approximately 25 times the size of the P1 ears. This is shown diagrammatically in Figure 5.4.

To study the growth of cartilage tissue the chondrogenic marker SOX9, the proliferation marker PCNA, and OilRedO were employed. SOX9 plays a key role in chondrocyte differentiation, and it first appears at P4, and seems to broadly activate by P7. Between P4 and

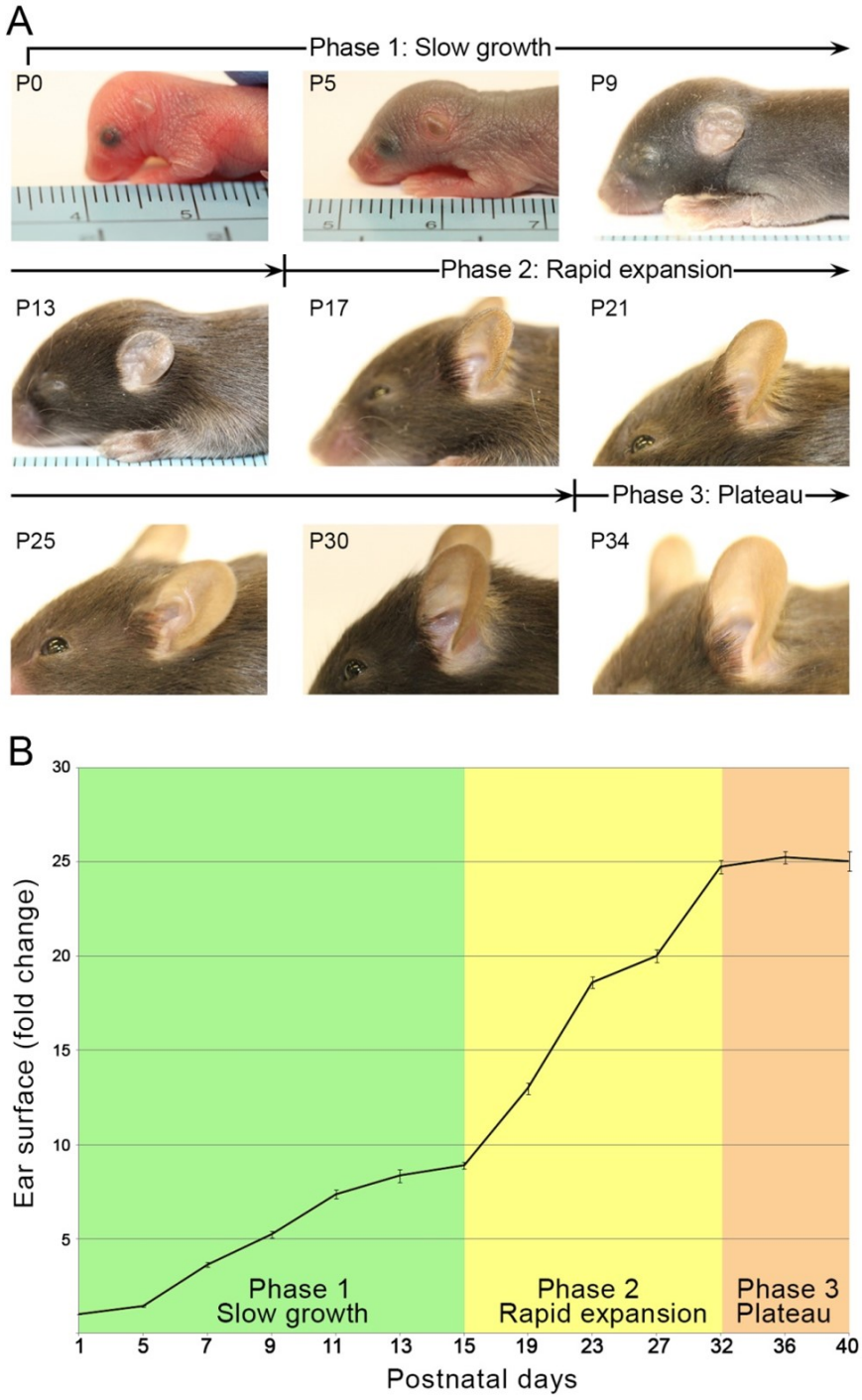



Figure 5.4: Phases of ear pinna growth in mice.
(A) Ear pinna in mice undergo significant changes in size and shape during the first month of growth. (B) Quantificaiton of ear surface measurements reveals two growth phases and a plateau phase during ear pinna growth.

P10, many SOX9-positive cells stain positive for PCNA. However, they are PCNA negative by P13. 5.5 OilRedO positive vacuoles first appear between P10 and P13. They rapidly enlarge petween P13 and one month, Figure 5.6 (a). From this data, commitment to the LC lineage occurs between P4 and P7. Once committed, LC progenitors proliferate between P4 and P13. Post-mitotic LCs differentiate and form lipid vacuoles starting at P10 and reach adult size by one month. Proliferation and lipogenesis partially overlap between P10-P13, Fig. 5.6 (b).

From the basis of the staining timeline presented above, it is possible to define several RNA-sequencing time points: P8 and P10 as the early and late proliferative phases respectively; P13 as the transition phase; and P21 and one month as the early and late differentiation phases, respectively. Between P8 and P13, LC progenitors were sorted as $tdTomato^{hi}$ cells from microdissected *Wnt1-Cre2;tdTomato* cartilage primordia. At P21 and one month, LCs were isolated via buoyancy. Buoyant cells at P13 and non-buoyant cells at P21 were depleted from respective samples upon processing. Analysis reveals that LC lineage transcriptome prominently changes with time (n=3/timepoint); full data set and analysis in published work. 2,397 genes are differentially expressed and organize into four-temporally dependent clusters via principal component analysis. Cell-cycle activators and pro-mitotic factors are abundant in LC progenitor cells, but are largely shutdown upon differentiation. This is contrasted with data indicating that cell cycle inhibitors are enriched in late differentiated LCs. The LC gene regulatory program is dominated by cell cycle genes, pro-chondrogenic transcription, and ECM factors in the early phase, and by lipogenesis machinery and specialized ECM factors in the late phase.

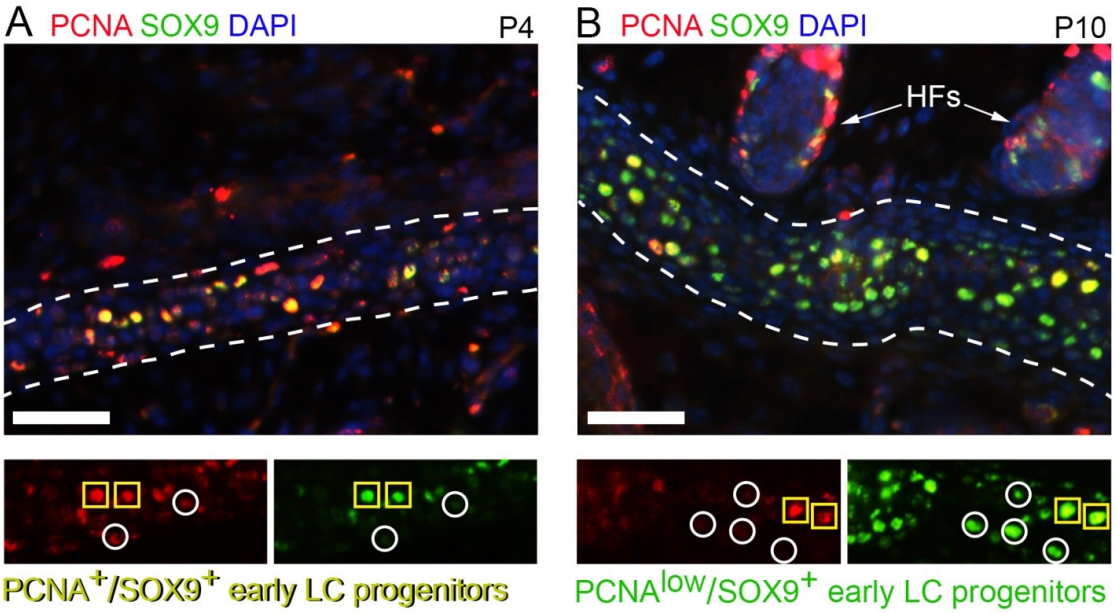



Figure 5.5: Expression patterns of SOX9 and PCNA in the developing ear cartilage. Immunostaining for SOX9 (green) and PCNA (red) in P4 (A) and P10 ear cartilage (B). For both time points, co-localization of markers is shown on the top panels. Bottom panels show PCNA and SOX9 expression separately within the same selected region. Single-positive cells are marked with white circles and double-positive cells with yellow squares. Double-positive cells are present at both time points. Compared to P10, P4 ear cartilage contains many PCNA-positive cells that do not express SOX9. In contrast, P10 ear cartilage contains many SOX9-positive cells that do not express PCNA, as compared to P4. Ear cartilage is marked with dashed lines. HFs – hair follicles, LCs – lipochondrocytes. Size bar: A, B – 25 $\mu$.

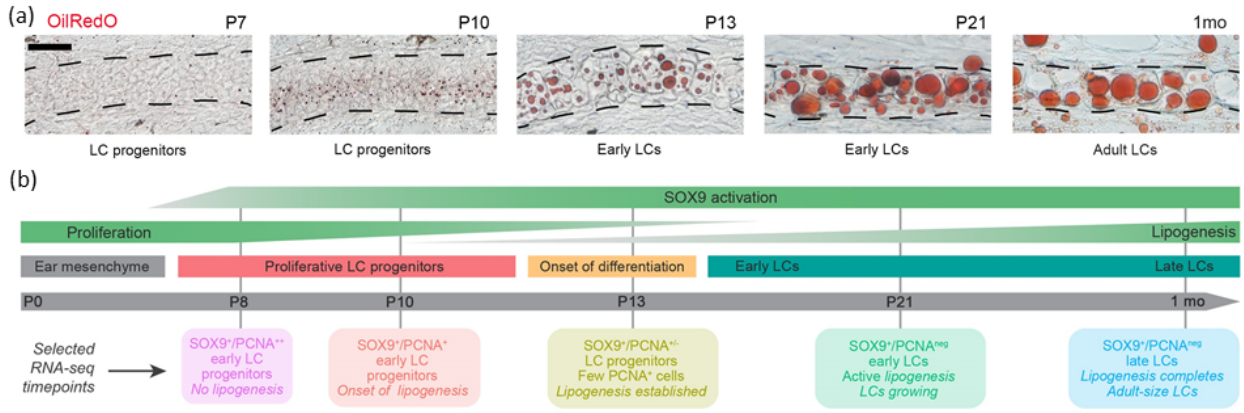



Figure 5.6: Lipogenesis dominates lipochondrocyte differentiation.
(a) OilRedO staining in the developing ear cartilage at five consecutive postnatal time points, days P7, P10, P13, P21 and 1 month of age. First OilRedO-positive lipid droplets appear between P10 and P13 and then prominently increase in size by P21 and 1 month. (b) Schematic illustration of the key stages in ear cartilage development. Patterns of proliferation, SOX9 expression and lipogenesis are at the top (green). Key stages in ear cartilage development are in the middle (colored bars). Selected RNA-seq timepoints are at the bottom (colored boxes).

## 5.5 Lipochondrocytes require *de novo* Lipogenesis

Our results indicate that the biogenesis of lipid vacuoles in LCs primarily occurs via *de novo* lipogenesis. A direct study and analysis of this result was enabled through the use of stimulated Raman scattering (SRS) microscopy. As noted in Chapter 4, deuterium labeling of molecules creates a unique peak in the cell silent region of the Raman spectra. Thus to study lipogenesis directly, spectral tracing of carbon-deuterium incorporation into lipid vacuoles of developing LCs was performed. We cultured P14 mouse ears for 72 hours in high glucose control media (n=3) or in glucose-free media supplemented with deuterated glucose (glucose-d7) (n=3). High carbon-deuterium (C-D) signal ( $2140cm^{-1}$ was detected in glucose-d7 treated lipochondrocytes after background subtraction (Fig 5.7 (b), but not in control lipochondrocytes. In the spontaneous Raman spectrum, C-D signal observed in the glucose-d7 treated LCs matches the C-D signal profile of pure deuterated glucose as shown in Figure 5.7 (c, red). Comparing images whose contrast is derived from the C-D

signal(Fig. 5.7 (b)) with the same spatial region at the C-H signal(Fig. 5.7 (a)) ( $2844c,^{-1}$ shows significant spatial overlap within the lipid vacuoles (Fig. 5.7 (d)). These data directly confirms that differentiating LCs grow lipid vacuoles via *de novo* lipogenesis.

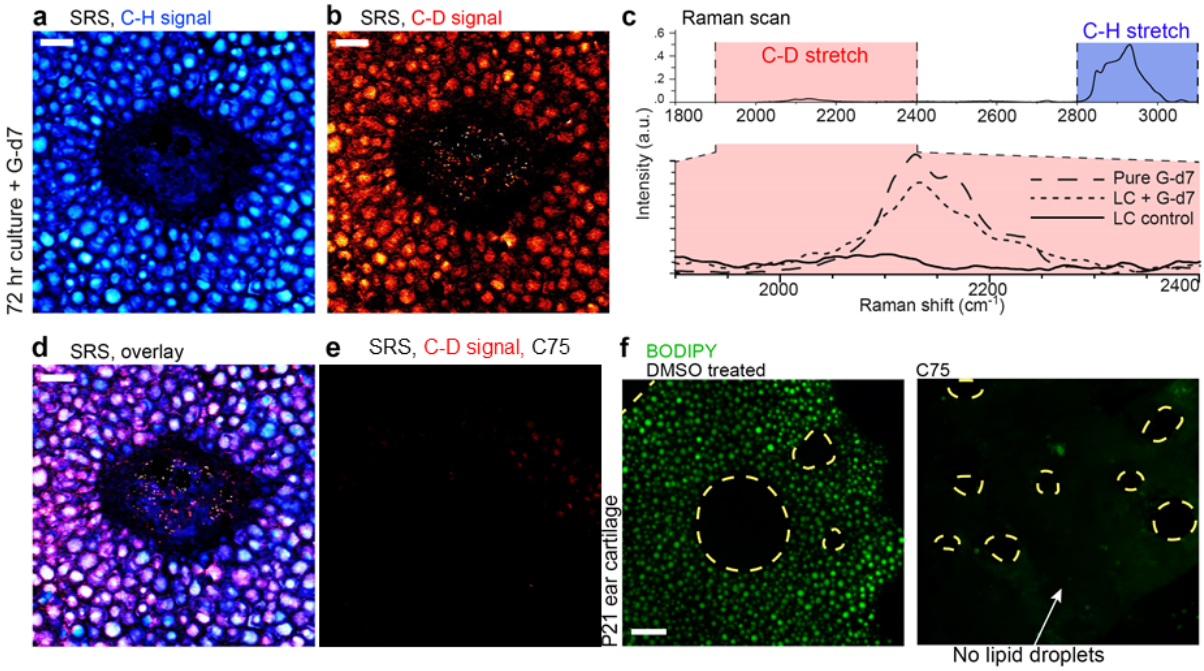



Figure 5.7: SRS Finds Direct Evidence of De Novo Lipogenesis
Stimulated Raman scattering (SRS) reveals that glucose-derived deuterium incorporates into lipid vacuoles of developing ear lipochondrocytes. Color-coded ear cartilage images at the C-H vibrational range $2940cm^{-1}$ (a), C-D vibration range $2100cm^{-1}$ (b), and overlay (d). Raman scan from deuterated glucose-cultured LC lipid vacuoles shows C-D stretch peak overlaps with C-D stretch peak of pure deuterated glucose (c, red region). Ear cartilage with inhibited lipogenesis is devoid of C-D signal in SRS (e). C75-treated ears show prominent decrease in $BODIPY^{+}$ lipid vacuoles. Scale bars: a,b,d,e - 25 $\mu m$, f - 50 $\mu m$.

Furthermore, we tested the functional significance of *de novo* lipogenesis during ear cartilage development. We studied changes in ear morphology at P21 following 11 topical daily treatments with Acetyl-CoA carboxylase inhibitors PR-05175157 (PF) and ND-646 (ND)[323;324]

or with C75, a fatty acid synthase inhibitor.[325] Sections from the C75 treated mice were then treated as above to 72 hours in high glucose control media (n=3). Upon imaging with SRS, there was a deficit of C-D signal as shown in 5.7 (e). What little signal does remain is likely produced by deuterium incorporation into non-lipid compounds such as protein. Additionally, staining with BODIPY showed sections treated with C75 to be devoid of lipid vacuoles unlike the DMSO treated control (Fig 5.7 (F)).

Significantly, we observed reduction in ear sizes with all three cases as shown in Figure 5.8 (a). ND and C75 produced significant reductions resulting in prominently smaller, misshapen ears, $88 \pm 2\%$ (Fig. 5.8 (d)) and $55 \pm 7\%$ in size (Fig. 5.8 (e)).

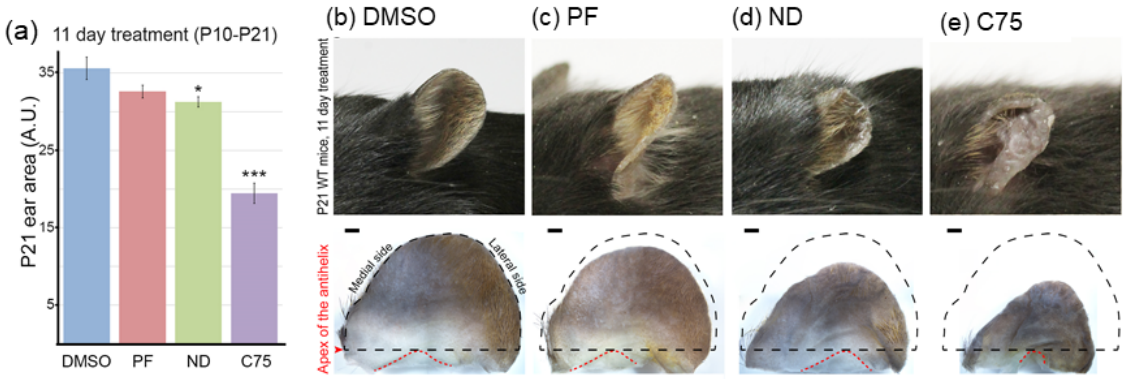



Figure 5.8: Inhibition of Key Enzymes Alters Morphology
Ears become smaller in mice topically treated with *de novo* lipogenesis inhibitors PF-05175157 (PF), ND-646 (ND), and C75 compared to DMSO control (a). Representative mice are ears are shown in b-e.

*De novo* lipogenesis was also disrupted genetically by inducing cartilage-specific deletion of *Acaca*, one of two acetyl-CoA carboxylases[326], in homozygous $Col2a1-CreER^T; Acaca^{fl/fl}$ mice. Mice were induced with four daily intra-peritoneal tamoxifen injections starting at P10, and ears were examined at P17. Compared to tamoxifen treated $Col2a1-CreER^T; Acaca^{+/+}$ control mice (n=3) (Fig. 5.9 (a,b)) , $Col2a1-CreER^T; Acaca^{fl/fl}$ mutant mice (n=3) (Fig. 5.9 (m,n)) develop misshapen ears that are $51 \pm 12\%$ smaller (Fig. 5.9 (e)). Lipid vacuole size measurements show smaller vacuoles in mutant compared to control LCs, with

a significant reduction in size distribution (Fig. 5.9 (f-h)). These data demonstrate that *de novo* lipogenesis is required for proper LC differentiation and ear morphogenesis.

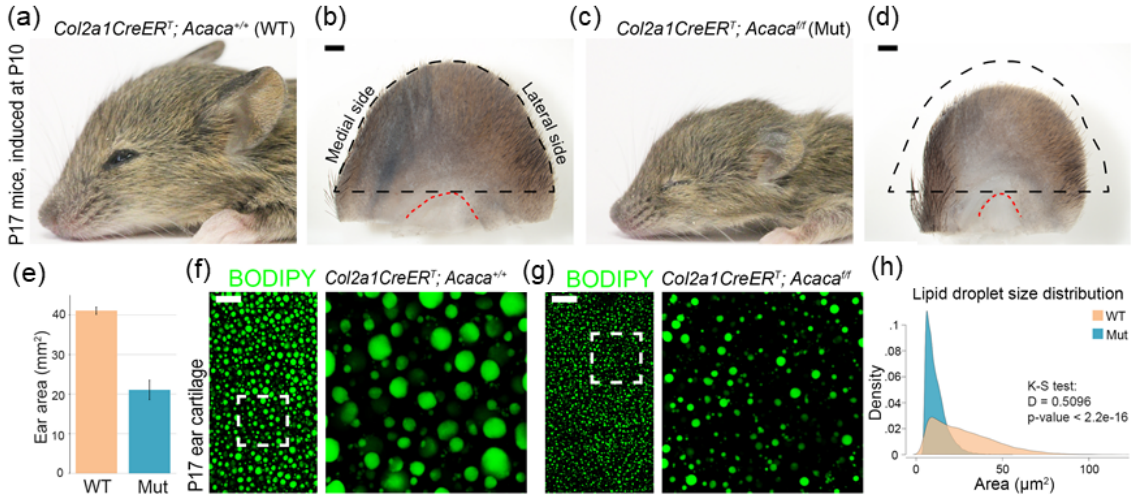



Figure 5.9: Genetic Inhibition Disrupts LC Differentiation
Inducible deletion of *Acaca* in $Col2a1-CreER^T$; $Acaca^{fl/fl}$ mice results in smaller, misshapen ears and smaller LC lipid vacuoles. Representative control (a-b) and mutant (c-d) mice and ears and BODIPY-stained ear cartilage (f-g) are shown. Size quantification for ear area is in (e) and for ear LC lipid vacuoles is in (h). Scale bars: f,g - 40 $\mu m$

## 5.6 Human Facial Cartilage Cells Accumulate Lipids

Considering the prevalence of lipochondrocytes in mice and other mammals, we profiled multiple human head and neck cartilages for the presence of intracelluar lipid vacuoles. At gestational week (GW) 20-21, human fetal ear cartilage already stains with Alcian blue, an acidic cationic dye that strongly binds to the sulfated glycosaminoglycans common to cartilaginous tissues as shown in Figure 5.10 (a). With immunohistochemistry COL8A1 was detected in human cartilage and adjacent dermis, but could only detect PLIN1 in dermal adipocytes (Fig. 5.10 (b)). Remarkedly, lintracellular lipid vacuoles were detected upon OilRedO staining in human fetal ear cartilage (Fig. 5.10 (c,d)). Using transmission electron microscopy, large intracellular lipid vacuoles in chondrocytes of the thyroid and epiglottic

cartilages as well as those in external ears and lateral nasal fold were shown (Fig. 5.10 (e-h)).

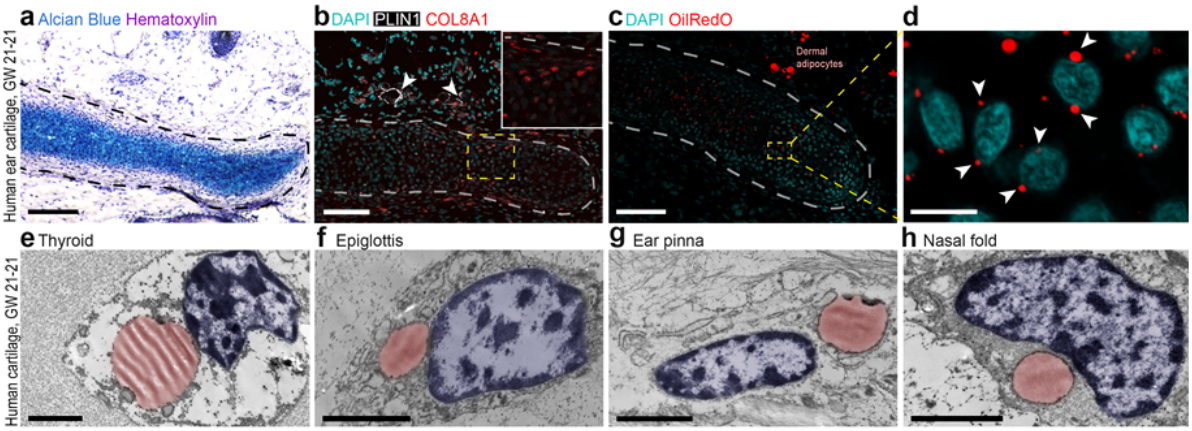



Figure 5.10: Human Facial Cartilages Accumulate Lipids
(a) Alcian blue staining of human fetal ear cartilage at GW 20-21. (b) Immunostaining patterns of COL8A1 and PLIN1 in human fetal ears show PLIN1 expression confined to dermal adipocytes and COL8A1 expression in chondrocytes and dermal cells. (c,d), OilRedO staining of GW 20-21 human ears shows formation of lipid droplets in dermal adipocytes (c) as well as in chondrocytes (c, magnified in d). (e-h) Electron micrographs of fine tissue sections including thyroid cartilage (e), epiglottis (f), ear pinna (g), and lateral nasal fold (h) show chondrocytes with large lipid droplets; nucleus and lipid droplets have been pseudo-colored purple and red, respectively.

A goal of this work then became to replicate human cartilage lipogenesis *in vitro*. Human embryonic stem cell (hESC)-derived neural crest cells were generated *in vitro* and differentiated into chondrocytes as previously described.[327;328] Chondrocyte pellets were maintained in chondrocyte differentiation medium for up to 65 days. At that stage, OilRedO staining of human chondrocyte pellets shows that many chondrocytes also accumulate lipids (Fig. 5.11 (a)). Similar to the results in tissue, stimulated Raman scattering microscopy reveals lipid accumulation and second harmonic generation (SHG) microscopy detects fibrillar collagen in these cultures(Fig. 5.11 (b)).[329]

In light of these results, it was desirable to observe chondrocyte maturation and lipid droplet growth in hESC-derived droplets at the transcriptional level using bulk RNA-sequencing across *in vitro* differentiation. These results are summarized here, but may be found in

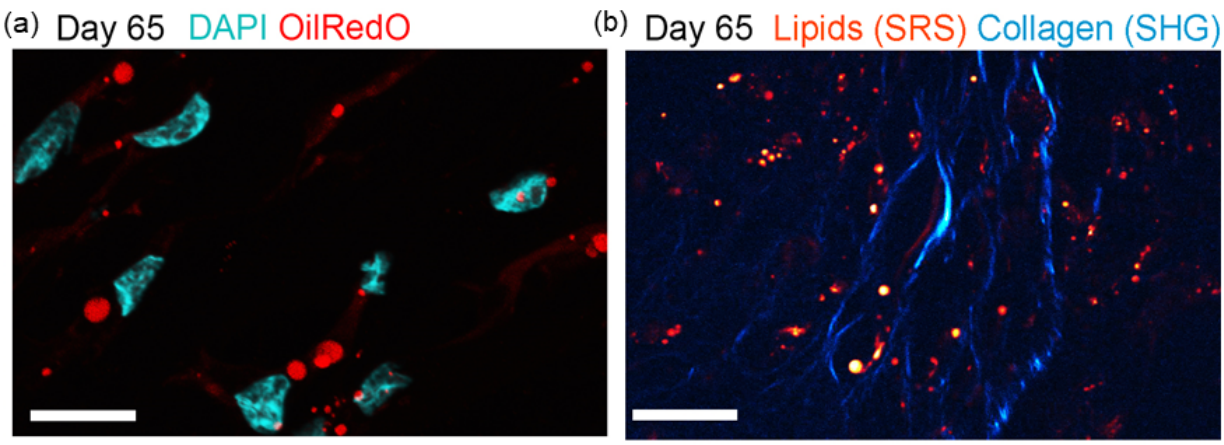



Figure 5.11: Staining and Nonlinear Microscopy Reveals Lipid Accumulation
(a) Oil Red O staining of Day 65 pellets shows acummulation of lipid droplets in chondrocytes. (b), Label-free imaging of lipids and fibrillar collagen using SRS and second harmonics generation, respectively. SRS (lipids) and SHG (collagen) signals have been pseudo-colored red and blue, respectively.

full detail in the published work. I.V. Day 21 was used as a starting point as it was the earliest point in which alcian blue staining is observed.[327] as well as Day 30 and Day 45. Principal component analysis (PCA) of these transcriptomes shows they are distinct from one another. Differential gene expression analysis shows 9,842 genes organizing into three main temporally-dependent clusters. Paralleling mouse LCs, human chondrocytes express high levels of structural genes and signaling genes related to cartilage development and maturation.[330–332] Chondrogenesis regulators encoded by ID2 and FOXA3 are expressed in the human model as well as several lipgenic factors.[333;334] Noticeably, the adipogenic master regulator *PPARG* is not detected.[335;336] In parallel with the mouse model, human chondrocytes show no expression of genes *ADIPOQ* and *RETN* which encode adipokines. Human chondrocytes prominently express genes involved in *de novo* lipogenesis, including *ACLY, ACACA, FASN,* and *SCD* In summary, these studies show that lipogenesis is a normal, developmentally-relevant process for facial cartilage morphogenesis. *In vitro* gene expression is remarkably similar between mouse and human cartilages.

## 5.7 Discussion of Results

In this work, lipochondroytes are rediscovered and characterized as a distinct lipid-laden cartilage cell type. Intriguingly, LCs nearly-exclusively rely on *de novo* lipogenesis for lipid vacuole synthesis, which likely enables them to differentiate to a highly uniform size. It is conceivable that using a finite number of large, uniform cells as a kind of biological "LEGO Blocks", LC-based cartilages attain highly consistent sizes and shapes, which can be essential for their function. Lipid vacuoles in LCs are highly stable even upon animal starvation, and very low expression levels of *Plin1* and *Lipe*, otherwise critical for triglyceride mobilization, are likely responsible for this effect. A similar molecular mechanism may protect specialized shock-absorbing adipose tissues in hip and knee joints from starvation-induced atrophy.[337]

Analogous to LCs, other cartilage and cartilage like-cells can increase their volume dramatically upon differentiation. In the notochord, inner cells develop large aqueous vacuoles[338;339], while in the growth plate of long bones chondrocytes undergo hypertrophy via cytoplasmic volume and organelle size and number expansion.[340] We posit that lipid vacuolation is a novel form of cartilage hypertrophy. The phylogenetic analysis presented in full detail in the published work, suggest that LCs were already present during hte late Jurassic, in the common ancestor of marsupials and eutherians. IT is conceivable that the lipochondrocyte is a much older cell type, but this remains to be investigated.

Rediscovery of LCs opens new research opportunities across a range of disciplines. Their unique lipid biology can prove useful in studying metabolic adaptations of cells, including to high free fatty acid levels, which are normally cytotoxic.[341] LC-rich cartilages will help to address the role of cellular vacuoles in tissue biomechanics and mechanisms of cell-based tissue morphogenesis. Since ear cartilage can restore after injury[342]., the LC lineage might enable studying cartilage stem cells and regeneration in a human-relevant context.

## 5.8 Study Specific Methodology

### 5.8.1 Glucose-d7 *Ex Vivo* Ear Culture

P14 ears were partially dissected by removing the caudal skin flap and exposing the cartilage, then cultured in glucose-d7 containing media. Briefly, glucose-d7 containing media was prepared with glucose-free DMEM (ThermoFisher Scientific), $25\mu molar$ glucose-d7 (Cambridge Isotope Laboratories), 10% FBS (Atlanta Biologicals), and 1X PenStrep. Tissues were cultured for 72 hours. Control samples were cultured for 72 hours in high glucose ($25\mu molar$ glucose) DMEM, 10% FBS, 1X PenStrep without glucose-d7 added. Samples were changed into fresh media every 24 hours. All samples were rinsed with 1X PBS twice for 5 minutes and fixed with 4% PFA for 1 hour and imaged.

### 5.8.2 SRS Microscopy

For full methodology, see Chapter 4. Ex vivo cultured ears were imaged through stimulated Raman scattering to visualize lipid content and track deuterium incorporation into lipid droplets. Stimulated Raman loss was measured using a combination of a fixed stokes beam at 1064 nm and a variable pump beam generated through an optical parametric oscillator (OPO, Levante Emerald, APE). For imaging of the CH2 lipid mode, the OPO was tuned to 817 nm and for deuterated imaging it was tuned to 868 nm. All images were taken in the forward direction through stimulated Raman loss (SRL). Additionally, linear Raman spectra were acquired for the P14 ear samples cultured for 72 hours and for pure standards using a confocal Raman microscope (InVia Confocal, Renishaw).

### 5.8.3 Mouse models

*Wnt1-Cre2* (JAX, #022137), *mT/mG* (JAX, #007576), *R26R* (JAX, # 003309), *tdTomato* (JAX, #007914), $Col2a1{-}CreER^T$ (JAX, #006774), *Retn-lacZ52*, *Adipoq-Cre* (JAX, #010803), *db/db* (JAX, #000697), $Acaca^{fl42}$ were used. In $Col2a1 - CreER^T; R26R$ mice, tamoxifen in corn oil was injected IP for four consecutive days starting at P7 at a dose of 75 mg/Kg for full induction. For low-dose induction, a single dose of tamoxifen in corn oil at 7.5 mg/Kg was injected IP at P7. For $Col2a1 - CreER^T; Acaca^{fl/fl}$ mice, full induction was performed as described above starting at P10.

### 5.8.4 OilRedO

OilRedO Figure 5.12 is a fat-soluble (lysochrome) dye used to stain neutral lipids and triglycerides. It has been demonstrated for use on frozen tissue sections, though it must be used without alcohol fixation to prevent removal of lipids. Research has shown that it can be used for qualitative and quantitative assessment of adipocytes and lipid droplets.[343;344] Though it has been noted that it is not a perfect solution for detection of lipids as their trends often do not match with biochemical analysis.[197]

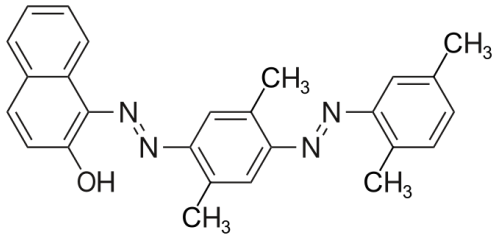



Figure 5.12: Structure of the Diazo Dye Oil Red O

### 5.8.5 Histochemistry, immunostaining, and imaging

For lacZ staining, tissues were fixed in 4% PFA for 30 minutes at room temperature, rinsed in 1X PBS and incubated in lacZ buffer at $37°C$ for 5 minutes, then transferred to lacZ buffer with X-Gal (VWR) and incubated at $37°C$ until signal developed. For OilRedO staining, tissues were fixed in 4% PFA for 8 hours at $4°C$, rinsed in 1X PBS, then submerged in 60% isopropanol for 1 minute followed by 6.25 mg/ml OilRedO in isopropanol for 30 minutes. Tissues were rinsed in 60% isopropanol and imaged in 1X PBS. For BODIPY staining, tissues were incubated in $200\mu molar$ BODIPY 493/503 (Thermo Fisher) in 1X PBS for 30 minutes and imaged. For fluorescent free fatty acid incorporation assay, $100\mu l$ of $20\mu molar$ C1-BODIPY-C12 were injected peritoneally. Adult one-month old mice received single injection and were chased for 6 hours. P10 mice received eight injections with 24-hour interval and were chased 6 hours after the last injection. The primary antibodies used were rabbit anti-SOX9 (1:250; Millipore), rabbit anti-FASN (1:250; Cell Signaling Technology), rabbit anti-PLIN1 (1:750; Cell Signaling Technology), rabbit anti-COL8A1 (1:500; Antibodies-Online), mouse anti-MYOC (1:250; ProteinTech), rabbit anti-ACACA (1:50; Cell Signaling Technology), rabbit anti-CEBPA (1:100; Cell Signaling Technology), rabbit anti-CEBPB (1:200; Cell Signaling Technology), mouse anti-PCNA (1:200; Abcam). Secondary antibodies used were Alexa Fluor 488 and 555 goat anti-rabbit (ThermoFisher) and goat anti-mouse (ThermoFisher) at 1:1000. Stained sections were mounted with non-hardening mounting medium with DAPI (Vector Labs). For mouse anti-PCNA and rabbit anti-SOX9, immunostaining was performed on paraffin sections with heat-based antigen retrieval; for other antibodies frozen tissue sections were used.

### 5.8.6 Measurements

Cell area and ear pinna area was measured in ImageJ using the polygon selection tool and the Measure function. Lipid droplet size distribution was measured using the *Lipid Droplets Tool* macro for ImageJ using a lower bound of $5\mu m$. Ear pinna area measurements were standardized using natural ear landmarks (apex of the antihelix) for all samples. A two-sided Kolmogorov-Smirnov test was used to analyze statistical significance between distributions.

### 5.8.7 Modified Diet Experiments

Male C57BL/6J mice were fed *ad libitum* with a high fat chow (for 39 weeks, starting at P21, or placed under caloric restriction for 72 hours with water only starting at P33. Control mice were fed *ad libitum* with normal chow for 39 weeks starting at P21. The obesity model mice (db/db) were fed *ad libitum* with normal chow for 39 weeks starting at P21.

### 5.8.8 Topical Drug Treatment

C75 (Cayman Chemical), ND-646 (MedChemExpress), and PF 05175157 (TOCRIS) were dissolved individually in DMSO at $40mmolar$, $5mmolar$, and $50mmolar$ concentrations, respectively. $20\mu l$ of either drug were painted on the ears of WT mice for 10 consecutive days, starting at P11. Changes to ear morphology were monitored daily, and final size was measured on day 10 of treatment, at P21. Control mice received topical treatment of DMSO vehicle only (VWR).

# Chapter 6

# Exploring the Origins of Meibum Lipids with SRS Microscopy

Parts of this chapter were published in 2020 in The Ocular Surface under the title *Eicosapentaenoic acid (EPA) activates* PPAR$\gamma$ *signaling leading to cell cycle exit, lipid accumulation, and autophagy in human meibomian gland epithelial cells(hMGEC)* by Kim *et. al.*

## 6.1 Meibomian Gland Dysfunction

Meibomian gland dysfunction(MGD) describes a condition in which the meibomian glands, holocrine-type exocrine glands responsible for producing the lipid-layer of the tear film, cease to properly function resulting in deformities to the tear film and functional abnormalities.[345;346] MGD can lead to ocular surface disease, discomfort, eyelid inflammation, and most importantly for this work, evaporative dry eye disease. The tear film of the eye is responsible for sustaining and protecting the eye from the environment by regulating pH, oxygen, carbon dioxide, and nutrient levels at the surface as well as protecting the eye from desiccation.[347] A diagram of the tear film is shown in Figure 6.1, used with permission from Vicnesh et. al.

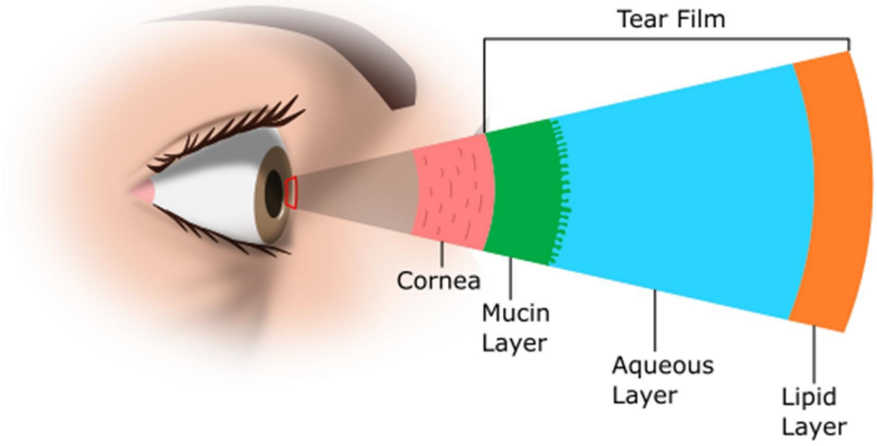



Figure 6.1: Layers of the Tear Film
The tear film forms a protective barrier over the cornea. It is composed of three layers: a lipid layer (orange), an aqueous layer (blue), and a mucin layer (green). Figure is reproduced with permission from Vicnesh et. al. 2020.[347]

Sustained disruption of any layer of the tear film can result in disease, and MGD is no different. In healthy meibomian glands, meibum (the lipid secretion) is delivered to the surface of the eye where it coats the aqueous layer preventing evaporation. The meibum secretion is primarily composed of wax esters, cholesterol, oleic acid, and cholesterol esters.[348;349] Significant changes in the secretion rate of meibum or in the chemical composition can result in disruption to the tear film and subsequent dry eye disease.[34] The mechanisms of this disruption are contested though macroscopic effects can be observed in blockages of the ducts of the glands themselves. Diagnosis of dry eye disease is usually done through assessment of the tear break-up time (TBUT), wherein the stability (or instability as the case may be) of the tear film is measured through the use of a fluorescein reporter. The break-up time is a measure of the time between last blink and the observance of a dark spot in the fluorescein distribution. Generally speaking, a TBUT less than ten seconds suggests an unstable tear film.[350]

Much work has gone into assessing the origins of both dry eye disease and meibomium gland dysfunction by multiple labs including ours.[68;199;201;214;303;351] Investigations have ranged from characterizing excised glands from rodents to humans. Various analysis of the individual components of meibum have been studied in multiple works. Cell models have been made from mouse, rabbit, and human tissues; each having its own benefits and drawbacks in gene and lipid expression. Machine learning frameworks have also assessed meibum from diseased and healthy patients. Unfortunately, each work adds a piece to the puzzle, but has failed to give a complete and conclusive model for the biochemical origins of meibomian gland dysfunction. In this work, we assess the effect of various gene pathways in meibomian cell models and attempt to provide insight into the morphogenesis of meibomian glands and the origins of their lipids.

## 6.2 PPAR$\gamma$ Signaling in Meibocytes

### 6.2.1 Introduction

As mentioned above, meibomian gland dysfunction (MGD) is a cause of evaporative dry eye disease (EDED) which commonly affects older individual or patients on Accutane therapy.[352;353] EDED patients exhibit shortened tear film break-up time, increased tear osmolarity, and corneal epithelial damage and inflammation leading to symptoms of chronic pain and discomfort that is thought to be due to the loss or atrophy of the meibomian glands with altered quantity or quality of the meibum secretions in the presence of a normal functioning lacrimal gland responsible for the aqueous layer of the tear film.[353] Despite interest and much work, knowledge regarding the molecular and cellular mechanisms controlling meibocyte differentiation and holocrine secretion are limited.

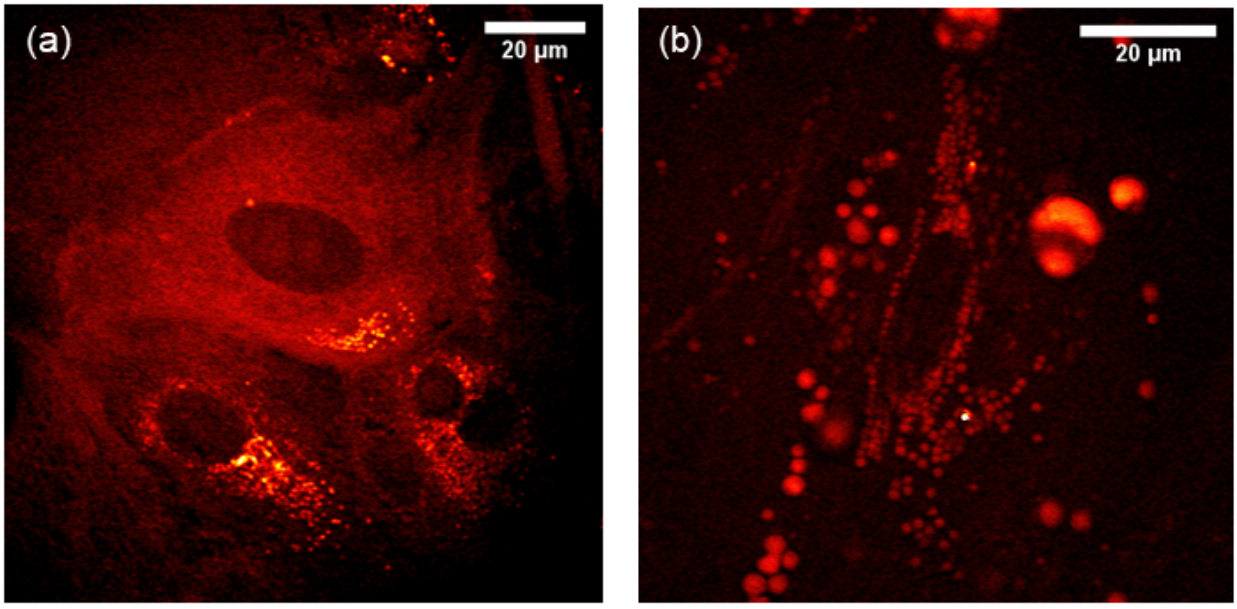



Figure 6.2: Rosiglitazone Application Leads to Lipid Accumulation
(a) control cell cultured and (b) cells treated with rosiglitazone imaged at 2840 cm$^{-1}$ with SRS microscopy. Application of rosiglitazone leads to upregulation of PPAR$\gamma$ and induces lipid accumulation.

Past work has shown that expression and post-translational modification of peroxisome pro-

liferator activated receptor gamma (PPAR$\gamma$) significantly decreases with age in both human and mouse models.[354;355] PPAR$\gamma$ is a nuclear receptor sensitive to lipid binding that regulated lipid storage and glucose metabolism. It has been referred to as the master regulator of adipocyte regulation.[356] It plays a crucial role in lipid synthesis and storage in both adipocytes and sebocytes.[357–359] PPAR$\gamma$ expression coincides with the initial synthesis of lipid around past-natal day 3.[355] Furthermore, PPAR$\gamma$ activation by the synthetic agonist, rosiglitazone, is associated with up-regulation of PPAR$\gamma$ response genes, PPAR$\gamma$ sumoylation, and cytoplasmic export leading to lipid accumulation in both cultured human and mouse acinar cells or meibocytes.[360–362] As an example, the striking morphological differences between control cells and cell culture treated with rosiglitazone is shown in Figure 6.2. These observations suggest that PPAR$\gamma$ plays an important role in the differentiation and holocrine secretion of the meibomian gland.

Although a synthetic agonist was useful to investigate the role of PPAR$\gamma$ signaling, endogenous ligands for PPAR$\gamma$ may have broader specificity and activity. Unfortunately, endogenous ligands for PPAR$\gamma$ have not been identified, although various fatty acid derivatives including eicosanoids have shown to have the ability to enhance lipid production by meibocytes in culture[363]. In this study, we hypothesized that Eicosapentaenoic acid (EPA), which belongs to omega-3 fatty acids, could serve as a PPAR$\gamma$ ligand in immortalized human meibomian gland epithelial cells (hMGEC). Previous work has shown that dietary supplementation of omega-3 fatty acids improved signs and symptoms of dry eye disease including changes in meibum quality[364;365], investigating the effect of EPA on PPAR$\gamma$ signaling and lipid synthesis in meibocytes would be valuable.

Herein, we establish that the natural PPAR$\gamma$ ligand, EPA, similar to the synthetic agonist, rosiglitazone, induces cell cyle exit mediated by decreased expression of cyclin D1 and increased expression of p21 and p27. Futhermore, both agonists lead to the accumulation of lipid that is synthesized de novo and/or transported to lipid droplets within the smooth en-

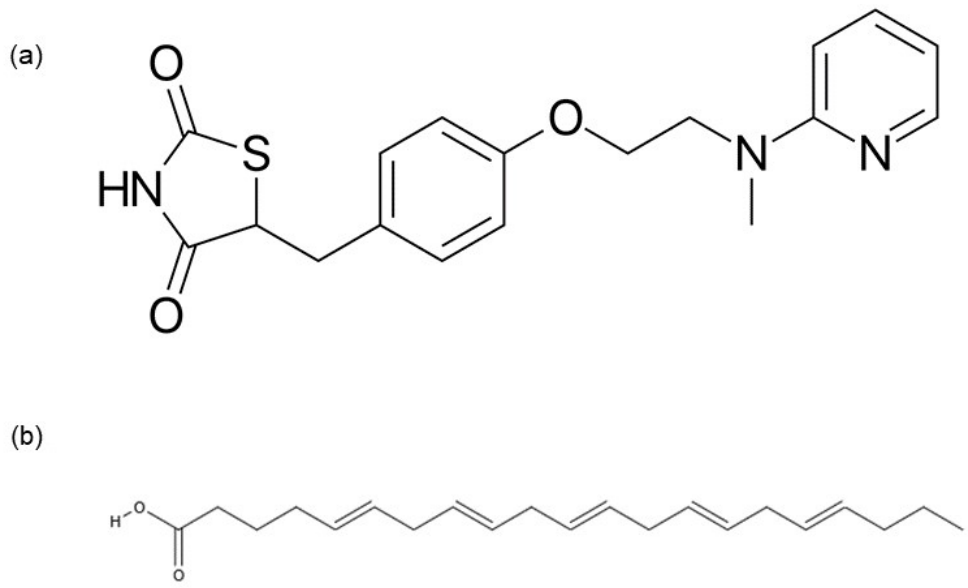



Figure 6.3: Molecular Structure of Rosiglitazone (a) Eicosapentanoic acid (b)

doplasmic reticulum(ER). PPAR$\gamma$ agonists also enhance autophagolysosome formation that appears critical for the maintenance of mitochondrial function and potentially meibocyte disintegration. Together, these finding support the hypothesis that PPAR$\gamma$ signaling controls meibocyte differentiation and lipid secretion in the meibomian gland.

### 6.2.2 EPA induced lipid accumulation via PPAR$\gamma$ signaling in meibocytes

As shown in Figure 6.4, a greater amount of lipid was accumulated in hMGECs as cells were exposed to EPA for longer times ($6d > 4d$). Furthermore, there was a dose dependent increase in lipid accumulation with increasing EPA concentration (20 $\mu$M $<$ 50 $\mu$M). To evaluate whether this lipid accumulation was dependent on PPAR$\gamma$ signaling cells were treated with a specific PPAR$\gamma$ antagonist, T0070907. While EPA significantly increased the production of lipid, pretreatment with T0070907 followed by EPA inhibited this response (Fig. 6.4 (d)), indicating that enchanged lipid accumulation by EPA was due to activation

of PPAR$\gamma$ signaling.

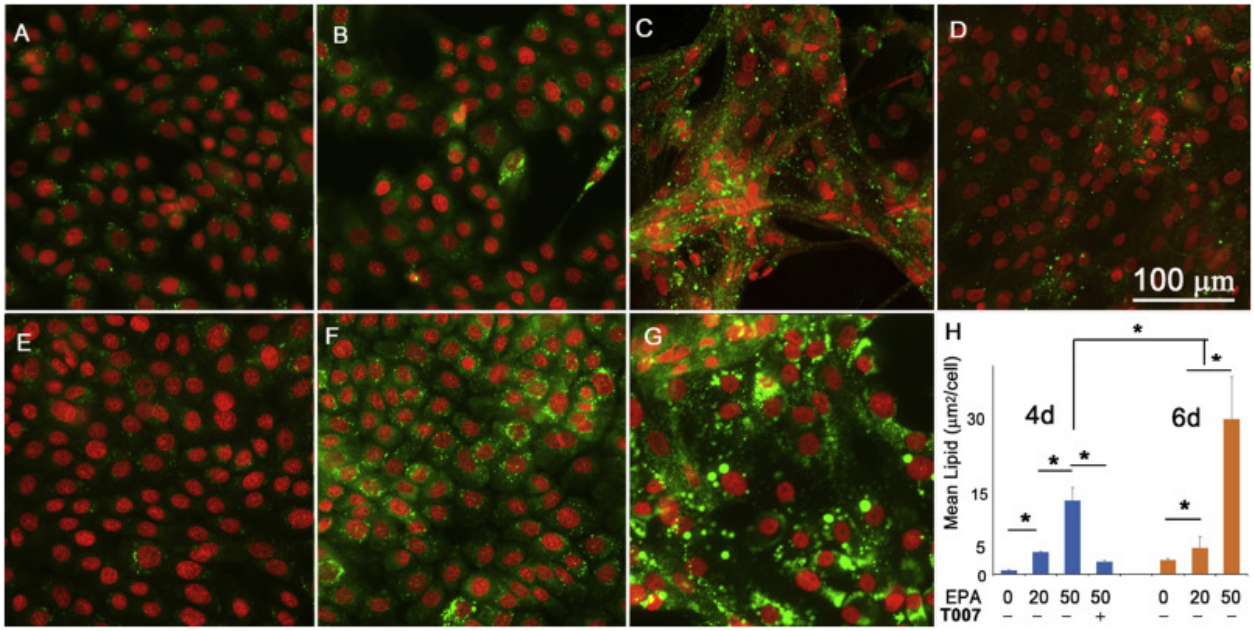



Figure 6.4: Effect of EPA on lipid synthesis in hMGEC
(A) hMGEC cultured in DMEM/F12/EGF for 4 days, (B) Cultured in DMEM/F12/EGF with 20 $\mu$M EPA, (C) with 50 $\mu$M EPA, and (D) with 50 $\mu$M EPA plus 10 $\mu$M T0070907 for 4 days. (E) Cultured in DMEM/F12/EGF for 6 days, (F) with 20 $\mu$M EPA, and (G) with 50 $\mu$M EPA. (H) Bar graph showing a significant increase of lipid synthesis in cells cultured in DMEM/F12/EGF with EPA in time and concentration dependent manners via PPAR$\gamma$ signaling (*: P ¡ 0.05).

We used stimulated Raman scattering (SRS) microscopy to evaluate the chemical composition of the lipid droplets. Hyperspectral SRS analysis allowed access to the chemical profile of the lipid inside the lipid droplets. By probing the carbon-hydrogen stretching mode, 2840 cm$^{-1}$, SRS is able to image lipid droplets in high detail.[33;37;366;367] By interrogating different Raman modes in each image, SRS was used to build hyperspectral data stacks that revealed chemical information about every pixel in a given spatial region of the sample. For this work, the spectral range between 2750 cm$^{-1}$ and 3050 cm$^{-1}$ was interrogated with $\sim$ 6 cm$^{-1}$ resolution to fully capture the Raman spectra of carbon-hydrogen vibrational dynamics. This region was particularly important as it includes information about lipid and protein content including an assessment of saturated and unsaturated fatty acids.

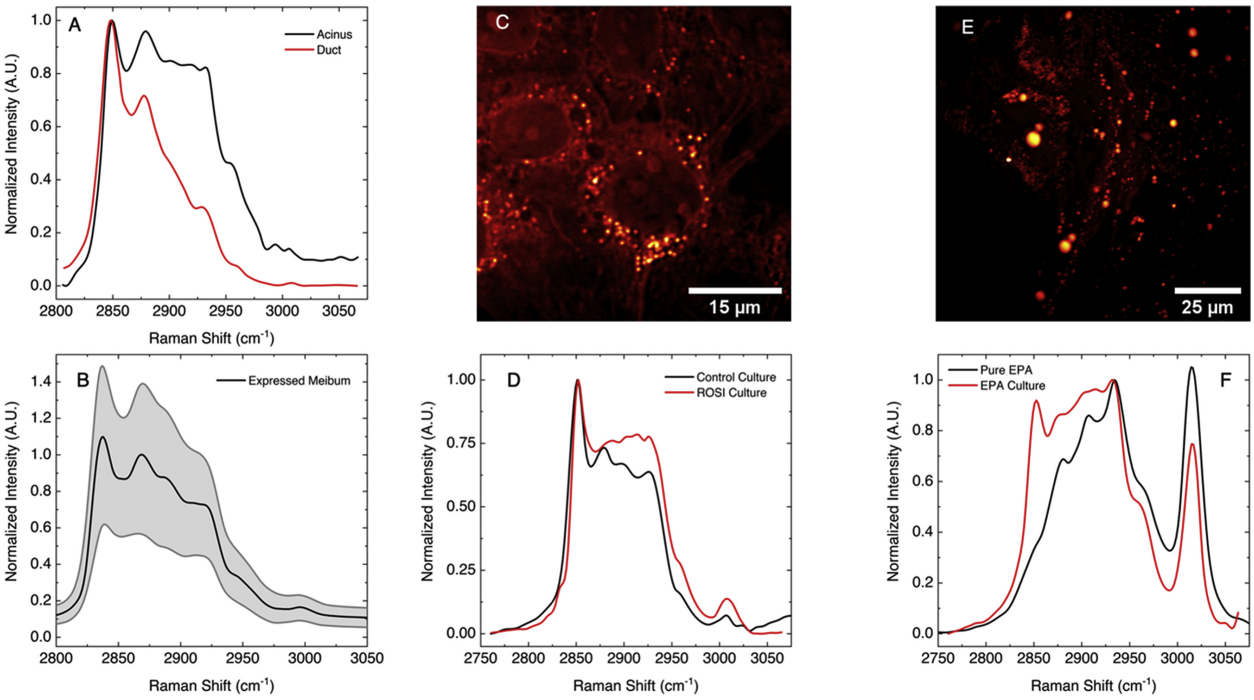



Figure 6.5: SRS Analysis of Lipid Droplet Composition in HMGEC
(A) SRS spectrum of lipids in the acinus (black) and duct (red) of an excised human meibomian gland. Data is re-plotted from Ref. Paugh et al.[214]. (B) Average SRS spectrum from expressed human meibum (black). Grey area shows the spatial variation in the smear. Data is re-plotted from Paugh et. al. (C) SRS image at 2850 $cm^{-1}$ of hMGEC cultured in DMEM/F12/EGF. (D) Average SRS spectrum obtained from 10 lipid droplets in hMGEC cultured in DMEM/F12/EGF (black) and cells exposed to Rosi (red). (E) SRS image at 2850 $cm^{-1}$ of hMGEC treated with EPA. (F) Average SRS spectrum obtained from 10 lipid droplets in EPA treated cells (red) and from pure EPA (black).

Figure 6.5 (a) shows the SRS spectrum measured at two locations in an excised human meibomian gland, one from lipid droplets in the acinus (black line) and one from the lipid in the duct (red) as produced previously.[214] The peak near 2840 $cm^{-1}$ corresponds to the symmetric $CH_2$ stretching mode, characteristic of all aliphatic lipids. The peak near 2880 $cm^{-1}$ is present mostly in samples with a high concentration of saturated fatty acids, and is thus an indication of the presence of lipids that contain such fatty acid chains. The large shoulder near 2930 $cm^{-1}$ is often interpreted as the presence of methyl stretches, which can be expected to be strong if an appreciable amount of protein is contributing to the signal collected from the focal probing volume. Comparing the SRS spectrum from lipid in the acinus and the duct, we may conclude that more protein is present at the lipid droplet locations in the

acini than what can be found at the locations in the duct, i.e. lipid-rich material in the duct is virtually devoid of protein. In Fig. 6.5 (b), the mean SRS spectrum (black line) is shown from expressed human meibum obtained from a healthy patient as reported previously.[214] The grey area shows the variation in the SRS spectrum at different locations in the meibum smear. The spectrum shows the same characteristic peaks at 2850 $cm^{-1}$ and 2880 $cm^{-1}$, as well as a shallow shoulder near 2930 $cm^{-1}$. The latter peak suggests that besides meibum lipids, non-negligible amounts of protein are present in the expressed human meibum.[34;68;214]

A representative SRS image of hMGEC control cells taken at 2850 $cm^{-1}$ is shown in Fig. 6.5(c), where the bright spots indicate the lipid droplets. 6.5(d) depicts the spectrum of lipid droplets (black line) obtained by averaging the SRS spectrum from 10 individual droplets. Peaks at 2850 $cm^{-1}$ and 2880 $cm^{-1}$ are observed, although their relative ratio differs from the SRS spectrum obtained from droplets in meibocytes in the acini of the excised gland (6.5(a)). In addition, the shoulder near 2930 $cm^{-1}$ shows a different structure. Together, this indicates that the exact lipid composition in the lipid droplets of cultured hMGEC control cells differs from the lipid composition found in meibocytes in the gland tissue.

An SRS spectrum of hMGECs exposed to rosiglitazone is also presented in Figure 6.5(d), and shows that the peak at 2880 $cm^{-1}$ is much less prominent. This is a potential indication of the lower concentration of saturated lipids. Different degrees of lipid saturation can have a profound effect on lipid fluidity, which has a strong effect on the $2870-2930$ $cm^{-1}$ vibrational energy range.[368–370] The peak near 3020 $cm^{-1}$ is attributed to the carbon-hydrogen stretching vibration of the methine (=CH-) group, providing additional evidence that unsaturated lipids are present at higher concentrations than what has been observed in expressed human meibum.

The SRS image of EPA treated hMGECs is shown in Figure 6.5(e), indicating that the size and number of the lipid droplets is increased with EPA treatment. The average SRS spectrum of lipid droplets found in hMGEC cells treated with EPA is also shown by the

red line in Figure 6.5(f). The spectrum shows some significant differences with the spectral features observed for human meibum as well as the lipid found in control and rosiglitazone treated cells. A prominent shoulder near 2950 $cm^{-1}$ is observed, as well as a very strong peak near 3030 $cm^{-1}$. The latter peak suggests a high degree of unsaturated lipids. The SRS spectrum of pure EPA is also shown by the black line in Figure 6.5(f). It can be seen that EPA exhibitys a strong peak near 2950 $cm^{-1}$ and $3030 cm^{-1}$, suggesting that a large amount of EPA has been absorbed by or transported to the lipid droplets following EPA treatment.

### 6.2.3 EPA induced upregulation of lipogenic genes by activating PPAR$\gamma$ signaling

Previously previous work demonstrates that the specific, synthetic PPAR$\gamma$ agonist, rosiglitazone (Rosi), upregulates the expression of PPAR$\gamma$ response genes related to lipid synthesis at the transcriptional level.[361;362] In this experiment the effects of EPA were evaluated, on expression of PPAR$\gamma$ response genes. As shown in Figure 6.6, EPA significantly upregulated mRNAs in hMGEC encoding PLIN2 (Fig. 6.6(a)), ELOVL4 (Fig. 6.6(b)), and SOAT1 (Fig. 6.6 (d)) by 2.7, 3.0, and 2.1 folds on average after 2 days respectively, and by 4.7, 2.4, and 3.2 folds after 4 days, respectively. These effects were blocked by the addition of the PPAR$\gamma$ antagonist, T0070907 (*: $P < 0.05$).

### 6.2.4 EPA and rosiglitazone induced cell cycle exit of meibocytes

To evaluate whether EPA induces cell cycle exit similar to that previously observed for for the specific synthetic PPAR$\gamma$ agonist, Ki-67 labelling was examined after treatment with EPA. Ki-67 is a nuclear protein that is a marker of cells undergoing cell division.[371] As shown in Figure 6.7, about 24% of hMGECs cultured in control, differentiation media containing

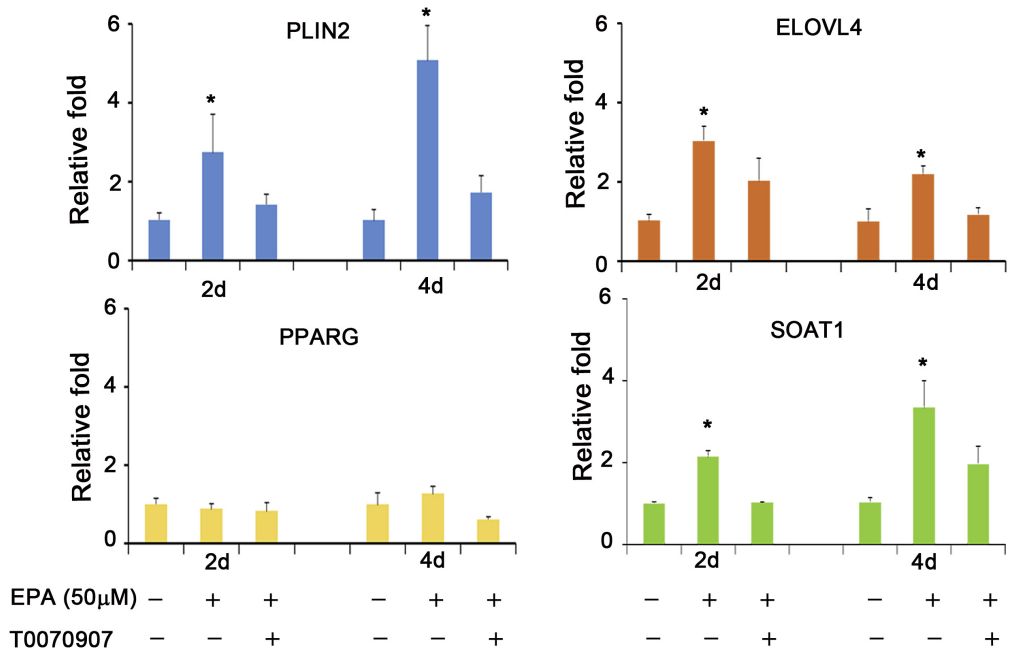



Figure 6.6: Effect of PPARγ Signaling on mRNA expression.
EPA significantly upregulated expression of (A) PLIN2, (B) ELOVL4, and (D) SOAT1 by 2.7, 3.0, and 2.1 folds on average after 2 days, and by 4.7, 2,4, and 3.2 folds after 4 days, respectively (*: P ¡ 0.05) in hMGEC. A PPARγ antagonist T0070907 significantly abrogated EPA-induced upregulation of these genes to the similar level with control group.(C) PPARG mRNA expression was not significantly altered by EPA treatment.

DMEM/F12 with EGF showed positive labeling by Ki-67 (Fig. 6.7(a)). By comparison, cells treated with EPA showed significantly reduced Ki-67 labeling after 4 days in culture (Fig. 6.7(b)), and this effect was significantly reversed by the addition of the specific PPARγ antagonist T0070907 (Fig. 6.7(c)). Together, these data (Fig. 6.7(d)) indicate that EPA induces cell cycle exit mediated by PPARγ receptor signaling, a similar finding to that of the synthetic PPARγ agonist, Rosi.[361] Further research on cell cycle proteins was examined through the use of western blotting. These results are presented in the published work.[201]

### 6.2.5 Discussion

This work expands upon previous studies of the role of PPARγ in regulating meibocyte differentiation[361], and evaluates the effect of the natural PPAR ligand, EPA, that broadly

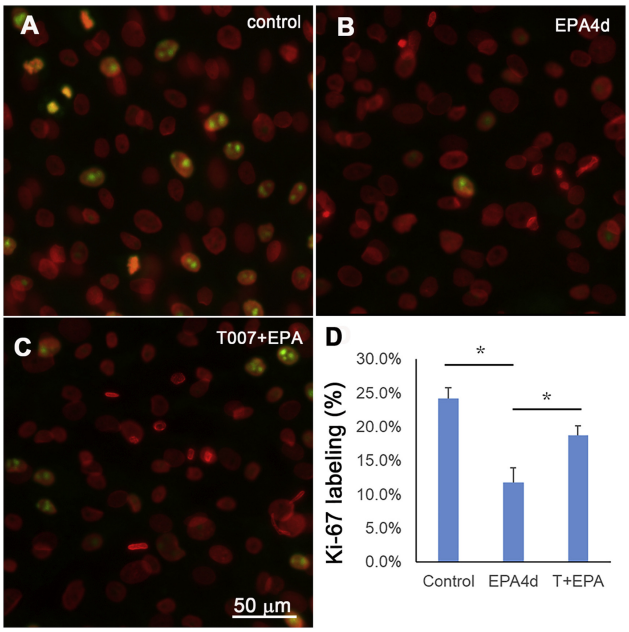



Figure 6.7: Effect of EPA on Ki-67 labeling in cultured hMGEC.
(A) Control cells, which were grown in DMEM/F12 with EGF for 4d showed about 24% positive labeling (green) and (B) EPA treatment induced a significant reduction of Ki67 labeling. (C) Co-treatment of PPAR$\gamma$ antagonist T0070907 with EPA showed a similar labelling to control. (D) Bar graph showing Ki-67 labeling index (*: P ¡ 0.05).

activates PPAR signaling through $\alpha$,$\beta/\delta$ and $\gamma$ isoforms[363;372]. In this study we confirm that EPA, through specific PPAR$\gamma$ receptor signaling induces cell cycle exit, lipogenic gene expression and the accumulation of neutral lipids, similar to that of the specific, syntheticPPAR$\gamma$ agonist, rosiglitazone [10]. While little is known regarding control of meibocyte cell growth and differentiation, this process has been extensively studied in adipogenesis where PPAR$\gamma$ agonist have been shown to induce the later stages of adipocyte differentiation through up-regulation of cyclin kinase inhibitors (CKI) and adipocyte specific genes, where these are molecularly linked to ensure irreversible terminal differentiation.[373] Our findings that EPA up-regulates p21/Kip1 and p27 Waf1/Cip1 are consistent with that of CKIs that are up-regulated by PPAR$\gamma$ in adipocytes. While there are unique differences between these two cell types, as one stores and the other secretes lipid, these findings suggest that there are parallels between these two cells regarding the molecular program regulating cell differentiation.

Regarding the expression of lipogenic genes by EPA, PLIN2, ELOVL4 and SOAT1 were

shown to be up-regulated. PLIN2 is a lipid droplet associated protein considered to be a maker of lipid accumulation in various tissues.[362;374;375] PLIN2 stimulates the uptake of long chain fatty acids that represent a prominent component of meibum lipids. Higher level of expression has been observed in more mature meibocytes located toward the center of the acini and it was hence suggested to be a differentiation marker for mature meibocytes.[376] ELOVL4 and SOAT1 are known to play important roles in meibum lipid synthesis and are necessary to synthesize very long chain fatty acids and cholesterol ester, respectively.[377] Considering that these very long chain lipids and cholesterol esters are major meibum lipid species, modulation of ELOVL4 and SOAT1 expression by PPAR$\gamma$ signaling could have relevant clinical implications in the development of MGD. Overall, these findings indicate that transcriptional up-regulation of these genes are dependent on PPAR$\gamma$ receptor signaling. By comparison, EPA treatment did not change expression of PPARG, a different finding from rosiglitazone treatment described in our previous study.[361] This data indicates that each natural PPAR ligand may not show exactly the same response as that obtained by specific, synthetic PPAR$\gamma$ agonists.

Additionally, our findings regarding the effects of EPA on hMGEC are consistent with those reported by Hampel et al., who evaluated the effects of both docosahexaenoic acid (DHA) and EPA in combination, showing synergistic effects at a concentration of $100\mu M$ each that peaked 24 h after treatment.[378] Our findings are different in that EPA alone at lower doses than those used by Hampel, produced significantly increased accumulation of neutral lipid that increase in size and number from 4 to 6 days, compared to the decreasing effect at 72 h detected by Hampel et al. This difference is likely due to the different differentiation culture conditions used.[379–382] First, serum was removed from the differentiation media to eliminate serum lipids and other factors that could influence cell differentiation. This elimination of serum required the addition of lipid free albumin to act as a lipid carrier for EPA, as fatty acids alone are cytotoxic. It is interesting to note that our more pronounced and prolonged effect on lipid synthesis suggests that serum, while showing some ability to induce differen-

tiation of hMGEC,[381;382] also contains factors that are potentially inhibitory for meibocyte differentiation. Further study of these effects may help in understanding the overall value of these cells to probing the molecular mechanisms of meibocyte differentiation.

While EPA was shown to significantly enhance lipid droplet accumulation, probing of the lipid contents using SRS microscopy failed to show a similar Raman profile to that detected in meibum from human eyelids or excreta.[214] Unfortunately, SRS cannot specifically identify individual lipid classes; however, our findings are consistent with earlier reports indicating that hMGEC lipids do not resemble those normally identified in expressed meibum.[379;380;383] As we have previously reported, several lipogenic genes are not expressed by hMGECs in culture and are not up-regulated following treatment with either rosiglitazone or EPA.[362] Of particular note is the loss of AWAT 1/2 expression, which is a critical enzyme required for the synthesis of wax esters that represent 40% of the total meibum neutral lipids.[377] The failure of PPAR$\gamma$ activation to induce expression of this enzyme suggests that meibum specific lipid synthesis is not fully controlled through PPAR$\gamma$ signaling and that additional complex signaling cascades as yet to be discovered may be involved in complete meibocyte differentiation.

SRS did show that lipids droplets accumulated in hMGEC when treated with either Rosi or EPA, indicating that there is both *de novo* lipid (DNL) synthesis and transport of lipid into the accumulating lipid droplets. Since treatment of hMGEC with Rosi alone was not in the presence of serum, the only source for the accumulation of lipids would be DNL through fatty acid synthesis. However, the SRS analysis of lipid droplets in EPA treated cells suggested the presence of EPA within the droplets. As SRS has a voxel resolution of $1\mu m^3$, it is not likely that this signal was obtained from extracellular lipid. The fact that meibocytes in culture can synthesize DNL meibum was first established for bovine meibomian glands[384], and later for rabbit meibomian glands.[385] A more recent report, however, suggests that meibomian glands predominantly use circulating lipids for biosynthesis of meibum.[386] This is in distinct

contrast to that of sebaceous glands that rely predominantly on DNL. Further study of lipid synthesis is needed to confirm these unique differences between meibomian and sebaceous glands.

### 6.2.6 Study specific materials and methods

#### Cultivation and differentiation of meibocytes

Immortalized human meibomian gland epithelial cells (hMGEC), a gnerous gift from Dr. Sullivan (Schepens Eye Research Institute), were grown in Keratinocyte Serum Free Media (KSFM, Invitrogen-Gibco, Grand Island, NY) as previously described.[361] At 80% confluence, differentiation was induced by culturing cells in DMEM-F12 (Gibco, Grand Island, NY) supplemented with Epidermal Growth Factor (EGF, 10 ng/ml, Sigma) and Bovine serum albumin (fatty acid free-BSA, 3 mg/ml, Sigma) with or without PPAR$\gamma$ agonist, rosiglitazone ($30\mu M$, Sigma, St. Louis, MO) or EPA ($20-50\mu M$, Sigma). EPA stock was prepared as a solution in ethanol and aliquoted at $-20^{\circ}C$ in tightly sealed vials in the dark. Further dilutions of the stock solution into pre-warmed DMEM/F12 media containing fatty acid free albumin was made prior to media change and a fresh preparation is used for experiments. For PPAR$\gamma$ signaling studies, a specific PPAR$\gamma$ antagonist, $10\mu M$ of T0070907 (Tocris, Minneapolis, MN) was added 1 h prior to EPA treatment.

#### RNA isolation and lipogenic gene expression

The expression of 4 PPAR$\gamma$ lipogenic response genes were evaluated including Perilipin 2 (PLIN2, NM_001122), elongation of very long chain fatty acid 4 (ELOVL4, NM_022726), peroxisome proliferator activated receptor gamma (PPAR$\gamma$, NM_138712), and Sterol O-acyltransferase (SOAT1, NM_001252511). Expression was measured using the quantitative

real-time PCR as previously reported.[361] Relative quantification was performed using the Comparative Ct method using GAPDH as the normalizing housekeeper gene.

**Assessment of cell cycling and lipid production**

For immunostaining, hMGEC were cultured on glass coverslips pre-coated with 10% bovine collagen I (Purecol, Advanced BioMatrix, Carlsbad, CA). After achieving 80% confluence, cells were exposed to $50\mu M$ EPA for 4–6 days and then fixed in 2% paraformaldehyde. Cells were then stained with antibodies to Ki67 (Abcam, Cambridge, MA) to determine the effect of EPA on cell cycling, and LipidTox (Invitrogen, Carlsbad, CA) to assess lipid synthesis as previously described.[355]

**Live imaging of ER, lysosome, autophagosome, and lipid droplets**

To explore intracellular localization of lipid droplets with subcellular organelles, after differentiation with rosiglitazone or EPA, lipid droplets were co-stained with BODIPY 493/503 and ER-Tracker or LysoTracker following the manufacture's (Molecular Probes) instruction.

**Stimulated Raman spectroscopic analysis of meibocyte lipids**

Cells were seeded onto 35 mm glass bottom well plates and after reaching 80% confluence were exposed to $50\mu M$ EPA or $30\mu M$ Rosi for 5 days. Cells were then washed and fixed with 2% paraformaldehyde. After fixation, cell samples were imaged with a homebuilt SRS microscope discussed in detail in previous chapters. Each sample was kept in saline buffer prior to and during imaging. Images were acquired with $10\mu s$ pixel dwell times and with 10 averages to improve signal-to-noise. Once a region of the samples with many cells was identified, hyperspectral data was acquired. Multiple image stacks were acquired from different

areas of each culture sample. Image analysis was carried out in Fiji and spectral data was analyzed using Origin and Matlab.[387]

**Statistical analysis**

All numeric results are reported as mean ± standard error. Differences between groups were assessed by Kruskal-Wallis one-way analysis of variance on ranks and Tukey multiple comparisons (Sigma Stat version 4.0, Systat Software Inc, Point Richmond, CA). All experiments were repeated at least 3 times and a P value of $< 0.05$ was considered statistically significant.

### 6.2.7 Conclusions

The work above demonstrate that PPAR$\gamma$ activation, induced by both rosiglitazone and EPA, leads to cell cycle exit, lipid production and accumulation, and autophagy during differentiation. While in this work, we did not discuss the experiments addressing autophagy, a full writeup may be found in the published work.[201] Given that PPAR$\gamma$ signaling has a significant effect on lipid production, transport, and storage in meibocytes and that the literature is unclear as to a preference between serum lipid uptake vs. *de novo* lipgenesis, further research into this area should be conducted.

## 6.3 *De Novo* Lipogenesis and Lipid Uptake in Meibogenesis

### 6.3.1 Introduction

Following on the work in Section 6.2, we wanted to further examine the origin of lipids produced by meibocyte cells in culture. In section 6.2.5, it was mentioned that the literature is conflicting as to whether meibomian glands predominantly use *de novo* lipogenesis or circulating lipids for lipid synthesis. *De novo* lipogenesis has been established in both bovine and rabbit meibomian glands.[384;385] However, Esler et. al. claim that meibum is primarily formed from transport of serum lipids.[386] Numerous methods including various forms of mass spectroscopy have been employed to address this question. We hypothesized that stimulated Raman scattering microscopy coupled with deuterium tags would provide direct evidence of one or both processes.

As discussed in Chapters 4 and 5, spectral tracing of deuterium labeled carbon with stimulated Raman scattering microscopy is a powerful tool for following metabolic pathways.[34;40;41;388] Using this technique various labs have demonstrated metabolic tracing of amino acids into protein, cholesterol storage, and conversion of glucose to many different other molecules. Figure 6.8 from Zhang et. al. demonstrates how deuterium from small precursor molecules can be incorporated through a number of different biochemical pathways.[40] Given the success we experienced with this technique while working with lipochondrocytes, it was a natural step to take in our studies on meibum. The first step of which was to assess a number of deuterated precursors for absorption into cell culture.

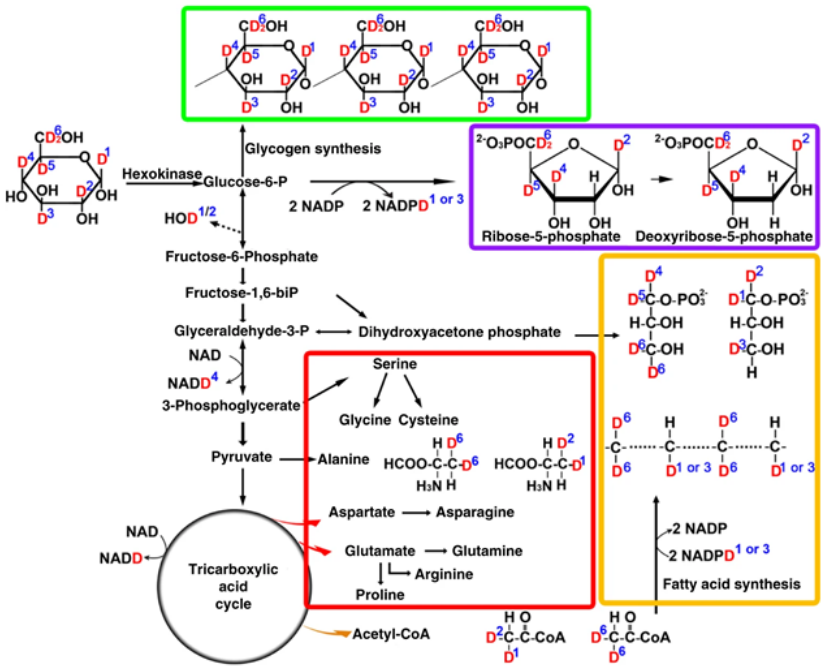



Figure 6.8: Deuterium Transfer Along Major Biosynthetic Pathways
Labeling of small precursor molecules such as glucose with deuterium allows for transfer along several biosynthetic pathways. Used with permission from Zhang et. al.[40]

### 6.3.2 Assessment of Uptake of Deuterated Precursors

With numerous sources disagreeing about the source of lipid in meibum glands and meibocyte models, we decided to test a number of different deuterated compounds for for metabolic tracing. Based on knowledge of the metabolic pathways for glucose in general but particularly for fatty acids, four deuterated compounds were chosen: $D_7$-glucose, $D_3-$acetate, $D_5$-eicosapentaenoic acid, $D_{31}$-palmitic acid. The structure of each molecule is shown in Figure 6.9.

In this study, glucose was chosen as it acts as a precursor for *de novo* lipogenesis through the glycolytic metabolic pathway. However, it does present some challenges as it is used a precursor for biosynthesis of many classes of molecules, not just lipids. In our imaging studies, therefore, we would expect to see some deuterium labeling across the cells in protein, nucleic acids, and amino acids, among others. The full spontaneous Raman spectra for $D_7$-glucose is

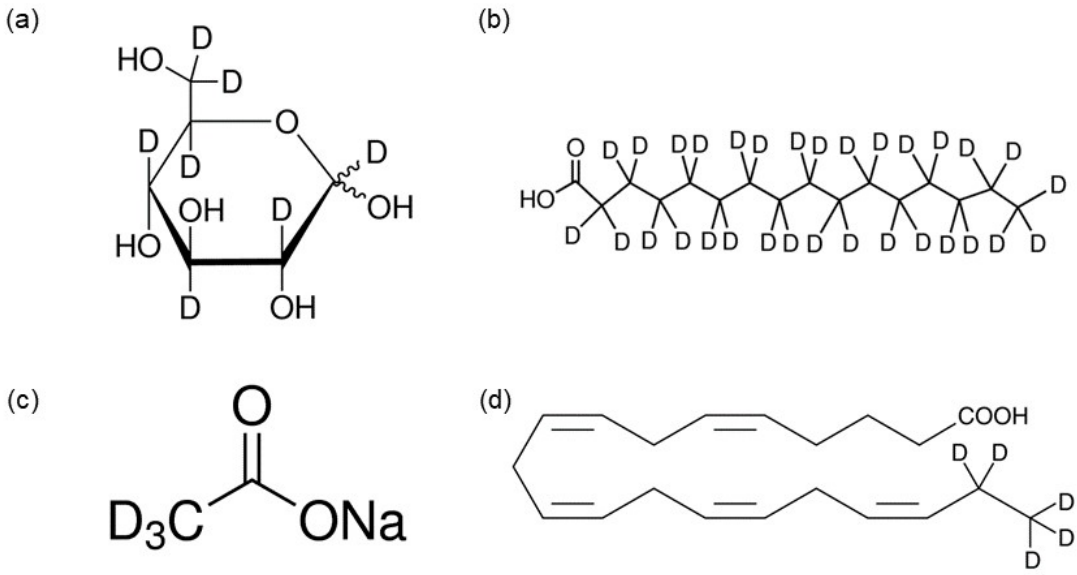



Figure 6.9: Structure Diagrams of Deuterated Molecules
(a) $D_7$-glucose, (b) $D_{31}$-palmitic acid, $D_3-$acetate, $D_5$-eicosapentaenoic acid

shown as the black line in Figure 6.10(a) and a zoom-in on just the carbon-deuterium modes are shown in (b) with the Raman shift of the most intense peak annotated. It is important to note that in the general case, fully deuterated molecules will not be synthesized as many non-deuterated carbons will be available from various sources in the cell and media. This greatly decreases the number of oscillators present in each Raman measurement.

Rabbit derived meibocytes were cultured to near passage before the addition of the deuterated glucose. Cells were treated for seven days with either 0.2% (w/v) or 0.3% (w/v) deuterated glucose. The media changed every two to three days. We are grateful to the laboratory of Dr. James Jester for access to this novel cell line. The full protocol is found later in this chapter. An important consideration that likely impacted this experiment is that $D_7$-glucose is supplemented into the media, but does not supplant the protonated glucose. The specialized media needed to maintain these cells is not available in a glucose free version. Thus, compared to literature and to our work on lipochondrocyes it is expected that a lower CD signal will be detected in this cell culture.

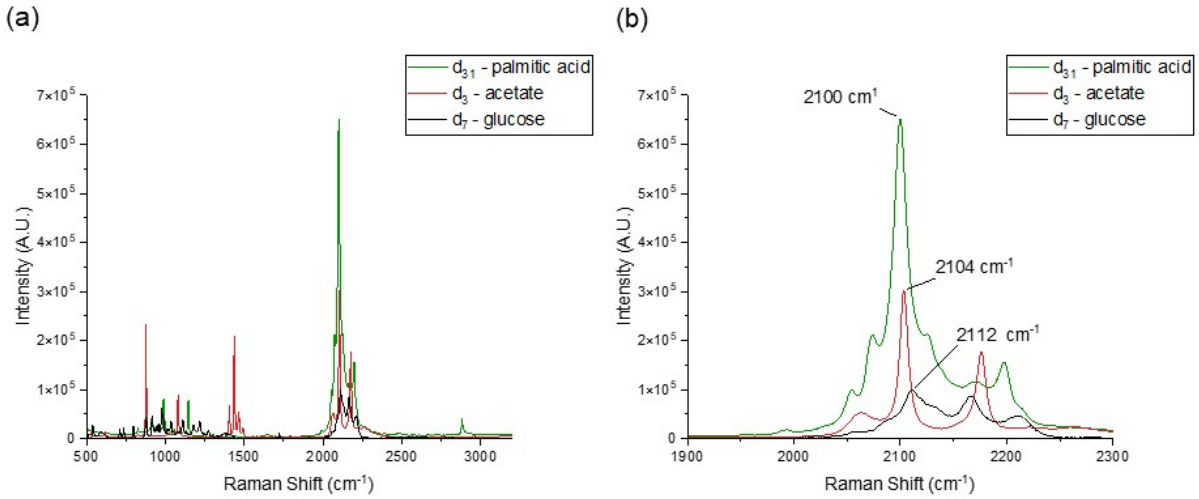



Figure 6.10: Spontaneous Raman Scattering Spectra of Deuterated Compounds (a) overview spontaneous Raman spectra of deuterated glucose, acetate, and palmitic acid. Nearly complete deuteratation leads to almost complete elimination of the vibrational modes usually found around 2900 cm$^{-1}$. (b) Cell-silent region of the Raman spectrum. Deuteration creates signal in an otherwise silent region centered around 2100 cm$^{-1}$.

Figure 6.11 shows representative results of our imaging attempts with meibocytes cultured in deuterated glucose. In an attempt to maximize the signal acquired, a rather long pixel dwell time was used, 110 $\mu$s for the carbon-deuterium contrast image. Additionally, the lock-in amplifer was set to a high gain. Images (a) and (c) are the usual SRS image taken at 2840 cm$^{-1}$ where contrast can be assigned to mostly lipids. The upper row images (a) and (b) are from the 0.2% $D_7$-glucose treated cells, while the lower row (c) and (d) are from the 0.3% $D_7$-glucose stock. For the carbon-deuterium images, an on-resonance image was acquired at 2140 cm$^{-1}$, chosen by varying the acquisition wavelength to find a peak, and an off-resonance image was acquired at 2435 cm$^{-1}$. The off-resonance signal was subtracted from the on-resonance signal in order to remove the background from the image.

As is somewhat evident from the first two images, the treatment with deuterated glucose yielded very weak albeit positive signal. Prior to processing and optimization in ImageJ, the 0.2% sample has a signal to noise ratio (SNR) of only 2:1 at 2140 cm$^{-1}$ whereas in the lipid

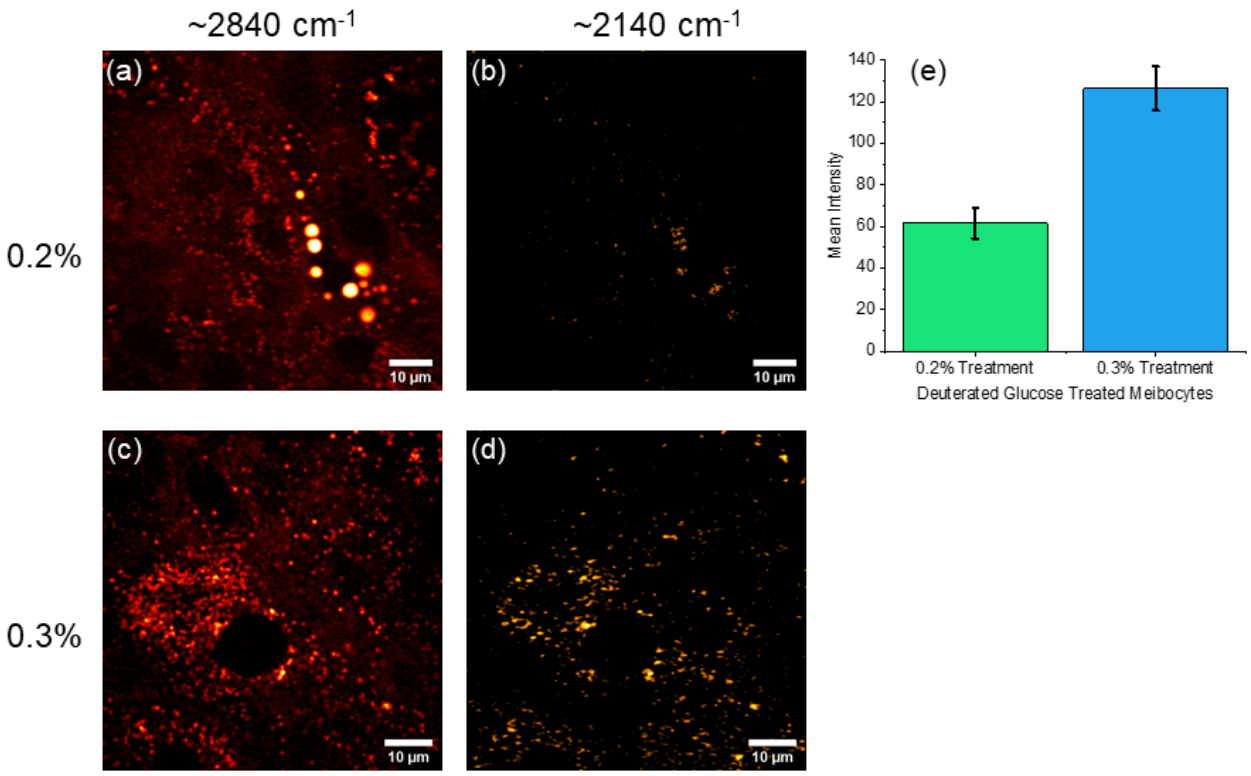



Figure 6.11: Deuterium Incorporated from Deuterated Glucose
(a) RB-14 meibcytes culuted with 0.2% $D_7 - glucose$ imaged at 2840 cm$^{-1}$ where lipids provide a strong contrast. (b) The same area imaged at 2140 cm$^{-1}$ where signal corresponds to carbon-deuterium oscillators. (c) RB-14 cultured in 0.3% glucose imaged at 2840 cm$^{-1}$. (d) Carbon deuterium signal at the same area as (c). (e) Analysis of 2140 cm$^{-1}$ signal in 5 lipid droplets in each image shows greatly enhanced signal from a small increase in deuterated glucose concentration indicating a threshold effect.

image at 2840 cm$^{-1}$ the SNR is closer to 10. In order to improve the quality of the image, the smooth function, a rolling average algorithm, in ImageJ was used.[387] The processed image is shown in Fig. 6.11(b). Increasing the applied concentration of deuterated glucose did show improved, but still weak signal as shown in Fig. 6.11(d). To quantify the difference, the mean grey value of five of the brightest droplets was calculated for each image. The mean is shown in the bar graph, Fig. 6.11 (d). The standard deviation is given as the error bars in the plot. This result points to the likely-hood that at 0.2% the concentration of C-D oscillators is in many points very close to or below the detection limit for our microscope. In SRS spectroscopy and microscopy, the signal is linearly dependent on the concentration

of oscillators in the focal volume. In this case, however, we see a much larger increase in signal compared to the increase in glucose concentration. It is plausible that this increase was enough to boost signal into the detectable regime.

As a second check for *de novo* lipogenesis, $D_3-$Na-acetate was chosen. A number of studies over several decades have shown that Na-acetate is used as a substrate for lipogenesis.[389–392] The protocol for exposure to acetate was the same as for glucose above. Cultures were initially exposed to three separate concentrations of deuterated acetate: 1 $\mu$M, 10 $\mu$M, and 100 $\mu$M. We hypothesized that if the meibocytes utilize *de novo* lipogenesis then deuterated carbon from acetate will be incorporated into the lipids.

As with $D_7$-glucose cells, carbon deuterium images were taken at 2840 cm$^{-1}$ for on-resonance and an off-resonance image was taken at 2435 cm$^{-1}$. In this case images were taken with a 50 $\mu$s pixel dwell time and 10 acquisitions were used in a Kalman filter. No signal was detected with sSRS microscopy at 1 $\mu$M $D_3-$acetate. However, at 10 $\mu$M, and 100 $\mu$MM appreciable signal was detected as shown in Figure 6.12. For the 10 $\mu$M sample, signal was present, but it was very faint (Fig. 6.12(a, b). It was necessary to use smoothing filter with adjustments to contrast in order to easily recognize signal that corresponded to the droplets in the C-H image.

At a 100 $\mu$M concentration of $D_3-$acetate the SRS signal became significant. C-H images are shown in Figure 6.12 (c, e). C-D images are given by Fig. 6.12(d, f). It was no longer necessary to apply a smoothing filter to images to identify droplets incorporating C-D oscillators. Additionally, the droplets much more clearly co-localize to the lipid droplets of the C-H images. We were concerned about this level of acetate effecting cell viability, however, LipidTox staining revealed no obvious markers of cytotoxicity.

Given our previous result that EPA appeared to be sequestered within lipid droplets, it is perhaps not surprising that we chose to examine it here as well. Culture conditions were the

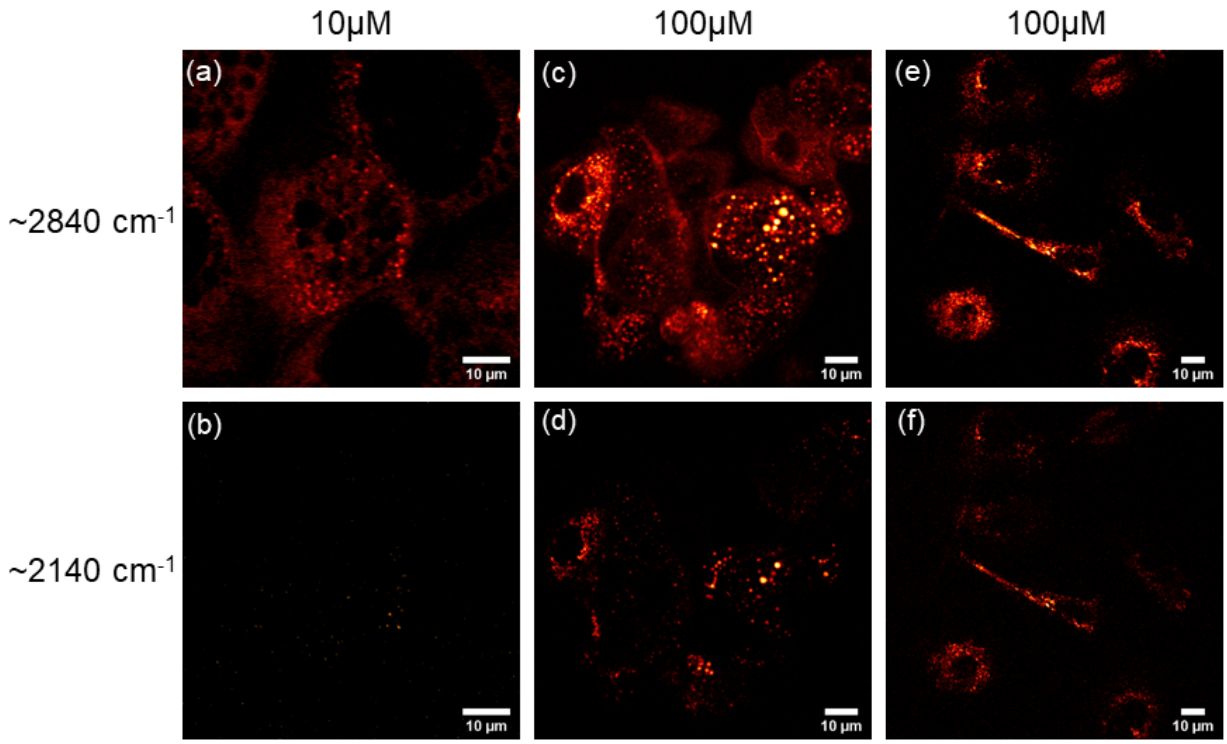



Figure 6.12: SRS Imaging of Deuterium Incorporated from Deuterated Acetate
10 $\mu$M of $D_3$ acetate produced limited signal in lipid droplets as shown in (b). Images (a, c, e) show the C-H lipid signal in SRS microscopy for the corresponding area below. (d, f) at 100 $\mu$M concentration the deuterium signal greatly increases and spatially overlaps with the lipid signal.

same as above with the addition of 50 $\mu$M $D_5$-EPA as per specifications in 6.2. In using EPA, our major goal was to form another check on our previous results. As EPA is incorporated into lipid droplets, a carbon-deuterium signal should become apparent. Assuming that the cells in culture are not starved, the detection of the deuterium signal in the lipid droplets would suggest full incorporation of the EPA. The EPA molecule itself has very few deuterons for its molecular weight. The images in Figure 6.13 show an example of this work. I would like to thank Yong Li for aiding in the imaging process for these cells as part of his graduate training.

As can be seen in both cases, there is a fairly strong carbon-deuterium signal that overlaps with many of the lipid droplets shown in the methylene images in the top row. Notably,

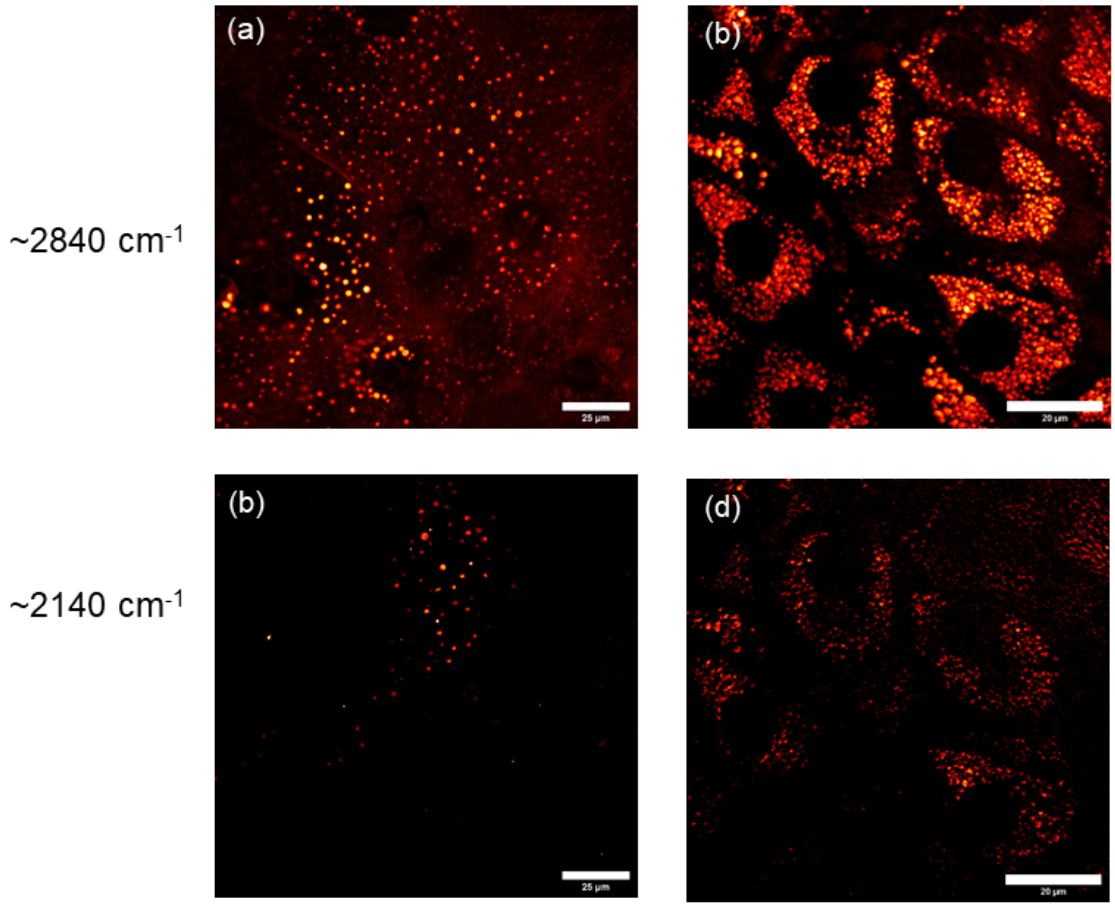



Figure 6.13: SRS Imaging of Deuterium Incorporated from Deuterated EPA
SRS images of RB-14 cells imaged with CH contrast ( 2840 $cm^{-1}$ (a, b) and with CD contrast 2140 $cm^{-1}$ (c, d). Images (a, c) and (b, d) are from the same spatial areas but different replicates of D-EPA exposed culture.

the treatment with EPA showed the expected results from our previous work. There is a significant presence of lipid droplets accumulating in the cells. The detection of the carbon-deuterium bond in the lipid droplets suggests that EPA is trafficked into the lipid droplets. While the inclusion of EPA alone, is not enough to rule out *de novo* lipogenesis, it does seem to indicate lipid uptake is happening in the cells and that EPA is being stored as any other neutral lipid.

The preceding results show that RB-14 meibocytes are capable of uptake of glucose and acetate as precursor molecules and catabolizing them for energy storage. The inclusion of EPA suggests that the cells are capable of storing it as well, however, as demonstrated in

the previous work EPA works to upregulate PPAR$\gamma$ signaling and stimulate the production of lipids. If the cells uptake circulating lipids as well, the upregulation caused by EPA could stimulate the cells into increased uptake.

To test the uptake of less complex fully saturated fatty acids, we exposed the cells to palmitic acid (Fig. 6.9(b)). Palmitic acid is the most common fatty acid and appears in the human body through both diet and lipogenesis.[393] Additionally, it may be important in meibogenesis as it has been shown that levels of palmitic acid are lower in patients with MGD.[394;395] Thus, if palmitic acid is shown to be taken up by the meibocyte model, it may indicate that fatty acid metabolism is an important component of the MGD disease model.

As before, rabbit derived meibocytes were cultured to near passage and treated with 50 $\mu$M palmitic acid for seven days. At 100 $\mu$M concentration, palmitic acid proved cytotoxic and cells could not grow. Neutral lipids are known to be toxic at high enough concentration, and LipidTox staining was performed to check against neutral lipid accumulation. Because of the threat of lipid toxicity, neutral lipids must be mixed with a carrier and in all the cases above Albumax (Gibco) was used. Albumax is a proprietary blend of lipid rich bovine serum albumin.

Figure 6.14 shows representative results from SRS imaging of cells treated with $D_{31}$-palmitic acid. The boxed area in (a) is shown in a second image taken with a higher magnification in (b), and the same area as (a) is shown with the methylene stretch contrast in (c). It is interesting to note that in these samples there was very low signal produced by the C-H signal generally attributed to lipids. However, it is not possible to say conclusively that this is due to primary uptake of deuterated palmitic acid. It is possible that palmitic acid may have changed the lipid expression in these cells.

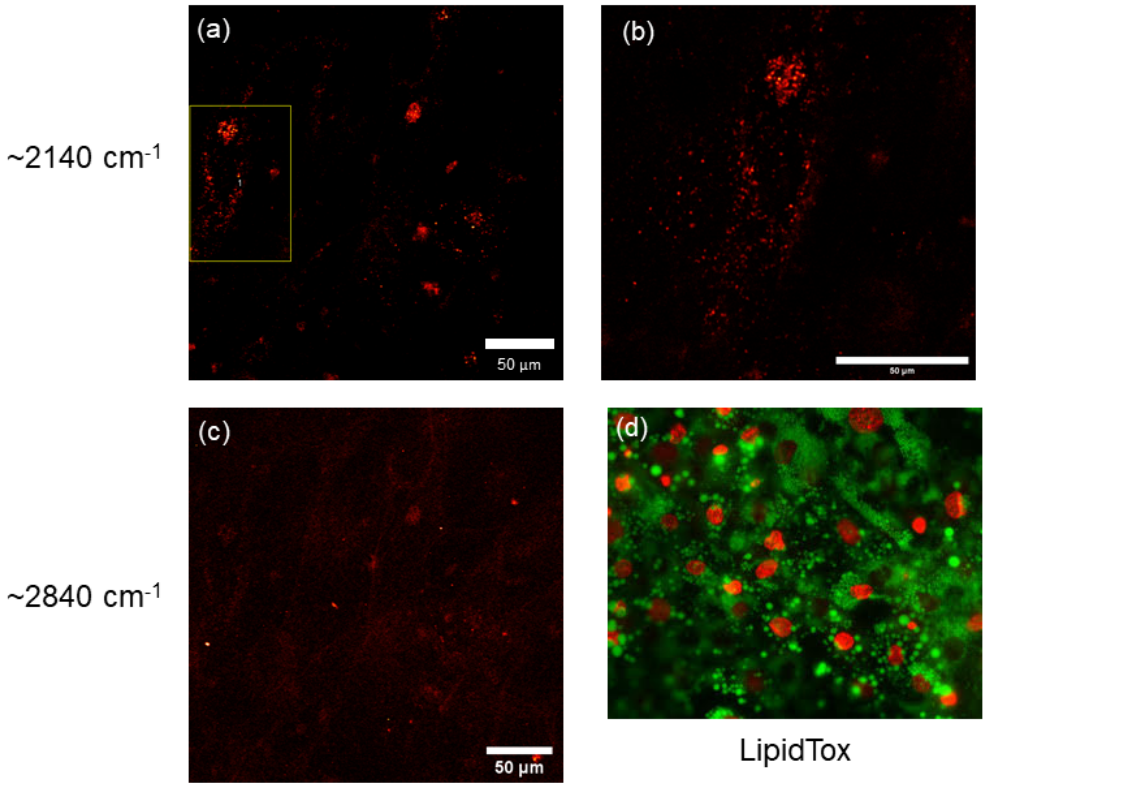



Figure 6.14: SRS Imaging of Deuterium Incorporated from Palmitic Acid
(a,c) Wide area image of RB-14 meibocytes cultured in deuterated palmitic acid. Image (b) is an image taken at greater magnification from the yellow square in image (a). (d) LipidTox staining and fluorescent imaging from RB-14 cells from this replicate. Lipid droplets are present, but not toxic at these concentrations.

### 6.3.3 Acetate or Lipid

At this point, I should note that this portion of our study is still ongoing as of writing. Imaging of one replicate has been completed, but encountered difficulties in instrumentation and culture. I present preliminary data here, but will generally be unable to draw statistically significant conclusions from it. I would also like to thank graduate student Yong Li who has been my partner in carrying out this work.

The results in the previous section, suggest that it is possible for meibocytes to use both

lipid uptake and *de novo* lipogenesis for production of lipid droplets. This is perhaps not a surprising result as literature has suggested both individually.[384–386] After this result, we sought to simplify our experiment in order better assess meibogenesis.

As was discussed in Section 6.2, the culture conditions are highly influential on the production of lipids in meibocytes. In all culture conditions, it was necessary to remove serum (commonly bovine serum albumin), as the fatty acids and other lipids can act on PPAR$\gamma$ and influence the lipodome of the cells.[382] Additionally, work has shown that serum can influence keratinazation of the cells.[396] Conversely, serum can have a detrimental affect on differentiation among other effects.[381;382] Originally, serum was replaced with lipid free albumin. However, in latter experiments, including the ones just discussed, Albumax was used, which as noted is a lipid rich albumin. We conjectured that this might be having an influence on the RB-14 cells. In the second round of experiments we chose to use only $D_3$-acetate and $D_{31}$-palmitic acid as our metabolic probes. We decided to compare culture with and without Albumax given the potential of unwanted signaling from the unknown lipids in it. The additional culture conditions are summarized in Table 6.1. In order to promote formation of lipid droplets rosiglitazone was added as a second experimental factor as it is the most studied PPAR$\gamma$ signaling molecule to date.

| 100 $\mu M$ Acetate (D3) | 50 $\mu M$ Palmitic Acid (D31) |
|---|---|
| (1) fatty acid free BSA | (5)fatty acid free BSA |
| (2) fatty acid free BSA + rosiglitazone | (6) fatty acid free BSA + rosiglitazone |
| (3) Albumax | (7) Albumax |
| (4) Albumax + rosiglitazone | (8) Albumax + rosiglitazone |

Table 6.1: Culture Additions for RB-14 Meibocytes

As mentioned above, in conducting these experiments we encountered equipment difficulties. As such we decided to image a number of the samples using the CARS modality of the Leica SP8 Falcon (Leica Microsystems) at the Beckman Laser Institute at UCI. This system uses ultrashort ($\sim$ 100 fS) laser pulses. This limits its spectral resolution, but is capable of

differentiating carbon-deuterium modes vs. carbon hydrogen. Samples 2-4 were interrogated using the Potma Labs SRS setup, while samples 4-8 were imaged using the CARS modality of the Leica system. We were unable to obtain images from samples one and six. These samples were damaged in processing and showed only cellular debris under the microscope. This adds to the need for further replicates of this work. It may be that those with negligible contrast were problematic culture, or this may indicate that those conditions do not allow for meibogenesis. The latter case if shown to be statistically significant would interesting for this work.

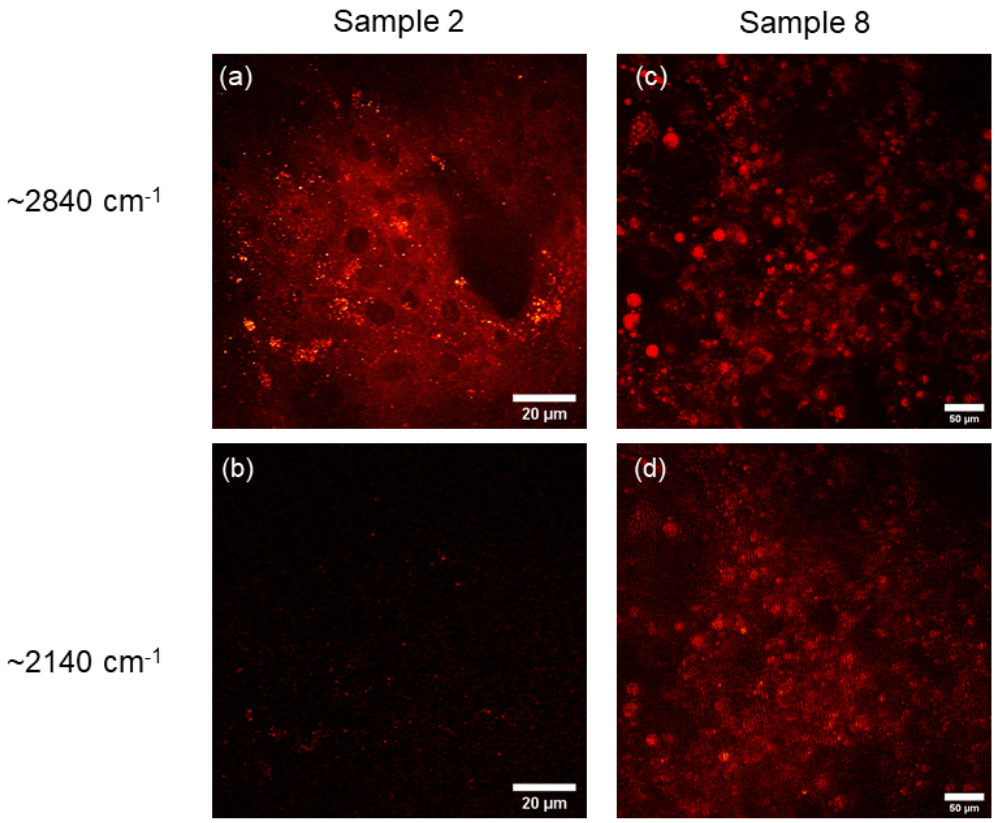



Figure 6.15: CRS Images of Meibocytes with Acetate and Palmitic Acid
RB-14 meibocytes were cultured with deuterate acetate, fatty acid free BSA, and rosiglitazone and imaged with SRS for CH (a) and CD signals (b). Cells cultured with deuterated palmitic acid, albumax, and rosiglitazone imaged for CH (c) and CD (b) signal with CARS.

The results of this most recent study are shown in Figure 6.15, and the total results of the study are summarized in Table 6.2. As seen from the table, this iteration of the experiment

is rather inconclusive. Only two of the iterations showed a positive deuterium signal, and two of the samples were unable to be analyzed. That said one each of acetate and palmitic acid were positive for a deuterium signal. Sample two was imaged with SRS and showed a weak, but visible deuterium signal. Sample 8 was imaged with CARS. It was necessary in this case to check subtract a fluorescent background that can occur with ultrashort pulses. After correction, this sample showed the characteristic nonresonant background of CARS, but also shows areas of more intense signal that overlaps with lipid in the CH region. While it is not possible to draw conclusions from this, both samples that showed positive signal were stimulated with rosiglitazone.

| Sample | Lipid Positive | Deuterium Positive |
|---|---|---|
| (1) acetate + fatty acid free BSA | Sample Damaged | Sample Damaged |
| (2) acetate + fatty acid free BSA + rosi | + | + (Weak) |
| (3) acetate + Albumax | + | - |
| (4) acetate + Albumax + rosi | + | Inconclusive |
| (5) PA + fatty acid free BSA | - | - |
| (6) PA + fatty acid free BSA + rosi | Sample Damaged | - |
| (7) PA + Albumax | + | 0- |
| (8) PA + Albumax + rosi | + | + |

Table 6.2: Summarized Results of Acetate and Lipid Experiments

In the case of these experiments, SRS would be the preferred method for imaging due to the lack of a nonresonant background. We were unable to produce reliable images consistently during the time period we were running these experiments. This was caused by system problems with the laser system running the microscope that introduced significant fluctuations in laser power as well as angle shifts in the beam path. Once those issues are resolved these experiments should be much more consistently performed.

### 6.3.4 Discussion

The experiments described in this section, unfortunately, do not lead to any concrete conclusions. We are unable to definitively say that meibocytes prefer lipid synthesis over lipid transport or vice versa. That being said we do provide reasonable evidence that the cells are capable of utilizing both pathways as demonstrated through the detection of carbon-deuterium signal in both the cases of glucose and palmitic acid treatment. These results, if confirmed through further experiments, may provide for a middle ground between the two extremes that currently exist in literature. This result is notable as the meibomium gland is often compared to the sebaceous gland which is thought to use *de novo* lipogenesis for forming its lipid products. If meibocytes are shown to reliably use lipid transport, these results could provide further impetus for studying the effects of dietary lipids on meibomian secretions and meibomian gland dysfunction. To this end, we have proposed further experiments involving dietary supplement with deuterated glucose in mouse models.

### 6.3.5 Study specific methodologies

#### Culture of RB-14 Meibocytes

The meibocytes used in the studies in this section are a rabbit derived culture currently being prepared by the laboratory of Dr. James Jester at UCI. A full workup that protocol is currently being prepared for publication. Here we summarize that protocol.

Rb-14 cells were grown in Cnt.BM-1 basal media with Accutase +Y in a T75 flask to near confluence. The media is a serum free formulation used to establish the meibomian gland progenitor cells extracted from rabbit meibomian glands. It uses low calcium supplemented with EGF and FGF10. Y-inhibitor was used to block actin filament receptor signaling as it enhances cell proliferation and maintains differentiated state. Cells were passed with

Accutase +Y and more than half were resuspended in BM+Y, and 1 mL was added to coverslips previously coated with 10% collagen. Cells were then allowed to grow for two days under incubation with five percent carbon dioxide at 37°C. After two days, cells were treated with basal media with 1 mM calcium chloride plus the reagents in Table 6.1. Cells grown with acetate were grown with 100 $\mu M$ $D_3$ - Na acetate. Fatty acid free bovine serum albumin or Albumax were added at a concentration of 30 mg/mL. Rosi in all samples was added at a concentration of 30 $\mu M$. $D_{31}$-palmitic acid was added at a concentration of 50 $\mu M$. All media was filtered for sterility, and during the seven day growth period media was refreshed every two to three days. After seven days, cells were fixed with 2% paraformaldehyde.

**Spontaneous Raman spectra acquisition**

Spontaneous Raman spectra were acquired on the system described in Chapter 4. The illumination source was the 532nm laser. The grating was set to 2400 l/mm. Illumination time was ten seconds with ten accumulations using the Renishaw syncroscan settings that allows for an extended scanning range.

**Coherent anti-Stokes Raman scattering imaging**

CARS images were acquired on the Leica SP8 Falcon (Leica Microsystems) system at the Beckman Laser Institue (BLI) at UCI. Our thanks to Dr. Mihaela Balu and Amanda Dirkin for the use and training on that system.

### 6.3.6 Conclusion

Stimulated Raman scattering microscopy combined with isotopic labels creates several pathways for studying metabolism within cells. Herein, we have demonstrated that deuterium

labeling of both simple precursor molecules and saturated and unsaturated fatty can be used to interrogate metabolic processes in cell cultures. Our results suggest that meibocytes are capable of utilizing multiple pathways for the accumulation of lipids, though at this time we are unable to conclusively identify a preferred pathway. Further investigations with these techniques promise to provide further results with better significance and specificity.

# Chapter 7

# The Search for Raman Probes: Isocyanides and Elusive Natural Products

## 7.1 Introduction

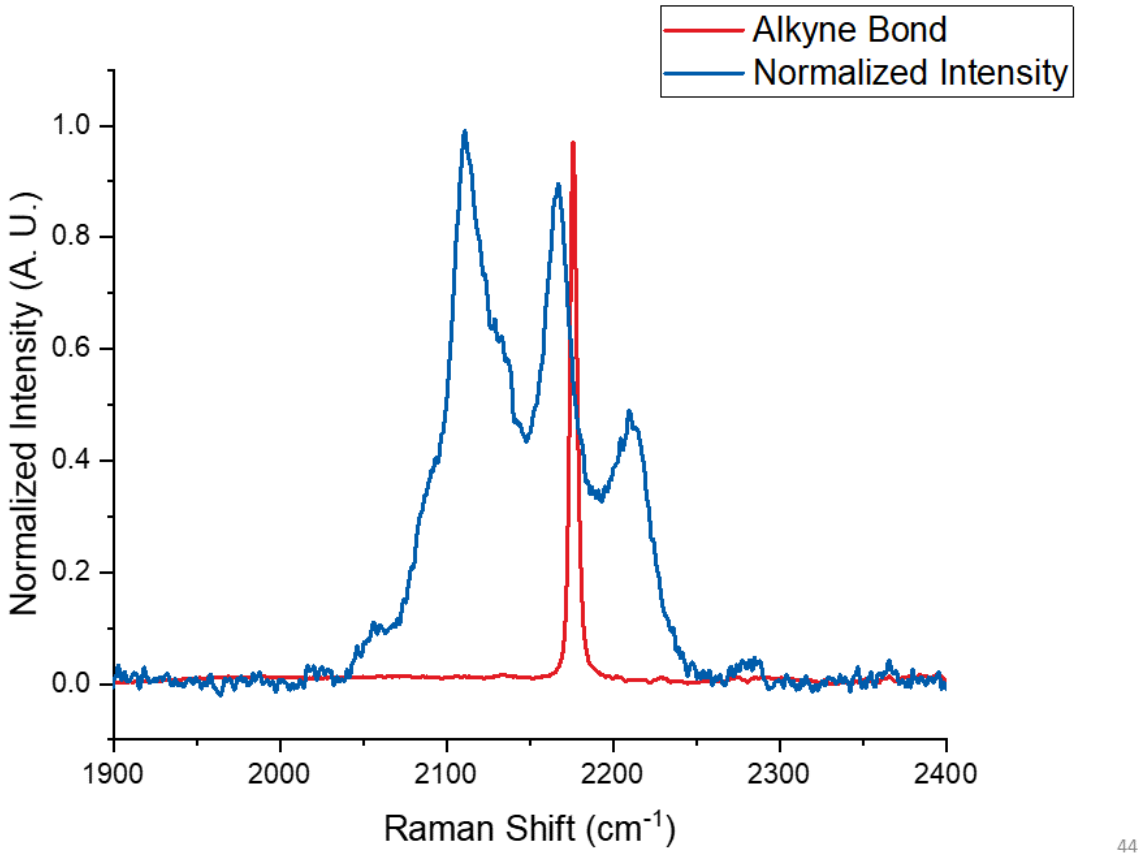



Figure 7.1: Normalized Raman Spectra in the Cell-Silent Region
The normalized spontaneous Raman spectra are shown for deuterated glucose (blue) and the alkyne bond of a functionalized thioglycoside.

Given the utility shown by deuterium tagging in the previous chapters, it is not surprising that many labs are working on expanding their potential into tangible results. While powerful, there are some downsides to using deuterium labeling. The carbon-deuterium bond produces a Raman spectrum that is quite wide compared to other bioorthogonal tags that are currently used in literature such as the alkyne or nitrile functional groups.[267?] Figure 7.1 shows the CD spectrum of $D_7$-glucose (blue) compared to the alkyne peak of a functionalized thioglycoside (red). The full-width at half maximum (FWHM) of the alkyne bond spans only 4 $cm^{-1}$ whereas the width of the CD modes spans more than 100 $cm^{-1}$. The wide

spectral range of the CD modes limits the versatility of deuteration as a labeling strategy as nearly any organic functional groups that are deuterated will have broad spectra that may overlap with the spectra of other chemical species.

In addition to the limited spectral sensitivity of isotopic labeling, there is another disadvantage that is worth discussing. In practice, deuterium labeling is widely used through the deuteration of small molecules such as glucose. Deuterated glucose is relatively affordable and abundant as isotopic labels go, and so is accessible for experiments. However, glucose metabolism is fundamental to many metabolic processes of nearly any animal cell. Thus, as deuterated glucose is used for various purposes inside cells and tissues the deuterons are shuffled off nonspecifically to many different classes of molecules further obscuring the spectral meaning of any Raman measurement. Other forms of tagging involving deuterium have also been shown in literature. Deuterium dioxide (heavy water) has been used successfully in several experiments, and it has been shown that molecular classes can be distinguished from the various spectra.[41] The pallet created by $D_2O$ labeling is shown in Figure 7.2 (a) reproduced from Shi et al.[41] with permission. This method has been tested successfully from cells to live animals. An example of my own work with $D_2O$ labeling is shown in Fig. 7.2 (b).

Although the $D_2O$ labeling offers a general view of metabolic activity, it does not provide specific information about a given metabolite or metabolic pathway. To follow specific pathways, more specific vibrational tags are needed. As a solution to these problems and as a way to further enhance the imaging capabilities of the novel third-order sum frequency generation microscopy (TSFG) that we previously developed[397;398], we undertook a line of study to develop *infrared* sensitive small-molecule bioorthogonal probes. To further that effort, a process of computational studies was carried out to better understand and predict the Raman and IR signal of these molecules.

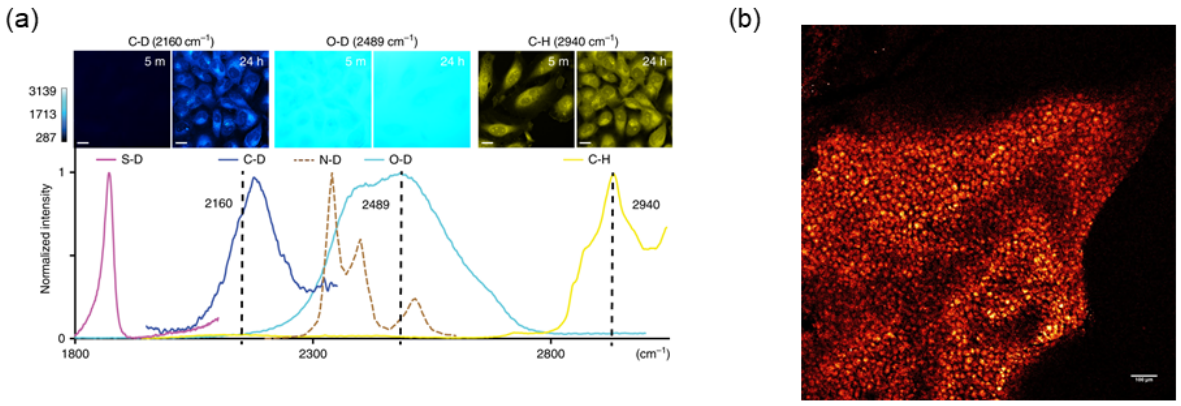



Figure 7.2: Deuterium Oxide Labeling and SRS Imaging
(a) Culturing cells or tissues in deuterium oxide leads to isotopic labeling of a range of molecules, reproduced with permission from Shi et al.[41]. (b) Excised mouse pinna tissue cultured in heaby water shows incorporation of deuterium. Imaged at 2140 $cm^{-1}$ with SRS microscopy.

## 7.2 Predicting & Characterizing Isocyanides

Our work in this area developed from work with the laboratories of Dr. Jennifer Prescher and Dr. Christopher Vanderwal. While working with them, it was realized that several pharmaceutical and natural compounds possess the (ICN), or isonitrile, functional group.[399–401] The ICN functional group possesses a Raman active mode in the cell silent region much like other nitrile and alkyne molecules.[44;49;50;53;191;249;402] The first compound I analyzed was the antiplasmodial isocyanoterpene, 7,20-diisocyanoadociane (DICA), on which the Vanderwal group had recently developed a novel synthesis.[403] DICA is an antimalarial first isolated from sea sponge in 1976.[404–406] Results of our intial studies are shown in Figure 7.3 The Raman spectra was measured on the Renishaw InVia system with 785 nm laser excitation (a). The ICN peak around 2120 $cm^{-1}$ was surprisingly strong, surpassing the strength of the CH modes. From this, the SRS signal of DICA was measured through hyperspectral imaging (c, d).

Next, we attempted imaging of the malaria parasite inside of red blood cells. Samples were acquired from the laboratory of Dr. Karine Le Roch at UC Riverside. Imaging was conducted

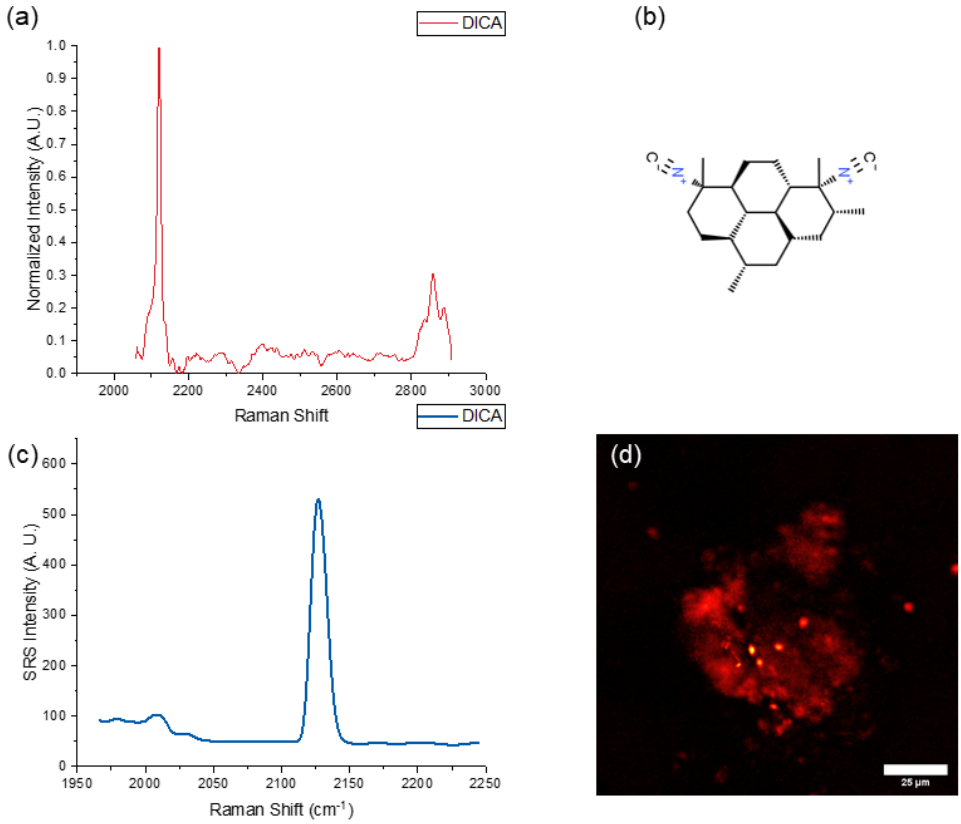



Figure 7.3: Spontaneous and Stimulated Raman Scattering Spectra of DICA
(a) Spontaneous Raman spectra of 7,20-diisocyanodociane (DICA) (b) Molecular structure of DICA (c) SRS spectra acquired from the sample of DICA shown in (d).

with SRS micrsocopy. Unfortunately, we were unable to identify DICA specifically in the samples. Signal in the silent range was dominated by a non-resonant pump-probe signal. This signal likely originated from hemozoin, often called malaria pigment, which is a waste product composed of heme molecules.[407]

### 7.2.1 A Brief Review of DFT

Following our study of DICA, we realized that the isocyanide moiety had potential for use as a Raman tag especially given that it is found in a number of non-mammalian natural products.[408;409] To better understand the vibrational properties of the ICN tag, we selected

twelve small molecule tags to model using density functional theory (DFT). Along with these twelve, three other simple cell-silent region molecules were chosen to compare against. Table 7.1 lists the molecules studied.

| | |
|---|---|
| 1-pentyl isocyanide | cyclohexyl isocyanide |
| toluenesulfonylmethyl isocyanide (TosMIC) | trimethylsilymethyl isocyanide |
| 5-ethynyl-2'-deoxyuridine (EdU) | $D_6$-dimethyl sulfoxide |
| 2,6-dimethylphenyl isocyanide | diethyl isocyanomethylphosphonate |
| 4-chlorophenyl isocyanide | isopropyl isocyanide |
| 4-methoxyphenyl isocyanide | methylbenzyl isocyanide |
| benzyl isocyanide | methyl isocyanoacetate |
| $D_8$-glycerol | |

Table 7.1: List of Molecules for DFT Calculations
Twelve isocyanide molecules were chosen for examination with density functional theory (DFT), and three other compounds with vibrational signals in the cell silent region.

A full review of DFT is beyond the scope of this work. Here, I will summarize the essentials for understanding this work. At its most basic, DFT is an approximate method to solving the Schrödinger Equation for complicated and interacting particles.[410] It is most commonly applied to the ground-state electronic structure problem.[411] In all but the most simple of cases, the Schrödinger Equation becomes impossible to solve analytically, and many approximations have been made since the advent of quantum mechanics.[412] In DFT the exact position of electrons are not solved for, instead a *density functional* is defined giving the probability of an electron at a given point in space. One of the fundamental theorems of DFT is the first Hohenberg-Kohn theorem "The ground-state energy from the Schrödinger equation is a unique functional of the electron density." The second is that "The electron density that minimizes the energy of the overall functional is the true electron density corresponding to the full solution of the Schrödinger equation." In practice, we do not know the true functional of a given system, and a variational approach is taken to minimize the functional. It is an entire field of research to develop functionals and basis sets that accurately approximate the "true" functional for a given system.[413;414]

Much work has gone into identifying and optimizing various methods and basis sets for vibrational spectroscopy.[415–417] Unfortunately, there is no standard method and basis set that makes accurate predictions for all molecules across the whole of the Raman and IR spectra. Different methods tend to overestimate polarizability and underestimate dipole moments or vice versa.[418] Keeping this in mind we decided to compare several different modalities and basis sets to determine one that fits well for the estimation of the isocyanide Raman shift. When we refer to a calculation we will use the format: method/basis_set.

### 7.2.2 Predicting Peak Position

| | |
|---|---|
| PBE/tzvp | B3LYP/tzvp |
| PBE/Sadlej-pVTZ | |

Table 7.2: Functionals and Basis Sets Used in Calculations

Our chosen methods are shown in table 7.2. We chose to compare two of the most widely used functionals. The PBE functional (short for Perdew, Burke, and Ernzerhof) is a pure DFT functional meaning it does not incorporate any of the Hartree-Fock exchange energy.[419]. The B3LYP functional, however, is a hybrid functional.[420] It is widely used as it generally gives good results on average. The downside of using a hybrid functional is that it is computationally more intense. For a given basis set, a hybrid functional will generally take more time to converge.[413] Of the two basis sets examined, TZVP was chosen at the recommendation of Dr. Patrick El Khoury, as a smaller basis set that is generally good for estimating Raman and IR peaks.[421] By comparison, the Sadlej-pVTZ basis set is larger, and generally gives better results for Raman peak intensity.[422] Basis sets were acquired from the Basis Set Exchange.[423–425] All measurements were done using Gaussian 16 software.[426]

The results of the computations are given in table 7.3 for PBE/tzvp, and in table 7.4 for B3LYP/tzvp. For each combination, the energy at convergence, the predicted primary cell silent region mode, and the predicted scattering activity is given.

| Molecule | Energy (Hartree) | Vibrational Mode $cm^{-1}$ | Scattering Activity $A^4/AMU$ |
|---|---|---|---|
| 1-Pentyl Isocyanide-ICN | -289.67 | 2152.92 | 140.75 |
| 2,6-dimethylphenyl-ICN | -402.698 | 2108.97 | 443.1713 |
| 4-chlorophenyl-ICN | -783.575 | 2117.61 | 790.8 |
| 4-methoxyphenyl-ICN | -438.578 | 2119 | 748.55 |
| Benzy-ICN | -363.41 | 2148.04 | 118.4 |
| cyclohexyl-ICN | -327.75 | 2141.53 | 161.86 |
| Diethyl Isocyanomethylphosphonate | -857.06 | 2151.74 | 137.06 |
| DMSO-d6 | -552.896 | 2133.27 | 143.85 |
| Edu | -911.249 | 2154.61 | 902.3676 |
| Glycerol-d8 | -344.521 | 2130.82 | 134.01 |
| Isopropyl-ICN | -211.135 | 2142.59 | 109.29 |
| Methyl benzyl-ICN | -402.685 | 2144.42 | 124.36 |
| Methyl Isocyanoacetate | -360.295 | 2164.09 | 114.6847 |
| TosMIC | -951.012 | 2137.71 | 339.29 |
| trimethylsilymethyl-ICN | -540.982 | 2142.29 | 152.37 |

Table 7.3: PBE/tzvp results of DFT Calculations

| Molecule | Energy (Hartree) | Vibrational Mode $cm^{-1}$ | Scattering Activity $A^4/AMU$ |
|---|---|---|---|
| 1-Pentyl Isocyanide-ICN | -290.078 | 2236.62 | 117.25 |
| 2,6-dimethylphenyl-ICN | -403.229 | 2197.74 | 400.884 |
| 4-chlorophenyl-ICN | -784.18 | 2205.64 | 662.71 |
| 4-methoxyphenyl-ICN | -439.125 | 2206.15 | 646.08 |
| Benzyl-ICN | -363.889 | 2231.96 | 104.65 |
| cyclohexyl-ICN | -328.2 | 2226.88 | 135.04 |
| Diethyl Isocyanomethylphosphonate | -857.961 | 2235.54 | 113.19 |
| DMSO-d6 | -553.274 | 2179.6 | 130.95 |
| Edu | -912.287 | 2221.79 | 823.57 |
| Glycerol-d8 | -344.914 | 2126.43 | 103.04 |
| Isopropyl-ICN | -211.43 | 2227.27 | 95.76 |
| Methyl benzyl-ICN | -403.219 | 2227.83 | 107.64 |
| Methyl Isocyanoacetate | -360.72 | 2246.14 | 94.27 |
| TosMIC | -951.854 | 2222.7 | 253.88 |
| trimethylsilymethyl-ICN | -541.508 | 2226.94 | 131 |

Table 7.4: B3LYP/tzvp results of DFT Calculations

| Molecule | Measured Shift $cm^{-1}$ | Predicted PBE/tzvp | Predicted PBE/Sadlej-pVT | Predicted B3LYP/tzvp |
|---|---|---|---|---|
| 1-Pentyl Isocyanide-ICN | 2148 | 2152.92 | 2137.32 | 2236.62 |
| 2,6-dimethylphenyl-ICN | 2123 | 2108.97 | 2095.31 | 2197.74 |
| 4-chlorophenyl-ICN | 2299 | 2117.61 | 2101.27 | 2205.64 |
| 4-methoxyphenyl-ICN | 2122 | 2119 | 2103.01 | 2206.15 |
| Benzyl-ICN | 2151 | 2148.04 | 2132.74 | 2231.96 |
| Diethyl Isocyanomethylphosphonate | 2157 | 2151.74 | 2137.02 | 2235.54 |
| Edu | 2123 | 2154.61 | | 2221.79 |
| Glycerol-d8 | 2112 | 2130.82 | 2134.94 | 2126.43 |
| Isopropyl-ICN | 2147 | 2142.59 | 2126.84 | 2227.27 |
| TosMIC | 2154 | 2137.71 | 2123.15 | 2222.7 |
| trimethylsilymethyl-ICN | 2142 | 2142.29 | 2126.69 | 2226.94 |

Table 7.5: Comparison of Predicted Values vs. Measured Values

For comparison with experimental data, table 7.5 shows the measured value of the Raman shift and the predicted value for each method. The percent error of the isonitrile peak for each predicted measurement vs. the real measurement is shown in 7.6. It should be noted that a few of the modeled compounds were not replicated in experimental conditions. This was due to the volatility and hazardous nature of those specific compounds. Isocyanides are famously noted for their pungent smell amongst their more serious hazards.[427]

Because each peak value is in the range of $2000cm^{-1}$, the absolute percent error gives a somewhat false view of the accuracy if the position of the isonitrile peak is of central importance. In order to better analyze the accuracy of each DFT method, the percent error was recalculated using only the last three digits of the Raman shift. From this, the mean error for each method and basis set was calculated along with the standard deviation of that mean. This is shown in Figure 7.4(a).

In Figure 7.4 (b), the normalized spontaneous Raman spectra for four of the isocyanide compounds plus EdU is shown. While most of the compounds have narrow bandwidth. 4-chlorophenyl isocyanide presents a spectrum unlike any of the others. Its spectrum also does not correspond to any of the calculated spectra. It is possible that there is some

| Molecule | PE PBE/tzvp | PE PBE/Sadlej-PVTZ | PE B3LYP/tzvp |
|---|---|---|---|
| 1-Pentyl Isocyanide-ICN | 0.22905 | 0.23019 | 4.1257 |
| 2,6-dimethylphenyl-ICN | 0.66086 | 0.66959 | 3.52049 |
| 4-chlorophenyl-ICN | 7.88995 | 8.6324 | 4.0609 |
| 4-methoxyphenyl-ICN | 0.14138 | 0.14265 | 3.9656 |
| Benzyl-ICN | 0.13761 | 0.13879 | 3.76383 |
| Diethyl Isocyanomethylphosphonate | 0.24386 | 0.24614 | 3.64117 |
| Edu | 1.48893 | – | 4.65332 |
| Glycerol-d8 | 0.8911 | 0.88152 | 0.68324 |
| Isopropyl-ICN | 0.2054 | 0.20735 | 3.73871 |
| TosMIC | 0.75627 | 0.76726 | 3.18942 |
| trimethylsilymethyl-ICN | 0.01354 | 0.01364 | 3.96545 |

Table 7.6: Percent Error Between Predicted Values and Measured Values

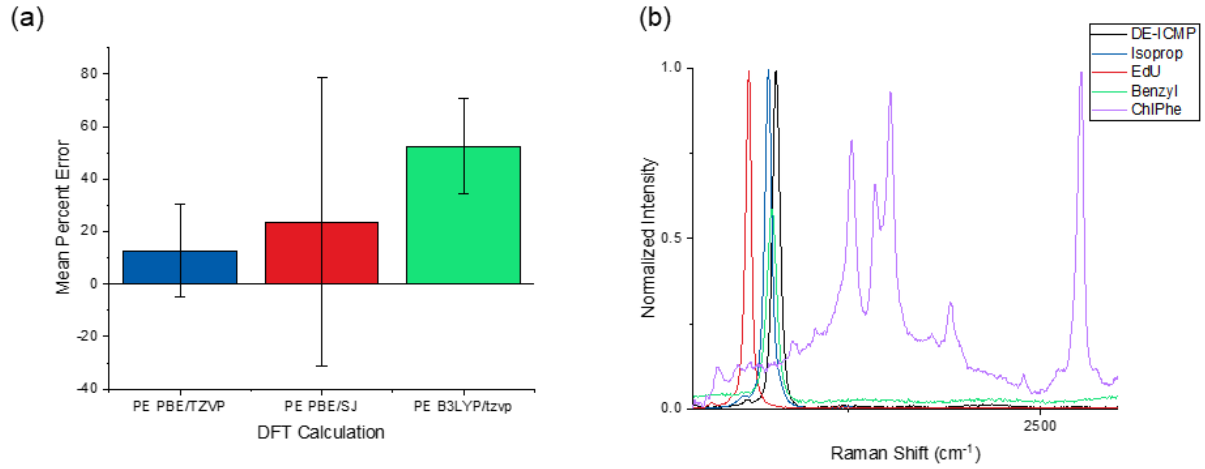



Figure 7.4: Mean Error Between Predicted and Measured Spectra
(a) The mean percent error for each calculation is displayed. Error bars display the standard deviation from the mean. (b) Normalized spontaneous Raman scattering spectra of four isocyanide compounds and EdU.

contamination, though steps were taken to preserve the sample at purchase purity of 97%.

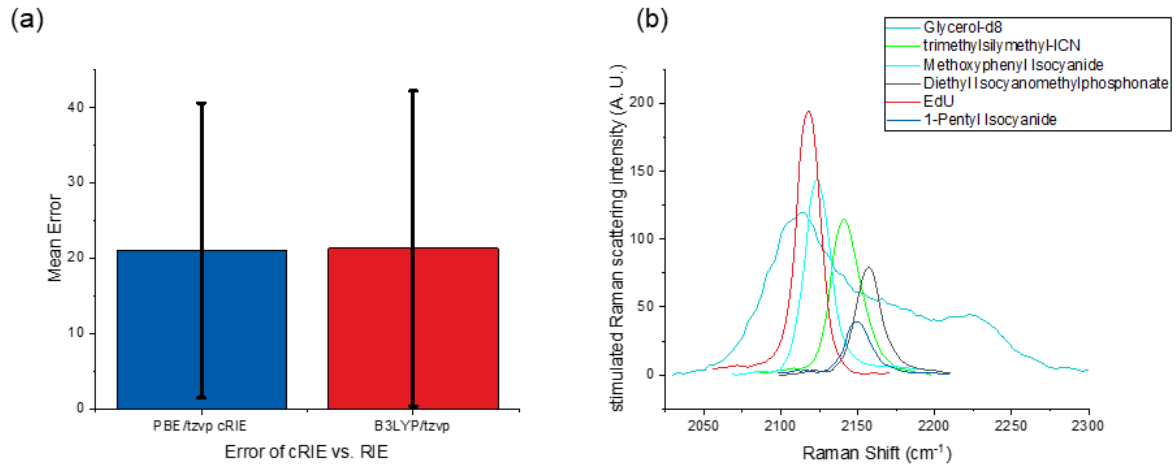



Figure 7.5: Mean Error between cRIE and measured RIE
(a) The mean percent error for each cRIE calculation is displayed. Error bars display the standard deviation from the mean. There is no statistical significance between the two methods. (b) Stimulated Raman scattering spectra of four isocyanide compounds, EdU, and deuterated glycerol.

### 7.2.3 EdU: A Molecular Standard for SRS

The inclusion of EdU in this study is for more than just a convenient alkyne bond. As Raman tags have become more prevalent in literature, the need for a convenient comparison has arose. While in traditional Raman spectroscopy, the Raman scattering cross section, $\sigma$, would normally be used, it is a somewhat difficult measurement to make, and literature values offer differ significantly. Recent authors have settled on normalizing the response of their tags to the response of EdU.[50;235] This "Relative Intensity to EdU" (RIE) value is convenient for quick comparison, and it extends into computational work as well. The computed relative intensity to EdU (cRIE), can be quickly calculated for computed molecules. Table 7.7 displays the measured and computed RIE for 5 different compounds measured with SRS spectroscopy.

| Molecule | RIE | cRIE-PBE/tzvp | cRIE - B3LYP/tzvp |
|---|---|---|---|
| 1-Pentyl Isocyanide-ICN | 0.20381 | 0.15598 | 0.14237 |
| 4-methoxyphenyl-ICN | 0.74824 | 0.82954 | 0.78449 |
| Diethyl Isocyanomethylphosphonate | 0.41434 | 0.15189 | 0.13744 |
| Edu | 1 | 1 | 1 |
| Glycerol-d8 | 0.5998 | 0.14851 | 0.12511 |
| trimethylsilymethyl-ICN | 0.58826 | 0.16886 | 0.15906 |

Table 7.7: Measured and Computed RIE

## 7.3 Discussion

In this project, we attempted to show the power of density functional theory calculations to predict parameters of Raman scattering. The development of successful Raman tags often requires many iterations of small changes on molecules in order to develop a successful palette. Above, we showed three DFT methods for predicting the position of the isocyanide peak with differing levels of complexity. PBE/tzvp was the simplest method used and often the quickest whereas both PBE/Sadlej-pVTZ and B3LYP/tzvp were much more computationally expensive. PBE/tzvp showed the smallest amount of error ($12.68 \pm 17.7$ %) between measured and calculated values. This is in comparison to the other two methods both of which had significantly larger errors. This seems to follow other literature that B3LYP overestimates the polarizability of molecules.

In the second part of this project, we attempted to use the same DFT methods to predict the relative intensities of Raman modes. This would be very useful in designing probes as it would allow quick elimination of all but the strongest possibilities when generating possible probes. However, we have shown in Figure 7.5 that there is no statistical difference in either method, and that neither method predicts the Raman response in any meaningful way. Future work should explore other basis sets that may have better predictive power in this frequency regime.

## 7.4 Specific Methods

### Peak Fitting of Spectra

Peak fitting and calculation of full-width at half max was carried out using OriginPro 2021b software (OriginLab Corporation, Northampton, MA, USA). The peaks are fitted with a Lorentzian lineshape. All plots are given with B-spline smoothing. Background subtraction was carried out in Renishaw Wire (Renishaw Inc., Wotton-under-Edge, UK) and/or with ManiWin32 software.

### Density Functional Theory Calculations

DFT calculations were carried out in Gaussian 16 software (Gaussian, Inc., Wallingford CT). Calculations were performed on the Greenplanet high-performance computing cluster at UCI. We would like to thank Dr. Nathan Crawford for much assistance. Greenlanet is supported by NSF Grant CHE-0840513.

### Stimulated Raman Scattering Spectroscopy

Stimulated Raman scattering spectroscopy was carried out in the picosecond laser lab of Dr. Ara Apkarian at UCI. We thank him for his support during our equipment downtime. The system is based on an APE picoEmerald combined pump and Stokes source (APE, Berlin, Germany). SRL signal was detected on an APE photodiode and lockin detector. Combined beams were focused onto the sample with an Olympus 100x 1.2NA oil immersion objected and collected in the forward direction with an Olympus 1.4 NA condensing optic.

# Chapter 8

# Conclusion & Future Directions

## 8.1 Introduction

In this work, I have outlined the current state of coherent Raman scattering microscopy with a special emphases on the sub-field of stimulated Raman scattering. The field is a growing one and has seen tremendous growth in development and applicability over the last twenty years. Much of the work has focused on demonstrating the utility of both CARS and SRS to the field of lipid metabolism, and in that field it has seen great success. However, it has not managed to get into the hands of as many users as might be desired. One reason for this is the high cost of the lasers and other equipment needed and a lack of commercial turn-key systems keeps the technique away from many users without a background in nonlinear optics. However, another reason for the lack of adoption may be related to the lack of specificity in the technique.

As described in Chapter 3, Raman scattering probes molecular polarizability and is particularly sensitive to vibrations on the level of molecular functional groups. While this has been a boon through much of the technique's history in spectroscopy, where the samples of interest are often pure or nearly pure compounds, it is limiting to a degree in biological imaging. All proteins, nucleic acids, lipids, and other biomolecules have very similar structure with similar functional groups. Correspondingly, the Raman scattering spectrum of many biomolecules is very similar between classes of compounds, e.g. it is generally not possible to discriminate between two generic proteins when measuring in a cell. Because of this much of the history of SRS imaging (Chapter 2) and CRS imaging more broadly, has been limited to visualizing the spatial distribution of classes of molecules such as discriminating lipid from protein. Because of this lack of specificity, CRS microscopy has been largely typecast as only useful for imaging lipid droplets. To advance the field and increase the user base, it is necessary to develop a more specific approach. In my doctoral work, I have demonstrated a means by which to increase the specificity of Raman imaging through isotopic labeling and bioorthogonal tags.

## 8.2 Isotope Labeling in Lipochondrocytes

In Chapter 5, I demonstrated how deuterium labeling of glucose is highly useful in assessing the metabolism of lipochondrocytes. As discussed, lipochondrocytes were a barely recognized cell type that has very little description in literature. It is distinctly different, in both gene expression and morphology, from adipocytes, but it is also distinct from the chondrocytes among which they are found. The cells high expression of lipid made SRS imaging an idel technique just to visualize the lipid distribution. We were able to take it a step further however. By culturing lipochondrocytes in deuterated glucose, we demonstrated this this lipid is formed through catabolism of glucose in *de novo lipogenesis*. Figure 5.7 shows this graphically. The single lipid bearing vacuole of these cells is imaged with a signal that matches in peak location the deuterated glucose standard.

While not tested in this particular work, lipochondrocyes and SRS microscopy may be an excellent model system for studying lipogenesis in the future. Much like the carbon-hydrogen vibrations measured around 2900 $/rmcm^{-1}$, the carbon-deuterium band, is composed of multiple overlapping vibrational modes. In future work, deuterated probes could be used to study the affect of various genes on the production of unsaturated fatty acids as the unsaturated bond has a unque peak in CD spectra. This could lead to study and imaging of specific lipid production based on gene regulation

## 8.3 Imaging Lipid Distribution & Lipid Origins

The results in Chapter 5 produced very clean and relatively easy to interpret results. In the work in Chapter 6, we sought to apply the lessons learned in bioorthogonal imaging to a more complicated system. Research on the origins meibomian gland dysfunction is, at this point, a staple of research and collaboration in our lab. My first project in Potma labs, was

to image meibum secretions, and I have expanded on our work here. First SRS was used in the more traditional ways to visualize lipid droplets in human derived meibocytes. Using hyperspectral imaging, I was able to show that morphologically EPA exposure increases lipid production, but that the aggregate spectrum does not match that of human meibum. Thus, more research into the pathways of meibogenesis is needed.

In the second part of Chapter 5, I applied isotopic labeling to several molecules in an attempt to address the origins of meibum lipids. Deuterium labeling combined with SRS microscopy was able to show that rabbit derived meibocytes were able to uptake and utilize both deuterated glucose and deuterated acetate; suggesting that lipid production is through *de novo lipogenesis*. With the same technique, I was able to show that the same cell model under similar conditions was also capable of storing both deuterated eicosapentaenoic acid and deuterated palmitic acid. While further studies have been hampered by equipment failures, the work thus far suggests the utilization of both uptake and lipogenesis in meibocyte lipid production.

## 8.4 Towards More Specific Probes

In the last part of this work, I explored the use of DFT simulations to predict Raman scattering properties of isocyanides. While only half successful, I was able to show that the fairly fast calculation scheme PBE/tzvp is able to accurately predict the Raman shift of most isocyanides to within 10 $/rmcm^{-1}$. This may be useful for future work developing probes for both nonlinear Raman imaging as well as IR modalities.

## 8.5 Final Thoughts

The field of SRS imaging is a capable modality with many exciting applications in the pipeline and even more waiting to be discovered. In the hands of its practitioners it has dramatically grown, and it has made meaningful contributions to biomedical science. While often touted as a "label-free" imaging modality, it may be the application of a new generation of labels, where the contrast to intrinsic, but the functional groups are not, that opens the technique to more users and more applications. Molecular probes combined with continually evolving advances in machine learning, detection sensitivity, and more affordable lasers may advance SRS and CARS into facility microscopes in the not too distant future.

# Bibliography


[1] M D Duncan, J Reintjes, and T J Manuccia. Scanning coherent anti-Stokes Raman microscope. *Optics Letters*, 7(8):350, 1982. ISSN 0146-9592. doi: 10.1364/ol.7.000350.

[2] Yanping Li, Binglin Shen, Shaowei Li, Yihua Zhao, Junle Qu, and Liwei Liu. Review of Stimulated Raman Scattering Microscopy Techniques and Applications in the Biosciences. *Advanced Biology*, 5(1):2000184, 2021. ISSN 2701-0198. doi: 10.1002/adbi.202000184.

[3] M.D. Duncan. Molecular discrimination and contrast enhancement using a scanning coherent anti-stokes Raman microscope. *Optics Communications*, 50(5):307–312, 1984. ISSN 0030-4018. doi: 10.1016/0030-4018(84)90173-1.

[4] M. D. Duncan, J. Reintjes, and T. J. Manuccia. A review of the NRL CARS microscope. *AIP Conference Proceedings*, (160):631, 1987. doi: https://doi.org/10.1063/1.36835.

[5] Andreas Zumbusch, Gary R. Holtom, and X. Sunney Xie. Three-Dimensional Vibrational Imaging by Coherent Anti-Stokes Raman Scattering. *Phys. Rev. Lett.*, 82: 4142—4145, 1999. doi: 10.1103/physrevlett.82.4142. URL `https://link.aps.org/doi/10.1103/PhysRevLett.82.4142`.

[6] M. Antia. MICROSCOPY:Imaging Living Cells The Friendly Way. *Science*, 284(5419): 1445a–1445, 1999. ISSN 0036-8075. doi: 10.1126/science.284.5419.1445a.

[7] Ji-Xin Cheng, Y. Kevin Jia, Gengfeng Zheng, and X. Sunney Xie. Laser-Scanning Coherent Anti-Stokes Raman Scattering Microscopy and Applications to Cell Biology. *Biophysical Journal*, 83(1):502–509, 2002. ISSN 0006-3495. doi: 10.1016/s0006-3495(02)75186-2.

[8] Conor L. Evans, Eric O. Potma, Mehron Puoris'haag, Daniel Côté, Charles P. Lin, and X. Sunney Xie. Chemical imaging of tissue in vivo with video-rate coherent anti-Stokes Raman scattering microscopy. *Proceedings of the National Academy of Sciences of the United States of America*, 102(46):16807–16812, 2005. ISSN 0027-8424. doi: 10.1073/pnas.0508282102.

[9] Brian G. Saar, Yining Zeng, Christian W. Freudiger, Yu-San Liu, Michael E. Himmel, X. Sunney Xie, and Shi-You Ding. Label-Free, Real-Time Monitoring of Biomass

Processing with Stimulated Raman Scattering Microscopy. *Angewandte Chemie*, 122 (32):5608–5611, 2010. ISSN 1521-3757. doi: 10.1002/ange.201000900.

[10] Jeffrey L Suhalim, John C Boik, Bruce J Tromberg, and Eric O Potma. The need for speed. *Journal of Biophotonics*, 5, 2012. ISSN 1864-063X. doi: 10.1002/jbio.201200002.

[11] Eric O. Potma, Wim P. de Boeij, Peter J. M. van Haastert, and Douwe A. Wiersma. Real-time visualization of intracellular hydrodynamics in single living cells. *Proceedings of the National Academy of Sciences*, 98(4):1577–1582, 2001. ISSN 0027-8424. doi: 10.1073/pnas.98.4.1577.

[12] Keiji Ibata, Shinichi Takimoto, Toshinori Morisaku, Atsushi Miyawaki, and Masato Yasui. Analysis of Aquaporin-Mediated Diffusional Water Permeability by Coherent Anti-Stokes Raman Scattering Microscopy. *Biophysical Journal*, 101(9):2277–2283, 2011. ISSN 0006-3495. doi: 10.1016/j.bpj.2011.08.045.

[13] Ying-Chun Yu, Yoshiro Sohma, Shinichi Takimoto, Takayuki Miyauchi, and Masato Yasui. Direct visualization and quantitative analysis of water diffusion in complex biological tissues using CARS microscopy. *Scientific Reports*, 3(1):2745, 2013. doi: 10.1038/srep02745.

[14] Bertr Lucotte, M., Chloe Powell, Jay R. Knutson, Christian A. Combs, Daniela Malide, Zu-Xi Yu, Mark Knepper, Keval D. Patel, Anna Pielach, Errin Johnson, Lyudmyla Borysova, Kim A. Dora, and Robert S. Balaban. Direct visualization of the arterial wall water permeability barrier using CARS microscopy. *Proceedings of the National Academy of Sciences*, 114(18):4805—4810, 2017. ISSN 0027-8424. doi: 10.1073/pnas.1620008114. URL `http://www.pnas.org/content/114/18/4805`.

[15] Thuc T. Le, Shuhua Yue, and Ji-Xin Cheng. Shedding new light on lipid biology with coherent anti-Stokes Raman scattering microscopy. *Journal of Lipid Research*, 51(11):3091–3102, 2010. ISSN 0022-2275. doi: 10.1194/jlr.r008730.

[16] Thomas Hellerer, Claes Axäng, Christian Brackmann, Per Hillertz, Marc Pilon, and Annika Enejder. Monitoring of lipid storage in Caenorhabditis elegans using coherent anti-Stokes Raman scattering (CARS) microscopy. *Proceedings of the National Academy of Sciences*, 104(37):14658–14663, 2007. ISSN 0027-8424. doi: 10.1073/pnas.0703594104.

[17] Shuhua Yue and Ji-Xin Cheng. Deciphering single cell metabolism by coherent Raman scattering microscopy. *Current Opinion in Chemical Biology*, 33:46–57, 2016. ISSN 1367-5931. doi: 10.1016/j.cbpa.2016.05.016.

[18] Chi Zhang, Junjie Li, Lu Lan, and Ji-Xin Cheng. Quantification of Lipid Metabolism in Living Cells through the Dynamics of Lipid Droplets Measured by Stimulated Raman Scattering Imaging. *Analytical Chemistry*, 89(8):4502–4507, 2017. ISSN 0003-2700. doi: 10.1021/acs.analchem.6b04699.

[19] Thuc T. Le, Ingeborg M. Langohr, Matthew J. Locker, Michael Sturek, and Ji-Xin Cheng. Label-free molecular imaging of atherosclerotic lesions using multimodal nonlinear optical microscopy. *Journal of Biomedical Optics*, 12(5):054007–054007–10, 2007. ISSN 1083-3668. doi: 10.1117/1.2795437.

[20] Han-Wei Wang, Ingeborg M. Langohr, Michael Sturek, and Ji-Xin Cheng. Imaging and Quantitative Analysis of Atherosclerotic Lesions by CARS-Based Multimodal Nonlinear Optical Microscopy. *Arteriosclerosis, Thrombosis, and Vascular Biology*, 29(9): 1342–1348, 2009. ISSN 1079-5642. doi: 10.1161/atvbaha.109.189316.

[21] Jeffrey L. Suhalim, Chao-Yu Chung, Magnus B. Lilledahl, Ryan S. Lim, Moshe Levi, Bruce J. Tromberg, and Eric O. Potma. Characterization of Cholesterol Crystals in Atherosclerotic Plaques Using Stimulated Raman Scattering and Second-Harmonic Generation Microscopy. *Biophysical Journal*, 102(8):1988–1995, 2012. ISSN 0006-3495. doi: 10.1016/j.bpj.2012.03.016.

[22] Haifeng Wang, Yan Fu, Phyllis Zickmund, Riyi Shi, and Ji-Xin Cheng. Coherent Anti-Stokes Raman Scattering Imaging of Axonal Myelin in Live Spinal Tissues. *Biophysical Journal*, 89(1):581–591, 2005. ISSN 0006-3495. doi: 10.1529/biophysj.105.061911.

[23] Yan Fu, T B Huff, Han-Wei Wang, Ji-Xin Cheng, and Haifeng Wang. Ex vivo and in vivo imaging of myelin fibers in mouse brain by coherent anti-Stokes Raman scattering microscopy. *Optics Express*, 16(24):19396, 2008. doi: 10.1364/oe.16.019396.

[24] Francis P. Henry, Daniel Côté, Mark A. Randolph, Esther A. Z. Rust, Robert W. Redmond, Irene E. Kochevar, Charles P. Lin, and Jonathan M. Winograd. Real-Time In Vivo Assessment of the Nerve Microenvironment with Coherent Anti–Stokes Raman Scattering Microscopy. *Plastic and Reconstructive Surgery*, 123(2S):123S–130S, 2009. ISSN 0032-1052. doi: 10.1097/prs.0b013e318191c5b8.

[25] Craig Brideau, Kelvin W. C. Poon, Pina Colarusso, and Peter K. Stys. Excitation parameters optimized for coherent anti-Stokes Raman scattering imaging of myelinated tissue. *Journal of Biomedical Optics*, 24(4):046502, 2019. ISSN 1083-3668. doi: 10.1117/1.jbo.24.4.046502.

[26] Damon DePaoli, Émile Lemoine, Katherine Ember, Martin Parent, Michel Prud'homme, Léo Cantin, Kevin Petrecca, Frédéric Leblond, and Daniel C Côté. Rise of Raman spectroscopy in neurosurgery: a review. *Journal of Biomedical Optics*, 25 (05):1, 2020. ISSN 1083-3668. doi: 10.1117/1.jbo.25.5.050901.

[27] Thuc T Le, Terry B Huff, and Ji-Xin Cheng. Coherent anti-Stokes Raman scattering imaging of lipids in cancer metastasis. *BMC Cancer*, 9(1):42, 2009. doi: 10.1186/1471-2407-9-42.

[28] Mariana C. Potcoava, Gregory L. Futia, Jessica Aughenbaugh, Isabel R. Schlaepfer, and Emily A. Gibson. Raman and coherent anti-Stokes Raman scattering microscopy studies of changes in lipid content and composition in hormone-treated breast and

prostate cancer cells. *Journal of Biomedical Optics*, 19(11):111605–111605, 2014. ISSN 1083-3668. doi: 10.1117/1.jbo.19.11.111605.

[29] Jue Hou, Joshua Williams, Elliot L. Botvinick, Eric O. Potma, and Bruce J. Tromberg. Visualization of Breast Cancer Metabolism Using Multimodal Nonlinear Optical Microscopy of Cellular Lipids and Redox State. *Cancer Research*, 78 (10):2503—2512, 2018. ISSN 0008-5472. doi: 10.1158/0008-5472.can-17-2618. URL `http://cancerres.aacrjournals.org/content/78/10/2503`.

[30] Li Li, Haifeng Wang, and Ji-Xin Cheng. Quantitative Coherent Anti-Stokes Raman Scattering Imaging of Lipid Distribution in Coexisting Domains. *Biophysical Journal*, 89(5):3480–3490, 2005. ISSN 0006-3495. doi: 10.1529/biophysj.105.065607.

[31] Eric O. Potma and X. Sunney Xie. Direct Visualization of Lipid Phase Segregation in Single Lipid Bilayers with Coherent Anti-Stokes Raman Scattering Microscopy. *ChemPhysChem*, 6(1):77–79, 2005. ISSN 1439-7641. doi: 10.1002/cphc.200400390.

[32] Delong Zhang, Mikhail N Slipchenko, and Ji-Xin Cheng. Highly Sensitive Vibrational Imaging by Femtosecond Pulse Stimulated Raman Loss. *The Journal of Physical Chemistry Letters*, 2(11):1248–1253, 2011. ISSN 1948-7185. doi: 10.1021/jz200516n.

[33] Dan Fu, Yong Yu, Andrew Folick, Erin Currie, Robert V. Farese, Tsung-Huang Tsai, Xiaoliang Sunney Xie, and Meng C. Wang. In Vivo Metabolic Fingerprinting of Neutral Lipids with Hyperspectral Stimulated Raman Scattering Microscopy. *Journal of the American Chemical Society*, 136(24):8820–8828, 2014. ISSN 0002-7863. doi: 10.1021/ja504199s.

[34] Alba Alfonso-García, Simon G. Pfisterer, Howard Riezman, Elina Ikonen, and Eric O. Potma. D38-cholesterol as a Raman active probe for imaging intracellular cholesterol storage. *Journal of Biomedical Optics*, 21(6):061003–061003, 2016. ISSN 1083-3668. doi: 10.1117/1.jbo.21.6.061003.

[35] Lu Wei, Yong Yu, Yihui Shen, Meng C. Wang, and Wei Min. Vibrational imaging of newly synthesized proteins in live cells by stimulated Raman scattering microscopy. *Proceedings of the National Academy of Sciences*, 110(28):11226–11231, 2013. ISSN 0027-8424. doi: 10.1073/pnas.1303768110.

[36] Lu Wei, Yihui Shen, Fang Xu, Fanghao Hu, Jamie K. Harrington, Kimara L. Targoff, and Wei Min. Imaging Complex Protein Metabolism in Live Organisms by Stimulated Raman Scattering Microscopy with Isotope Labeling. *ACS Chemical Biology*, 10(3): 901–908, 2015. ISSN 1554-8929. doi: 10.1021/cb500787b.

[37] Junjie Li and Ji-Xin Cheng. Direct Visualization of De novo Lipogenesis in Single Living Cells. *Scientific Reports*, 4(1):6807, 2014. doi: 10.1038/srep06807.

[38] Jue Hou, Nellone E. Reid, Bruce J. Tromberg, and Eric O. Potma. Kinetic Analysis of Lipid Metabolism in Breast Cancer Cells via Nonlinear Optical Microscopy. *Biophysical Journal*, 119(2):258–264, 2020. ISSN 0006-3495. doi: 10.1016/j.bpj.2020.06.007.

[39] Dongkwan Lee, Jiajun Du, Rona Yu, Yapeng Su, James R Heath, and Lu Wei. Visualizing Subcellular Enrichment of Glycogen in Live Cancer Cells by Stimulated Raman Scattering. *Analytical Chemistry*, 92(19):13182–13191, 2020. ISSN 0003-2700. doi: 10.1021/acs.analchem.0c02348.

[40] Luyuan Zhang, Lingyan Shi, Yihui Shen, Yupeng Miao, Mian Wei, Naixin Qian, Yinong Liu, and Wei Min. Spectral tracing of deuterium for imaging glucose metabolism. *Nature Biomedical Engineering*, 3(5):402–413, 2019. doi: 10.1038/s41551-019-0393-4.

[41] Lingyan Shi, Chaogu Zheng, Yihui Shen, Zhixing Chen, Edilson S. Silveira, Luyuan Zhang, Mian Wei, Chang Liu, Carmen de Sena-Tomas, Kimara Targoff, and Wei Min. Optical imaging of metabolic dynamics in animals. *Nature Communications*, 9(1):2995, 2018. doi: 10.1038/s41467-018-05401-3. URL `https://doi.org/10.1038/s41467-018-05401-3`.

[42] Zhixing Chen, Daniel W. Paley, Lu Wei, Andrew L. Weisman, Richard A. Friesner, Colin Nuckolls, and Wei Min. Multicolor Live-Cell Chemical Imaging by Isotopically Edited Alkyne Vibrational Palette. *Journal of the American Chemical Society*, 136 (22):8027–8033, 2014. ISSN 0002-7863. doi: 10.1021/ja502706q.

[43] Lu Wei, Fanghao Hu, Yihui Shen, Zhixing Chen, Yong Yu, Chih-Chun Lin, Meng C Wang, and Wei Min. Live-cell imaging of alkyne-tagged small biomolecules by stimulated Raman scattering. *Nature Methods*, 11(4), 2014. ISSN 1548-7091. doi: 10.1038/nmeth.2878.

[44] Senlian Hong, Tao Chen, Yuntao Zhu, Ang Li, Yanyi Huang, and Xing Chen. Live-Cell Stimulated Raman Scattering Imaging of Alkyne-Tagged Biomolecules. *Angewandte Chemie International Edition*, 53(23):5827–5831, 2014. ISSN 1521-3773. doi: 10.1002/anie.201400328.

[45] Fanghao Hu, Zhixing Chen, Luyuan Zhang, Yihui Shen, Lu Wei, and Wei Min. Vibrational Imaging of Glucose Uptake Activity in Live Cells and Tissues by Stimulated Raman Scattering. *Angewandte Chemie International Edition*, 54(34):9821–9825, 2015. ISSN 1521-3773. doi: 10.1002/anie.201502543.

[46] Tyler Weeks, Iwan Schie, Laura J. den Hartigh, John C. Rutledge, and Thomas Huser. Lipid-cell interactions in human monocytes investigated by doubly-resonant coherent anti-Stokes Raman scattering microscopy. *Journal of Biomedical Optics*, 16(2):021117–021117–5, 2011. ISSN 1083-3668. doi: 10.1117/1.3544585.

[47] Hyeon Jeong Lee, Wandi Zhang, Delong Zhang, Yang Yang, Bin Liu, Eric L. Barker, Kimberly K. Buhman, Lyudmila V. Slipchenko, Mingji Dai, and Ji-Xin Cheng. Assessing Cholesterol Storage in Live Cells and C. elegans by Stimulated Raman Scattering Imaging of Phenyl-Diyne Cholesterol. *Scientific Reports*, 5(1):7930, 2015. doi: 10.1038/srep07930.

[48] Xiaoqi Lang and Kevin Welsher. Mapping solvation heterogeneity in live cells by hyperspectral stimulated Raman scattering microscopy. *The Journal of Chemical Physics*, 152(17):174201, 2020. ISSN 0021-9606. doi: 10.1063/1.5141422.

[49] Hiroyuki Yamakoshi, Kosuke Dodo, Masaya Okada, Jun Ando, Almar Palonpon, Katsumasa Fujita, Satoshi Kawata, and Mikiko Sodeoka. Imaging of EdU, an Alkyne-Tagged Cell Proliferation Probe, by Raman Microscopy. *Journal of the American Chemical Society*, 133(16):6102–6105, 2011. ISSN 0002-7863. doi: 10.1021/ja108404p.

[50] Hiroyuki Yamakoshi, Kosuke Dodo, Almar Palonpon, Jun Ando, Katsumasa Fujita, Satoshi Kawata, and Mikiko Sodeoka. Alkyne-Tag Raman Imaging for Visualization of Mobile Small Molecules in Live Cells. *Journal of the American Chemical Society*, 134(51):20681–20689, 2012. ISSN 0002-7863. doi: 10.1021/ja308529n.

[51] Sangdeok Shim, Christina M. Stuart, and Richard A. Mathies. Resonance raman cross-sections and vibronic analysis of rhodamine 6g from broadband stimulated raman spectroscopy. *ChemPhysChem*, 9(5):697–699, 2008. ISSN 1439-7641. doi: https://doi.org/10.1002/cphc.200700856.

[52] Lixue Shi, Hanqing Xiong, Yihui Shen, Rong Long, Lu Wei, and Wei Min. Electronic Resonant Stimulated Raman Scattering Micro-Spectroscopy. *The Journal of Physical Chemistry B*, 122(39):9218–9224, 2018. ISSN 1520-6106. doi: 10.1021/acs.jpcb.8b07037.

[53] Lu Wei, Zhixing Chen, Lixue Shi, Rong Long, Andrew V. Anzalone, Luyuan Zhang, Fanghao Hu, Rafael Yuste, Virginia W. Cornish, and Wei Min. Super-multiplex vibrational imaging. *Nature*, 544(7651):465–470, 2017. ISSN 0028-0836. doi: 10.1038/nature22051.

[54] Fanghao Hu, Chen Zeng, Rong Long, Yupeng Miao, Lu Wei, Qizhi Xu, and Wei Min. Supermultiplexed optical imaging and barcoding with engineered polyynes. *Nature Methods*, 15(3):194–200, 2018. ISSN 1548-7091. doi: 10.1038/nmeth.4578.

[55] Hanqing Xiong, Lixue Shi, Lu Wei, Yihui Shen, Rong Long, Zhilun Zhao, and Wei Min. Stimulated raman excited fluorescence spectroscopy and imaging. *Nature Photonics*, 13(6):412–417, 2019. ISSN 1749-4885. doi: 10.1038/s41566-019-0396-4.

[56] Dario Polli, Vikas Kumar, Carlo M. Valensise, Marco Marangoni, and Giulio Cerullo. Broadband coherent raman scattering microscopy. *Laser & Photonics Reviews*, 12 (9):1800020, 2018. doi: https://doi.org/10.1002/lpor.201800020. URL `https://onlinelibrary.wiley.com/doi/abs/10.1002/lpor.201800020`.

[57] Chien-Sheng Liao and Ji-Xin Cheng. In Situ and In Vivo Molecular Analysis by Coherent Raman Scattering Microscopy. *Annual Review of Analytical Chemistry*, 9 (1):69–93, 2016. ISSN 1936-1327. doi: 10.1146/annurev-anchem-071015-041627.

[58] George W H Wurpel, Juleon M Schins, and Michiel Müller. Chemical specificity in three-dimensional imaging with multiplex coherent anti-Stokes Raman scattering microscopy. *Optics Letters*, 27(13):1093, 2002. ISSN 0146-9592. doi: 10.1364/ol.27.001093.

[59] Ji-xin Cheng, Andreas Volkmer, Lewis D. Book, and X. Sunney Xie. Multiplex Coherent Anti-Stokes Raman Scattering Microspectroscopy and Study of Lipid Vesicles. *The Journal of Physical Chemistry B*, 106(34):8493–8498, 2002. ISSN 1520-6106. doi: 10.1021/jp025771z.

[60] Tak W Kee and Marcus T Cicerone. Simple approach to one-laser, broadband coherent anti-Stokes Raman scattering microscopy. *Optics Letters*, 29(23):2701, 2004. ISSN 0146-9592. doi: 10.1364/ol.29.002701.

[61] Charles H. Camp Jr, Young Jong Lee, John M. Heddleston, Christopher M. Hartshorn, Angela R. Hight Walker, Jeremy N. Rich, Justin D. Lathia, and Marcus T. Cicerone. High-speed coherent Raman fingerprint imaging of biological tissues. *Nature Photonics*, 8(8):627–634, 2014. ISSN 1749-4885. doi: 10.1038/nphoton.2014.145.

[62] Fa-Ke Lu, Minbiao Ji, Dan Fu, Xiaohui Ni, Christian W. Freudiger, Gary Holtom, and X. Sunney Xie. Multicolor stimulated Raman scattering microscopy. *Molecular Physics*, 110(15-16):1927–1932, 2012. ISSN 0026-8976.

[63] Keisuke Seto, Yoshinao Okuda, Eiji Tokunaga, and Takayoshi Kobayashi. Development of a multiplex stimulated Raman microscope for spectral imaging through multichannel lock-in detection. *Review of Scientific Instruments*, 84(8):083705, 2013. ISSN 0034-6748. doi: 10.1063/1.4818670.

[64] B. Marx, L. Czerwinski, R. Light, M. Somekh, and P. Gilch. Multichannel detectors for femtosecond stimulated Raman microscopy – ideal and real ones. *Journal of Raman Spectroscopy*, 45(7):521–527, 2014. ISSN 1097-4555. doi: 10.1002/jrs.4528.

[65] William Rock, Mischa Bonn, and Sapun H Parekh. Near shot-noise limited hyperspectral stimulated Raman scattering spectroscopy using low energy lasers and a fast CMOS array. *Optics Express*, 21(13):15113, 2013. doi: 10.1364/oe.21.015113.

[66] Mikhail N. Slipchenko, Robert A. Oglesbee, Delong Zhang, Wei Wu, and Ji-Xin Cheng. Heterodyne detected nonlinear optical imaging in a lock-in free manner. *Journal of Biophotonics*, 5(10):801–807, 2012. ISSN 1864-0648. doi: 10.1002/jbio.201200005.

[67] Chi Zhang, Kai-Chih Huang, Bartek Rajwa, Junjie Li, Shiqi Yang, Haonan Lin, Chiensheng Liao, Gregory Eakins, Shihuan Kuang, Valery Patsekin, J Paul Robinson, and Ji-Xin Cheng. Stimulated Raman scattering flow cytometry for label-free single-particle analysis. *Optica*, 4(1):103, 2017. doi: 10.1364/optica.4.000103.

[68] Chia-Yu Lin, Jeffrey L. Suhalim, Chyong Ly Nien, Miloš D. Miljković, Max Diem, James V. Jester, and Eric. O. Potma. Picosecond spectral coherent anti-Stokes Raman scattering imaging with principal component analysis of meibomian glands. *Journal*

*of Biomedical Optics*, 16(2):021104–021104–9, 2011. ISSN 1083-3668. doi: 10.1117/1.3533716.

[69] Steve Bégin, Bryan Burgoyne, Vincent Mercier, Alain Villeneuve, Réal Vallée, and Daniel Côté. Coherent anti-Stokes Raman scattering hyperspectral tissue imaging with a wavelength-swept system. *Biomedical Optics Express*, 2(5):1296–1306, 2011. ISSN 2156-7085. doi: 10.1364/boe.2.001296.

[70] Erik T. Garbacik, Jennifer L. Herek, Cees Otto, and Herman L. Offerhaus. Rapid identification of heterogeneous mixture components with hyperspectral coherent anti-Stokes Raman scattering imaging. *Journal of Raman Spectroscopy*, 43(5):651–655, 2012. ISSN 1097-4555. doi: 10.1002/jrs.4064.

[71] Yasuyuki Ozeki, Wataru Umemura, Kazuhiko Sumimura, Norihiko Nishizawa, Kiichi Fukui, and Kazuyoshi Itoh. Stimulated Raman hyperspectral imaging based on spectral filtering of broadband fiber laser pulses. *Optics Letters*, 37(3):431, 2012. ISSN 0146-9592. doi: 10.1364/ol.37.000431.

[72] Sergey P. Laptenok, Vijayakumar P. Rajamanickam, Luca Genchi, Tual Monfort, Yeonwoo Lee, Imran I. Patel, Andrea Bertoncini, and Carlo Liberale. Fingerprint-to-CH stretch continuously tunable high spectral resolution stimulated Raman scattering microscope. *Journal of Biophotonics*, 12(9):e201900028, 2019. ISSN 1864-063X. doi: 10.1002/jbio.201900028.

[73] Thomas Hellerer, Annika M.K. Enejder, and Andreas Zumbusch. Spectral focusing: High spectral resolution spectroscopy with broad-bandwidth laser pulses. *Applied Physics Letters*, 85(1):25–27, 2004. ISSN 0003-6951. doi: 10.1063/1.1768312.

[74] Israel Rocha-Mendoza, Wolfgang Langbein, and Paola Borri. Coherent anti-Stokes Raman microspectroscopy using spectral focusing with glass dispersion. *Applied Physics Letters*, 93(20):201103, 2008. ISSN 0003-6951. doi: 10.1063/1.3028346.

[75] Adrian F. Pegoraro, Andrew Ridsdale, Douglas J. Moffatt, Yiwei Jia, John Paul Pezacki, and Albert Stolow. Optimally chirped multimodal CARS microscopy based on a single Ti:sapphire oscillator. *Optics Express*, 17(4):2984, 2009. ISSN 1094-4087. doi: 10.1364/oe.17.002984.

[76] Esben Ravn Andresen, Pascal Berto, and Hervé Rigneault. Stimulated Raman scattering microscopy by spectral focusing and fiber-generated soliton as Stokes pulse. *Optics Letters*, 36(13):2387, 2011. ISSN 0146-9592. doi: 10.1364/ol.36.002387.

[77] Ruoyu He, Zhiping Liu, Yongkui Xu, Wei Huang, Hong Ma, and Minbiao Ji. Stimulated raman scattering microscopy and spectroscopy with a rapid scanning optical delay line. *Optics Letters*, 42(4):659, feb 2017. doi: 10.1364/ol.42.000659.

[78] Xavier Audier, Nicolas Forget, and Hervé Rigneault. High-speed chemical imaging of dynamic and histological samples with stimulated Raman micro-spectroscopy. *Optics Express*, 28(10):15505, 2020. doi: 10.1364/oe.390850.

[79] Mohammed S Alshaykh, Chien-Sheng Liao, Oscar E Sandoval, Gregory Gitzinger, Nicolas Forget, Daniel E Leaird, Ji-Xin Cheng, and Andrew M Weiner. High-speed stimulated hyperspectral Raman imaging using rapid acousto-optic delay lines. *Optics Letters*, 42(8):1548, 2017. ISSN 0146-9592. doi: 10.1364/ol.42.001548.

[80] Kideog Bae, Wei Zheng, and Zhiwei Huang. Spatial light-modulated stimulated Raman scattering (SLM-SRS) microscopy for rapid multiplexed vibrational imaging. *Theranostics*, 10(1):312–322, 2020. ISSN 1838-7640. doi: 10.7150/thno.38551.

[81] Pascal Berto, Camille Scotté, Frédéric Galland, Hervè Rigneault, and Hilton B de Aguiar. Programmable single-pixel-based broadband stimulated Raman scattering. *Optics Letters*, 42(9):1696, 2017. ISSN 0146-9592. doi: 10.1364/ol.42.001696.

[82] Luca Genchi, Andrea Bucci, Sergey P Laptenok, Alessandro Giammona, and Carlo Liberale. Hadamard-transform spectral acquisition with an acousto-optic tunable filter in a broadband stimulated Raman scattering microscope. *Optics Express*, 29(2):2378, 2021. doi: 10.1364/oe.415752.

[83] Jennifer P Ogilvie, Emmanuel Beaurepaire, Antigoni Alexandrou, and Manuel Joffre. Fourier-transform coherent anti-Stokes Raman scattering microscopy. *Optics Letters*, 31(4):480, 2006. ISSN 0146-9592. doi: 10.1364/ol.31.000480.

[84] Ryo Kinegawa, Kotaro Hiramatsu, Kazuki Hashimoto, Venkata Ramaiah Badarla, Takuro Ideguchi, and Keisuke Goda. High-speed broadband Fourier-transform coherent anti-stokes Raman scattering spectral microscopy. *Journal of Raman Spectroscopy*, 50(8):1141–1146, 2019. ISSN 0377-0486. doi: 10.1002/jrs.5630.

[85] Alex Soares Duarte, Christoph Schnedermann, and Philipp Kukura. Wide-Field Detected Fourier Transform CARS Microscopy. *Scientific Reports*, 6(1):37516, 2016. doi: 10.1038/srep37516.

[86] Miu Tamamitsu, Yusuke Sakaki, Tasuku Nakamura, G. Krishna Podagatlapalli, Takuro Ideguchi, and Keisuke Goda. Ultrafast broadband Fourier-transform CARS spectroscopy at 50,000 spectra/s enabled by a scanning Fourier-domain delay line. *Vibrational Spectroscopy*, 91:163–169, 2017. ISSN 0924-2031. doi: 10.1016/j.vibspec.2016.07.007.

[87] Takuro Ideguchi, Simon Holzner, Birgitta Bernhardt, Guy Guelachvili, Nathalie Picqué, and Theodor W. Hänsch. Coherent Raman spectro-imaging with laser frequency combs. *Nature*, 502(7471):355–358, 2013. ISSN 0028-0836. doi: 10.1038/nature12607.

[88] Risako Kameyama, Shigekazu Takizawa, Kotaro Hiramatsu, and Keisuke Goda. Dual-Comb Coherent Raman Spectroscopy with near 100% Duty Cycle. *ACS Photonics*, 8 (4):975–981, 2020. ISSN 2330-4022. doi: 10.1021/acsphotonics.0c01656.

[89] Citation report for topic stimulated raman scattering 1962-2020. Technical report, Web of Science Core Collection, Clarivate Analytics, 2021.

[90] T. H. Maiman. Stimulated Optical Radiation in Ruby. *Nature*, 187(4736):493–494, 1960. ISSN 0028-0836. doi: 10.1038/187493a0.

[91] Charles H. Townes. The first laser. In Laura Garwin and Tim Lincoln, editors, *A Century of Nature: Twenty-One Discoveries that Changed Science and the World*, chapter 8, pages 107–112. University of Chicago Press, first edition, 2003. ISBN 0-226-28413-1.

[92] Maria Göppert-Mayer. *Über Elementarakte mit zwei Quantensprüngen*. PhD thesis, Georg-August-Universität Göttingen, 1930.

[93] P. A. Franken, A. E. Hill, C. W. Peters, and G. Weinreich. Generation of Optical Harmonics. *Physical Review Letters*, 7(4):118–119, 1961. ISSN 0031-9007. doi: 10.1103/physrevlett.7.118.

[94] W. Kaiser and C. G. B. Garrett. Two-Photon Excitation in $CaF_2$:$Eu^{2+}$. *Phys. Rev. Lett.*, 7:229—231, 1961. doi: 10.1103/physrevlett.7.229. URL `https://link.aps.org/doi/10.1103/PhysRevLett.7.229`.

[95] R. W. Terhune, P. D. Maker, and C. M. Savage. Optical Harmonic Generation in Calcite. *Physical Review Letters*, 8(10):404–406, 1962. ISSN 0031-9007. doi: 10.1103/physrevlett.8.404.

[96] John Kerr LL.D. XL. A new relation between electricity and light: Dielectrified media birefringent. *The London, Edinburgh, and Dublin Philosophical Magazine and Journal of Science*, 50(332):337–348, 1875. ISSN 1941-5982. doi: 10.1080/14786447508641302.

[97] John Kerr LL.D. LIV. A new relation between electricity and light: Dielectrified media birefringent (Second paper). *The London, Edinburgh, and Dublin Philosophical Magazine and Journal of Science*, 50(333):446–458, 1875. ISSN 1941-5982. doi: 10.1080/14786447508641319.

[98] E. F. Kingsbury. The Kerr Electrostatic Effect. *Review of Scientific Instruments*, 1 (1):22–32, 1930. ISSN 0034-6748. doi: 10.1063/1.1748632.

[99] Frank G. Dunnington. The Electrooptical Shutter—its Theory and Technique. *Physical Review*, 38(8):1506–1534, 1931. ISSN 0031-899X. doi: 10.1103/physrev.38.1506.

[100] F. J. McClung and R. W. Hellwarth. Giant Optical Pulsations from Ruby. *Journal of Applied Physics*, 33(3):828–829, 1962. ISSN 0021-8979. doi: 10.1063/1.1777174.

[101] James P. O'Donovan. Generation of extremely high peak power optical pulsations from ruby utilizing the pulsed-reflector mode. Master's thesis, U.S. Naval Postgraduate School, 1962. URL `http://hdl.handle.net/10945/12256`.

[102] A. Dadieu, K. W. F. Kohlrausch, and Alexander Hollaender. The Raman Effect in Organic Substances and its Use in Chemical Problems. *Journal of the Optical Society of America*, 21(5):286, 1931. ISSN 0030-3941. doi: 10.1364/josa.21.000286.

[103] J.H.S. Green, W. Kynaston, and A.S. Lindsey. The vibrational spectra of benzene derivatives—I Nitrobenzene, the benzoate ion, alkali metal benzoates and salicylates. *Spectrochimica Acta*, 17(5):486–502, 1961. ISSN 0371-1951. doi: 10.1016/0371-1951(61)80103-3.

[104] E. J. Woodbury and W.K. Ng. Ruby laser operation in near IR. *Proceedings of the Institute of Radio Engineers*, 50:2367, 1962.

[105] G. F. Smith. Research on Coherent Generation of Optical Radiation. Technical report, Hughes Research Laboratores, Contract AF 33(616)-8233, October 1962. URL `https://apps.dtic.mil/dtic/tr/fulltext/u2/296785.pdf`.

[106] N. Bloembergen. The Stimulated Raman Effect. *American Journal of Physics*, 35(11):989–1023, 11 1967. ISSN 0002-9505. doi: 10.1119/1.1973774.

[107] Gisela Eckhardt, R. W. Hellwarth, F. J. McClung, S. E. Schwarz, D. Weiner, and E. J. Woodbury. Stimulated Raman Scattering From Organic Liquids. *Phys. Rev. Lett.*, 9:455—457, 1962. doi: 10.1103/physrevlett.9.455. URL `https://link.aps.org/doi/10.1103/PhysRevLett.9.455`.

[108] J. A. Armstrong, N. Bloembergen, J. Ducuing, and P. S. Pershan. Interactions between Light Waves in a Nonlinear Dielectric. *Physical Review*, 127(6):1918–1939, 1962. ISSN 0031-899X. doi: 10.1103/physrev.127.1918.

[109] Y. R. Shen and N. Bloembergen. Theory of Stimulated Brillouin and Raman Scattering. *Physical Review*, 137(6A):A1787–A1805, 1965. ISSN 0031-899X. doi: 10.1103/physrev.137.a1787.

[110] Chen-Show Wang. Theory of Stimulated Raman Scattering. *Physical Review*, 182(2):482–494, 1969. ISSN 0031-899X. doi: 10.1103/physrev.182.482.

[111] N. Bloembergen and Y. R. Shen. Coupling Between Vibrations and Light Waves in Raman Laser Media. *Physical Review Letters*, 12(18):504–507, 1964. ISSN 0031-9007. doi: 10.1103/physrevlett.12.504.

[112] R. W. Hellwarth. Theory of Stimulated Raman Scattering. *Phys. Rev.*, 130:1850—1852, 1963. doi: 10.1103/physrev.130.1850. URL `https://link.aps.org/doi/10.1103/PhysRev.130.1850`.

[113] R. W. Terhune and P. D. Maker. Nonlinear Optics. *Bull. Am. Phys. Soc.*, 1963.

[114] Tatsuo Yajima and Masamoto Takatsuji. Higher order optical mixing of raman laser light in nonlinear dielectric media. *Journal of the Physical Society of Japan*, 19(12):2343–2344, 1964. doi: 10.1143/JPSJ.19.2343.

[115] P. D. Maker and R. W. Terhune. Study of Optical Effects Due to an Induced Polarization Third Order in the Electric Field Strength. *Physical Review*, 137(3A):801–818, 1965.

[116] R W Minck, R W Terhune, and W G Rado. Laser-Stimulated Raman Effect and Resonant Four-Photon Interactions in gases $H_2$, $D_2$, and $CH_4$. *Applied Physics Letters*, 3(10):181–184, 1963. ISSN 0003-6951. doi: 10.1063/1.1753840.

[117] Gisela Eckhardt, D P Bortfeld, and M Geller. Stimulated Emission of Stokes and Anti-Stokes Raman Lines from Diamond, Calcite, and alpha-Sulfur Single Crystals. *Applied Physics Letters*, 3(8):137–138, 1963. ISSN 0003-6951. doi: 10.1063/1.1753903.

[118] T R Loree, R C Sze, and D L Barker. Efficient Raman shifting of ArF and KrF laser wavelengths. *Applied Physics Letters*, 31(1):37–39, 1977. ISSN 0003-6951. doi: 10.1063/1.89470.

[119] A S Eremenko, S N Karpukhin, and A I Stepanov. Stimulated Raman scattering of the second harmonic of a neodymium laser in nitrate crystals. *Soviet Journal of Quantum Electronics*, 10(1):113–114, 1980. ISSN 0049-1748. doi: 10.1070/qe1980v010n01abeh009872.

[120] A. M. Ivanchyuk, M. A. Terpogosyan, P. A. Shachverdov, V. D. Belayev, V. L. Ermolaev, and N. P. Ticonova. SRS of the Second Harmonic of Neodymium Laser in Nitrate Crystals. *Optical Spectroscopy*, 59:572–573, 1985.

[121] R H Stolen, E P Ippen, and A R Tynes. Raman Oscillation in Glass Optical Waveguide. *Applied Physics Letters*, 20(2):62–64, 1972. ISSN 0003-6951. doi: 10.1063/1.1654046.

[122] K.X. Liu and E. Garmire. Understanding the formation of the SRS Stokes spectrum in fused silica fibers. *IEEE Journal of Quantum Electronics*, 27(4):1022–1030, 1991. ISSN 0018-9197. doi: 10.1109/3.83337.

[123] K O Hill, B S Kawasaki, and D C Johnson. Low-threshold cw Raman laser. *Applied Physics Letters*, 29(3):181–183, 1976. ISSN 0003-6951. doi: 10.1063/1.89016.

[124] Chinlon Lin and Rogers H Stolen. Backward Raman amplification and pulse steepening in silica fibers. *Applied Physics Letters*, 29(7):428–431, 1976. ISSN 0003-6951. doi: 10.1063/1.89107.

[125] Jean Christophe Bouteiller. Raman fiber lasers for optical communication application. *Annales Des Télécommunications*, 58(9-10):1342–1363, 2003. ISSN 0003-4347. doi: 10.1007/bf03001734.

[126] Luigi Sirleto and Maria Antonietta Ferrara. Fiber Amplifiers and Fiber Lasers Based on Stimulated Raman Scattering: A Review. *Micromachines*, 11(3):247, 2020. ISSN 2072-666X. doi: 10.3390/mi11030247.

[127] J. A. Giordmaine and W. Kaiser. Light Scattering by Coherently Driven Lattice Vibrations. *Physical Review*, 144(2):676–688, 1965. ISSN 0031-899X. doi: 10.1103/physrev.144.676.

[128] A. Laubereau, D. von der Linde, and W. Kaiser. Decay Time of Hot TO Phonons in Diamond. *Physical Review Letters*, 27(12):802–805, 1971. ISSN 0031-9007. doi: 10.1103/physrevlett.27.802.

[129] R. R. Alfano and S. L. Shapiro. Optical Phonon Lifetime Measured Directly with Picosecond Pulses. *Physical Review Letters*, 26(20):1247–1251, 1971. ISSN 0031-9007. doi: 10.1103/physrevlett.26.1247.

[130] A.J. DeMaria, W.H. Glenn Jr., M.J. Brienza, and M.E. Mack. Picosecond laser pulses. *Proceedings of the IEEE*, 57(1):2–25, 1969. ISSN 0018-9219. doi: 10.1109/proc.1969.6864.

[131] E.B. Treacy. Compression of picosecond light pulses. *Physics Letters A*, 28(1):34–35, 1968. ISSN 0375-9601. doi: 10.1016/0375-9601(68)90584-7.

[132] A. Laubereau and W. Kaiser. Vibrational dynamics of liquids and solids investigated by picosecond light pulses. *Reviews of Modern Physics*, 50(3):607–665, 1978. ISSN 0034-6861. doi: 10.1103/revmodphys.50.607.

[133] R L Fork, B I Greene, and C V Shank. Generation of optical pulses shorter than 0.1 psec by colliding pulse mode locking. *Applied Physics Letters*, 38(9):671–672, 1981. ISSN 0003-6951. doi: 10.1063/1.92500.

[134] Donna Strickland and Gerard Mourou. Compression of amplified chirped optical pulses. *Optics Communications*, 55(6):447–449, 1985. ISSN 0030-4018. doi: 10.1016/0030-4018(85)90151-8.

[135] D E Spence, P N Kean, and W Sibbett. 60-fsec pulse generation from a self-mode-locked Ti:sapphire laser. *Optics Letters*, 16(1):42, 1991. ISSN 0146-9592. doi: 10.1364/ol.16.000042.

[136] Keith A Nelson, R J Dwayne Miller, D R Lutz, and M D Fayer. Optical generation of tunable ultrasonic waves. *Journal of Applied Physics*, 53(2):1144–1149, 1982. ISSN 0021-8979. doi: 10.1063/1.329864.

[137] Margaret M. Robinson, Yong-Xin Yan, Edward B. Gamble, Leah Ruby Williams, Jeffrey S. Meth, and Keith A. Nelson. Picosecond impulsive stimulated brillouin scattering: Optical excitation of coherent transverse acoustic waves and application to time-domain investigations of structural phase transitions. *Chemical Physics Letters*, 112(6):491–496, 1984. ISSN 0009-2614. doi: 10.1016/0009-2614(84)85764-4.

[138] S. De Silvestri, J.G. Fujimoto, E.P. Ippen, Edward B. Gamble, Leah Ruby Williams, and Keith A. Nelson. Femtosecond time-resolved measurements of optic phonon dephasing by impulsive stimulated raman scattering in $\alpha$-perylene crystal from 20 to 300 K. *Chemical Physics Letters*, 116(2-3):146–152, 1985. ISSN 0009-2614. doi: 10.1016/0009-2614(85)80143-3.

[139] S Ruhman, Alan G Joly, and Keith A Nelson. Time-resolved observations of coherent molecular vibrational motion and the general occurrence of impulsive stimulated scattering. *The Journal of Chemical Physics*, 86(11):6563–6565, 1987. ISSN 0021-9606. doi: 10.1063/1.452400.

[140] Lisa Dhar, John A. Rogers, and Keith A. Nelson. Time-resolved vibrational spectroscopy in the impulsive limit. *Chemical Reviews*, 94(1):157–193, 1994. ISSN 0009-2665. doi: 10.1021/cr00025a006.

[141] J. Chesnoy and A. Mokhtari. Resonant impulsive-stimulated Raman scattering on malachite green. *Physical Review A*, 38(7):3566–3576, 1988. ISSN 1050-2947. doi: 10.1103/physreva.38.3566.

[142] S.L. Dexheimer, Q. Wang, L.A. Peteanu, W.T. Pollard, R.A. Mathies, and C.V. Shank. Femtosecond impulsive excitation of nonstationary vibrational states in bacteriorhodopsin. *Chemical Physics Letters*, 188(1-2):61–66, 1992. ISSN 0009-2614. doi: 10.1016/0009-2614(92)85089-s.

[143] Taiha Joo and A.C. Albrecht. Vibrational frequencies and dephasing times in excited electronic states by femtosecond time-resolved four-wave mixing. *Chemical Physics*, 173(1):17–26, 1993. ISSN 0301-0104. doi: 10.1016/0301-0104(93)80213-s.

[144] David W. McCamant, Philipp Kukura, and Richard A. Mathies. Femtosecond time-resolved stimulated raman spectroscopy: application to the ultrafast internal conversion in β-carotene. *The Journal of Physical Chemistry A*, 107(40):8208–8214, oct 2003. ISSN 1089-5639. doi: 10.1021/jp030147n.

[145] Philipp Kukura, David W McCamant, and Richard A Mathies. Femtosecond stimulated Raman spectroscopy. *Annual review of physical chemistry*, 58:461–88, 2007. ISSN 0066-426X. doi: 10.1146/annurev.physchem.58.032806.104456.

[146] Neil A. Smith and Stephen R. Meech. Optically-heterodyne-detected optical kerr effect (ohd-oke): Applications in condensed phase dynamics. *International Reviews in Physical Chemistry*, 21(1):75–100, 2002. doi: 10.1080/01442350110092701.

[147] D. Heiman, R. W. Hellwarth, M. D. Levenson, and Graham Martin. Raman-induced kerr effect. *Phys. Rev. Lett.*, 36:189–192, Jan 1976. doi: 10.1103/PhysRevLett.36.189.

[148] E. Ploetz, S. Laimgruber, S. Berner, W. Zinth, and P. Gilch. Femtosecond stimulated Raman microscopy. *Applied Physics B*, 87(3):389—393, 2007. ISSN 1432-0649. doi: 10.1007/s00340-007-2630-x. URL `https://doi.org/10.1007/s00340-007-2630-x`.

[149] Christian W. Freudiger, Wei Min, Brian G. Saar, Sijia Lu, Gary R. Holtom, Chengwei He, Jason C. Tsai, Jing X. Kang, and X. Sunney Xie. Label-Free Biomedical Imaging with High Sensitivity by Stimulated Raman Scattering Microscopy. *Science*, 322(5909): 1857—1861, 2008. ISSN 0036-8075. doi: 10.1126/science.1165758. URL `http://science.sciencemag.org/content/322/5909/1857`.

[150] Conor L. Evans and X. Sunney Xie. Coherent Anti-Stokes Raman Scattering Microscopy: Chemical Imaging for Biology and Medicine. *Annual Review of Analytical Chemistry*, 1(1):883—909, 2008. doi: 10.1146/annurev.anchem.1.031207.112754. URL https://doi.org/10.1146/annurev.anchem.1.031207.112754.

[151] Ji-Xin Cheng and Xiaoliang Sunney Xie, editors. *Coherent Raman Scattering Microscopy*. CRC Press, Baton Rouge, 2013.

[152] Alba Alfonso-García, Richa Mittal, Eun Seong Lee, and Eric O. Potma. Biological imaging with coherent Raman scattering microscopy: a tutorial. *Journal of Biomedical Optics*, 19(7):071407–071407, 2014. ISSN 1083-3668. doi: 10.1117/1.jbo.19.7.071407.

[153] Leica TCS CARS: First Confocal System With CARS Imaging. Technical report, Wiley Analytical Science, 2012.

[154] Eric O. Potma, Wim P. de Boeij, and Douwe A. Wiersma. Femtosecond Dynamics of Intracellular Water Probed with Nonlinear Optical Kerr Effect Microspectroscopy. *Biophysical Journal*, 80(6):3019–3024, 2001. ISSN 0006-3495. doi: 10.1016/s0006-3495(01)76267-4. URL http://www.sciencedirect.com/science/article/pii/S0006349501762674.

[155] B. Levine and C. Bethea. Ultrahigh sensitivity stimulated Raman gain spectroscopy. *IEEE Journal of Quantum Electronics*, 16(1):85–89, 1980. ISSN 0018-9197. doi: 10.1109/jqe.1980.1070342.

[156] Dennis P Strommen and Kazuo Nakamoto. Resonance Raman spectroscopy. *Journal of Chemical Education*, 54(8):474, 1977. ISSN 0021-9584. doi: 10.1021/ed054p474.

[157] Lu Wei and Wei Min. Electronic Preresonance Stimulated Raman Scattering Microscopy. *The Journal of Physical Chemistry Letters*, 9(15):4294–4301, 2018. ISSN 1948-7185. doi: 10.1021/acs.jpclett.8b00204.

[158] Martin Moskovits. Surface-enhanced spectroscopy. *Rev. Mod. Phys.*, 57:783–826, 1985. URL https://link.aps.org/doi/10.1103/RevModPhys.57.783.

[159] Christy L Haynes, Adam D. Mcfarland, and R. P. Van Duyne. Surface-enhanced raman spectroscopy. *Analytical Chemistry*, 2005.

[160] Xiang Wang, Sheng-Chao Huang, Shu Hu, Sen Yan, and Bin Ren. Fundamental understanding and applications of plasmon-enhanced Raman spectroscopy. *Nature Reviews Physics*, 2(5):253–271, 2020. doi: 10.1038/s42254-020-0171-y.

[161] B. F. Levine, C. V. Shank, and J. P. Heritage. Surface vibrational spectroscopy using stimulated raman scattering. *IEEE J. Quantum Electron.*, 15:1418–1432, 1979.

[162] J.P. Heritage, J.G. Bergman, A. Pinczuk, and J.M. Worlock. Surface picosecond raman gain spectroscopy of a cyanide monolayer on silver. *Chem. Phys. Lett.*, 67(2):229–232, 1979.

[163] Emily L. Keller, Nathaniel C. Brandt, Alyssa A. Cassabaum, and Renee R. Frontiera. Ultrafast surface-enhanced Raman spectroscopy. *Analyst*, 140(15):4922–4931, 2015. ISSN 0003-2654. doi: 10.1039/c5an00869g.

[164] H. Kumar Wickramasinghe, Marc Chaigneau, Ryohei Yasukuni, Gennaro Picardi, and Razvigor Ossikovski. Billion-Fold Increase in Tip-Enhanced Raman Signal. *ACS Nano*, 8(4):3421–3426, 2014. ISSN 1936-0851. doi: 10.1021/nn406263m.

[165] A. Diaspro and P. Bianchini. Optical nanoscopy. *La Rivista del Nuovo Cimento*, 43 (8):385–455, 2020. ISSN 0393-697X. doi: 10.1007/s40766-020-00008-1.

[166] Stefan W Hell and Jan Wichmann. Breaking the diffraction resolution limit by stimulated emission: stimulated-emission-depletion fluorescence microscopy. *Optics Letters*, 19(11):780, 1994. ISSN 0146-9592. doi: 10.1364/ol.19.000780.

[167] Li Gong and Haifeng Wang. Suppression of stimulated Raman scattering by an electromagnetically-induced-transparency–like scheme and its application for super-resolution microscopy. *Physical Review A*, 92(2):023828, 2015. ISSN 1050-2947. doi: 10.1103/physreva.92.023828.

[168] Li Gong and Haifeng Wang. Breaking the diffraction limit by saturation in stimulated-Raman-scattering microscopy: A theoretical study. *Physical Review A*, 90(1):013818, 2014. ISSN 1050-2947. doi: 10.1103/physreva.90.013818.

[169] W. Ruchira Silva, Christian T. Graefe, and Renee R. Frontiera. Toward Label-Free Super-Resolution Microscopy. *ACS Photonics*, 3(1):79–86, 2016. ISSN 2330-4022. doi: 10.1021/acsphotonics.5b00467.

[170] Christian T Graefe, David Punihaole, Celina M Harris, Michael J Lynch, Ryan Leighton, and Renee R Frontiera. Far-Field Super-Resolution Vibrational Spectroscopy. *Analytical Chemistry*, 91(14):8723–8731, 2019. ISSN 0003-2700. doi: 10.1021/acs.analchem.9b01731.

[171] Li Gong, Wei Zheng, Ying Ma, and Zhiwei Huang. Saturated stimulated-raman-scattering microscopy for far-field superresolution vibrational imaging. *Phys. Rev. Applied*, 11:034041, Mar 2019. doi: 10.1103/PhysRevApplied.11.034041.

[172] Y. Bi, C. Yang, Y. Chen, Y. Chen, S. Yan, G. Yang, Y. Wu, G. Zhang, and P. Wang. Near-resonance enhanced label-free stimulated raman scattering microscopy with spatial resolution near 130nm. *Light Sci. Appl.*, 7:81, 2018. doi: 10.1038/s41377-018-0082-1.

[173] Shaul Mukamel. *Principles of Nonlinear Optical Spectroscopy*. Oxford University Press, 1 edition, 1995.

[174] Chao-Yu Chung, Julie Hsu, Shaul Mukamel, and Eric O. Potma. Controlling stimulated coherent spectroscopy and microscopy by a position-dependent phase. *Physical Review A*, 87(3):033833, 2013. ISSN 1050-2947. doi: 10.1103/physreva.87.033833.

[175] Richard C. Prince, Renee R. Frontiera, and Eric O. Potma. Stimulated Raman Scattering: From Bulk to Nano. *Chemical Reviews*, 117(7):5070—5094, 2017. doi: 10.1021/acs.chemrev.6b00545. URL https://doi.org/10.1021/acs.chemrev.6b00545.

[176] Philipp Kukura, David W. McCamant, Sangwoon Yoon, Daniel B. Wandschneider, and Richard A. Mathies. Structural Observation of the Primary Isomerization in Vision with Femtosecond-Stimulated Raman. *Science*, 310(5750):1006–1009, 2005. ISSN 0036-8075. doi: 10.1126/science.1118379.

[177] Masayuki Yoshizawa, Yasuhiro Hattori, and Takayoshi Kobayashi. Femtosecond time-resolved resonance raman gain spectroscopy in polydiacetylene. *Phys. Rev. B*, 49: 13259–13262, May 1994. doi: 10.1103/PhysRevB.49.13259. URL https://link.aps.org/doi/10.1103/PhysRevB.49.13259.

[178] M. Yoshizawa, H. Aoki, and H. Hashimoto. Vibrational relaxation of the $2A_g^-$ excited state in all-trans-$\beta$-carotene obtained by femtosecond time-resolved raman spectroscopy. *Phys. Rev. B*, 63:180301, Apr 2001. doi: 10.1103/PhysRevB.63.180301. URL https://link.aps.org/doi/10.1103/PhysRevB.63.180301.

[179] Daniel R. Dietze and Richard A. Mathies. Femtosecond stimulated raman spectroscopy. *ChemPhysChem*, 17(9):1224–1251, 2016. doi: https://doi.org/10.1002/cphc.201600104.

[180] David W. McCamant, Philipp Kukura, Sangwoon Yoon, and Richard A. Mathies. Femtosecond broadband stimulated raman spectroscopy: Apparatus and methods. *Review of Scientific Instruments*, 75(11):4971–4980, 2004. doi: 10.1063/1.1807566.

[181] Shaul Mukamel and Jason D. Biggs. Communication: Comment on the effective temporal and spectral resolution of impulsive stimulated raman signals. *The Journal of Chemical Physics*, 134(16):161101, 2011. doi: 10.1063/1.3581889.

[182] Yue-Chao Wu, Bin Zhao, and Soo-Y. Lee. Time-dependent wave packet averaged vibrational frequencies from femtosecond stimulated raman spectra. *The Journal of Chemical Physics*, 144(5):054104, 2016. doi: 10.1063/1.4941057.

[183] Michele Marrocco. Vectorial descriptions of nonlinear Raman microscopy. *Journal of Raman Spectroscopy*, 41(8):882–889, 2010. ISSN 1097-4555. doi: 10.1002/jrs.2672.

[184] Ji-Xin Cheng, Andreas Volkmer, and X Sunney Xie. Theoretical and experimental characterization of coherent anti-Stokes Raman scattering microscopy. *Journal of the Optical Society of America B*, 19(6):1363, 2002. ISSN 0740-3224. doi: 10.1364/josab.19.001363.

[185] B. Richards and E. Wolf. Electromagnetic diffraction in optical systems, II. Structure of the image field in an aplanatic system. *Proceedings of the Royal Society of London. Series A. Mathematical and Physical Sciences*, 253(1274):358–379, 1959. ISSN 0080-4630. doi: 10.1098/rspa.1959.0200.

[186] Hanqing Xiong, Naixin Qian, Zhilun Zhao, Lingyan Shi, Yupeng Miao, and Wei Min. Background-free imaging of chemical bonds by a simple and robust frequency-modulated stimulated Raman scattering microscopy. *Optics Express*, 28(10):15663, 2020. doi: 10.1364/oe.391016.

[187] Dan Fu, Fa-Ke Lu, Xu Zhang, Christian Freudiger, Douglas R. Pernik, Gary Holtom, and Xiaoliang Sunney Xie. Quantitative Chemical Imaging with Multiplex Stimulated Raman Scattering Microscopy. *Journal of the American Chemical Society*, 134(8): 3623–3626, 2012. ISSN 0002-7863. doi: 10.1021/ja210081h.

[188] Julien Réhault, Francesco Crisafi, Vikas Kumar, Gustavo Ciardi, Marco Marangoni, Giulio Cerullo, and Dario Polli. Broadband stimulated raman scattering with fourier-transform detection. *Opt. Express*, 23(19):25235–25246, Sep 2015. doi: 10.1364/OE.23.025235. URL `http://www.opticsexpress.org/abstract.cfm?URI=oe-23-19-25235`.

[189] A. Ragni, G. Sciortino, M. Sampietro, G. Ferrari, and D. Polli. Multi-channel lock-in based differential front-end for broadband raman spectroscopy. *Integration*, 67: 44–49, 2019. ISSN 0167-9260. doi: https://doi.org/10.1016/j.vlsi.2019.03.001. URL `https://www.sciencedirect.com/science/article/pii/S0167926018305315`.

[190] Chi Zhang, Delong Zhang, and Ji-Xin Cheng. Coherent Raman Scattering Microscopy in Biology and Medicine. *Annual Review of Biomedical Engineering*, 17(1):1–31, 2014. ISSN 1523-9829. doi: 10.1146/annurev-bioeng-071114-040554.

[191] W. J. Tipping, M. Lee, A. Serrels, V. G. Brunton, and A. N. Hulme. Stimulated Raman scattering microscopy: an emerging tool for drug discovery. *Chem. Soc. Rev.*, 45:2075–2089, 2016. doi: 10.1039/c5cs00693g. URL `http://dx.doi.org/10.1039/C5CS00693G`.

[192] Fanghao Hu, Lixue Shi, and Wei Min. Biological imaging of chemical bonds by stimulated Raman scattering microscopy. *Nature Methods*, 16(9):830–842, 2019. ISSN 1548-7091. doi: 10.1038/s41592-019-0538-0.

[193] Andrew H Hill and Dan Fu. Cellular Imaging Using Stimulated Raman Scattering Microscopy. *Analytical Chemistry*, 91(15):9333–9342, 2019. ISSN 0003-2700. doi: 10.1021/acs.analchem.9b02095.

[194] Brian G. Saar, Christian W. Freudiger, Jay Reichman, C. Michael Stanley, Gary R. Holtom, and X. Sunney Xie. Video-Rate Molecular Imaging in Vivo with Stimulated Raman Scattering. *Science*, 330(6009):1368–70, 2010. ISSN 0036-8075. doi: 10.1126/science.1197236.

[195] Delong Zhang, Ping Wang, Mikhail N Slipchenko, and Ji-Xin Cheng. Fast vibrational imaging of single cells and tissues by stimulated Raman scattering microscopy. *Accounts of Chemical Research*, 47(8), 2014. ISSN 0001-4842. doi: 10.1021/ar400331q.

[196] Y. Ozeki and K. Itoh. Stimulated Raman scattering microscopy for live-cell imaging with high contrast and high sensitivity. *Laser Physics*, 20(5):1114–1118, 2010. ISSN 1054-660X. doi: 10.1134/s1054660x10090318.

[197] Andrew Folick, Wei Min, and Meng C Wang. Label-free imaging of lipid dynamics using Coherent Anti-stokes Raman Scattering (CARS) and Stimulated Raman Scattering (SRS) microscopy. *Current Opinion in Genetics & Development*, 21(5):585–590, 2011. ISSN 0959-437X. doi: 10.1016/j.gde.2011.09.003.

[198] Chen Cao, Dong Zhou, Tao Chen, Aaron M Streets, and Yanyi Huang. Label-Free Digital Quantification of Lipid Droplets in Single Cells by Stimulated Raman Microscopy on a Microfluidic Platform. *Analytical Chemistry*, 88(9):4931–4939, 2016. ISSN 0003-2700. doi: 10.1021/acs.analchem.6b00862.

[199] Alba García, Jerry Paugh, Marjan Farid, Sumit Garg, James Jester, and Eric Potma. A machine learning framework to analyze hyperspectral stimulated Raman scattering microscopy images of expressed human meibum. *Journal of Raman Spectroscopy*, 48 (6):803–812, 2017. ISSN 1097-4555. doi: 10.1002/jrs.5118.

[200] Mridula Sunder, Neha Acharya, Smitha Nayak, and Nirmal Mazumder. Optical spectroscopy and microscopy techniques for assessment of neurological diseases. *Applied Spectroscopy Reviews*, pages 1–40, 2020. ISSN 0570-4928. doi: 10.1080/05704928.2020.1851237.

[201] Sun Woong Kim, Chang Rae Rho, Jinseor Kim, Yilu Xie, Richard C. Prince, Khawla Mustafa, Eric O. Potma, Donald J. Brown, and James V. Jester. Eicosapentaenoic acid (EPA) activates PPAR$\gamma$ signaling leading to cell cycle exit, lipid accumulation, and autophagy in human meibomian gland epithelial cells (hMGEC). *The Ocular Surface*, 18(3):427–437, 2020. ISSN 1542-0124. doi: 10.1016/j.jtos.2020.04.012.

[202] Kai-Chih Huang, Junjie Li, Chi Zhang, Yuying Tan, and Ji-Xin Cheng. Multiplex Stimulated Raman Scattering Imaging Cytometry Reveals Lipid-Rich Protrusions in Cancer Cells under Stress Condition. *iScience*, 23(3):100953, 2020. ISSN 2589-0042. doi: 10.1016/j.isci.2020.100953.

[203] Chun-Rui Hu, Delong Zhang, Mikhail N. Slipchenko, Ji-Xin Cheng, and Bing Hu. Label-free real-time imaging of myelination in the Xenopus laevis tadpole by in vivo stimulated Raman scattering microscopy. *Journal of Biomedical Optics*, 19(8):086005–086005, 2014. ISSN 1083-3668. doi: 10.1117/1.jbo.19.8.086005.

[204] Fa-Ke Lu, Srinjan Basu, Vivien Igras, Mai P. Hoang, Minbiao Ji, Dan Fu, Gary R. Holtom, Victor A. Neel, Christian W. Freudiger, David E. Fisher, and X. Sunney Xie. Label-free dna imaging in vivo with stimulated raman scattering microscopy. *Proceedings of the National Academy of Sciences*, 112(37):11624–11629, 2015. ISSN 0027-8424. doi: 10.1073/pnas.1515121112. URL `https://www.pnas.org/content/112/37/11624`.

[205] Xu Zhang, Maarten B. J. Roeffaers, Srinjan Basu, Joseph R. Daniele, Dan Fu, Christian W. Freudiger, Gary R. Holtom, and X. Sunney Xie. Label-Free Live-Cell Imaging of Nucleic Acids Using Stimulated Raman Scattering Microscopy. *ChemPhysChem*, 13 (4):1054–1059, 2012. ISSN 1439-7641. doi: 10.1002/cphc.201100890.

[206] Luyuan Zhang and Wei Min. Bioorthogonal chemical imaging of metabolic changes during epithelial–mesenchymal transition of cancer cells by stimulated Raman scattering microscopy. *Journal of Biomedical Optics*, 22(10):1, 2017. ISSN 1083-3668. doi: 10.1117/1.jbo.22.10.106010.

[207] Richa Mittal, Mihaela Balu, Tatiana Krasieva, Eric O. Potma, Laila Elkeeb, Christopher B. Zachary, and Petra Wilder-Smith. Evaluation of stimulated raman scattering microscopy for identifying squamous cell carcinoma in human skin. *Lasers in Surgery and Medicine*, 45(8):496–502, 2013. ISSN 1096-9101. doi: 10.1002/lsm.22168.

[208] Minbiao Ji, Daniel A. Orringer, Christian W. Freudiger, Shakti Ramkissoon, Xiaohui Liu, Darryl Lau, Alexandra J. Golby, Isaiah Norton, Marika Hayashi, Nathalie Y. R. Agar, Geoffrey S. Young, Cathie Spino, Sandro Santagata, Sandra Camelo-Piragua, Keith L. Ligon, Oren Sagher, and X. Sunney Xie. Rapid, Label-Free Detection of Brain Tumors with Stimulated Raman Scattering Microscopy. *Science Translational Medicine*, 5(201):201ra119–201ra119, 2013. ISSN 1946-6234. doi: 10.1126/scitranslmed.3005954.

[209] Kseniya S. Shin, Andrew T. Francis, Andrew H. Hill, Mint Laohajaratsang, Patrick J. Cimino, Caitlin S. Latimer, Luis F. Gonzalez-Cuyar, Laligam N. Sekhar, Gordana Juric-Sekhar, and Dan Fu. Intraoperative assessment of skull base tumors using stimulated Raman scattering microscopy. *Scientific Reports*, 9(1):20392, 2019. doi: 10.1038/s41598-019-56932-8.

[210] Barbara Sarri, Rafaël Canonge, Xavier Audier, Emma Simon, Julien Wojak, Fabrice Caillol, Cécile Cador, Didier Marguet, Flora Poizat, Marc Giovannini, and Hervé Rigneault. Fast stimulated Raman and second harmonic generation imaging for intraoperative gastro-intestinal cancer detection. *Scientific Reports*, 9(1):10052, 2019. doi: 10.1038/s41598-019-46489-x.

[211] Lauren A. Austin, Sam Osseiran, and Conor L. Evans. Raman technologies in cancer diagnostics. *Analyst*, 141(2):476–503, 2015. ISSN 0003-2654. doi: 10.1039/c5an01786f.

[212] J Moger, N Garrett, and Begley -D of Raman .... Imaging cortical vasculature with stimulated Raman scattering and two-photon photothermal lensing microscopy. *Journal of Raman Spectroscopy*, 2012. doi: 10.1002/jrs.3156.

[213] Ping Wang, Junjie Li, Pu Wang, Chun-Rui Hu, Delong Zhang, Michael Sturek, and Ji-Xin Cheng. Label-Free Quantitative Imaging of Cholesterol in Intact Tissues by Hyperspectral Stimulated Raman Scattering Microscopy. *Angewandte Chemie International Edition*, 52(49):13042–13046, 2013. ISSN 1521-3773. doi: 10.1002/anie.201306234.

[214] Jerry R. Paugh, Alba Alfonso-Garcia, Andrew Loc Nguyen, Jeffrey L. Suhalim, Marjan Farid, Sumit Garg, Jeremiah Tao, Donald J. Brown, Eric O. Potma, and James V. Jester. Characterization of expressed human meibum using hyperspectral stimulated Raman scattering microscopy. *The Ocular Surface*, 17(Ocul Surf 5 2007):151–159, 2018. ISSN 1542-0124. doi: 10.1016/j.jtos.2018.10.003.

[215] Kun Miao and Lu Wei. Live-Cell Imaging and Quantification of PolyQ Aggregates by Stimulated Raman Scattering of Selective Deuterium Labeling. *ACS Central Science*, 6(4):478–486, 2020. ISSN 2374-7943. doi: 10.1021/acscentsci.9b01196.

[216] Lingyan Shi, Anthony A. Fung, and Andy Zhou. Advances in stimulated Raman scattering imaging for tissues and animals. *Quantitative Imaging in Medicine and Surgery*, 11(3):1078101–1071101, 2020. ISSN 2223-4306. doi: 10.21037/qims-20-712.

[217] Benjamin Figueroa, Walter Fu, Tai Nguyen, Kseniya Shin, Bryce Manifold, Frank Wise, and Dan Fu. Broadband hyperspectral stimulated Raman scattering microscopy with a parabolic fiber amplifier source. *Biomedical Optics Express*, 9(12):6116, 2018. ISSN 2156-7085. doi: 10.1364/boe.9.006116.

[218] Minbiao Ji, Michal Arbel, Lili Zhang, Christian W. Freudiger, Steven S. Hou, Dongdong Lin, Xinju Yang, Brian J. Bacskai, and X. Sunney Xie. Label-free imaging of amyloid plaques in Alzheimer's disease with stimulated Raman scattering microscopy. *Science Advances*, 4(11):eaat7715, 2018. ISSN 2375-2548. doi: 10.1126/sciadv.aat7715.

[219] Sicong He, Cong Ye, Qiqi Sun, Christopher K.S. Leung, and Jianan Y. Qu. Label-free nonlinear optical imaging of mouse retina. *Biomedical Optics Express*, 6(3):1055, feb 2015. doi: 10.1364/boe.6.001055.

[220] Shuya Satoh, Yoichi Otsuka, Yasuyuki Ozeki, Kazuyoshi Itoh, Akinori Hashiguchi, Ken Yamazaki, Hiroyuki Hashimoto, and Michiie Sakamoto. Label-free visualization of acetaminophen-induced liver injury by high-speed stimulated Raman scattering spectral microscopy and multivariate image analysis. *Pathology International*, 64(10): 518–526, 2014. ISSN 1440-1827. doi: 10.1111/pin.12206.

[221] Zi Wang, Wei Zheng, Stephen Chin-Ying Hsu, and Zhiwei Huang. Optical diagnosis and characterization of dental caries with polarization-resolved hyperspectral stimulated Raman scattering microscopy. *Biomedical Optics Express*, 7(4):1284–1293, 2016. ISSN 2156-7085. doi: 10.1364/boe.7.001284.

[222] Bohan Zhang, Hanlin Xu, Jun Chen, Xiaoxia Zhu, Yu Xue, Yifan Yang, Jianpeng Ao, Yinghui Hua, and Minbiao Ji. Highly specific and label-free histological identification of microcrystals in fresh human gout tissues with stimulated Raman scattering. *Theranostics*, 11(7):3074–3088, 2021. ISSN 1838-7640. doi: 10.7150/thno.53755.

[223] Chen Zeng, Fanghao Hu, Rong Long, and Wei Min. A ratiometric Raman probe for live-cell imaging of hydrogen sulfide in mitochondria by stimulated Raman scattering. *Analyst*, 143:4844–4848, 2018. doi: 10.1039/c8an00910d. URL `http://dx.doi.org/10.1039/C8AN00910D`.

[224] Lu Wei, Fanghao Hu, Zhixing Chen, Yihui Shen, Luyuan Zhang, and Wei Min. Live-Cell Bioorthogonal Chemical Imaging: Stimulated Raman Scattering Microscopy of Vibrational Probes. *Accounts of Chemical Research*, 49(8):1494—1502, 2016. doi: 10.1021/acs.accounts.6b00210. URL `https://doi.org/10.1021/acs.accounts.6b00210`.

[225] Georgette Azemtsop Matanfack, Jan Rüger, Clara Stiebing, Michael Schmitt, and Jürgen Popp. Imaging the invisible—Bioorthogonal Raman probes for imaging of cells and tissues. *Journal of Biophotonics*, 13(9):e202000129, 2020. ISSN 1864-063X. doi: 10.1002/jbio.202000129.

[226] George R. Littlejohn, Jessica C. Mansfield, Jacqueline T. Christmas, Eleanor Witterick, Mark D. Fricker, Murray R. Grant, Nicholas Smirnoff, Richard M. Everson, Julian Moger, and John Love. An update: improvements in imaging perfluorocarbon-mounted plant leaves with implications for studies of plant pathology, physiology, development and cell biology. *Frontiers in Plant Science*, 5:140, 2014. doi: 10.3389/fpls.2014.00140.

[227] Qingyan Hu, Li-Lin Tay, Matthew Noestheden, and John Paul Pezacki. Mammalian Cell Surface Imaging with Nitrile-Functionalized Nanoprobes: Biophysical Characterization of Aggregation and Polarization Anisotropy in SERS Imaging. *Journal of the American Chemical Society*, 129(1):14–15, 2007. ISSN 0002-7863. doi: 10.1021/ja0670005.

[228] Jason M. Crawford, Cyril Portmann, Xu Zhang, Maarten B. J. Roeffaers, and Jon Clardy. Small molecule perimeter defense in entomopathogenic bacteria. *Proceedings of the National Academy of Sciences*, 109(27):10821–10826, 2012. ISSN 0027-8424. doi: 10.1073/pnas.1201160109.

[229] Fanghao Hu, Lu Wei, Chaogu Zheng, Yihui Shen, and Wei Min. Live-cell vibrational imaging of choline metabolites by stimulated Raman scattering coupled with isotope-based metabolic labeling. *Analyst*, 139(10):2312–2317, 2014. ISSN 0003-2654. doi: 10.1039/c3an02281a.

[230] Yihui Shen, Fang Xu, Lu Wei, Fanghao Hu, and Wei Min. Live-Cell Quantitative Imaging of Proteome Degradation by Stimulated Raman Scattering. *Angewandte Chemie International Edition*, 53(22):5596–5599, 2014. ISSN 1521-3773. doi: 10.1002/anie.201310725.

[231] Henk-Jan van Manen, Aufried Lenferink, and Cees Otto. Noninvasive Imaging of Protein Metabolic Labeling in Single Human Cells Using Stable Isotopes and Raman Microscopy. *Analytical Chemistry*, 80(24):9576–9582, 2008. ISSN 0003-2700. doi: 10.1021/ac801841y.

[232] Nanna M. Sijtsema, Johannes J. Duindam, Gerwin J. Puppels, Cees Otto, and Jan Greve. Imaging with Extrinsic Raman Labels. *Applied Spectroscopy*, 50(5):545–551, 1996. ISSN 0003-7028. doi: 10.1366/0003702963905989.

[233] Jing Ni, Robert J Lipert, G Brent Dawson, and Marc D Porter. Immunoassay Readout Method Using Extrinsic Raman Labels Adsorbed on Immunogold Colloids. *Analytical Chemistry*, 71(21):4903–4908, 1999. ISSN 0003-2700. doi: 10.1021/ac990616a.

[234] Konrad Meister, Johanna Niesel, Ulrich Schatzschneider, Nils Metzler-Nolte, Diedrich A. Schmidt, and Martina Havenith. Label-Free Imaging of Metal–Carbonyl Complexes in Live Cells by Raman Microspectroscopy. *Angewandte Chemie International Edition*, 49(19):3310–3312, 2010. ISSN 1521-3773. doi: 10.1002/anie.201000097.

[235] Kristel Sepp, Martin Lee, Marie T J Bluntzer, G Vignir Helgason, Alison N Hulme, and Valerie G Brunton. Utilizing Stimulated Raman Scattering Microscopy To Study Intracellular Distribution of Label-Free Ponatinib in Live Cells. *Journal of Medicinal Chemistry*, 63(5):2028–2034, 2019. ISSN 0022-2623. doi: 10.1021/acs.jmedchem.9b01546.

[236] Haozheng Li, Yong Cheng, Huajun Tang, Yali Bi, Yage Chen, Guang Yang, Shoujing Guo, Sidan Tian, Jiangshan Liao, Xiaohua Lv, Shaoqun Zeng, Mingqiang Zhu, Chenjie Xu, Ji-Xin Cheng, and Ping Wang. Imaging Chemical Kinetics of Radical Polymerization with an Ultrafast Coherent Raman Microscope. *Advanced Science*, 7 (10):1903644, 2020. ISSN 2198-3844. doi: 10.1002/advs.201903644.

[237] Richard Prince, Peixun Fan, Yongfeng Lu, Tommaso Baldacchini, and Eric O. Potma. Visualizing tpp structures with coherent raman scattering microscopy. In T. Baldacchini, editor, *Three-Dimensional Microfabrication Using Two-Photon Polymerization*, pages 229–249. William Andrew, 2020. doi: 10.1016/b978-0-12-817827-0.00055-2.

[238] Taewoo Lee, Haridas Mundoor, Derek G Gann, Timothy J Callahan, and Ivan I Smalyukh. Imaging of director fields in liquid crystals using stimulated Raman scattering microscopy. *Optics Express*, 21(10):12129, 2013. doi: 10.1364/oe.21.012129.

[239] Julien Duboisset, Pascal Berto, Paulina Gasecka, Fatma-Zohra Bioud, Patrick Ferrand, Hervé Rigneault, and Sophie Brasselet. Molecular Orientational Order Probed by Coherent Anti-Stokes Raman Scattering (CARS) and Stimulated Raman Scattering (SRS) Microscopy: A Spectral Comparative Study. *The Journal of Physical Chemistry B*, 119(7):3242–3249, 2015. ISSN 1520-6106. doi: 10.1021/jp5113813.

[240] Guillaume Fleury and Maarten B. J. Roeffaers. Resolving the Acid Site Distribution in Zn-Exchanged ZSM-5 with Stimulated Raman Scattering Microscopy. *Catalysts*, 10 (11):1331, 2020. doi: 10.3390/catal10111331.

[241] Jessica C Mansfield, George R Littlejohn, Mark P Seymour, Rob J Lind, Sarah Perfect, and Julian Moger. Label-free Chemically Specific Imaging in Planta with Stimulated Raman Scattering Microscopy. *Analytical Chemistry*, 85(10):5055–5063, 2013. ISSN 0003-2700. doi: 10.1021/ac400266a.

[242] Y. Suzuki, Y. Wakisaka, O. Iwata, A. Nakashima, T. Ito, M. Hirose, R. Domon, M. Sugawara, N. Tsumura, H. Watarai, T. Shimobaba, K. Suzuki, K. Goda, and Y. Ozeki. High-speed stimulated Raman scattering microscopy for studying the metabolic diversity of motile Euglena gracilis. In Kevin K. Tsia and Keisuke Goda, editors, *High-Speed*

*Biomedical Imaging and Spectroscopy: Toward Big Data Instrumentation and Management II*, volume 10076, pages 1 – 6. International Society for Optics and Photonics, SPIE, 2017. doi: 10.1117/12.2250455. URL `https://doi.org/10.1117/12.2250455`.

[243] Wei Shen, Cynthia Collings, Muyang Li, Jake Markovicz, John Ralph, Shawn D Mansfield, and Shi-You Ding. Imaging Changes in Cell Walls of Engineered Poplar by Stimulated Raman Scattering and Atomic Force Microscopy. *ACS Sustainable Chemistry & Engineering*, 7(12):10616–10622, 2019. ISSN 2168-0485. doi: 10.1021/acssuschemeng.9b01166.

[244] Takanori Iino, Kenji Hashimoto, Takuya Asai, Kazuyuki Kuchitsu, and Yasuyuki Ozeki. Multicolour chemical imaging of plant tissues with hyperspectral stimulated Raman scattering microscopy. *Analyst*, 2020. ISSN 0003-2654. doi: 10.1039/d0an02181d.

[245] Mikhail N. Slipchenko, Hongtao Chen, David R. Ely, Yookyung Jung, M. Teresa Carvajal, and Ji-Xin Cheng. Vibrational imaging of tablets by epi-detected stimulated Raman scattering microscopy. *Analyst*, 135(10):2613–2619, 2010. ISSN 0003-2654. doi: 10.1039/c0an00252f.

[246] Brian G Saar, L Rodrigo Contreras-Rojas, X Sunney Xie, and Richard H Guy. Imaging Drug Delivery to Skin with Stimulated Raman Scattering Microscopy. *Molecular Pharmaceutics*, 8(3):969–975, 2011. ISSN 1543-8384. doi: 10.1021/mp200122w.

[247] Benjamin Figueroa, Tai Nguyen, Sutthilug Sotthivirat, Wei Xu, Timothy Rhodes, Matthew S Lamm, Ronald L Smith, Christopher T John, Yongchao Su, and Dan Fu. Detecting and Quantifying Microscale Chemical Reactions in Pharmaceutical Tablets by Stimulated Raman Scattering Microscopy. *Analytical Chemistry*, 2019. ISSN 0003-2700. doi: 10.1021/acs.analchem.9b01269.

[248] Barbara Sarri, Rafaël Canonge, Xavier Audier, Valérie Lavastre, Géraldine Pénarier, Jean Alie, and Hervé Rigneault. Discriminating polymorph distributions in pharmaceutical tablets using stimulated Raman scattering microscopy. *Journal of Raman Spectroscopy*, 50(12):1896–1904, 2019. ISSN 0377-0486. doi: 10.1002/jrs.5743.

[249] William J. Tipping, Martin Lee, Alan Serrels, Valerie G. Brunton, and Alison N. Hulme. Imaging drug uptake by bioorthogonal stimulated Raman scattering microscopy. *Chemical Science*, 8(8):5606–5615, 2017. ISSN 2041-6520. doi: 10.1039/c7sc01837a.

[250] Natalie L. Garrett, Bhumika Singh, Andrew Jones, and Julian Moger. Imaging microscopic distribution of antifungal agents in dandruff treatments with stimulated Raman scattering microscopy. *Journal of Biomedical Optics*, 22(6):066003–066003, 2017. ISSN 1083-3668. doi: 10.1117/1.jbo.22.6.066003.

[251] Andrew T Francis, Tai T Nguyen, Matthew S Lamm, Ryan Teller, Seth P Forster, Wei Xu, Timothy Rhodes, Ronald L Smith, Jesse Kuiper, Yongchao Su, and Dan Fu. In Situ Stimulated Raman Scattering (SRS) Microscopy Study of the Dissolution of

Sustained-Release Implant Formulation. *Molecular Pharmaceutics*, 15(12):5793–5801, 2018. ISSN 1543-8384. doi: 10.1021/acs.molpharmaceut.8b00965.

[252] W. Ruchira Silva, Emily L. Keller, and Renee R. Frontiera. Determination of resonance raman cross-sections for use in biological sers sensing with femtosecond stimulated raman spectroscopy. *Analytical Chemistry*, 86(15):7782–7787, 2014. doi: 10.1021/ac501701h.

[253] Hanqing Xiong and Wei Min. Combining the best of two worlds: Stimulated raman excited fluorescence. *The Journal of Chemical Physics*, 153(21):210901, 2020. doi: 10.1063/5.0030204.

[254] M. Fleischmann, P.J. Hendra, and A.J. McQuillan. Raman spectra of pyridine adsorbed at a silver electrode. *Chemical Physics Letters*, 26(2):163 – 166, 1974. ISSN 0009-2614. doi: https://doi.org/10.1016/0009-2614(74)85388-1. URL `http://www.sciencedirect.com/science/article/pii/0009261474853881`.

[255] David L. Jeanmaire and Richard P. Van Duyne. Surface raman spectroelectrochemistry: Part i. heterocyclic, aromatic, and aliphatic amines adsorbed on the anodized silver electrode. *Journal of Electroanalytical Chemistry and Interfacial Electrochemistry*, 84(1):1 – 20, 1977. ISSN 0022-0728. doi: 10.1016/s0022-0728(77)80224-6. URL `http://www.sciencedirect.com/science/article/pii/S0022072877802246`.

[256] John Wessel. Surface-enhanced optical microscopy. *J. Opt. Soc. Am. B*, 2(9):1538–1541, Sep 1985. doi: 10.1364/JOSAB.2.001538. URL `http://josab.osa.org/abstract.cfm?URI=josab-2-9-1538`.

[257] L. Novotny and N. van Hulst. Antennas for light. *Nature Photonics*, 5:83–90, 2011.

[258] Katrin Kneipp, Yang Wang, Harald Kneipp, Lev T. Perelman, Irving Itzkan, Ramachandra R. Dasari, and Michael S. Feld. Single molecule detection using surface-enhanced raman scattering (sers). *Phys. Rev. Lett.*, 78:1667–1670, Mar 1997. doi: 10.1103/PhysRevLett.78.1667. URL `https://link.aps.org/doi/10.1103/PhysRevLett.78.1667`.

[259] E. C. Le Ru, M. Meyer, and P. G. Etchegoin. Proof of single-molecule sensitivity in surface enhanced raman scattering (sers) by means of a two-analyte technique. *The Journal of Physical Chemistry B*, 110(4):1944–1948, 2006. ISSN 1520-6106. doi: 10.1021/jp054732v.

[260] Jon A. Dieringer, Robert B. Lettan, Karl A. Scheidt, and Richard P. Van Duyne. A frequency domain existence proof of single-molecule surface-enhanced raman spectroscopy. *Journal of the American Chemical Society*, 129(51):16249–16256, 2007. ISSN 0002-7863. doi: 10.1021/ja077243c.

[261] C. K. Chen, A. R. B. de Castro, Y. R. Shen, and F. DeMartini. Surface coherent anti-stokes raman spectroscopy. *Phys. Rev. Lett.*, 43:946–949, Sep 1979. doi: 10.1103/PhysRevLett.43.946. URL `https://link.aps.org/doi/10.1103/PhysRevLett.43.946`.

[262] Renee R. Frontiera, Anne-Isabelle Henry, Natalie L. Gruenke, and Richard P. Van Duyne. Surface-enhanced femtosecond stimulated raman spectroscopy. *The Journal of Physical Chemistry Letters*, 2(10):1199–1203, 2011. ISSN 1948-7185. doi: 10.1021/jz200498z. PMID: 26295326.

[263] Cheng Zong and Ji-Xin Cheng. Origin of dispersive line shapes in plasmon-enhanced stimulated raman scattering microscopy. *Nanophotonics*, 10(1):617–625, 2020. ISSN 2192-8606. doi: 10.1515/nanoph-2020-0313.

[264] Cheng Zong, Ranjith Premasiri, Haonan Lin, Yimin Huang, Chi Zhang, Chen Yang, Bin Ren, Lawrence D. Ziegler, and Ji-Xin Cheng. Plasmon-enhanced stimulated Raman scattering microscopy with single-molecule detection sensitivity. *Nature Communications*, 10(1):5318, 2019. doi: 10.1038/s41467-019-13230-1.

[265] Faezeh Tork Ladani and Eric Olaf Potma. Dyadic green's function formalism for photoinduced forces in tip-sample nanojunctions. *Phys. Rev. B*, 95:205440, May 2017. doi: 10.1103/PhysRevB.95.205440. URL `https://link.aps.org/doi/10.1103/PhysRevB.95.205440`.

[266] I. Rajapaksa and H. Kumar Wickramasinghe. Raman spectroscopy and microscopy based on mechanical force detection. *Applied Physics Letters*, 99(16):161103, 2011. doi: 10.1063/1.3652760.

[267] Shaowei Li, Siyu Chen, Jie Li, Ruqian Wu, and W. Ho. Joint space-time coherent vibration driven conformational transitions in a single molecule. *Phys. Rev. Lett.*, 119: 176002, Oct 2017. doi: 10.1103/PhysRevLett.119.176002.

[268] Maria Göppert-Mayer. Elementary processes with two quantum transitions. *Annalen der Physik*, 9(401):273–294, 1931. doi: https://doi.org/10.1002/andp.200910358.

[269] S. Fine and W. P. Hansen. Optical second harmonic generation in biological systems. *Appl. Opt.*, 10(10):2350–2353, Oct 1971. doi: 10.1364/AO.10.002350. URL `http://ao.osa.org/abstract.cfm?URI=ao-10-10-2350`.

[270] Isaac Freund and Moshe Deutsch. Second-harmonic microscopy of biological tissue. *Opt. Lett.*, 11(2):94–96, Feb 1986. doi: 10.1364/OL.11.000094. URL `http://ol.osa.org/abstract.cfm?URI=ol-11-2-94`.

[271] W Denk, JH Strickler, and WW Webb. Two-photon laser scanning fluorescence microscopy. *Science*, 248(4951):73–76, 1990. ISSN 0036-8075. doi: DOI:10.1126/science.2321027.

[272] C. V. RAMAN and K. S. KRISHNAN. A new type of secondary radiation. *Nature*, 121:501 EP –, 03 1928. URL `https://doi.org/10.1038/121501c0`.

[273] M. Schmitt and J. Popp. Raman spectroscopy at the beginning of the twenty-first century. *Journal of Raman Spectroscopy*, 37(1-3):20–28, 2006. doi: 10.1002/jrs.1486. URL `https://onlinelibrary.wiley.com/doi/abs/10.1002/jrs.1486`.

[274] Abdullah Chandra Sekhar Talari, Zanyar Movasaghi, Shazza Rehman, and Ihtesham ur Rehman. Raman spectroscopy of biological tissues. *Applied Spectroscopy Reviews*, 50(1):46–111, 2015. doi: 10.1080/05704928.2014.923902. URL `https://doi.org/10.1080/05704928.2014.923902`.

[275] E. Garmire, F. Pandarese, and C. H. Townes. Coherently driven molecular vibrations and light modulation. *Phys. Rev. Lett.*, 11:160–163, Aug 1963. doi: 10.1103/PhysRevLett.11.160. URL `https://link.aps.org/doi/10.1103/PhysRevLett.11.160`.

[276] R. P. Feynman, R. B. Leighton, and M. L. Sands. *The Feynman lectures on physics*, chapter 17. Addison-Wesley Pub. Co., Reading, Mass, 1963.

[277] R. Shankar. *Fundamentals of physics 1: mechanics, relativity, and thermodynamics*, chapter 17. Yale University Press, New Haven, Conn, 2019.

[278] William Ralph Bennet Jr. *The science of musical sound*. ASA Press, 2018.

[279] Paul Horowitz and Winfield Hill. *The art of electronics*. Cambridge University Press, New York, NY, third edition, 2015.

[280] Daniel C. Harris and Michael D. Bertolucci. *Symmetry and spectroscopy an introduction to vibrational and electronic spectroscopy*. Dover Publications, New York, New York, 1989.

[281] Derek A. Long. *The Raman Effect*. John Wiley & Sons, 2002.

[282] John R. Ferraro, Kazuo Nakamoto, and Chris W. Brown. *Introductory Raman Spectrocopy*. Academic Press, 2003.

[283] I. F. Almog, M. S. Bradley, and V. Bulovic. The Lorentz Oscillator and its applications. Master's thesis, MIT, 2011.

[284] Hervé Rigneault and Pascal Berto. Tutorial: Coherent Raman light matter interaction processes. *APL Photonics*, 3(9):091101, 2018. doi: 10.1063/1.5030335.

[285] A. F. J. Levi. *Essential Classical Mechanics for Device Physics*, chapter Chapter 5. Morgan & Claypool Publishers, 2016.

[286] R. P. Feynman, R. B. Leighton, and M. L. Sands. *The Feynman Lectures on Physics*, chapter Chapter 1: Atoms in Motion, page 1. Addison-Wesley Pub. Co., 1963.

[287] Wei Min, Christian W. Freudiger, Sijia Lu, and X. Sunney Xie. Coherent Nonlinear Optical Imaging: Beyond Fluorescence Microscopy. *Physical Chemistry*, 62(1), 2011. ISSN 0066-426X. doi: 10.1146/annurev.physchem.012809.103512.

[288] Kevin T Crampton, Aram Zeytunyan, Alexander S Fast, Faezeh T Ladani, Alba Alfonso-Garcia, Mayukh Banik, Steven Yampolsky, Dmitry A Fishman, Eric O Potma,

and V Ara Apkarian. Ultrafast Coherent Raman Scattering at Plasmonic Nanojunctions. *The Journal of Physical Chemistry C*, 120(37):20943–20953, 2016. ISSN 1932-7447. doi: 10.1021/acs.jpcc.6b02760.

[289] Robert W. Boyd. *Nonlinear Optics*. Academic Press, 3 edition, 2008.

[290] Soo-Y Lee, Donghui Zhang, David W McCamant, Philipp Kukura, and Richard A Mathies. Theory of femtosecond stimulated Raman spectroscopy. *The Journal of Chemical Physics*, 121(8):3632–3642, 2004. ISSN 0021-9606. doi: 10.1063/1.1777214.

[291] Eric Olaf Potma and Shaul Mukamel. *Coherent Raman Scattering Microscopy*, chapter Chapters Two and Three. CRC Press, 2013.

[292] E.A. Marx, E. Rutherford, E. Gehrcke, R. Seeliger, W.L.F. Hallwachs, and J.S. Townsend. *Handbuch der radiologie*. Number v. 1 in Handbuch der Radiologie: unter Mitwirkung von A. Bestelmeyer. Akademische Verlagsgesellschaft, 1920. URL `https://books.google.com/books?id=SBo4AQAAMAAJ`.

[293] Gregory W Faris and Richard A Copeland. Wavelength dependence of the Raman cross section for liquid water. *Applied Optics*, 36(12):2686, 1997. ISSN 0003-6935. doi: 10.1364/ao.36.002686.

[294] Bruce R Marshall and Raymond C Smith. Raman scattering and in-water ocean optical properties. *Applied Optics*, 29(1):71, 1990. ISSN 0003-6935. doi: 10.1364/ao.29.000071.

[295] N. Abe, M. Wakayama, and M. Ito. Absolute Raman intensities of liquids. *Journal of Raman Spectroscopy*, 6(1):38–41, 1977. ISSN 1097-4555. doi: 10.1002/jrs.1250060109.

[296] M J Colles and J E Griffiths. Relative and Absolute Raman Scattering Cross Sections in Liquids. *The Journal of Chemical Physics*, 56(7):3384–3391, 1972. ISSN 0021-9606. doi: 10.1063/1.1677709.

[297] K T Schomacker, J K Delaney, and P M Champion. Measurements of the absolute Raman cross sections of benzene. *The Journal of Chemical Physics*, 85(8):4240–4247, 1986. ISSN 0021-9606. doi: 10.1063/1.451795.

[298] Yan-Jie Tian, Jian Zuo, Liu-Yang Zhang, Zuo-Wei Li, Shu-Qin Gao, and Guo-Hui Lu. Study of resonance Raman cross section of aqueous $\beta$ -carotene at low concentrations. *Applied Physics B*, 87(4):727–730, 2007. ISSN 0946-2171. doi: 10.1007/s00340-007-2633-7.

[299] Douglas B. Murphy and Michael W. Davidson. *Fundamentals of Light Microscopy and Electronic Imaging*. Wiley-Blackwell, second edition, 2013.

[300] Valentina Parodi, Emanuela Jacchetti, Roberto Osellame, Giulio Cerullo, Dario Polli, and Manuela Teresa Raimondi. Nonlinear Optical Microscopy: From Fundamentals to Applications in Live Bioimaging. *Frontiers in Bioengineering and Biotechnology*, 8: 585363, 2020. ISSN 2296-4185. doi: 10.3389/fbioe.2020.585363.

[301] Paul Campagnola. Second Harmonic Generation Imaging Microscopy: Applications to Diseases Diagnostics. *Analytical Chemistry*, 83(9):3224–3231, 2011. ISSN 0003-2700. doi: 10.1021/ac1032325.

[302] Andrew M. Weiner. *Ultrafast Optics*. Wiley, 2009.

[303] Jeffrey L Suhalim, Geraint J Parfitt, Yilu Xie, Cintia S Pavia, Stephen C Pflugfelder, Tejas N Shah, Eric O Potma, Donald J Brown, and James V Jester. Effect of desiccating stress on mouse meibomian gland function. *The Ocular Surface*, 12(1):59–68, 2014. ISSN 9498249962. doi: 10.1016/j.jtos.2013.08.002.

[304] Marketa Kaucka and Igor Adameyko. Evolution and development of the cartilaginous skull: From a lancelet towards a human face. *Seminars in Cell & Developmental Biology*, 91:2–12, 2017. ISSN 1084-9521. doi: 10.1016/j.semcdb.2017.12.007.

[305] Alison G. Cole and Brian K. Hall. The nature and significance of invertebrate cartilages revisited: distribution and histology of cartilage and cartilage-like tissues within the Metazoa. *Zoology*, 107(4):261–273, 2004. ISSN 0944-2006. doi: 10.1016/j.zool.2004.05.001.

[306] Oscar A. Tarazona, Leslie A. Slota, Davys H. Lopez, GuangJun Zhang, and Martin J. Cohn. The genetic program for cartilage development has deep homology within Bilateria. *Nature*, 533(7601):86–89, 2016. ISSN 0028-0836. doi: 10.1038/nature17398.

[307] Y Chai, X Jiang, Y Ito, P Bringas, J Han, D H Rowitch, P Soriano, A P McMahon, and H M Sucov. Fate of the mammalian cranial neural crest during tooth and mandibular morphogenesis. *Development*, 127(8):1671–1679, 2000. ISSN 0950-1991. doi: 10.1242/dev.127.8.1671.

[308] Marianne E. Bronner and Nicole M. LeDouarin. Development and evolution of the neural crest: An overview. *Developmental Biology*, 366(1):2–9, 2012. ISSN 0012-1606. doi: 10.1016/j.ydbio.2011.12.042.

[309] B. McBratney-Owen, S. Iseki, S.D. Bamforth, B.R. Olsen, and G.M. Morriss-Kay. Development and tissue origins of the mammalian cranial base. *Developmental Biology*, 322(1):121–132, 2008. ISSN 0012-1606. doi: 10.1016/j.ydbio.2008.07.016.

[310] Qixuan Wang, Ji Won Oh, Hye-Lim Lee, Anukriti Dhar, Tao Peng, Raul Ramos, Christian Fernando Guerrero-Juarez, Xiaojie Wang, Ran Zhao, Xiaoling Cao, Jonathan Le, Melisa A Fuentes, Shelby C Jocoy, Antoni R Rossi, Brian Vu, Kim Pham, Xiaoyang Wang, Nanda Maya Mali, Jung Min Park, June-Hyug Choi, Hyunsu Lee, Julien M D Legrand, Eve Kandyba, Jung Chul Kim, Moonkyu Kim, John Foley, Zhengquan Yu, Krzysztof Kobielak, Bogi Andersen, Kiarash Khosrotehrani, Qing Nie, and Maksim V Plikus. A multi-scale model for hair follicles reveals heterogeneous domains driving rapid spatiotemporal hair growth patterning. *eLife*, 6:e22772, 2017. doi: 10.7554/elife.22772.

[311] Franz Leydig. Lehrbuch der Histologie des Menschen und der Thiere. 1857. doi: 10.5962/bhl.title.4845.

[312] T Akisaka and H Yamamoto. Freeze-fracture image of elastic cartilage in rat epiglottis. *Journal of electron microscopy*, 28(1):12–9, 1979. ISSN 0022-0744.

[313] Douglas R. Anderson. The ultrastructure of elastic and hyaline cartilage of the rat. *American Journal of Anatomy*, 114(3):403–433, 1964. ISSN 1553-0795. doi: 10.1002/aja.1001140305.

[314] Z Bradamante, L Kostović-Knezevic, B Levak-Svajger, and A Svajger. Differentiation of the secondary elastic cartilage in the external ear of the rat. *The International journal of developmental biology*, 35(3):311–20, 1991. ISSN 0214-6282.

[315] Ljiljana Kostović-Knežević, Želimir Bradamante, and Anton Švajger. Ultrastructure of elastic cartilage in the rat external ear. *Cell and Tissue Research*, 218(1):149–160, 1981. ISSN 0302-766X. doi: 10.1007/bf00210101.

[316] R. Mallinger and P. Böck. Differentiation of extracellular matrix in the cellular cartilage ("Zellknorpel") of the mouse pinna. *Anatomy and Embryology*, 172(1):69–74, 1985. ISSN 0340-2061. doi: 10.1007/bf00318945.

[317] Ellen Holm Nielsen. The elastic cartilage in the normal rat epiglottis. *Cell and Tissue Research*, 173(2):179–191, 1976. ISSN 0302-766X. doi: 10.1007/bf00221374.

[318] Charles F. Sanzone and Edward J. Reith. The development of the elastic cartilage of the mouse pinna. *American Journal of Anatomy*, 146(1):31–71, 1976. ISSN 1553-0795. doi: 10.1002/aja.1001460103.

[319] Anton Švajger. Chondrogenesis in the external ear of the rat. *Zeitschrift für Anatomie und Entwicklungsgeschichte*, 131(3):236–242, 1970. ISSN 0044-2232. doi: 10.1007/bf00520966.

[320] Jacqueline M Tabler, Maggie M Rigney, Gordon J Berman, Swetha Gopalakrishnan, Eglantine Heude, Hadeel Adel Al-lami, Basil Z Yannakoudiadkis, Rebecca D Fitch, Christopher Carter, Steven Vokes, Karen J Liu, Shahragim Tajbakhsh, SE Roian Egnor, and John B Wallingford. Cilia-mediated Hedgehog signaling controls form and function in the mammalian larynx. *eLife*, 6:e19153, 2017. doi: 10.7554/elife.19153.

[321] Xinjun He, Shinsuke Ohba, Hironori Hojo, and Andrew P. McMahon. AP-1 family members act with Sox9 to promote chondrocyte hypertrophy. *Development*, 143(16):3012–3023, 2016. ISSN 0950-1991. doi: 10.1242/dev.134502.

[322] Neal Anthwal and Hannah Thompson. The development of the mammalian outer and middle ear. *Journal of Anatomy*, 228(2):217–232, 2016. ISSN 1469-7580. doi: 10.1111/joa.12344.

[323] David A. Griffith, Daniel W. Kung, William P. Esler, Paul A. Amor, Scott W. Bagley, Carine Beysen, Santos Carvajal-Gonzalez, Shawn D. Doran, Chris Limberakis, Alan M. Mathiowetz, Kirk McPherson, David A. Price, Eric Ravussin, Gabriele E. Sonnenberg, James A. Southers, Laurel J. Sweet, Scott M. Turner, and Felix F. Vajdos. Decreasing the Rate of Metabolic Ketone Reduction in the Discovery of a Clinical Acetyl-CoA Carboxylase Inhibitor for the Treatment of Diabetes. *Journal of Medicinal Chemistry*, 57(24):10512–10526, 2014. ISSN 0022-2623. doi: 10.1021/jm5016022.

[324] Robert U Svensson, Seth J Parker, Lillian J Eichner, Matthew J Kolar, Martina Wallace, Sonja N Brun, Portia S Lombardo, Jeanine L Van Nostrand, Amanda Hutchins, Lilliana Vera, Laurie Gerken, Jeremy Greenwood, Sathesh Bhat, Geraldine Harriman, William F Westlin, H James Harwood, Alan Saghatelian, Rosana Kapeller, Christian M Metallo, and Reuben J Shaw. Inhibition of acetyl-CoA carboxylase suppresses fatty acid synthesis and tumor growth of non-small-cell lung cancer in preclinical models. *Nature Medicine*, 22(10):1108–1119, 2016. ISSN 1078-8956. doi: 10.1038/nm.4181.

[325] Richard Flavin, Stephane Peluso, Paul L Nguyen, and Massimo Loda. Fatty acid synthase as a potential therapeutic target in cancer. *Future Oncology*, 6(4):551–562, 2010. ISSN 1479-6694. doi: 10.2217/fon.10.11.

[326] JangEun Lee, Matthew C. Walsh, Kyle L. Hoehn, David E. James, E. John Wherry, and Yongwon Choi. Regulator of Fatty Acid Metabolism, Acetyl Coenzyme A Carboxylase 1, Controls T Cell Immunity. *The Journal of Immunology*, 192(7):3190–3199, 2014. ISSN 0022-1767. doi: 10.4049/jimmunol.1302985.

[327] Gustavo A. Gomez, Maneeshi S. Prasad, Nabjot Sandhu, Patrick B. Shelar, Alan W. Leung, and Martín I. García-Castro. Human neural crest induction by temporal modulation of WNT activation. *Developmental Biology*, 449(2):99–106, 2019. ISSN 0012-1606. doi: 10.1016/j.ydbio.2019.02.015.

[328] Alan W. Leung, Barbara Murdoch, Ahmed F. Salem, Maneeshi S. Prasad, Gustavo A. Gomez, and Martín I. García-Castro. WNT/$\beta$-catenin signaling mediates human neural crest induction via a pre-neural border intermediate. *Development*, 143(3):398–410, 2016. ISSN 0950-1991. doi: 10.1242/dev.130849.

[329] Xiyi Chen, Oleg Nadiarynkh, Sergey Plotnikov, and Paul J Campagnola. Second harmonic generation microscopy for quantitative analysis of collagen fibrillar structure. *Nature Protocols*, 7(4):654–669, 2012. ISSN 1754-2189. doi: 10.1038/nprot.2012.009.

[330] Andrea Vortkamp, Kaechoong Lee, Beate Lanske, Gino V. Segre, Henry M. Kronenberg, and Clifford J. Tabin. Regulation of Rate of Cartilage Differentiation by Indian Hedgehog and PTH-Related Protein. *Science*, 273(5275):613–622, 1996. ISSN 0036-8075. doi: 10.1126/science.273.5275.613.

[331] Yingzi Yang, Lilia Topol, Heuijung Lee, and Jinling Wu. Wnt5a and Wnt5b exhibit distinct activities in coordinating chondrocyte proliferation and differentiation. *Development*, 130(5):1003–1015, 2003. ISSN 0950-1991. doi: 10.1242/dev.00324.

[332] Trevor L Cameron, Daniele Belluoccio, Peter G Farlie, Bent Brachvogel, and John F Bateman. Global comparative transcriptome analysis of cartilage formation in vivo. *BMC Developmental Biology*, 9(1):20, 2009. ISSN 1471-213X. doi: 10.1186/1471-213x-9-20.

[333] Andreia Ionescu, Elena Kozhemyakina, Claudia Nicolae, Klaus H. Kaestner, Bjorn R. Olsen, and Andrew B. Lassar. FoxA Family Members Are Crucial Regulators of the Hypertrophic Chondrocyte Differentiation Program. *Developmental Cell*, 22(5):927–939, 2012. ISSN 1534-5807. doi: 10.1016/j.devcel.2012.03.011.

[334] Tomoko Sakata-Goto, Katsu Takahashi, Honoka Kiso, Boyen Huang, Hiroko Tsukamoto, Mitsuru Takemoto, Tatsunari Hayashi, Manabu Sugai, Takashi Nakamura, Yoshifumi Yokota, Akira Shimizu, Harold Slavkin, and Kazuhisa Bessho. Id2 controls chondrogenesis acting downstream of BMP signaling during maxillary morphogenesis. *Bone*, 50(1):69–78, 2012. ISSN 8756-3282. doi: 10.1016/j.bone.2011.09.049.

[335] Dong Wang and Hei Sook Sul. Upstream Stimulatory Factor Binding to the E-box at -65 Is Required for Insulin Regulation of the Fatty Acid Synthase Promoter*. *Journal of Biological Chemistry*, 272(42):26367–26374, 1997. ISSN 0021-9258. doi: 10.1074/jbc.272.42.26367.

[336] BM Spiegelman, P Puigserver, and Z Wu. Regulation of adipogenesis and energy balance by PPAR$\gamma$ and PGC-1. *International Journal of Obesity*, 24(Suppl 4):S8–S10, 2000. ISSN 0307-0565. doi: 10.1038/sj.ijo.0801492.

[337] Rachel K. Zwick, Christian F. Guerrero-Juarez, Valerie Horsley, and Maksim V. Plikus. Anatomical, Physiological, and Functional Diversity of Adipose Tissue. *Cell Metabolism*, 27(1):68–83, 2018. ISSN 1550-4131. doi: 10.1016/j.cmet.2017.12.002.

[338] Kathryn Ellis, Jennifer Bagwell, and Michel Bagnat. Notochord vacuoles are lysosome-related organelles that function in axis and spine morphogenesis. *Journal of Cell Biology*, 200(5):667–679, 2013. ISSN 0021-9525. doi: 10.1083/jcb.201212095.

[339] D S Adams, R Keller, and M A Koehl. The mechanics of notochord elongation, straightening and stiffening in the embryo of Xenopus laevis. *Development*, 110(1):115–130, 1990. ISSN 0950-1991. doi: 10.1242/dev.110.1.115.

[340] J A Buckwalter, D Mower, R Ungar, J Schaeffer, and B Ginsberg. Morphometric analysis of chondrocyte hypertrophy. *The Journal of Bone & Joint Surgery*, 68(2):243–255, 1986. ISSN 0021-9355. doi: 10.2106/00004623-198668020-00010.

[341] M Cnop, J C Hannaert, A Hoorens, D L Eizirik, and D G Pipeleers. Inverse Relationship Between Cytotoxicity of Free Fatty Acids in Pancreatic Islet Cells and Cellular Triglyceride Accumulation. *Diabetes*, 50(8):1771–1777, 2001. ISSN 0012-1797. doi: 10.2337/diabetes.50.8.1771.

[342] Ashley W. Seifert, Stephen G. Kiama, Megan G. Seifert, Jacob R. Goheen, Todd M. Palmer, and Malcolm Maden. Skin shedding and tissue regeneration in African spiny

mice (Acomys). *Nature*, 489(7417):561–565, 2012. ISSN 0028-0836. doi: 10.1038/nature11499.

[343] Nils A Kraus, Franziska Ehebauer, Benedikt Zapp, Bianca Rudolphi, Bettina J Kraus, and Daniel Kraus. Quantitative assessment of adipocyte differentiation in cell culture. *Adipocyte*, 5(4):351–358, 2016. ISSN 2162-3945. doi: 10.1080/21623945.2016.1240137.

[344] Annika Mehlem, Carolina E Hagberg, Lars Muhl, Ulf Eriksson, and Annelie Falkevall. Imaging of neutral lipids by oil red O for analyzing the metabolic status in health and disease. *Nature Protocols*, 8(6):1149–1154, 2013. ISSN 1754-2189. doi: 10.1038/nprot.2013.055.

[345] Priyanka Chhadva, Raquel Goldhardt, and Anat Galor. Meibomian Gland Disease The Role of Gland Dysfunction in Dry Eye Disease. *Ophthalmology*, 124(11):S20–S26, 2017. ISSN 0161-6420. doi: 10.1016/j.ophtha.2017.05.031.

[346] Jana Dietrich, Fabian Garreis, and Friedrich Paulsen. Pathophysiology of Meibomian Glands – An Overview. *Ocular Immunology and Inflammation*, pages 1–8, 2021. ISSN 0927-3948. doi: 10.1080/09273948.2021.1905856.

[347] Jahmunah Vicnesh, Shu Lih Oh, Joel Koh En Wei, Edward J. Ciaccio, Kuang Chua Chua, Louis Tong, and U. Rajendra Acharya. Thoughts concerning the application of thermogram images for automated diagnosis of dry eye – A review. *Infrared Physics & Technology*, 106:103271, 2020. ISSN 1350-4495. doi: 10.1016/j.infrared.2020.103271.

[348] Gary N. Foulks and Anthony J. Bron. Meibomian Gland Dysfunction: A Clinical Scheme for Description, Diagnosis, Classification, and Grading. *The Ocular Surface*, 1(3):107–126, 2003. ISSN 1542-0124. doi: 10.1016/s1542-0124(12)70139-8.

[349] Igor A. Butovich, Eduardo Uchiyama, and James P. McCulley. Lipids of human meibum: mass-spectrometric analysis and structural elucidation 1. *Journal of Lipid Research*, 48(10):2220–2235, 2007. ISSN 0022-2275. doi: 10.1194/jlr.m700237-jlr200.

[350] Anthony J Bron. Diagnosis of Dry Eye. *Survey of Ophthalmology*, 45:S221–S226, 2001. ISSN 0039-6257. doi: 10.1016/s0039-6257(00)00201-0.

[351] James V. Jester, Eric Potma, and Donald J. Brown. PPAR$\gamma$ Regulates Mouse Meibocyte Differentiation and Lipid Synthesis. *The Ocular Surface*, 14(4):484–494, 2016. ISSN 1542-0124. doi: 10.1016/j.jtos.2016.08.001.

[352] A.J. Bron and J.M. Tiffany. The Contribution of Meibomian Disease to Dry Eye. *The Ocular Surface*, 2(2):149–164, 2004. ISSN 1542-0124. doi: 10.1016/s1542-0124(12)70150-7.

[353] William D. Mathers, William J. Shields, Mahipal S. Sachdev, W Matthew Petroll, and James V. Jester. Meibomian Gland Morphology and Tear Osmolarity: Changes with Accutane Therapy. *Cornea*, 10(4):286–290, 1991. ISSN 0277-3740. doi: 10.1097/00003226-199107000-00002.

[354] Chyong Jy Nien, Jerry R. Paugh, Salina Massei, Andrew J. Wahlert, Winston W. Kao, and James V. Jester. Age-related changes in the meibomian gland. *Experimental Eye Research*, 89(6):1021–1027, 2009. ISSN 0014-4835. doi: 10.1016/j.exer.2009.08.013.

[355] Chyong Jy Nien, Salina Massei, Gloria Lin, Hongshan Liu, Jerry R Paugh, Chia-Yang Liu, Winston Whei-Yang Kao, Donald J Brown, and James V Jester. The development of meibomian glands in mice. *Molecular vision*, 16:1132–40, 2010.

[356] Maryam Ahmadian, Jae Myoung Suh, Nasun Hah, Christopher Liddle, Annette R Atkins, Michael Downes, and Ronald M Evans. PPAR$\gamma$ signaling and metabolism: the good, the bad and the future. *Nature Medicine*, 19(5):557–566, 2013. ISSN 1078-8956. doi: 10.1038/nm.3159.

[357] Evan D Rosen, Pasha Sarraf, Amy E Troy, Gary Bradwin, Kathryn Moore, David S Milstone, Bruce M Spiegelman, and Richard M Mortensen. PPAR$\gamma$ Is Required for the Differentiation of Adipose Tissue In Vivo and In Vitro. *Molecular Cell*, 4(4):611–617, 1999. ISSN 1097-2765. doi: 10.1016/s1097-2765(00)80211-7.

[358] Robert L. Rosenfield, Dianne Deplewski, and Marianne E. Greene. Peroxisome Proliferator-Activated Receptors and Skin Development. *Hormone Research in Paediatrics*, 54(5-6):269–274, 2000. ISSN 1663-2818. doi: 10.1159/000053270.

[359] Nishit R. Trivedi, Zhaoyuan Cong, Amanda M. Nelson, Adam J. Albert, Lorraine L. Rosamilia, Surendra Sivarajah, Kathryn L. Gilliland, Wenlei Liu, David T. Mauger, Robert A. Gabbay, and Diane M. Thiboutot. Peroxisome Proliferator-Activated Receptors Increase Human Sebum Production. *Journal of Investigative Dermatology*, 126 (9):2002–2009, 2006. ISSN 0022-202X. doi: 10.1038/sj.jid.5700336.

[360] James V. Jester. Frontiers of Ocular Surface Regenerative Medicine. *The Ocular Surface*, 14(2):81, 2016. ISSN 1542-0124. doi: 10.1016/j.jtos.2016.02.002.

[361] Sun Woong Kim, Yilu Xie, Paul Q. Nguyen, Vickie T. Bui, Kelly Huynh, Jonathan S. Kang, Donald J. Brown, and James V. Jester. PPAR$\gamma$ regulates meibocyte differentiation and lipid synthesis of cultured human meibomian gland epithelial cells (hMGEC). *The Ocular Surface*, 2018. ISSN 1542-0124. doi: 10.1016/j.jtos.2018.07.004.

[362] Sun Woong Kim, Donald J. Brown, and James V. Jester. Transcriptome analysis after PPAR$\gamma$ activation in human meibomian gland epithelial cells (hMGEC). *The Ocular Surface*, 17(4):809–816, 2019. ISSN 1542-0124. doi: 10.1016/j.jtos.2019.02.003.

[363] Limei Wang, Birgit Waltenberger, Eva-Maria Pferschy-Wenzig, Martina Blunder, Xin Liu, Clemens Malainer, Tina Blazevic, Stefan Schwaiger, Judith M. Rollinger, Elke H. Heiss, Daniela Schuster, Brigitte Kopp, Rudolf Bauer, Hermann Stuppner, Verena M. Dirsch, and Atanas G. Atanasov. Natural product agonists of peroxisome proliferator-activated receptor gamma (PPAR$\gamma$): a review. *Biochemical Pharmacology*, 92(1): 73–89, 2014. ISSN 0006-2952. doi: 10.1016/j.bcp.2014.07.018.

[364] Marian S Macsai. The role of omega-3 dietary supplementation in blepharitis and meibomian gland dysfunction (an AOS thesis). *Transactions of the American Ophthalmological Society*, 106:336–56, 2008.

[365] Giuseppe Giannaccare, Marco Pellegrini, Stefano Sebastiani, Federico Bernabei, Matilde Roda, Leonardo Taroni, Piera Versura, and Emilio C. Campos. Efficacy of Omega-3 Fatty Acid Supplementation for Treatment of Dry Eye Disease. *Cornea*, Publish Ahead of Print(&NA;):&NA;, 2019. ISSN 0277-3740. doi: 10.1097/ico.0000000000001884.

[366] A Francis, K Berry, Y Chen, B Figueroa, and D Fu. Label-free pathology by spectrally sliced femtosecond stimulated Raman scattering (SRS) microscopy. 2017. doi: 10.1371/journal.pone.0178750.

[367] Dan Fu and X Sunney Xie. Reliable Cell Segmentation Based on Spectral Phasor Analysis of Hyperspectral Stimulated Raman Scattering Imaging Data. *Analytical Chemistry*, 86(9):4115–4119, 2014. ISSN 0003-2700. doi: 10.1021/ac500014b.

[368] Bruce P. Gaber and Warner L. Peticolas. On the quantitative interpretation of biomembrane structure by Raman spectroscopy. *Biochimica et Biophysica Acta (BBA) - Biomembranes*, 465(2):260–274, 1977. ISSN 0005-2736. doi: 10.1016/0005-2736(77)90078-5.

[369] Hilde A. Rinia, Koert N.J. Burger, Mischa Bonn, and Michiel Müller. Quantitative Label-Free Imaging of Lipid Composition and Packing of Individual Cellular Lipid Droplets Using Multiplex CARS Microscopy. *Biophysical Journal*, 95(10):4908–4914, 2008. ISSN 0006-3495. doi: 10.1529/biophysj.108.137737.

[370] RG Snyder, HL Strauss, and Elliger -CA of Physical. Carbon-hydrogen stretching modes and the structure of n-alkyl chains. 1. Long, disordered chains. 1982. doi: 10.1021/j100223a018.

[371] R Verheijen, H J Kuijpers, R van Driel, J L Beck, J H van Dierendonck, G J Brakenhoff, and F C Ramaekers. Ki-67 detects a nuclear matrix-associated proliferation-related antigen. II. Localization in mitotic cells and association with chromosomes. *Journal of Cell Science*, 92(4):531–540, 1989. ISSN 0021-9533. doi: 10.1242/jcs.92.4.531.

[372] Francisca Echeverría, Macarena Ortiz, Rodrigo Valenzuela, and Luis A. Videla. Long-chain polyunsaturated fatty acids regulation of PPARs, signaling: Relationship to tissue development and aging. *Prostaglandins, Leukotrienes and Essential Fatty Acids (PLEFA)*, 114:28–34, 2016. ISSN 0952-3278. doi: 10.1016/j.plefa.2016.10.001.

[373] Ron F. Morrison and Stephen R. Farmer. Role of PPAR$\gamma$ in Regulating a Cascade Expression of Cyclin-dependent Kinase Inhibitors, p18(INK4c) and p21(Waf1/Cip1), during Adipogenesis*. *Journal of Biological Chemistry*, 274(24):17088–17097, 1999. ISSN 0021-9258. doi: 10.1074/jbc.274.24.17088.

[374] Maik Dahlhoff, Emanuela Camera, Mauro Picardo, Christos C. Zouboulis, Lawrence Chan, Benny Hung-Junn Chang, and Marlon R. Schneider. PLIN2, the major perilipin regulated during sebocyte differentiation, controls sebaceous lipid accumulation in vitro and sebaceous gland size in vivo. *Biochimica et Biophysica Acta (BBA) - General Subjects*, 1830(10):4642–4649, 2013. ISSN 0304-4165. doi: 10.1016/j.bbagen.2013.05.016.

[375] Yu Takahashi, Akihiro Shinoda, Haruhiko Kamada, Makoto Shimizu, Jun Inoue, and Ryuichiro Sato. Perilipin2 plays a positive role in adipocytes during lipolysis by escaping proteasomal degradation. *Scientific Reports*, 6(1):20975, 2016. doi: 10.1038/srep20975.

[376] Miki Kutsuna, Toshio Kodama, Michihiro Sumida, Ayako Nagai, Masakatsu Higashine, Wei Zhang, Yasuhito Hayashi, Atsushi Shiraishi, and Yuichi Ohashi. Presence of adipose differentiation-related protein in rat meibomian gland cells. *Experimental Eye Research*, 84(4):687–693, 2007. ISSN 0014-4835. doi: 10.1016/j.exer.2006.12.007.

[377] Igor A. Butovich. Meibomian glands, meibum, and meibogenesis. *Experimental Eye Research*, 163:2–16, 2017. ISSN 0014-4835. doi: 10.1016/j.exer.2017.06.020.

[378] Ulrike Hampel, Magret Krüger, Carolina Kunnen, Fabian Garreis, Mark Willcox, and Friedrich Paulsen. In vitro effects of docosahexaenoic and eicosapentaenoic acid on human meibomian gland epithelial cells. *Experimental Eye Research*, 140:139–148, 2015. ISSN 0014-4835. doi: 10.1016/j.exer.2015.08.024.

[379] Ulrike Hampel, Antje Schröder, Todd Mitchell, Simon Brown, Peta Snikeris, Fabian Garreis, Carolina Kunnen, Mark Willcox, and Friedrich Paulsen. Serum-Induced Keratinization Processes in an Immortalized Human Meibomian Gland Epithelial Cell Line. *PLOS ONE*, 10(6):e0128096, 2015. doi: 10.1371/journal.pone.0128096.

[380] Wendy R. Kam, Yang Liu, Juan Ding, and David A. Sullivan. Do Cyclosporine A, an IL-1 Receptor Antagonist, Uridine Triphosphate, Rebamipide, and/or Bimatoprost Regulate Human Meibomian Gland Epithelial Cells?Human Meibomian Gland Epithelial Cells. *Investigative Ophthalmology & Visual Science*, 57(10):4287–4294, 2016. ISSN 1552-5783. doi: 10.1167/iovs.16-19937.

[381] Shaohui Liu, Mark P. Hatton, Payal Khandelwal, and David A. Sullivan. Culture, Immortalization, and Characterization of Human Meibomian Gland Epithelial Cells. *Investigative Ophthalmology & Visual Science*, 51(8):3993–4005, 2010. ISSN 1552-5783. doi: 10.1167/iovs.09-5108.

[382] David A. Sullivan, Yang Liu, Wendy R. Kam, Juan Ding, Karin M. Green, Scott A. Shaffer, Mark P. Hatton, and Shaohui Liu. Serum-Induced Differentiation of Human Meibomian Gland Epithelial CellsDifferentiation of Meibomian Gland Epithelial Cells. *Investigative Ophthalmology & Visual Science*, 55(6):3866–3877, 2014. ISSN 1552-5783. doi: 10.1167/iovs.13-13407.

[383] Yang Liu, Wendy R. Kam, Juan Ding, and David A. Sullivan. Can Tetracycline Antibiotics Duplicate the Ability of Azithromycin to Stimulate Human Meibomian Gland Epithelial Cell Differentiation?. *Cornea*, 34(3):342–346, 2015. ISSN 0277-3740. doi: 10.1097/ico.0000000000000351.

[384] P. E. Kolattukudy, Linda M. Rogers, and Nicholas Nicolaides. Biosynthesis of lipids by bovine meibomian glands. *Lipids*, 20(7):468–474, 1985. ISSN 0024-4201. doi: 10.1007/bf02534238.

[385] Julia M. Duerden and John M. Tiffany. Lipid synthesis in vitro by rabbit Meibomian gland tissue and its inhibition by tetracycline. *Biochimica et Biophysica Acta (BBA) - Lipids and Lipid Metabolism*, 1042(1):13–18, 1990. ISSN 0005-2760. doi: 10.1016/0005-2760(90)90050-8.

[386] William P. Esler, Gregory J. Tesz, Marc K. Hellerstein, Carine Beysen, Raja Sivamani, Scott M. Turner, Steven M. Watkins, Paul A. Amor, Santos Carvajal-Gonzalez, Frank J. Geoly, Kathleen E. Biddle, Julie J. Purkal, Mark Fitch, Clare Buckeridge, Annette M. Silvia, David A. Griffith, Matthew Gorgoglione, Lauren Hassoun, Suzana S. Bosanac, Nicholas B. Vera, Timothy P. Rolph, Jeffrey A. Pfefferkorn, and Gabriele E. Sonnenberg. Human sebum requires de novo lipogenesis, which is increased in acne vulgaris and suppressed by acetyl-CoA carboxylase inhibition. *Science Translational Medicine*, 11(492):eaau8465, 2019. ISSN 1946-6234. doi: 10.1126/scitranslmed.aau8465.

[387] Johannes Schindelin, Ignacio Arganda-Carreras, Erwin Frise, Verena Kaynig, Mark Longair, Tobias Pietzsch, Stephan Preibisch, Curtis Rueden, Stephan Saalfeld, Benjamin Schmid, Jean-Yves Tinevez, Daniel James White, Volker Hartenstein, Kevin Eliceiri, Pavel Tomancak, and Albert Cardona. Fiji: an open-source platform for biological-image analysis. *Nature Methods*, 9(7):676–682, 2012. ISSN 1548-7091. doi: 10.1038/nmeth.2019.

[388] Lingyan Shi, Yihui Shen, and Wei Min. Invited Article: Visualizing protein synthesis in mice with in vivo labeling of deuterated amino acids using vibrational imaging. *APL Photonics*, 3(9):092401, 2018. doi: 10.1063/1.5028134. URL `https://doi.org/10.1063/1.5028134`.

[389] J. Del Boca and J. P. Flatt. Fatty Acid Synthesis from Glucose and Acetate and the Control of Lipogenesis in Adipose Tissue. *European J. Biochem*, 1969.

[390] Xue Gao, Shu-Hai Lin, Feng Ren, Jin-Tao Li, Jia-Jia Chen, Chuan-Bo Yao, Hong-Bin Yang, Shu-Xia Jiang, Guo-Quan Yan, Di Wang, Yi Wang, Ying Liu, Zongwei Cai, Ying-Ying Xu, Jing Chen, Wenqiang Yu, Peng-Yuan Yang, and Qun-Ying Lei. Acetate functions as an epigenetic metabolite to promote lipid synthesis under hypoxia. *Nature Communications*, 7(1):11960, 2016. doi: 10.1038/ncomms11960.

[391] Guiping Gong, Xu Zhang, and Tianwei Tan. Simultaneously enhanced intracellular lipogenesis and $\beta$-carotene biosynthesis of Rhodotorula glutinis by light exposure with

sodium acetate as the substrate. *Bioresource Technology*, 295:122274, 2020. ISSN 0960-8524. doi: 10.1016/j.biortech.2019.122274.

[392] Kirsten L. Zambell, Mark D. Fitch, and Sharon E. Fleming. Acetate and Butyrate Are the Major Substrates for De Novo Lipogenesis in Rat Colonic Epithelial Cells. *The Journal of Nutrition*, 133(11):3509–3515, 2003. ISSN 0022-3166. doi: 10.1093/jn/133.11.3509.

[393] Gianfranca Carta, Elisabetta Murru, Sebastiano Banni, and Claudia Manca. Palmitic Acid: Physiological Role, Metabolism and Nutritional Implications. *Frontiers in Physiology*, 8:902, 2017. ISSN 1664-042X. doi: 10.3389/fphys.2017.00902.

[394] C Joffre, M Souchier, S Grégoire, S Viau, L Bretillon, N Acar, A M Bron, and C Creuzot-Garcher. Differences in meibomian fatty acid composition in patients with meibomian gland dysfunction and aqueous-deficient dry eye. *British Journal of Ophthalmology*, 92(1):116, 2008. ISSN 0007-1161. doi: 10.1136/bjo.2007.126144.

[395] Burkhardt S. Schuett and Thomas J. Millar. An investigation of the likely role of (O-acyl) $\omega$-hydroxy fatty acids in meibomian lipid films using (O-oleyl) $\omega$-hydroxy palmitic acid as a model. *Experimental Eye Research*, 115:57–64, 2013. ISSN 0014-4835. doi: 10.1016/j.exer.2013.06.016.

[396] Nagayoshi Asano, Ulrike Hampel, Fabian Garreis, Antje Schröder, Martin Schicht, Christian M. Hammer, and Friedrich Paulsen. Differentiation Patterns of Immortalized Human Meibomian Gland Epithelial Cells in Three-Dimensional Culture. *Investigative Ophthalmology & Visual Science*, 59(3):1343–1353, 2018. ISSN 1552-5783. doi: 10.1167/iovs.17-23266.

[397] Adam M. Hanninen, Richard C. Prince, Raul Ramos, Maksim V. Plikus, and Eric O. Potma. High-resolution infrared imaging of biological samples with third-order sum-frequency generation microscopy. *Biomed. Opt. Express*, 9(10):4807—4817, 2018. doi: 10.1364/boe.9.004807. URL `http://www.osapublishing.org/boe/abstract.cfm?URI=boe-9-10-4807`.

[398] A. M. Hanninen, R. C. Prince, and E. O. Potma. Triple Modal Coherent Nonlinear Imaging With Vibrational Contrast. *IEEE Journal of Selected Topics in Quantum Electronics*, 25(1):1–11, 2019. ISSN 1077-260X. doi: 10.1109/jstqe.2018.2846030.

[399] Irini Akritopoulou-Zanze. Isocyanide-based multicomponent reactions in drug discovery. *Current Opinion in Chemical Biology*, 12(3):324–331, 2008. ISSN 1367-5931. doi: 10.1016/j.cbpa.2008.02.004.

[400] Dexter C. Davis, Haroon Mohammad, Kwaku Kyei-Baffour, Waleed Younis, Cassidy Noel Creemer, Mohamed N. Seleem, and Mingji Dai. Discovery and characterization of aryl isonitriles as a new class of compounds versus methicillin- and vancomycin-resistant Staphylococcus aureus. *European Journal of Medicinal Chemistry*, 101:384–390, 2015. ISSN 0223-5234. doi: 10.1016/j.ejmech.2015.06.031.

[401] Yao-Bing Huang, Wenlong Cai, Antonio Del Rio Flores, Frederick F Twigg, and Wenjun Zhang. Facile Discovery and Quantification of Isonitrile Natural Products via Tetrazine-Based Click Reactions. *Analytical Chemistry*, 92(1):599–602, 2019. ISSN 0003-2700. doi: 10.1021/acs.analchem.9b05147.

[402] J. E. D. Davies and W. J. Wood. The Raman spectrum and structure of methyl isocyanide. *Journal of Raman Spectroscopy*, 1(4):383–385, 1973. ISSN 1097-4555. doi: 10.1002/jrs.1250010410.

[403] Alexander S. Karns, Bryan D. Ellis, Philipp C. Roosen, Zeinab Chahine, Karine G. Le Roch, and Christopher D. Vanderwal. Concise Synthesis of the Antiplasmodial Isocyanoterpene 7,20-Diisocyanoadociane. *Angewandte Chemie International Edition*, 58 (39):13749–13752, 2019. ISSN 1433-7851. doi: 10.1002/anie.201906834.

[404] J T Baker, R J Wells, W E Oberhaensli, and G B Hawes. A new diisocyanide of novel ring structure from a sponge. *Journal of the American Chemical Society*, 98(13): 4010–4012, 1976. ISSN 0002-7863. doi: 10.1021/ja00429a053.

[405] Hiroaki Miyaoka, Yusuke Okubo, Makiko Muroi, Hidemichi Mitome, and Etsuko Kawashima. A Formal Synthesis of Antimalarial Diterpenoid 7,20-Diisocyanoadociane. *Chemistry Letters*, 40(3):246–247, 2011. ISSN 0366-7022. doi: 10.1246/cl.2011.246.

[406] Hai-Hua Lu, Sergey V Pronin, Yevgeniya Antonova-Koch, Stephan Meister, Elizabeth A Winzeler, and Ryan A Shenvi. Synthesis of (+)-7,20-Diisocyanoadociane and Liver-Stage Antiplasmodial Activity of the Isocyanoterpene Class. *Journal of the American Chemical Society*, 138(23):7268–7271, 2016. ISSN 0002-7863. doi: 10.1021/jacs.6b03899.

[407] Andy J Chen, Kai-Chih Huang, Selina Bopp, Robert Summers, Puting Dong, Yimin Huang, Cheng Zong, Dyann Wirth, and Ji-Xin Cheng. Quantitative imaging of intraerythrocytic hemozoin by transient absorption microscopy. *Journal of Biomedical Optics*, 25(01):1, 2019. ISSN 1083-3668. doi: 10.1117/1.jbo.25.1.014507.

[408] M. S. Edenborough and R. B. Herbert. Naturally occurring isocyanides. *Natural Product Reports*, 5(3):229–245, 1988. ISSN 0265-0568. doi: 10.1039/np9880500229.

[409] Paul J Scheuer. Isocyanides and cyanides as natural products. *Accounts of Chemical Research*, 25(10):433–439, 1992. ISSN 0001-4842. doi: 10.1021/ar00022a001.

[410] David S. Sholl and Janice A. Steckel. *Density Functional Theory: A Practical Introduction*. John Wiley & Sons, Inc, 2009.

[411] Kieron Burke. *The ABC of DFT*. Department of Chemistry, UCI, 2007.

[412] Richard A. Friesner. Ab initio quantum chemistry: Methodology and applications. *Proceedings of the National Academy of Sciences of the United States of America*, 102 (19):6648–6653, 2005. ISSN 0027-8424. doi: 10.1073/pnas.0408036102.

[413] Dmitrij Rappoport, Nathan R. M Crawford, Filipp Furche, and Kieron Burke. What functional should I choose? Technical report, UCI, 2008.

[414] Brian C. Ferrari and Chris J. Bennett. A Comparison of Medium-Sized Basis Sets for the Prediction of Geometries, Vibrational Frequencies, Infrared Intensities and Raman Activities for Water. *Journal of Physics: Conference Series*, 1290(1):012013, 2019. ISSN 1742-6596. doi: 10.1088/1742-6596/1290/1/012013.

[415] James R Cheeseman and Michael J Frisch. Basis Set Dependence of Vibrational Raman and Raman Optical Activity Intensities. *Journal of Chemical Theory and Computation*, 7(10):3323–3334, 2011. ISSN 1549-9618. doi: 10.1021/ct200507e.

[416] Johannes Neugebauer, Markus Reiher, Carsten Kind, and Bernd A. Hess. Quantum chemical calculation of vibrational spectra of large molecules—Raman and IR spectra for Buckminsterfullerene. *Journal of Computational Chemistry*, 23(9):895–910, 2002. ISSN 1096-987X. doi: 10.1002/jcc.10089.

[417] Matthew S Barclay, Christopher G Elles, and Marco Caricato. Benchmark Study of Ground-State Raman Spectra in Conjugated Molecules. *Journal of Chemical Theory and Computation*, 16(1):612–620, 2019. ISSN 1549-9618. doi: 10.1021/acs.jctc.9b00960.

[418] A Leif Hickey and Christopher N Rowley. Benchmarking Quantum Chemical Methods for the Calculation of Molecular Dipole Moments and Polarizabilities. *The Journal of Physical Chemistry A*, 118(20):3678–3687, 2014. ISSN 1089-5639. doi: 10.1021/jp502475e.

[419] John P. Perdew, Kieron Burke, and Matthias Ernzerhof. Generalized Gradient Approximation Made Simple. *Physical Review Letters*, 77(18):3865–3868, 1996. ISSN 0031-9007. doi: 10.1103/physrevlett.77.3865.

[420] Axel D. Becke. Density-functional thermochemistry. III. The role of exact exchange. *The Journal of Chemical Physics*, 98(7):5648–5652, 1993. ISSN 0021-9606. doi: 10.1063/1.464913.

[421] Ansgar Schäfer, Christian Huber, and Reinhart Ahlrichs. Fully optimized contracted Gaussian basis sets of triple zeta valence quality for atoms Li to Kr. *The Journal of Chemical Physics*, 100(8):5829–5835, 1994. ISSN 0021-9606. doi: 10.1063/1.467146.

[422] Andrzej J. Sadlej. Medium-size polarized basis sets for high-level correlated calculations of molecular electric properties. *Collect. Czech. Chem. Commun.*, 53:1995–2016, 1988. doi: 10.1135/cccc19881995.

[423] David Feller. The role of databases in support of computational chemistry calculations. *J. Comput. Chem.*, 17:1571–1586, 1996. doi: 10.1002/(SICI)1096-987X(199610)17:13⟨1571::AID-JCC9⟩3.0.CO;2-P.

[424] Karen L. Schuchardt, Brett T. Didier, Todd Elsethagen, Lisong Sun, Vidhya Gurumoorthi, Jared Chase, Jun Li, and Theresa L. Windus. Basis set exchange: A community database for computational sciences. *J. Chem. Inf. Model.*, 47:1045–1052, 2007. doi: 10.1021/ci600510j.

[425] Benjamin P. Pritchard, Doaa Altarawy, Brett Didier, Tara D. Gibsom, and Theresa L. Windus. A new basis set exchange: An open, up-to-date resource for the molecular sciences community. *J. Chem. Inf. Model.*, 59:4814–4820, 2019. doi: 10.1021/acs.jcim.9b00725.

[426] M. J. Frisch, G. W. Trucks, H. B. Schlegel, G. E. Scuseria, M. A. Robb, J. R. Cheeseman, G. Scalmani, V. Barone, G. A. Petersson, H. Nakatsuji, X. Li, M. Caricato, A. V. Marenich, J. Bloino, B. G. Janesko, R. Gomperts, B. Mennucci, H. P. Hratchian, J. V. Ortiz, A. F. Izmaylov, J. L. Sonnenberg, D. Williams-Young, F. Ding, F. Lipparini, F. Egidi, J. Goings, B. Peng, A. Petrone, T. Henderson, D. Ranasinghe, V. G. Zakrzewski, J. Gao, N. Rega, G. Zheng, W. Liang, M. Hada, M. Ehara, K. Toyota, R. Fukuda, J. Hasegawa, M. Ishida, T. Nakajima, Y. Honda, O. Kitao, H. Nakai, T. Vreven, K. Throssell, J. A. Montgomery, Jr., J. E. Peralta, F. Ogliaro, M. J. Bearpark, J. J. Heyd, E. N. Brothers, K. N. Kudin, V. N. Staroverov, T. A. Keith, R. Kobayashi, J. Normand, K. Raghavachari, A. P. Rendell, J. C. Burant, S. S. Iyengar, J. Tomasi, M. Cossi, J. M. Millam, M. Klene, C. Adamo, R. Cammi, J. W. Ochterski, R. L. Martin, K. Morokuma, O. Farkas, J. B. Foresman, and D. J. Fox. Gaussian˜16 Revision C.01, 2016. Gaussian Inc. Wallingford CT.

[427] Derek Lowe. Things I Won't Work With: Small, Smelly Isocyanides. Technical report, Science Translational Medicine, 2010.